2020

A Role for Mindbomb 1 in Adenovirus Genome Delivery

Stephanie Sarbanes

A ROLE FOR MINDBOMB 1 IN ADENOVIRUS GENOME DELIVERY

A Thesis Presented to the Faculty of
The Rockefeller University
in Partial Fulfillment of the Requirements for
the degree of Doctor of Philosophy

by
Stephanie Sarbanes
June 2020

A ROLE FOR MINDBOMB 1 IN ADENOVIRUS GENOME DELIVERY

Stephanie Sarbanes, Ph.D.
The Rockefeller University 2020

The journey from plasma membrane to nuclear pore is a critical step in the lifecycle of DNA viruses, many of which must successfully deposit their genomes into the nucleus for replication. Viral capsids strategically navigate this vast distance (and all subsequent lifecycle steps) through the coordinated hijacking of a number of cellular proteins subsequently termed host factors. Given the virus' dependence on these proteins, host factors therefore represent valuable targets for therapeutic interventions. Still, the identity and function of many of these factors remains unknown. In this body of work, I will detail our own journey from initial identification to comprehensive characterization of one such host factor, Mindbomb 1 (MIB1), in the context of adenovirus infection. Adenoviruses (AdVs) are widespread and highly contagious DNA viruses that can cause severe respiratory illness in children and immune-compromised individuals. An initial genome-wide loss-of-function screen to identify host factors for this virus revealed MIB1, an E3 ubiquitin ligase best known for its role in neurodevelopment, as critical for AdV infectivity. In a series of mechanistic studies centered on the earliest stage of infection, we observed that in the absence of MIB1, viral capsids successfully traffic to the proximity of the nucleus but ultimately fail to deliver their genomes within. AdV infection is dependent on MIB1's primary action as an E3 ubiquitin ligase — to carry out ubiquitination, a post-translational modification widely capitalized upon by viruses for rapid manipulation of the host environment via altered protein localization, activity or turnover. Our work suggests that in the immediate vicinity of the nucleus, MIB1 may be required for the proteasomal degradation of one or more negative regulators of AdV infection. To identify this relevant MIB1-ubiquitination target, we turned to complementary proteomic approaches to determine proteins proximal to MIB1 upon AdV infection and those differentially ubiquitinated in its presence or absence. Using these unbiased approaches, we corroborated previous reports of MIB1 as a core component of centriollar satellites, dynamic structures localized to the intervening distance between centrosome and nucleus. Furthermore, both proteomic approaches independently pointed to an understudied yet evolutionarily-conserved role for MIB1 in regulating RNP granules and cytoskeleton within the perinuclear environment. Understanding the full relevance of these MIB1-regulated pathways to AdV infection and identifying the specific ubiquitination target responsible will be natural extensions of this work to fully dissect the mechanism of MIB1-mediated viral genome delivery. Together, this work highlights yet another creative way in which viruses recruit host cell machinery to facilitate their replication with the potential to inform the design of new antiviral treatments and emerging adenoviral vector-based therapies.

In my opinion, mon cher, it is easier to

control temperamental opera singers than

it is to control a scientist.

-Agatha Christie, *So Many Steps to Death*

Acknowledgements

Thank you Charlie for letting me be a part of the expansive Rice Lab Family for all these years. You have fostered such a unique lab environment that really values exploration, independence and generosity. I feel that I have grown in many ways in my time here to become a stronger and more caring person and scientist. Thank you to my committee members Professors Titia de Lange and Paul Bieniasz who have guided the course of my work here with their thoughtful advice and redirections. Thank you to Dr. Richard Vallee for kindly agreeing to serve as my external examiner. I want especially to thank Dr. Erik Falck-Pedersen at Weill Cornell for always taking the time to think through data with me and for his encouragement over the years all in addition to invaluable adenovirus-centric advice and reagents. Thank you to his post-doc Eric Lam, as well, who performed some of the pivotal early MIB1 experiments. A thank you to our collaborator Dr. Thijn Brummelkamp at the Netherlands Cancer Institute for guiding and analyzing the haploid screen that set this whole project in motion. I am also grateful to Dr. Urs Greber and Michael Bauer for sharing with us their data and expertise surrounding MIB1 and adenovirus entry. Thank you to Rice Lab Yingpu Yu and Lefteris Michailidis for their help with the HBV-centric work. I want to both formally acknowledge and personally thank the imaging, flow cytometry and proteomic resource center staff at Rockefeller University that helped me navigate various twist and turns in the project. In particular a big thank you to Søren Heissel who made all of the proteomics data come together— and who is always so wonderful to speak with. Throughout this whole experience, the Dean's Office has been a source of positivity and support particularly in preparing for the thesis in a turbulent time—special thank you to Cris Rosario and to Andrea Morris for guiding me towards the NIH where I will continue to pursue the lab life.

To all the members of the Rice Lab that have intersected with my lengthy tenure here—I am so honored and grateful to have worked with such brilliant but most importantly kind and generous people from all over the world. We have truly gone the distance (for some literally circumnavigating the island of Manhattan together—a bonding experience early on in my time in the lab). Thank you to Hachung and Bill who were the wonderful rotation mentors that made me want to join the Rice Lab in the first place. Thank you to the wonderful people that make the Rice Lab and me function everyday: Joe P, Glen, Aileen, Santa, Ellen and Sonia. I want to thank Hans-Heinrich Hoffmann for initiating the MIB1 project by performing the original Hap1 screen and early mechanistic studies. Having wandered around in the wilderness for several years pursuing a passion project, this MIB1 project (a continuation of my Rice-Lab-confused fascination with DNA viruses, and equipped with an endlessly entertaining name) was a lifeline and also meant that I finally had a direct mentor and partner-in-crime to bounce ideas off of. To Heinrich: it was a real "make it work" moment in the course of my PhD and I cannot thank you enough for sharing this with me.

Joe Luna. Goodness, where to begin…we are truly brother-sisters from other mother-misters. You have guided me and goofed with me since almost the day I arrived on campus and I could never. Have made it. Through this program. Without you. Period. I was joking when I told you you weren't allowed to leave before I graduate but endlessly grateful it has worked out that way. Other people I have informally taken hostage—Anesta, thank you for being my mom in the lab (my mom thanks you too!) and keeping me on track with those red-bin check-ups. Xianfang, my

one and only bay-mate in the cozy Rm 505. You were the first person I would share my most suspenseful new idea with and the first person to catch when I was down— I got so lucky.

Now for the lab ladies who shift the culture every time they walk in a room. Eliana and Andrea, thank you for your passion and energy—it is the most infectious thing in our virus-laden lab. Alison Ashbrook has MADE this entire experience by being an endless source of encouragement and joy. Alison, I think you may be one of the most amazing people I've ever met. Lauren is one of the more recent additions to the lab but has already become a wonderful friend and mentor. On top of all this, the two of you have guided me so much professionally this last year, helping me with editing, applying for post-docs etc. Each of you prove that hard work and scientific prowess can and should go side-by-side with compassion and enthusiasm. And when you start your own labs I will be forced to reapply to grad school just so I can join them.

To my fellow Rice lab students: thank you for solidarity in a vast sea of post-docs! In particular Ed for our stoop (and non-stoop) sessions and Mariel, who was my first friend in the Rice Lab and fellow lab spirit elf (the secret is at last revealed!). THIS COMMUNITY. Throughout the PhD, the Music and Medicine Orchestra has been an incredible source of joy and sanity. Thank you to my stand partner of 7 years Yaffa Vitberg and the whole cohort of Rockefeller cellists Stephen, Gabriella and Rachel. Thank you to former Rice Lab post-doc Melody Li for our late-night Faculty House sonata sessions. Thank you to the Faculty House front desk, especially Haroun, who calls out "Smileyyyyy" every time I walk in the door and makes it so I can't help but smile even on the days when science has got me down.

I am so lucky for the friendships ranging from kindergarten to graduate school that have sustained me. Becca, my dearest friend since I was 5 years old, Quinn and Alexandra for all the craft nights that translated into a love of DIY benchwork, Janelle (my West Coast Columbia soulmate), my OG roommates Stefi and He Tian, my new roomie Rochelle and fellow graduate students Sudha and Itzel. Hourinaz Behesti, I met you the first month I was here and it was that special scientific brand of fate. Our long summer night walks to the steps of the Met or really any street corner where we say we are going to part ways and then end up chatting for several more hours are some of my warmest memories. And thank you Jesse--your love and support has made this last crazy year so special and wonderful.

I am also grateful to those that put me on this path to begin with and who guided me along the way. My Towson High biology teacher Mrs. Damico made learning about biology creative and challenging. I read my first journal article in her class and learned that research was like being a detective which I liked the sound of. Thank you to everyone in the lab of Dr. Janice Clements at Johns Hopkins for showing me the camaraderie and intrigue of the research lab. Special thank you to Ken Witwer who was my fabulous mentor during those summers. Thank you to Emma who gave me the inverse rewarding experience of being a mentor myself. And thank you to the Columbia Core Curriculum for a foundation in philosophy, literature and arts that enriches my love of science.

I want to thank my big Greek family and my little Jewish family and call out a great aunt on either side. My glamorous Aunt Naomi (and the accompanying network of adoptive aunts Kate, Mary, Helene and Abby) with whom I share so many wonderful memories. Even though I have

lived in Manhattan throughout my time here, I feel truly at home when I am in Forest Hills watching PBS at your apartment or walking down Austin Street. To my elegant Aunt Zoe—thank you for instilling in our younger generation the importance of family and education—it is always such a special treat spending time with you.

I thank New York for being New York and for letting me be a part of what that is. I feel so grateful to have spent over a decade in this place and I leave feeling like I have explored, listened to, and eaten absolutely everything I could've dreamed of. I especially want to thank Ritz Diner on 62nd and 1st without whom none of this would have been possible—my work has been fueled mainly by your fries. Thank you to Rockefeller for being such a unique and beautiful environment. Rarely did I pass through the ironwork gates or walk along the cathedral of trees and not feel painfully aware that even in this long long program, it was still all incredibly fleeting.

To my family: it's hard to even believe I'm at last getting to write this to you since you have guided me through so many junctures when I didn't think it would be possible. And all it took was multiple Skype calls a day! Nico and Leo thank you for that sibling solidarity, I'm so excited that we are each moving on to new chapters in our lives and so proud of both of you. Dad—thank you for the random supportive texts and for some of the key conversations and omelet-making wisdom that got me through. Mom— thank you for being my best friend and for teaching me to find beauty and connections at all scales (cells to skyscrapers), value kindness above all and feel so deeply appreciative for all the wonderful things in my life. We made it! And you were right "It's all good". The two of you are an amazing team—I love you so much and I am so so happy to be coming home.

Table of Contents

List of Figures

List of Tables

List of Abbreviations

AA	amino acid
AdV	adenovirus
AdV5	adenovirus serotype 5
APEX2	apurinic/apyrimidinic endodeoxyribonuclease 2
CAR	coxsackie and adenovirus receptor
CHD	congenital heart disease
CRISPR	clustered regularly interspaced short palindromic repeats
DNA	deoxyribonucleic acid
dsDNA	double-stranded DNA
DUB	deubiquitinase
FC	fold change
FOV	field of view
GEQ	genome equivalents
GFP	green fluorescent protein
GO	gene ontology
HBV	Hepatitis B Virus
hpi	hours post-infection
HSV	Herpes Simplex Virus
IF	immunofluorescence
IP	immunoprecipitation
KD	knock-down
KO	knock-out
LC/MS-MS	liquid chromatography-tandem mass-spectrometry
LMB	leptomycin B
LVNC	left ventricular non-compaction cardiomyopathy
MIB1	Mindbomb1
MS	mass spectrometry
MT	microtubule
MTOC	microtubule-organizing center
NPC	nuclear pore complex
nt	nucleotide
P-bodies	processing bodies
PTM	post-translational modification
RING	Really Interesting New Gene
RISC	RNA-induced silencing complex
RNA	ribonucleic acid
RNP	ribonucleoprotein

siRNA	small interfering RNA
STAU2	staufen 2
TEM	transmission electron microscopy
TGN	trans-golgi network
TUBEs	Tandem Ubiquitin Binding Entitities
Ub	ubiquitin
Ub-IP	ubiquitin-Immunoprecipitation
UBD	ubiquitin-binding domain
UBL	ubiquitin-like
UPS	ubiquitin-proteasome system
vDNA	viral DNA
VIM	vimentin

Chapter I: Introduction

Rationale for Thesis

The mitigation of infectious disease has been one of the triumphs of modern science from the invention of vaccination against smallpox in 1796 through the development of the polio vaccine, antiretroviral therapy (ART) to curb HIV, and the recent cure for hepatitis C. However, many viruses still elude therapeutic intervention and cure and new viruses continue to emerge. Time and again, necessity, ingenuity and collaboration on the back of many incremental basic science discoveries have allowed us to meet these new challenges and inspires our hope that science will ultimately prevail to alleviate human suffering.

Adenoviruses are one family of viruses for which targeted therapies are still lacking despite a long history of research dating back to its discovery in 1952 as a latent virus within cultured adenoid tissue (from which it derived its name) (Rowe et al., 1953). The virus was quickly identified as the etiologic agent at the root of an "acute respiratory disease of recruits" (ARD) that had swept through military forces during WWII (Ginsberg et al., 1955). Today, adenovirus infection (while still prevalent among military personnel) is more often observed as a severe respiratory illness predominantly affecting children and immune-compromised individuals. Severe infection can result in meningitis, conjunctivitis and gastroinstestinal disease and recent outbreaks in hospitals and colleges have even resulted in fatalities (Khanal et al., 2018; Wold & Toth, 2013). And yet despite the fact that the extreme contagiousness of certain AdV serotypes continues to pose a serious public health concern, there are currently no publicly available vaccines and no specific antiviral treatments (Crenshaw et al., 2019; Khanal et al., 2018).

At the same time, adenoviruses are being increasingly reengineered as therapeutic vehicles to treat a variety of other diseases. Adenoviruses have long been attractive vectors for gene therapy due to their ability to carry and tolerate large insertions to their genome (Niemann & Kühnel, 2017). More recently, adenoviruses are under development as oncolytic agents. Engineered versions of AdV, lacking E1A and B and crippled in normal cells may specifically replicate in cancer cells that express oncoproteins that compensate for the functions of these genes in the virus lifecycle (Ungerechts et al., 2016). These adenoviruses can also deliver immune-modulating transgenes under the control of tumor-specific promoters (Berk, 2016). In this context, increasing the efficiency of the earliest stages of adenovirus infection, and ensuring successful entry and DNA delivery, is desirable. Our elucidation of critical steps at the early stage of the viral lifecycle in this thesis, therefore, finds application to both adenovirus as pathogen and adenovirus as aide.

Historically, adenoviruses have also been a powerful tool within basic biology—exposing fundamental aspects of cell biology through dramatic manipulation of host systems. Perhaps the most striking example of this was the discovery of splicing by Roberts and Sharp in 1977 (subsequently awarded the Nobel Prize in 1993). The high levels of production of late adenoviral mRNA synthesis as well as the ability to produce large quantities of viral genomes facilitated this discovery by visualization of R-loops by electron microscopy (Berk, 2016). Around the same time[1], adenoviruses 2 and 5 were used as model systems for the study of

[1] a true golden age in adenovirus virology

mRNA regulation due to the ability to examine stereotyped and highly-expressed populations of viral transcripts and proteins (Philipson et al., 1975; Lindberg et al., 1972). Adenoviruses have also contributed to our understanding of tumorigenesis due to their ability to transform cells in culture (Endter & Dobner, 2004)). Indeed, the widely-used cell line HEK293 (human embryonic kidney cells) was generated via incorporation of the E1 region of the adenovirus genome (Graham et al. 1977) .

In this thesis, I document our discovery of a new host factor for adenovirus infection, the E3 ubiquitin ligase, Mindbomb 1, and characterize its role in adenoviral DNA delivery. It is our hope that the identification of this host factor will aid in the development of targeted therapeutics against adenovirus or in the development of adenoviruses as viral vectors. However, I will also demonstrate the ways in which our increasing understanding of the mechanism by which MIB1 mediates adenovirus infection continues the tradition whereby adenovirus studies illuminate underlying cell biological processes.

An adenovirus overview: The virus, the lifecycle

When viewed at the epidemiological scale, adenoviruses (AdV) cause serious disease and are threats to human health. However, when viewed from the perspective of a single virion, AdVs are remarkable vessels, evolutionarily-crafted to efficiently deliver the viral genome to the nucleus and initiate a complex program that ensures viral replication and survival.

Though AdVs come in a large number of varieties encompassing over 60 serotypes grouped into 7 species/subgroups labeled A-G, they all share certain overarching features particularly at the level of virion structure and composition **(Figure 1.1)**. All AdVs possess non-enveloped icosahedral capsids (approx. 70-100 nm in diameter) made up largely of hexon subunits with fiber proteins (responsible for receptor engagement) extending from each of the penton vertices (Russell 2009). The main frame is then fortified by a series of smaller “cement” proteins. Within this stereotyped protein shell, lie the instructions for carrying out the full viral program, encoded within approximately 35-40 kilobases of linear double-stranded DNA. This DNA is organized in complex with viral proteins pVII, pV and mu with terminal protein (TP) covalently linked at its ends. Adenovirus 5 (AdV5), one of the subgroup C viruses and a widely-studied representative within adenovirus virology, will be the dominant focus of this work.

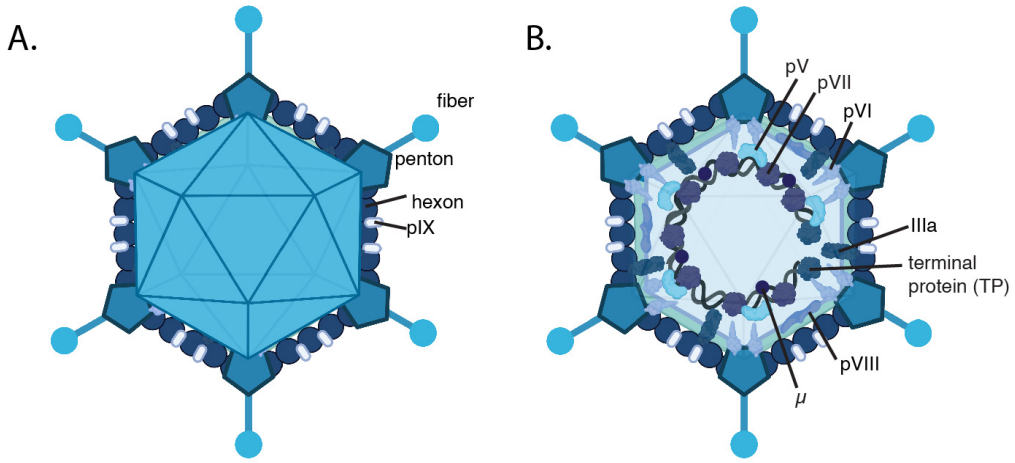

Figure 1.1 **Schematic of AdV5 capsid** with (A) outer capsid proteins and (B) inner capsid proteins labeled. (Modeled after depiction of virion structure in (Russell 2009), image generated using biorender.com).

The infectious lifecycle of AdV5 begins with the attachment of the fiber protein to the coxsackievirus and adenovirus receptor, CAR[2], on the plasma membrane, triggering endocytic uptake of the viral particle **(Figure 1.2)** (Bergelson et al., 1997). As this endosome matures and acidifies, the capsid becomes partially degraded, releasing its fibers and exposing the membrane-lytic pVI protein. Puncture of the endosome by pVI releases the particle into the cytoplasm (Wiethoff, Wodrich, Gerace, & Nemerow, 2005)[3]. The naked particle then couples with microtubules to traffic to the nucleus where it docks onto the nuclear pore complex (NPC). Here the capsid is dismantled and ejects its genome through the pore where it may begin to execute its viral gene expression program. Host RNA polymerase II initially transcribes the immediate early genes E1A and E1B. E1A then activates the transcription of early gene transcripts to produce viral proteins needed for DNA replication. Replication of the viral genome proceeds using a unique protein-based priming method and marks the transition to the "late" stage of infection (≈16 hpi). The amplified genomes then serve as templates for the large-scale production of late stage mRNAs encoding the structural proteins necessary for encapsidation. By this late stage, having usurped the cell's nuclear export and protein translation systems, the virus has coopted the host cell as a factory for the production of new virions. The structural proteins translated from these late transcripts are imported into the nucleus where they begin to package the nascent AdV genomes and assemble virions (Flint et al., 2004). These progeny virions are then released via cell lysis for dissemination throughout the host and spread to new hosts (Jiang et al., 2011; Tollefson et al., 1996).

[2] CAR, encoded by the gene CXADR, is expressed in numerous tissues particularly the brain (higher during development), cardiac muscle and epithelial cells (kidney, intestines, liver) where it localizes to the basolateral membrane and tight junctions (Freimuth et al. 2008).

[3] This is one notable point of divergence between adenovirus subgroups. While AdV5 rapidly escapes from the endosome and couples directly to dynein motors, Ad35 and AdV7 and AdV48 accumulate in late endoscopes and lysosomes and may traffic towards the nucleus within these membraneous organelles (Miyazawa et al., 2001) (Teigler et al., 2014).

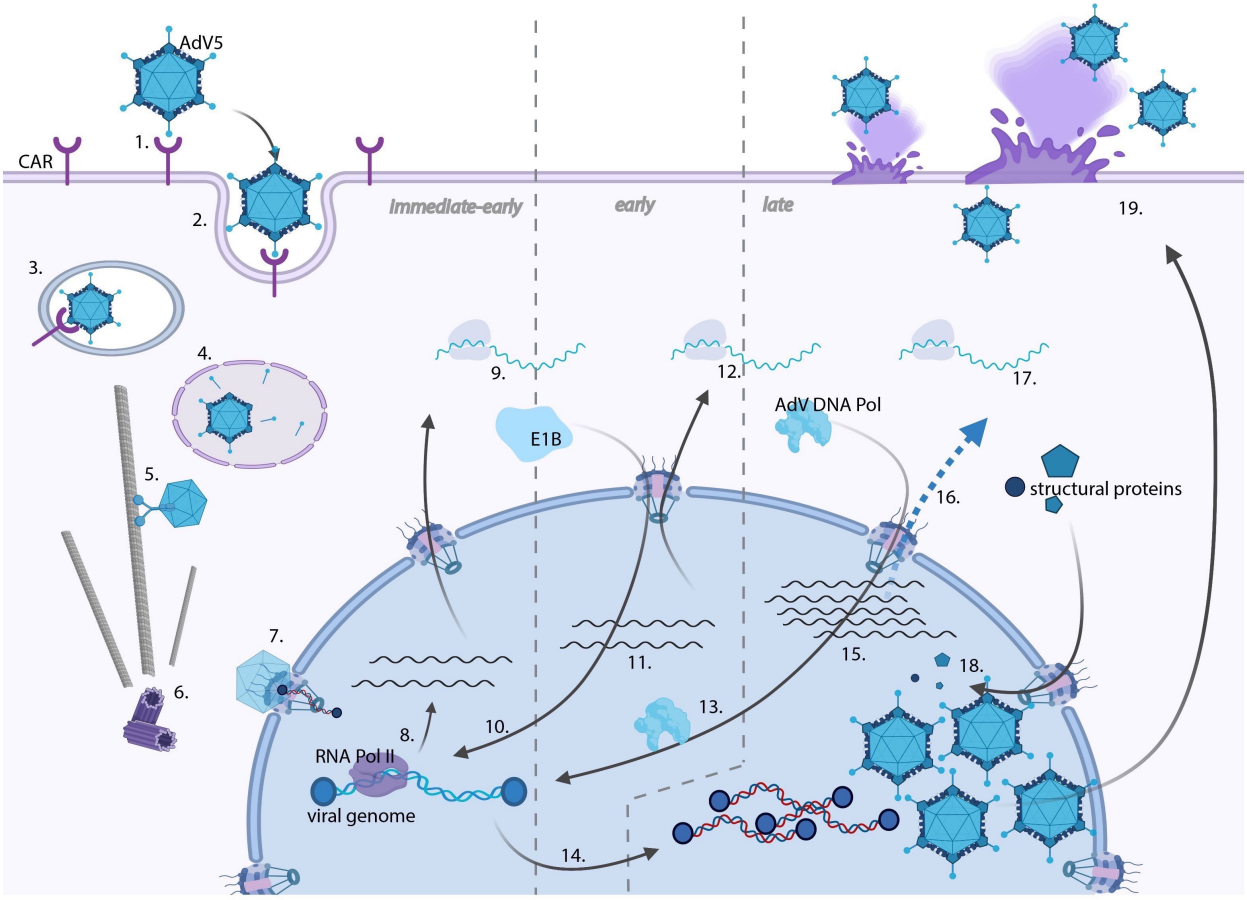

Figure 1.2 Schematic representation of full AdV5 lifecycle. (1) AdV5 particle binds CAR receptor on surface of host cell and undergoes receptor-mediated endocytosis (2) into early endosome (3). As endosome matures and acidifies, the fiber proteins are released and capsid is partially degraded resulting in exposure of pVI protein which lyses the endosome and releases the naked capsid into the cytoplasm (4). The released capsid couples to dynein to traffic along microtubules to the microtubule-organizing complex in the vicinity of the nucleus (5). The capsid transfers and docks to the NPC (7) and releases the viral genome into the nucleus. Here, RNA polymerase II begins transcription and translation of immediate early genes (8,9) including E1A. E1A then stimulates transcription of viral early genes by RNA polymerase II (10,11) which are exported to the cytoplasm and translated into the viral replication proteins (12) including the AdV-specific DNA polymerase. Replication of the incoming viral genome by this viral polymerase (13, 14) marks the transition to the late stage of infection and the additional templates are used to amplify transcription of late mRNA transcripts (15). These are selectively exported (despite shut-down of nuclear export for host mRNAs) and translated into the structural proteins (17). The imported capsid proteins and nascent viral genomes are packaged together into progeny virions (18) and released from the cell via autophagy-mediated cell lysis encompassing breach of both nuclear and plasma membranes (19). [Modeled after the depiction of the AdV lifecycle in Principles of Virology (Third Edition) Volume I. Molecular Biology. Flint, Enquist, Racaniello, Skalka, image generated using biorender.com]

As outlined above, the window between endocytosis at the plasma membrane and successful capsid disassembly and genome delivery at the NPC constitutes the earliest stage of infection and it is the window relevant to our study of MIB1 as a host factor for adenovirus. We will therefore, delve more into the complex early interactions between virus particle and host with particular emphasis on microtubule dynamics and interactions close to and upon arrival at the nuclear pore.

Microtubule contributions to adenoviral entry

Microtubules (MTs) are one of the three major cytoskeletal components of the cell and are rigid structures self-assembled via polymerization of alpha and beta-tubulin heterodimers. In addition to providing structural integrity to the cell, and orchestrating cell division, they also serve as tracks facilitating the efficient transport of cellular cargoes—including organelles, vesicles, and protein complexes. Directional trafficking of these cargoes is achieved through the net actions of a series of molecular motors along these polarized tracks with dyneins mediating "minus-end" (predominantly in towards the nucleus) and kinesins mediating "plus-end" directed transport (predominantly towards the periphery) (Hirokawa, Noda, & Okada, 1998; Hoyt, Hyman, & Bähler, 1997; Vallee & Sheetz, 1996). At the same time, MTs are themselves dynamic, constantly growing and shrinking in alternating phases marked by "catastrophe" and "rescue"[4] (Mitchison & Kirschner, 1984). The overall stability of MT polymers— modulated by associated protein factors and post-translational modifications of their tubulin subunits—can also have important implications for the ferrying of cargo.

MTs and MT motors have long been appreciated for their contribution to long-range AdV transport. Upon release from the endosome, minus-end directed transport via the dynein/dynactin complex guides the particle most of the distance to the nucleus by way of the centrosome lying in close proximity to the nuclear envelope.[5] Early studies of AdV trafficking demonstrated that blocking microtubule motion using anti-dynein antibodies or MT-depolymerizing drugs like nocodazole abrogated nuclear targeting (Kelkar et al., 2004; Leopold et al., 2000; Mabit et al., 2002). Most cellular cargoes utilize adaptor proteins to couple to MT motors. However, the coupling of the capsid to the dynein/dynactin motor complex is uniquely mediated through a direct interaction between hexon and dynein itself following a pH-dependent conformation change in hexon within the acidic endosome (Bremner et al., 2009). Particle tracking assays of fluorescently-labeled incoming AdV capsids revealed that viral particles actually undergo bidirectional transport, switching between dynein and kinesins (likely Kif5B) in a way that nevertheless enhances net minus-end velocity (Suomalainen et al., 1999; Zhou et al., 2018). Furthermore, receptor-engagement and entry of capsids trigger signaling pathways (PKA and p38 respectively) that further skew the competition between these two motors to favor

[4] very reminiscent of the dynamics of another biological process known as "graduate school". For example, the opportunity to work on the MIB1 project marked one critical transition indicative of "rescue"

[5] The centrosome is often but not always synonymous with the microtubule-organizing complex (MTOC) as the primary nucleation site for microtubules in the cell. For example, there are some cell types such as polarized epithelial cells or muscle cells that display non-centrosomal MTOCs (Sanchez & Feldman, 2017). However, in our main studied cell line (Hap1), in which we observe a single dominant puncta upon centrosome staining, we will refer to them largely interchangeably.

motility towards the nucleus —a prime example of ways in which the virus can rapidly alter the cellular environment by post-translational modification, in this case, phosophorylation (Scherer et al., 2014; Suomalainen et al., 2001).

One might assume that arrival at the centrosome all but ensures arrival at the nuclear pore given the seemingly trivial distance remaining between these two structures after the extended passage through the cytoplasm. However, work by Wang et al revealed that the transfer from microtubule organizing complex (MTOC) to nuclear pore complex (NPC) is in fact a highly coordinated process relying on spatial cues in the immediate vicinity of the nucleus (I.-H. Wang et al., 2017). Specifically, capsids must decouple from MTs upon MTOC arrival to prevent retention at the centrosomal hub of MT minus-ends via association with dynein. Unexpectedly, nuclear export via the CRM1 (XPO1) export pathway is critical to this process. Inhibition of this pathway by leptomycin B (LMB) results in dramatic retention of capsids at the MTOC and the loss of MT-independent drifting normally observed in immediate proximity to the nuclear envelope. This observation implies the existence of some as-yet-unidentified cargo of CRM1 export or a function of CRM1 directly that is necessary to trigger release of the capsid from minus-end motors[6] or to inhibit rebinding to MTs. (Bremner et al., 2009; Smith et al. 2008; Strunze et al., 2011; I.-H. Wang et al., 2017). One hypothesis put forward by Wang et al. is that CRM1 mediates the export of factors (histone deacetylases (HDACs), deglutamylases) that would remove post-translational modifications (acetylation, polyglutamylation) from perinuclear MTs in a way that decreases their affinity for MT motor proteins or alters their rigidity. Alternatively, CRM1 may act directly to assist binding to NPCs. Interestingly, in yeast *S. pombe*, the cargo-binding activity of CRM1 is necessary for the generation of non-centrosomal MTOCs docked at NPCs. In this case CRM1 itself acts as a binding site for the Mto1/2 complex which in turn recruits the gamma-tubulin complex to nucleate MTs (Bao et al., 2018). A phenomenon of MT nucleation directly from the nuclear envelope could certainly be relevant to AdV trafficking in the immediate vicinity of the NPC although no such organization has been noted by electron microscopy.

Nuclear entry by diverse viruses

The journey to the nucleus, detailed above for AdV, is a shared and requisite feature of many DNA (and even some RNA) viruses that rely upon the host nuclear machinery to replicate and transcribe their genomes. And yet arrival at this interface is just the first hurdle. The nuclear membrane then poses a formidable obstacle. Different viruses employ unique strategies to breach this barrier **(Figure 1.3)** (Fay & Panté, 2015; Whittaker & Helenius, 1998). Some DNA viruses such as HPV16 and specific retroviruses (RNA viruses with a DNA phase), such as MLV, wait for nuclear envelope breakdown during cell division to slip into this compartment (Aydin et al., 2014). Despite their small size, parvoviruses such as the minute virus of mice (MVM), actively induce disruption of the nuclear envelope independent of cell division and enter via these breached sites (Cohen et al., 2011).

However, other viruses, particularly those infecting post-mitotic cells, must use the primary mode of passage across this barrier, the selective gate of the nuclear pore complex (NPC). The NPC is made up of a scaffold of proteins called nucleoporins arranged as a ring embedded into

[6] although dynein has been observed still in association with capsid even at the NPC (Bremner et al., 2009)

the double membrane of the nuclear envelope to form a channel. Occupying the center of this channel is a gel-like web of disordered protein domains (FG-nups) of hydrophobic phenylalanine-glycine repeats separated by hydrophilic spacers that confer selectivity on the basis of size and charge. While small molecules, ions and even small proteins can traverse the pore passively, larger proteins or ribonucleoprotein (RNP) complexes require active transport. This active transport is mediated by a set of transport receptors that recognize and bind tags on specific cargo proteins (either nuclear localization (NLS) or export (NES) signals). [7]

Viruses too show distinct NPC interactions and transport largely based on the size of their capsids. Some capsids, such as the slender rod-shaped shell of baculovirus[8] or parvoviruses, like the 23 nm adeno-associated virus (AAV), can pass through the nuclear pore intact (Au et al., 2016; Kelich et al., 2015). Hepatitis B virus (HBV), due to intermediate capsid size (approx. 40 nm), is able to enter and transit through the channel of the pore through interaction with importin-α/β. However, it cannot pass through entirely, and is retained within the basket on the nucleoplasmic side of the pore via interaction with Nup153 (Rabe et al., 2003; Schmitz et al., 2010). Here it disassembles completely to release its DNA genome. By contrast, the bulky HSV capsid cannot enter the pore but docks onto the outside through an interaction with cytoplasmic Nup358 (also known as RANBP2) (Copeland et al., 2009; Ojala, et al., 2000). Binding triggers pressurized release of the genome through a specific portal at one structurally distinct vertex of the capsid, through the pore and into the nucleus while the capsid itself remains fixed as an empty shell on the cytoplasmic side of the pore. Uniquely among retroviruses, lentivirus nucleocapsids (such as that of HIV-1) access non-dividing cell nuclei by similarly docking at the pore via interaction with Nup358 but also require Nup153 of the nuclear basket for coordinated exit of the uncoated pre-integration complex into the nucleoplasm (Di Nunzio et al., 2012; Kane et al., 2018).

[7] In fact, the first NLS was recognized in the context of virus infection—the observation of an SV40 mutant unable to localize its SV40 large T-antigen to the nucleus (Kalderon et al., 1984).
[8] likely independent of transport factors and instead propelled by a rocket of polymerized actin!

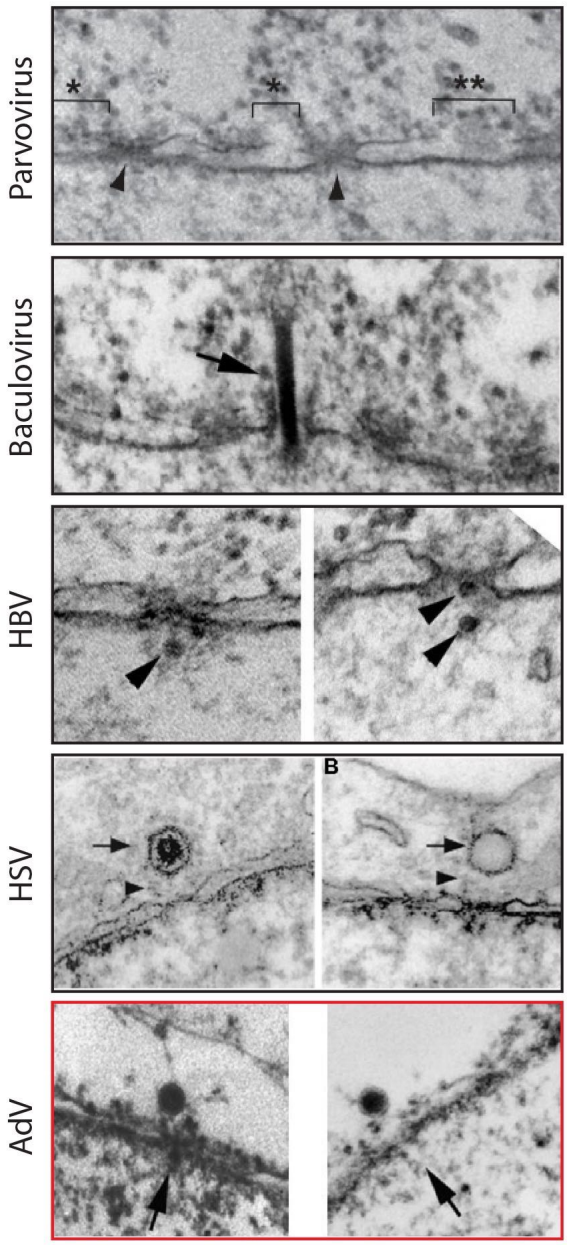

Figure 1.3 Viruses employ diverse mechanisms to deliver their genomes to the nucleus. Transmission electron microscopy (TEM) images showing the mechanisms by which various DNA viruses access the nuclear compartment (from top to bottom): Parvovirus MVM with nuclear pore (arrowheads) and breached membrane (brackets) (S. Cohen et al., 2011), Baculovirus AcNMPV oriented vertically to slip through pore intact (Au et al., 2016), HBV sitting within nuclear basket on nucleoplasmic face of the pore (Rabe et al., 2003), HSV-1 docked on cytoplasmic face of NPC before (left) and after (right) ejection of DNA (Ojala et al., 2000) and AdV2 docked on cytoplasmic face of NPC (Saphire et al., 2000). All images obtained directly from review by (Fay & Panté, 2015).

Adenovirus at the NPC: Docking, Disassembly, Delivery

Like HSV, the size of the AdV particle precludes passage through the pore. The AdV capsid must therefore dock on the cytoplasmic face of the NPC, and efficiently disassemble to release its DNA into the nucleus (Greber et al., 1997) **(Figure 1.4)**. Initial docking is mediated by a direct interaction between hexon and Nup214 (Cassany et al., 2015). Up until this point, the structural integrity of the viral capsid is beneficial for weathering the extracellular environment and for evading intracellular innate immune sensors and nucleases. However, upon successful arrival at the "drop-site" of the NPC, this stability becomes an impediment, necessitating active mechanisms for disassembly. A number of studies have illuminated the precise mechanisms that take place at the pore to facilitate that release. Early *in vitro* work showed hsc70 and classical nuclear import factors were required for AdV2 DNA import (Saphire et al., 2000). Histone H1 was shown to assist in genome delivery, not by interacting with the dsDNA viral genome, but through direct interaction with hexon, coupling the capsid to specific import factors, Impβ and Imp7. This coupling generates an active force in towards the nucleus that could assist disassembly of the already compromised capsid (Trotman et al., 2001).

Interestingly, MTs emerge as key players at this juncture as well. As discussed above, MT minus-end directed transport guides the long-range delivery of the capsid to the centrosome and must then be decoupled in order to permit transfer to the pore. However, once at the pore, Strunze et al. postulate that the capsid must switch tracks yet again, this time coupling to plus-end directed kinesin-1 to create a shear force countering the inward pull of histone transport factors that serves to physically "rip" the capsid apart (Strunze et al., 2011). Structural alteration of the capsid at the pore is evidenced by conformation-specific recognition by the anti-hexon antibody R70 only *after* genome release, with the empty capsid shells then clustered in aggregates pushed towards the periphery. The same nuclear pore/transport components (CRM1, Nup214) that facilitated the initial trafficking and docking of the capsid stay associated with these empty capsids and similarly relocalize to the periphery of the cell. Strunze et al. further speculate that the relocalization of these factors may compromise nuclear membrane integrity as a secondary means of increasing subsequent AdV capsid access to this compartment (although theoretically this should also limit subsequent capsid association with nuclear pores if these factors are necessary for docking).

How this final "track" change might be regulated to ensure accurate release is intriguing. Just as CRM1-mediated export is necessary to liberate capsids from the MTOC, this proposed mechanism implies the existence of spatial cues in the immediate vicinity of the nucleus that alter MT motor association, accessibility or dynamics yet again. Moreover, despite the exquisite details provided by the aforementioned studies, a complete picture of the factors mediating genome release in the immediate vicinity of the nucleus is still lacking. In this thesis, we narrow the contribution of MIB1 down to this specific step in virus infection, introducing a new player at this critical interface.

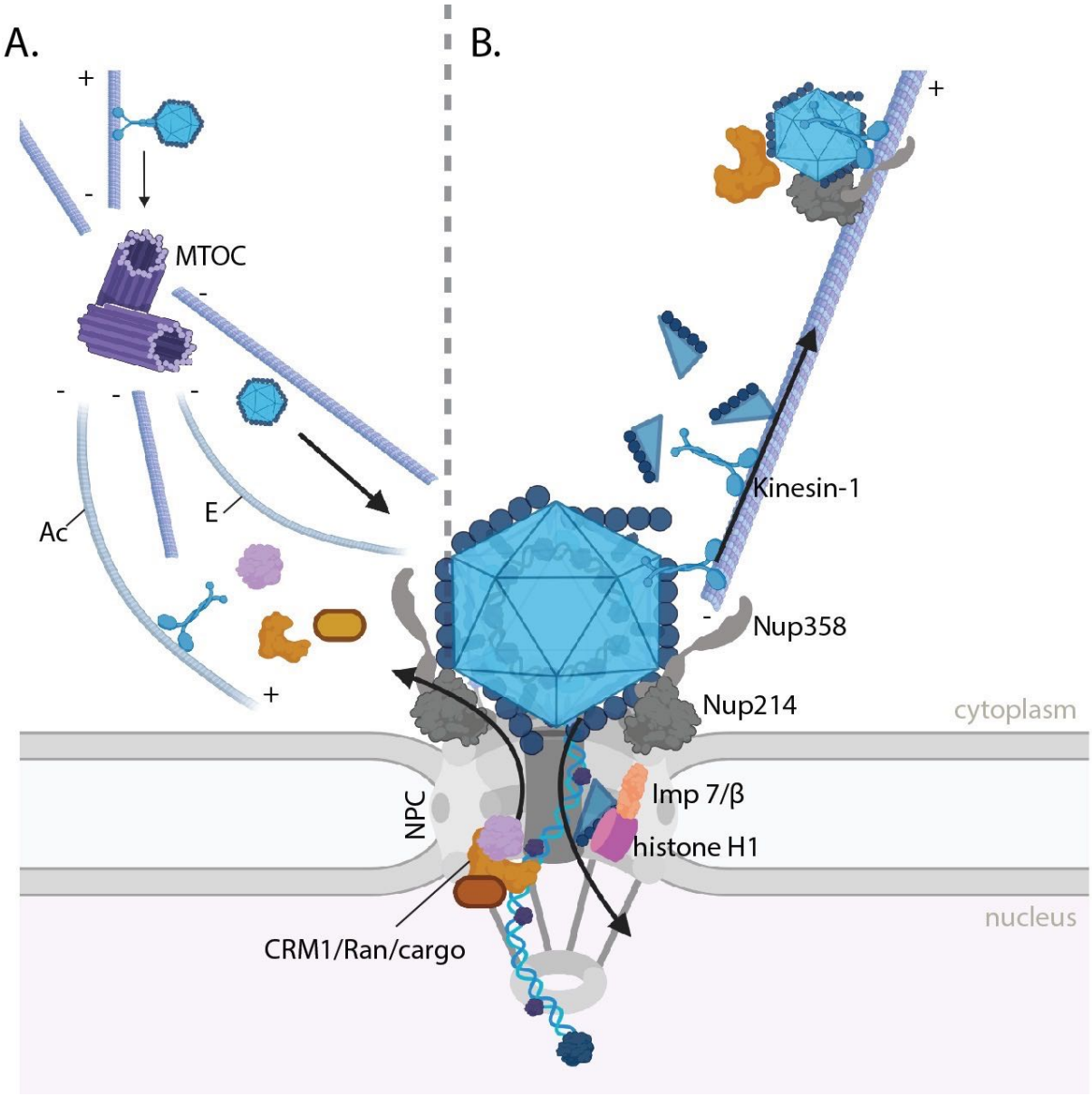

Figure 1.4 Schematic of AdV capsid disassembly and DNA release at the NPC. (A) Regulation of arrival at NPC: AdV capsid traffics to MTOC on dynein motors but must be subsequently uncoupled from these MTs to traverse the distance from MTOC to NPC. This uncoupling is facilitated by CRM1-mediated export through a still poorly understood mechanism that may require the actions of an exported cargo, perhaps altering the motor affinities or structural properties of the more flexible and curved post-translationally-modified (Ac=acetylation, E=glutamylation) MTs occupying the perinuclear vicinity. (B) Regulation of capsid docking and disassembly: AdV capsid docks directly on NPC via association between hexon and Nup214. Binding between hexon and histone H1 couples the capsid to import factors beta and 7 generating an inward force. Simultaneous coupling to kinesin-1 pulls the capsid towards the periphery generating a shear force. This plus-end transport of disassembled and empty capsids is accompanied by peripheral transport of the associated Nup358 and Nup214 dismantling the cytoplasmic NPC architecture. (Image generated using biorender.com)

History of Ubiquitin and the Ubiquitin-Proteasome Pathway

A better understanding of the role MIB1 might play in AdV infectivity, however, first requires a better understanding of MIB1 itself. Mindbomb1, the host factor we identified as critical for AdV infection, is a member of the RING E3 ubiquitin ligase family which (together with several other classes of ubiquitin ligases) act as the cellular effectors of ubiquitination. Ubiquitination is a widespread post-translational modification of proteins originally identified in the curious observation by Goldknopf and Busch of a protein (histone H2A) with two heads, or N-termini (**Figure 1.5A)** (Goldknopf & Busch, 1977). It was soon revealed in early bioinformatic work by L. Hunt and M. Dayhoff that this second N-terminus was identical in sequence to the small 8.6 kDa protein called "ubiquitin" and could be attributed to the covalent attachment of this 74-residue peptide to a lysine residue on another protein (Hunt & Dayhoff, 1977). This "ubiquitin" had already been identified by Gideon Goldstein in 1975 as a free peptide found in an obscure *in vitro* context to stimulate immunocyte differentiation (Goldstein et al., 1975). He dubbed it "ubiquitous immunopoietic polypeptide" (UBIP) for its ubiquitous appearance and speculated on its true biological function:

What, then, is the physiologic function of UBIP, since UBIP from such phylogenetically disparate sources as mammals and plants shows such uniformity by structural, functional, and immunological criteria? That UBIP should have been so rigorously conserved throughout this immense evolutionary time-span suggests a function vital to the living organism…The nature of that basic function is unknown and this proves a question that may have intrinsic importance in its own right – Goldstein et al.

It took the entirely independent study of ATP-dependent proteolysis by Hershko and Ciechanover to finally arrive at a complete picture of the anticipated function for ubiquitin so "vital to the living organism" (Varshavsky, 2006). Hershko observed in rabbit reticulocyte lysate that addition of a small polypeptide, that they had termed ATP-dependent proteolysis factor 1 (APF-1), to a protein substrate resulted in the breakdown of that protein (Hershko et al., 1980). It was subsequently revealed that APF-1 was none other than ubiquitin, again by another name (Wilkinson et al., 1980). Finally, further work by Hershko and Ciechanover revealed that this "ubiquitination" was carried out through the sequential action of three different classes of enzymes (Ciechanover et al., 1982; Hershko et al., 1983). E1 (of which there are only two in humans) "activates" the ubiquitin so that it may be conjugated to E2 (approx. 40 distinct proteins) which in turn transfers the modification onto the lysine of a given target protein via coordination with E3 (**Figure 1.5B[1]**). There are over six hundred of these E3 ubiquitin ligases in mammalian cells. The E3 ligases are therefore the main source of direct and combinatorial substrate selectivity within the ubiquitination pathway.

In these early studies, ubiquitin addition by this tripartite system was almost exclusively appreciated as a proteolysis signal. Specifically, the attachment of ubiquitin (or rather a chain of ubiquitin to be discussed below) acts as an adaptor for delivery of the associated protein to a large protein complex called the proteasome. Passage through the cylindrical barrel of the proteasome, lined with protease active sites, results in the systematic breakdown of the targeted protein into peptide fragments. Protein degradation up until this point was largely attributed to lysosomes and believed to be a relatively passive process merely required for the eventual

clearance of long-lived proteins (Varshavsky, 2006). Therefore, the Ubiquitin Proteasome System (UPS), more generally, marked an entirely new paradigm for dynamic cell regulation operating directly at the level of the pre-existing cellular effectors, proteins, rather than through the preceding bureaucratic stages of transcription or translation.

Ubiquitination: Diversity and Regulation

These early discoveries into the mediators of protein destruction breathed life into a vibrant and ever-expanding field. We now know that despite the notoriety of ubiquitin as "the molecular kiss of death", there are a variety of fates for ubiquitin-tagged proteins dependent on both the length and the nature of the ubiquitin linkage (Yau & Rape, 2016) **(Figure 1.5B[3])**. Hershko et al. had observed a distinct banding pattern upon incubation of ubiquitin with their target protein indicating that ubiquitin was actually forming chains off of the substrate (Hershko & Heller, 1985). These chains can be generated due to the presence of seven lysine residues (K6, K11, K27, K29, K33, K48, K63) within the sequence of ubiquitin itself **(Figure 1.5B[2])**. This allows ubiquitin to covalently conjugate to itself in distinct structural combinations that can be "read" differently by downstream effectors possessing ubiquitin-binding domains (UBDs). Linkage at K48 acts as the structural signal for the classical binding to the proteasome and subsequent degradation of ubiquitinated targets. K11 linkage leads to proteasomal degradation but tends to have more restricted targets in cell cycle regulators. By contrast, K63 and Met-1 linkages as well as monoubiquitination have been shown to have nonproteolytic roles such as regulating the interaction with protein binding partners and/or altering localization and protein trafficking (including nuclear transport) (Kulathu & Komander, 2012). Depending on both the substrate and E2 partner, individual E3 ubiquitin ligases can carry out more than one of these linkage types. MIB1, for example, has been documented performing K11-, K29-, K48- and K63- linkages dependent on the specific substrate (Čajánek et al., 2015).

Another class of proteins termed deubiquitinases (DUBs) are responsible for the removal of ubiquitin chains **(Figure 1.5B[4]).** Their activity counters the action of ubiquitin ligases in order to regenerate the pool of free ubiquitin available in the cell. The released chains are also being increasingly studied for their independent functions as signaling molecules. The regulation of DUBs adds another layer to the complex web of events governing post-translational protein fates. Ubiquitin-*like* modifications also increase the diversity of information potentially coded by post-translational modification and due to their similar modification of lysine residues may indirectly influence ubiquitination of specific substrates **(Figure 1.5B[5])**. These modifications include ISGylation, NEDDylation and SUMOylation which have well-characterized roles in innate immunity, meta-regulation of the cullin E3 ligases, and DNA repair respectively (Enchev et al., 2015; Ritchie & Zhang, 2004). Given our interest in genome delivery at the nuclear pore, it is worth noting the importance of sumoylation in nucleocytoplasmic transport (Melchior, 2000; Melchior et al., 2003). Nup358/RanBP2 is, in fact, a SUMO E3 ligase with RAN as one of its targets (and whose sumoylation is regulated by the competitive binding of transport factors such as CRM1) (Sakin et al., 2015). However, while Nup358 has been implicated in genome delivery for a number of viruses including adenovirus, whether this is dependent upon its SUMOylating activity (outside of RAN) remains unknown. Adding yet another degree of complexity, entirely distinct post-translational modifications (ex. phosphorylation/acetylation) have been identified on ubiquitin residues and alter its ability to perform certain types of linkages, its resistance to DUBs or its interaction with "readers" (Swatek & Komander, 2016).

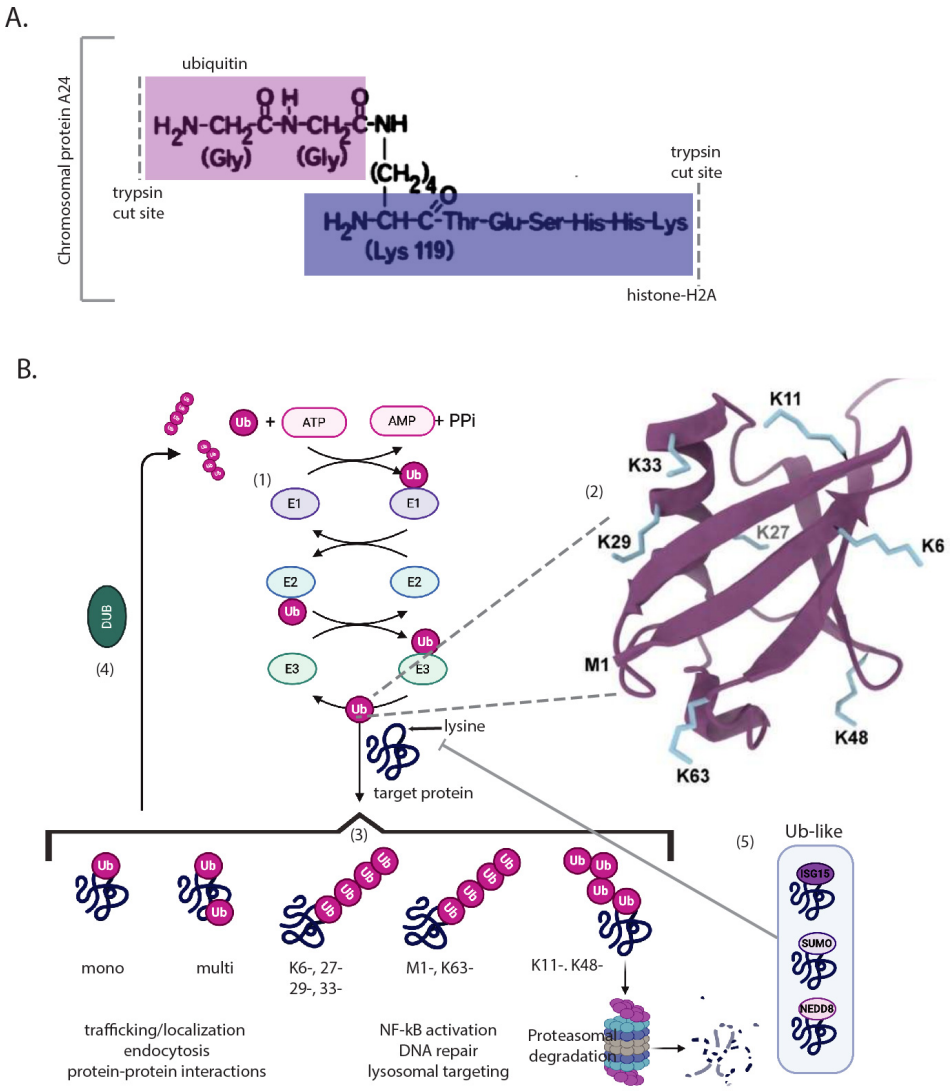

Figure 1.5 Regulation and diversity of ubiquitin as post-translational modification. (A) The tryptic peptide displaying two N-termini of chromosomal A24, a chimera of histone H2A and an unknown peptide (later identified as ubiquitin), the first reported observation of the covalently-linked PTM prior to the discovery of its identity or function. (Image modified from (Goldknopf & Busch, 1977)) (B) Overview of ubiquitination pathway: (1) The addition of ubiquitin to a target protein is accomplished through the sequential action of three enzymes. E1 activates ubiquitin and transfers it to E2. The E3 ligase then coordinates transfer of ubiquitin from the E2 to a lysine on the target protein. (2) The structure of ubiquitin showing the seven lysine residues that result in diverse poly-ubiquitination chains (3) Mono-, multi- and linkage-specific poly-ubiquitination structures govern the fate and function of the ubiquitinated target protein. (4) DUBs remove ubiquitin chains which can have independent signaling properties or be recycled into ubiquitin monomers. (5) UBL modifications: ISGylation, NEDDylation and SUMOylation can indirectly impact ubiquitin addition or removal. (Lysine-labeled ubiquitin structure obtained from (Dougherty et al., 2020) and overall schematic modified from template provided on biorender.com).

Ubiquitin Ligases in Drug Development

Other post-translational modification pathways such as phosphorylation and acetylation have long been valuable and rewarding targets for drug development. Similarly, the UPS has been successfully targeted in treatments for multiple myeloma (P. Cohen & Tcherpakov, 2010). These drugs such as Velcade (bortezemib), however, act by shutting down the system globally. As the delineators of target specificity, E3 ubiquitin ligases are, in theory, very attractive drug targets and so have continued to be pursued despite their historic intractability (Huang & Dixit, 2016). A small number of E3 ubiquitin ligase inhibitors have made it to clinical trials including inhibitors targeting the E3 ubiquitin ligase HDM2 (P. Cohen & Tcherpakov, 2010). As this E3 ubiquitin ligase targets p53 for degradation, the goal is for its inhibition to enhance the expression of this critical tumor suppressor. In the alternate case of the overexpression of oncogenes, where promoting ubiquitination and subsequent degradation of the target would be desirable, DUBs are also being explored as anticancer targets for inhibition due to their relative diversity and selectivity (Nicholson et al., 2007). Given the contribution of E3 ubiquitin ligases to diverse virus infections (to be discussed further below) targeting these pathways could also be a strategy to counter infectious disease. Most recently, a large-scale affinity purification mass-spectrometry strategy to identify host protein interactors with SARS-CoV-2 proteins revealed a strong interaction between viral Orf10 and multiple components of the CUL2(ZYG11B) complex (Gordon et al. 2020). This complex in turn requires neddylation of CUL2 for its ubiquitination activity. The drug Pevonedistat which targets this neddylating enzyme could therefore be tested in the hopes of interfering with the virus lifecycle. Nevertheless, truly capitalizing on the therapeutic potential of this protein family will first require a better understanding of the substrates of specific E3 ubiquitin ligases, like MIB1, and their downstream fates within different cell types and upon diverse stresses. The work presented in this thesis, similarly opens up a therapeutic avenue to counter AdV infection as targeting MIB1 would be a means to block virus infection. However, appreciating the broader consequences of MIB1 ubiquitination and its inhibition on constitutive cellular processes will be imperative.

Ubiquitination in Virus Infection

Given that post-translational modifications like ubiquitination allow for rapid manipulation of existing pools of proteins, they are pathways well-suited to the kinetics of many virus infections and serve as a powerful strategy for modifying the host cell to facilitate successful progression through the lifecycle. Viruses can either hijack cellular ubiquitination machinery, complex intimately with host E3 ligases or even encode their own (Isaacson & Ploegh, 2009). Viruses commonly use ubiquitination to quickly sever the sensing and signaling pathways that would allow the host to mount an antiviral innate immune response and alert other cells to the viral invader. KSHV-encoded K3 and K5 proteins ubiquitinate MHC class I proteins to sever antigen presentation of viral proteins and evade adaptive immune responses (by contrast, adenoviruses too reduce MHC class I but accomplish this transcriptionally) (Blair & Blair-Zajdel, 2004; Brulois et al., 2014). The protein Vif of HIV-1 acts as an adaptor to induce proteasomal degradation of the antiviral factor APOBEC3G to prevent it from mutagenizing the encapsidated viral genome (Stopak et al., 2003).

Many DNA viruses also utilize ubiquitination to disrupt cell cycle control typically through manipulation of p53. The human papilloma virus (HPV) encoded E6 protein activates the E3

ligase E6AP to promote ubiquitination and degradation of p53 (Scheffner et al., 1993). Similarly the HSV-1 encoded E3 ubiquitin ligase ICP0 degrades p53 to induce cell transformation. AdV, in particular, has proved a fascinating study of the contribution of ubiquitination to specific facets of the viral lifecycle. The viral proteins E1B55kDa and E4orf6 form a complex with cullin 5 to shutdown cellular DNA repair pathways in addition to also degrading p53 (Querido et al., 2001). By marking MRE11 and RAD51 for degradation, this ligase prevents aberrant DNA repair and concatamerization of the exposed ends of discrete AdV DNA genomes following replication (Stracker et al., 2002). More recently, an appreciation for less-studied non-degradative ubiquitination events has also emerged within the context of AdV infection. In this case, the very same E1B55kDA and E4orf6 complex ubiquitinates a number of RNA-binding proteins such as RALY and HNRNPC which leads not to their turnover but instead alters the ability of these proteins to bind viral RNA and alleviates their inhibition of late viral mRNA processing (Herrmann 2019).

Ubiquitination in adenoviral entry

Ubiquitination acts at various stages of the virus lifecycle. However, viral entry, usually lasting less than one to two hours, and precluding the ability of the virus or host to first mount a transcriptional response to alter the protein milieu, would be a step particularly dependent on this type of regulation. Influenza A virus (IAV), an RNA virus that like AdV replicates its genome in the nucleus, requires the UPS for proper trafficking to this compartment (Khor, McElroy, & Whittaker, 2003; Widjaja et al., 2010). When cells were treated with proteasome inhibitors, the viruses were internalized but failed to escape from endocytic compartments and were retained in the cytoplasm. A similar phenomenon was observed for murine coronaviruses (Yu & Lai, 2005). In HSV entry, upon proteasome inhibition, virus particles access the cytoplasm but no longer traffic to the perinuclear region[9] (in Vero cells) or alternatively, accumulate at the MTOC and fail to deliver their DNA to the nucleus (in THP-1 cells) (Delboy & Nicola, 2011; Sun et al. 2019). In dengue virus (DENV) and yellow fever virus (YFV) entry, ubiquitination is required for capsid uncoating and genome release. In this model, direct ubiquitination of the viral nucleocapsid recruits VCP/p97, a protein which can "extract' ubiquitinated proteins from larger complexes for subsequent proteasomal degradation (Byk et al. 2016; Ramanathan et al. 2020). In a fascinating example of proteasome-independent roles for ubiquitin in viral entry, IAV has also been found to package free ubiquitin chains within its capsid which, commensurate with release from the endosome, couple the capsid to MT motors normally involved in breaking up misfolded cellular protein aggregates (Banerjee et al., 2014). This association is thought to generate a shearing force that helps disperse the M1 shell and release the viral genome.

The work presented in this thesis centers largely around the AdV entry phase since we have narrowed the contribution of host factor MIB1 to the DNA delivery step of this virus lifecycle. Interestingly, there are already reported roles for ubiquitination in AdV entry involving direct modification of the capsid proteins themselves. Wodrich et al. identified a conserved PPxY motif in pVI recognized by certain HECT-E3-ubiquitin ligases, confirmed oligo-ubiquitination by the ligase Nedd4.2 and demonstrated that mutation of this motif impaired transport to the MTOC following endosome escape (Wodrich et al., 2010). This ubiquitination may not serve to

[9] although this is posited to be a rare proteasome-dependent yet ubiquitination-independent process as infection proceeded upon E1 inhibition in cells expressing a temperature-sensitive mutant of E1.

degrade pVI but rather to sequester Nedd4.2 in order to regulate autophagy. Two additional PPxY motifs in the N-terminus of penton facilitate binding to BAG3 (Gout et al., 2010). However, the actual ubiquitination of these sites was not confirmed. On the side of the host, treatment of colon cancer cells with MG132 boosted expression of CAR on the cell surface suggesting that the AdV receptor itself may be regulated by ubiquitination (N.-H. Zhang et al., 2008). The work described in this thesis adds to existing literature of ubiquitination in AdV entry by taking a more comprehensive approach intended to simultaneously capture changes to the ubiquitination of both viral and host proteins at this early stage of infection.

Mindbomb 1: A multi-faceted E3 ubiquitin ligase

Despite the vast literature on the contribution of ubiquitination to viral lifecycles, there were no reported roles for our particular E3 ubiquitin ligase, MIB1, in DNA virus infection. Instead, Mindbomb 1, as evident by its moniker, was best known for its critical roles within the nervous system particularly across neurodevelopment. In 1996, a genetic screen for abnormal brain morphology phenotypes in zebrafish yielded one mutant displaying a massive overproliferation of primary neurons (dramatically likened to an explosion) (**Figure 1.6A)** (Schier et al., 1996). In these *mib1* mutants, Notch signaling was dysregulated, preventing the proper specification of neurons from neuronal progenitors. The root of this phenotype was subsequently narrowed to mutation of the gene encoding Mindbomb 1. Specifically, K63 ubiquitination of the Notch receptor ligand, Delta, by Mindbomb1 at the plasma membrane results in its endocytosis. Endocytosis generates a mechanical force across the receptor ligand interface that exposes a cleavage site in the Notch receptor in the opposing cell. The cleaved intracellular fragment is then liberated to traffic to the nucleus where it acts as a transcription factor to specify cell fate (Itoh et al., 2003). In humans, mutations in MIB1 manifest as left ventricular non-compaction cardiomyopathy (LVNC) and congenital heart disease (CHD) also attributable to its role in Notch signaling (**Figure 1.6B)** (B. Li et al., 2018; Luxán et al., 2013).

While Notch signaling is the most phenotypically striking of MIB1's functions, MIB1 now has a number of other validated ubiquitination targets relevant to neurobiology including Epb41I5, SMN and Cdk5 (Choe et al., 2007; Kwon et al., 2013; Matsuda et al., 2016). MIB1 has also been implicated in other developmental signaling pathways such as Wnt signaling in a manner similar to the Notch ligand. However, in this case, ubiquitination of RYK by MIB1 at the plasma membrane promotes endocytosis followed by degradation (Berndt et al., 2011).

Despite these well-characterized functions at the plasma membrane, another major cellular role for MIB1 soon emerged, in proximity to the nucleus. In looking more closely at the early studies of RYK and Delta, overexpression of WT MIB1 alongside these targets in non-neuronal cell culture, resulted not only in their removal from the plasma membrane into vesicles (consistent with the role in endocytosis) but also in their aggregation to one large puncta adjacent to the nucleus. Subsequently, independent proteomics of endocytic adaptor proteins Eps15, epsin-1 and AziI (Cep131) identified MIB1 as a key component of centriollar satellites (**Figure 1.6C)** (Akimov et al., 2011; Villumsen et al., 2013). Centriollar satellites are distinct 70-100 nm granules that, as their name suggests, "orbit" the centrosome, moving to and away from this hub along MT tracks. Although their function is still poorly understood, these satellites are posited as sites of sequestration of centrosomal proteins whose localization and composition regulates ciliogenesis and the integration of cellular stress responses. Moreover, ubiquitination appears to

be the dominant mode of regulation in centriollar satellites and centrosomes with MIB1 emerging as one key effector (Didier et al., 2008; Lecland & Merdes, 2018). The defining scaffolding component of centriollar satellites, PCM1, directly binds and retains MIB1 in these structures despite also being a ubiquitination substrate of MIB1 targeted for degradation. Indeed, several DUBS localizing to centriollar satellites act to protect PCM1 from degradation in the presence of MIB1 either by directly clearing ubiquitin from PCM1 or by removing autoubiquitination events on MIB1 that would enhance the activity of the ligase (Douanne et al., 2019; K.-J. Han et al., 2018). By sequestering MIB1 in satellites, PCM1 prevents its association with the centrosome where it can ubiquitinate and degrade ciliogenesis factors like TALPID3. Similarly, stress-induced inactivation of MIB1 increases ciliogenesis suggesting MIB1 normally acts to suppress primary cilium formation (Villumsen et al., 2013). Additional targets of MIB1 K48 ubiquitination in this region include Plk4, involved in centriole duplication, and GABARAP, a regulator of autophagosome biogenesis (Čajánek et al., 2015; Joachim et al., 2017).

Lastly, while no role for MIB1 in DNA virus infection had been described, there were several studies linking MIB1 to RNA virus infections. Our study has identified MIB1 as a factor that assists AdV infection. By contrast, in a prime example of the ways in which the host widely utilizes ubiquitination to *counter* virus infection, MIB1 has been shown to enhance the innate immune response to RNA viruses. Specifically, upon infection with Sendai or Vesicular Stomatitis Virus (VSV), MIB1 ubiquitinates TBK1 through a K63 linkage that enhances its downstream signaling through IRF3/7. This results in stronger induction of the antiviral cytokine IFN (Li et al., 2011). Meanwhile, although still lacking any functional validation, the recent comprehensive study of the SARS-CoV-2 and human protein interactome unearthed MIB1 as one of 16 interacting partners of the viral protein Nsp9 in conjunction with 5 nuclear pore components (Gordon et al., 2020). Although the relevance of the nuclear pore for a cytoplasmically-replicating RNA virus is unclear and its interaction with Nsp9 may by independent of MIB1 entirely, the confluence of MIB1 with nuclear pore components including Nup214 (the known docking site for AdV) revealed by this interactome map is intriguing as we turn to its mechanism of action within the context of AdV infection.

Taken together, these studies exemplify the complex nature of MIB1's activity from the cell surface to the perinuclear region, embedded within a web of ubiquitination targets and interacting partners at each of those sites. How AdV infection intersects with the multi-faceted roles of MIB1 described above is a major focus of this work. While adenovirus infection begins with endocytosis at the plasma membrane and inevitably alludes to MIB1's role at this surface, the work we will describe in the upcoming sections narrowed the block on AdV infection in the absence of MIB1 to after arrival at the centrosome but prior to successful DNA delivery at the nucleus. It is MIB1's association with centriollar satellites and regulation of MT dynamics at the centrosome, then, that intrigued us the most as it placed MIB1 in precisely the region where AdV capsid delivery and disruption takes place. While AdV has long been observed to traffic to the MTOC, the specific contribution of these centriollar satellite substructures to this process was unexplored.

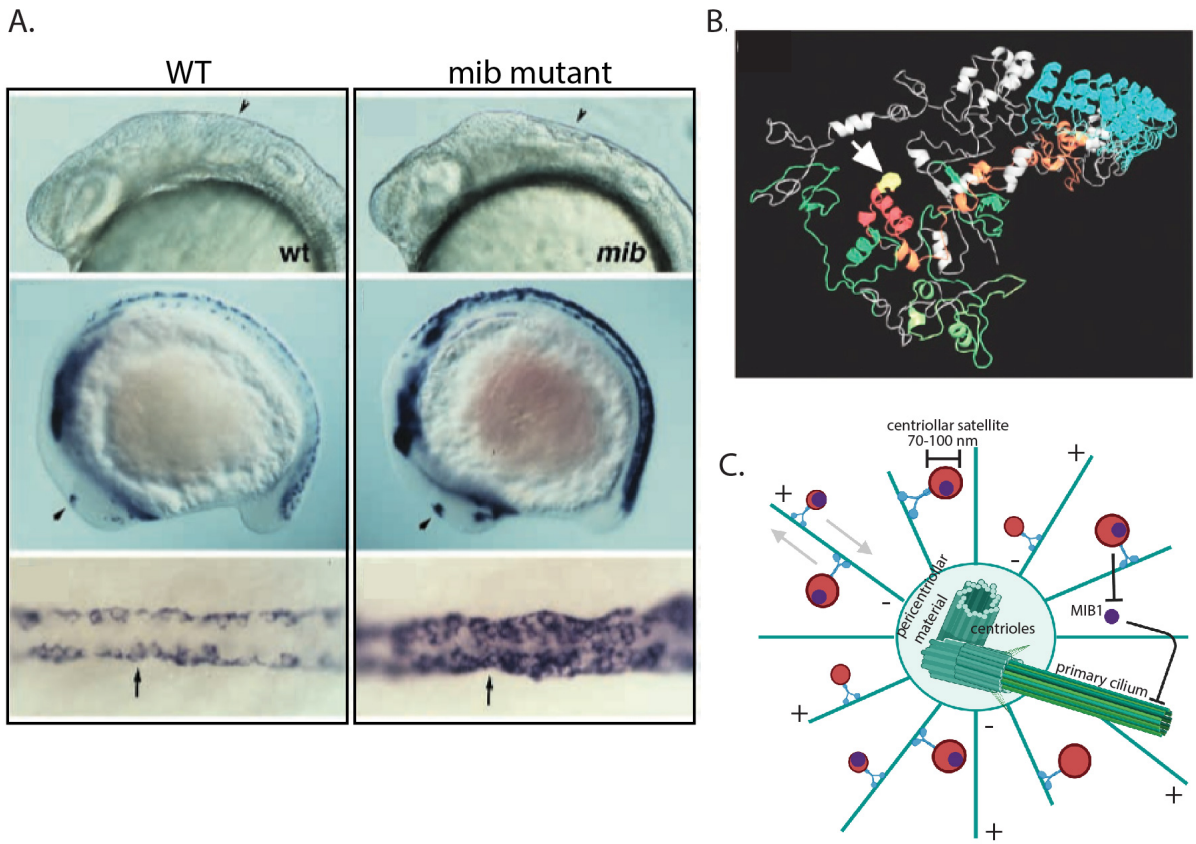

Figure 1.6 Diverse roles for MIB1: from Notch signaling to centriollar satellite regulation. (A and B) MIB1 roles in Notch signaling: (A) MIB1 was identified in zebrafish in mutant embryos displaying *top panel*: severely altered brain morphology with deformed hindbrain, *middle panel*: an overabundance of spinal neurons (dark purple), *bottom panel*: an overabundance of Rohon-Beard neurons (dark purple) in spinal cord (dorsal view). (Image adapted from (Schier et al., 1996)) (B) In silico model of human MIB1 showing predicted organization of the E3 ligases's substrate-binding domains (green), three RING domains (orange) and the coiled-coil domain between RING 2 and 3 (red) labeled for the V943F mutation (yellow with arrow) resulting in the disease phenotype left ventricular non-compaction cardiomyopathy (LVNC). (Image obtained from (Luxán et al., 2013)). (C) MIB1 is a key component of centriollar satellites and regulates centrosomal functions. Schematic depiction of centrosome. Mother and daughter centrioles (connected via a flexible linker) are surrounded by a cloud of proteins comprising the pericentriollar material (PCM). Discrete electron-dense granules termed centriollar satellites (red), traffic to and away from the centrioles along the MT tracks emanating from the PCM and regulate the functions of the centrosome. PCM1 is the dominant structural component of these satellites and helps sequesters MIB1 (purple) within centriollar satellites to regulate ciliogenesis. Among other pericentrosomal functions, when not sequestered, MIB1 traffics to the centrosome and results in the degradation of proteins required for primary cilium formation. (Image generated using biorender.com)

Summary of Thesis

In the following pages, I document the work I have performed over a number of years to characterize MIB1 as a host factor for AdV infection. In **Chapter II** I present the initial genome-wide loss-of-function screen conducted by postdoctoral researcher in the lab, Hans-Heinrich Hoffmann, that first identified MIB1 as a host factor, followed by validation across multiple cell lines and mutagenesis studies into the functions of MIB1 required for virus infectivity. This chapter also describes our efforts to examine the specificity of MIB1 as a host factor for AdV infection relative to other viruses particularly ones with similar lifecycle features. In **Chapter III**, I present a series of microscopy studies that dissect the precise step in the virus lifecycle mediated by MIB1. In the process, I reexamine more broadly the role of centriollar satellite and microtubule dynamics on AdV entry. In **Chapter IV**, I will highlight the use of two complementary proteomic approaches to characterize both MIB1's cellular context and identify potential ubiquitination targets. I will then conclude in **Chapter V** with some preliminary functional studies examining MIB1 ubiquitination candidates and their possible role in the AdV lifecycle.

Chapter II: Identification and characterization of Mindbomb 1 as a host factor for adenovirus infection

Introduction to haploid genetic screens

Cellular proteins required for virus infection, known as host factors, act at every stage of the viral lifecycle to facilitate its ultimate replication, spread and survival. Host factors, then, when non-essential for the host, can serve as potent antiviral drug targets. Genome-wide knock-out (KO) screens have been successfully employed to identify these host factors for a number of different viruses.

Genome-wide CRISPR KO screens have now emerged as a remarkably efficient means to generate loss-of-function mutations in a variety of genetic backgrounds (Puschnik et al., 2017). However, traditionally, performing genome-wide mutagenesis screens was hindered by the diploid or even polyploid nature of a number of human cell lines. Utilizing a unique cell line termed Hap1 derived from a chronic myelogenous leukemia cell line KBM-7 and possessing only a single copy of each allele[10], Carette et al. developed a simple and elegant way to conduct genome-wide loss-of-function screens in human cells (Carette et al., 2009). In this approach, Hap1 cells are transduced with "gene-trap" lentiviruses carrying a gene cassette containing a strong splice acceptor site followed by a selection marker. Integration thereby results in the disruption of individual genes via the introduced splice acceptor site generating a population of null mutants. Upon the addition of some selection pressure, such as cytolytic virus infection, only those cells now resistant to becoming infected will survive and expand. The resulting cells can be pooled and deep-sequenced, using the sequence of the integrated marker as a tag to identify the disrupted gene.

Haploid genetic screening has indeed proved a powerful method for identifying cellular determinants of virus infection. In an inaugural application to influenza virus, this approach successfully isolated components of the sialic acid synthesis pathway required for viral binding and entry and has since been used to identify receptors for adenovirus-associated virus (AAV), and the intracellular receptors for Ebola and Lassa viruses (Pillay & Carette, 2015). In our own lab, this screening approach had already been successfully employed for respiratory syncytial virus (RSV) to uncover a dependence on the calcium pump SPCA1 which was then extended to a number of RNA viruses (Hoffmann et al., 2017). We were eager to similarly apply this strategy to AdV in the hopes of identifying host factors that could represent new targets for therapeutic intervention.

Haploid screen identifies MIB1 as host factor for adenovirus infection

To identify human host factors required for AdV infection, postdoctoral researcher in the lab Hans-Heinrich Hoffmann began by infecting the mutagenized population of Hap1 cells with replication-competent GFP-expressing adenovirus 5 (AdV5). Those cells productively infected by AdV5 were gradually eliminated by cytopathic effects of the virus. The remaining cells, resistant to infection by AdV5, were then expanded, harvested for genomic DNA and submitted for sequencing to identify the genes disrupted by gene-trap insertion **(Figure 2.1A)**.

[10] with the exception of chromosome 8

Significance was subsequently determined by analyzing genes for both the orientation of the insertion relative to the gene and its enrichment (in number of distinct insertions events) over an unselected (i.e. uninfected) library processed in parallel. The screen and analysis were done in collaboration with Dr. Thijn Brummelkamp at Netherlands Cancer Institute.

Three genes emerged as dramatically enriched in the AdV5-infected population over uninfected controls, indicating that their disruption via insertional mutagenesis now protected cells from AdV5 infection and cytotoxicity and marking them as potential host factors necessary for AdV5 infection **(Figure 2.1B)**. Two of these genes were the well-known receptors of AdV5: *CXADR* encoding the coxsackievirus and adenovirus receptor (CAR) and integrin *ITGB5*, validating the effectiveness of the technique in identifying specific determinants of AdV infection (Bergelson, 1999; Bergelson et al., 1997; Wickham et al., 1994). The third gene identified by the screen was Mindbomb 1 (*MIB1*), a large E3 ubiquitin ligase with well-described roles in the Notch and Wnt signaling pathways during neural development and as a component of centriollar satellites. However, at the time, there were no reported roles for MIB1 in the context of DNA virus infection.

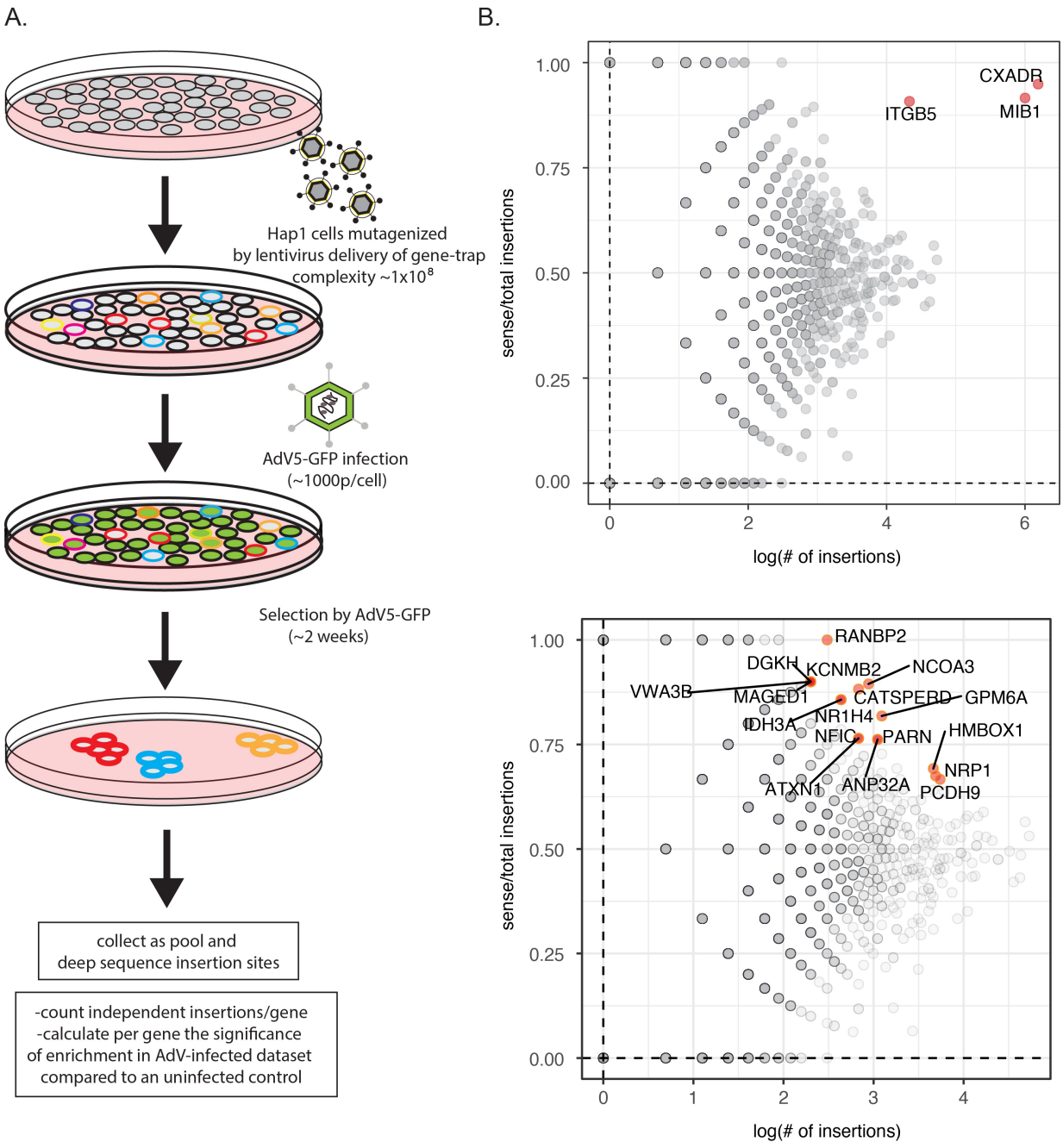

Figure 2.1 Haploid genetic screen identifies E3 ubiquitin ligase MIB1 as host factor necessary for AdV infection. (A) Schematic of haploid genetic screen for AdV infection. (B) Fishtail plot showing enrichment of genes in haploid screen upon AdV selection identified by deep-sequencing as number of distinct gene-trap insertions (x-axis; log[# of insertions]) and the ratio of sense over total insertions (y-axis) per gene. Significant hits (FDR < 0.05) in red and labeled by gene name. (C) Fishtail plot in (B) following omission of top three hits (CXADR, ITGB5 and MIB1) constituting second tier hits. Significant hits (FDR < 0.05 with at least 10 insertion events and ratio of sense over total insertions >=0.65) in red and labeled by gene name.

Validation of AdV5 phenotype in MIB1 CRISPR KO clones

To validate MIB1 as a necessary host factor for AdV infection, we generated Hap1 cells deficient for MIB1 using CRISPR-Cas9 editing and two independent single guide RNAs (sgRNAs) targeting exons 1 and 2 of MIB1 respectively **(Figure 2.2A,B,C)**. To rule out the possibility of CRISPR off-target effects, we reconstituted each of the selected sequence- and western blot-confirmed MIB1 KO clonal populations to constitutively express WT MIB1 (generated as bulk-selected stable cell lines) **(Figure 2.2B,C)**.[11] Hap1 WT, MIB1 KO and WT-MIB1 reconstituted clones (as well as CAR KO clones used as a control for complete inhibition of AdV5 infection) were infected with two different recombinant AdV5-GFP reporter viruses. Replication-competent AdV5-GFP, lacking only E4orf3, is capable of viral replication and spread to surrounding cells following the initial round of infection at 24-30 hpi. In contrast, the replication-incompetent AdV5-GFP cannot progress to later stages of infection (encompassing mRNA transcription, genome replication and virion progeny production) due to the absence of viral proteins E1A and E1B. While WT Hap1 cells robustly supported AdV5 infection, all MIB1 KO cells were severely impaired in infection by either replication-incompetent or -competent AdV5-GFP infection. This reduction was observed both at the level of the percentage of GFP-positive cells as well as the mean fluorescence intensity (MFI) within this population of infected (ie. GFP-positive) cells. The reconstitution of MIB1 KO clones with WT MIB1 restored infection in all cases[12] **(Figure 2.3 A,B)**. Taken together these observations corroborated our findings from the screen and highlighted MIB1 as a potent host factor for AdV5 infection. Inhibition of even the replication-incompetent AdV in MIB1 KO cells, also served as our initial indication that MIB1 acts at a step in the viral lifecycle prior to progression to late-stage infection.

Additional CRISPR KOs of MIB1 generated in A549s, STAT1-/- human fibroblasts (STAT1-/- hFIBs), HepG2-NTCP and Huh7.5-NTCP cells and partial KO in HeLa cells also displayed dramatic inhibition of AdV5 infection indicating MIB1's importance to AdV infection in diverse cellular contexts **(Figure 2.4)**.[13] A549s and HeLas were prioritized due to their ubiquitous use in AdV studies. The STAT1-/- hFIBs are unable to respond to IFN signaling due

[11] Of note, MIB1 levels may be tightly regulated as reconstitution of Hap1 WT, in particular, as well as MIB1 KO clones 1-2 and 2-2 with WT MIB1 displayed reduced cell growth kinetics **(Figure 2.2D)**. Small differences in cell growth kinetics can have an outsize impact in Hap1 cells in which cell number triples daily (WT=3.08x/day). MIB1 KO clone 2-1 and its WT MIB1-reconstituted counterpart, due to their robust and comparable cell growth kinetics, were the clonal cell lines selected for all subsequent mechanistic and proteomic studies described throughout the rest of the thesis.

[12] Although in all cases % GFP and MFI increased upon WT MIB1 reconstitution relative to the corresponding KO clone, discrepancies between % GFP-positive and MFI of these GFP-positive cells were observed when cross-comparing the different WT MIB1-reconstituted KO clones. For example, clone 1-2 displayed much higher MFI despite lower overall % of GFP-positive cells relative to clone 1-1. This might reflect clonal differences in the efficiency of WT MIB1 expression in each bulk-reconstituted population (% GFP), variable distribution of MIB1 expression at the level of individual reconstituted cells within the selected bulk population (MFI) or differences in cell growth kinetics (particularly notable for WT MIB1-reconstituted clone 1-2 in which a strikingly higher MFI correlates with decreased cell growth kinetics and might reflect reduced cell division-mediated dilution of GFP signal).

[13] Although we were unable to efficiently rescue AdV infection upon MIB1 reconstitution in several of these other cell lines such as A549 and HepG2-NTCP. (To be discussed in more detail below in the discussion of our work on HBV).

to the lack of the signal transducer STAT1. MIB1 had been shown to be an antiviral factor in the context of RNA virus infection by boosting expression of IFN. Inhibition of AdV5 infection upon MIB1 KO in the context of the STAT1-/- hFIBSs indicated that the effect of MIB1 in AdV infection was likely independent of the IFN signaling pathway. It also confirmed that the role of MIB1 applied in a more primary cellular context and was not just a phenomenon of transformed cell lines.

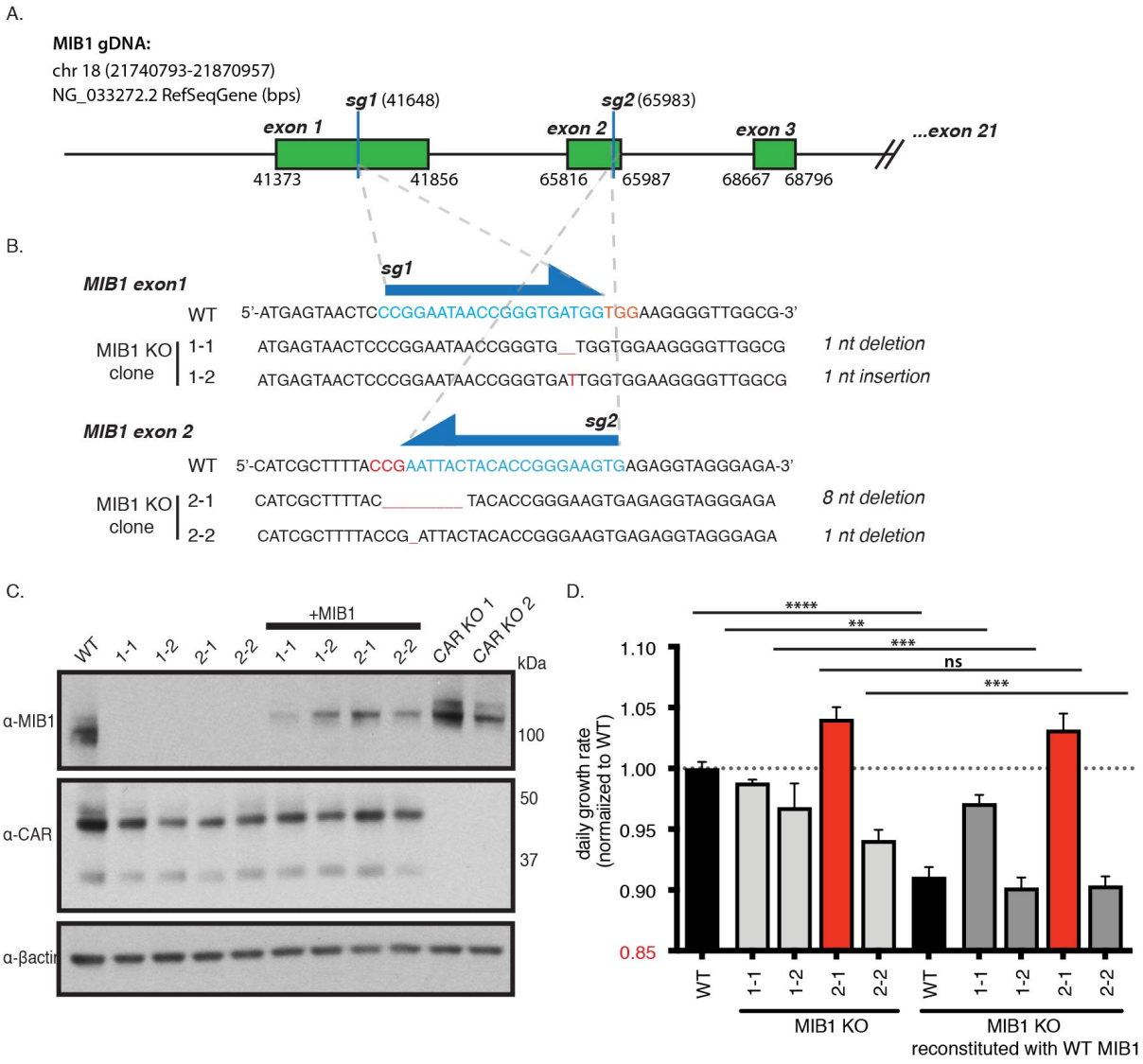

Figure 2.2 Generation and validation of MIB1 KO clones in Hap1 cells using CRISPR-Cas9 gene-editing. (A) Schematic of MIB1 gDNA labeled with early exons (green) and sgRNA target sites within each exon (blue line) (numbering of bps derived from NG_033272.2 RefSeqGene). (B) Expansion of sgRNA-encompassing region from (A) of parental WT sequence with targeting sgRNA sequence (blue) and PAM site (red) indicated. Subsequent sequencing of MIB1 KO clones confirmed successful CRISPR-Cas9 mediated gene disruption with sgRNAs targeting either exon 1 (1-1, 1-2) or exon 2 (2-1, 2-2). (C) Western blot of WT Hap1s, set of four sequence-verified MIB1 CRISPR KO clones in (B), MIB1 KO clones reconstituted with WT MIB1 and CAR CRISPR KO clones assessing expression of MIB1, CAR (both isoforms), and b-actin (loading control). (D) Cell viability assay (Cell Titer Glo) of Hap1 WT cells, MIB1 KO clones and WT MIB1-reconstituted cells WT and KO clones (averaged across 5 technical replicates) (** = p-value .0012).

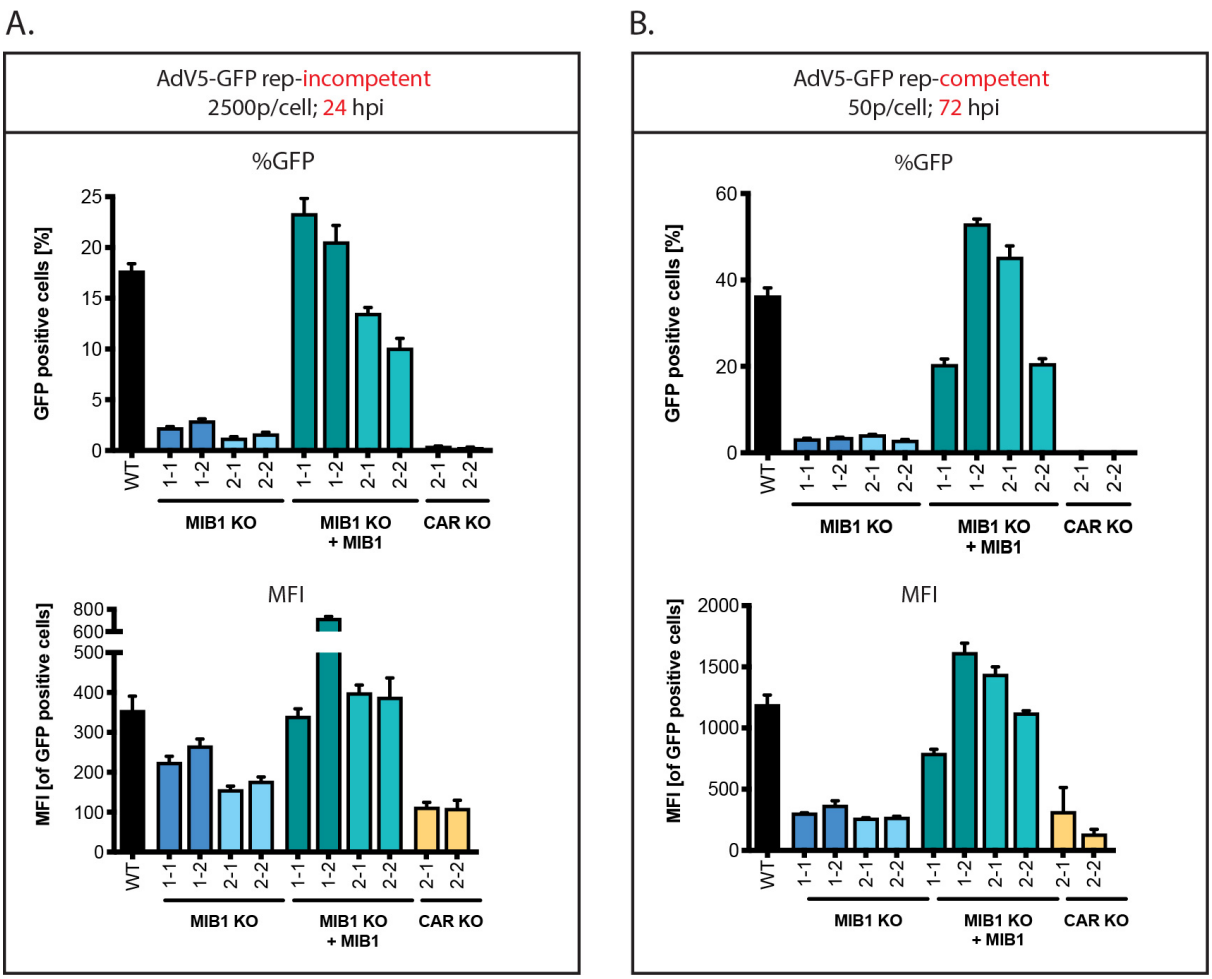

Figure 2.3 Replication-competent and -incompetent AdV5 infection of Hap1 cells is MIB1-dependent. Infection of Hap1 WT cells, MIB1 KO clones, WT MIB1-reconstituted KO clones and CAR KO clones with (A) replication-incompetent AdV5-GFP at MOI of 2500 p/cell for 24hpi and (B) replication-competent AdV5-GFP at MOI of 50 p/cell for 72 hpi. In both cases, at the indicated timepoint, harvested cells were analyzed by flow cytometry and plotted as the percentage of GFP-positive cells and the mean fluorescence intensity (MFI) of only the GFP-positive cell population.

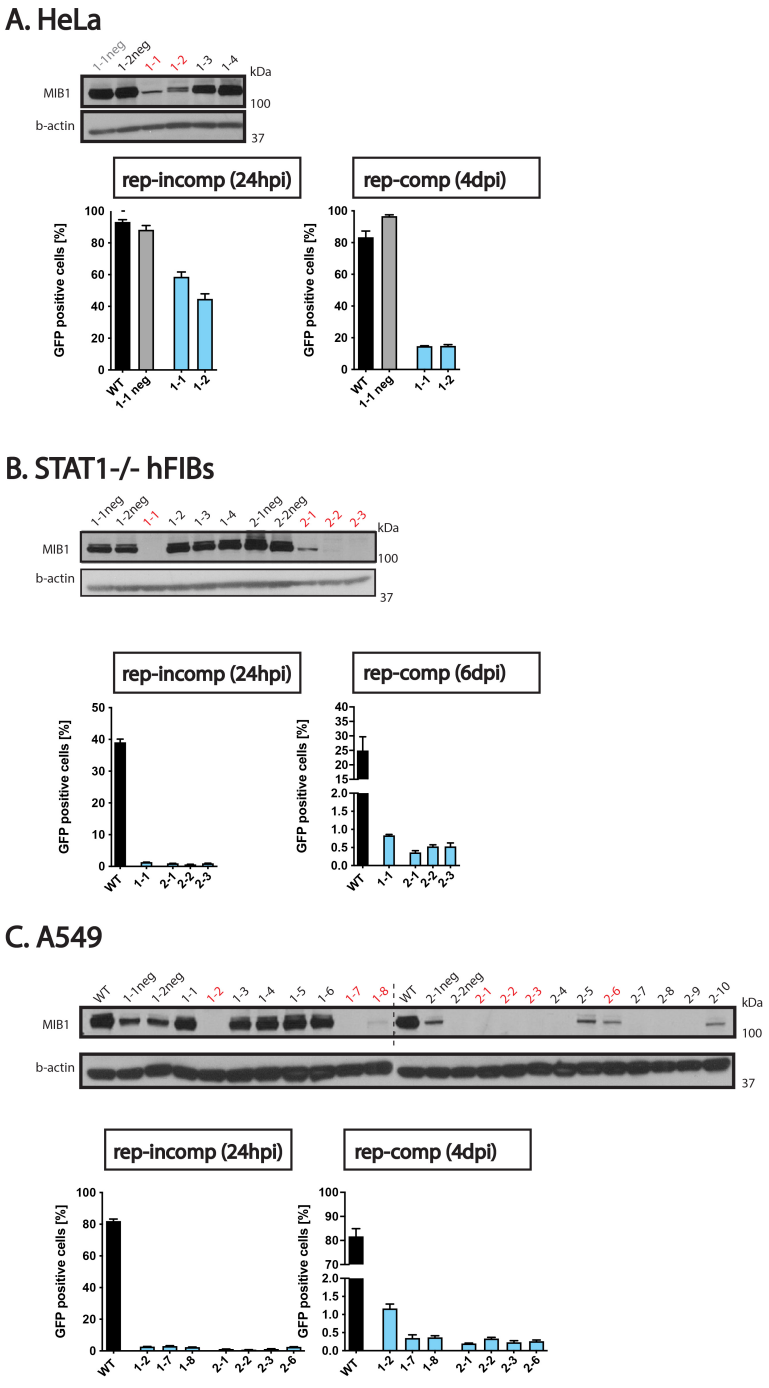

Figure 2.4 AdV5 infection is dependent on MIB1 expression in diverse cellular contexts. MIB1 full or partial KO clones were generated in (A) HeLa, (B) A549 and (C) STAT1-/- human fibroblasts by CRISPR-Cas9 editing using guide RNAs targeting exon 1 or exon 2 and screened for MIB1 expression level and b-actin (loading control) via Western blot. WT cells and a select set of full (A549 and STAT1-/- hFib) or partial (HeLa) MIB1 KO clones (indicated in red) and MIB1 WT clone (1-1 neg in grey) were infected with replication-incompetent (MOI=2000 p/cell) or replication-competent (MOI=25 p/cell) AdV5-GFP. At the indicated timepoint, harvested cells were analyzed by flow cytometry and plotted as the percentage of GFP-positive cells.

MIB1 is a host factor for multiple AdV serotypes

MIB1 emerged from the screen as the sole additional host factor for AdV5 infection besides known viral receptors. Given MIB1's well-characterized roles in regulating surface level expression of Notch and Wnt receptors, we were curious whether the effects of MIB1 were mediated by indirect modulation of CAR receptor expression. Western blot for CAR in Hap1 cells showed comparable expression levels between WT and MIB1 KO Hap1 cell lines **(Figure 2.2C)**. CAR-independence of the observed AdV5 inhibition was further confirmed by infection with alternate AdV serotypes that utilize distinct entry receptors. While AdV2 similarly utilizes the CAR receptor, AdV7 and AdV35 utilize desmoglein-2 (DSG-2) and CD46 respectively **(Figure 2.5A)** (H. Wang et al., 2011). Infections with GFP-reporter virus of AdV5 (AdVCiG) modified to express the fiber proteins of either AdV7 (AdVCiG-F7) or AdV35 (AdVCiG-F35) were still highly impaired in MIB1 KO cells as measured by percentage of infected cells **(Figure 2.5B)** (Gall et al., 1996; Schoggins et al., 2003). Similar inhibition was observed upon infection with WT AdV2, AdV7 and AdV35 definitively placing the function of MIB1 in AdV infection downstream of receptor engagement **(Figure 2.5C)**.

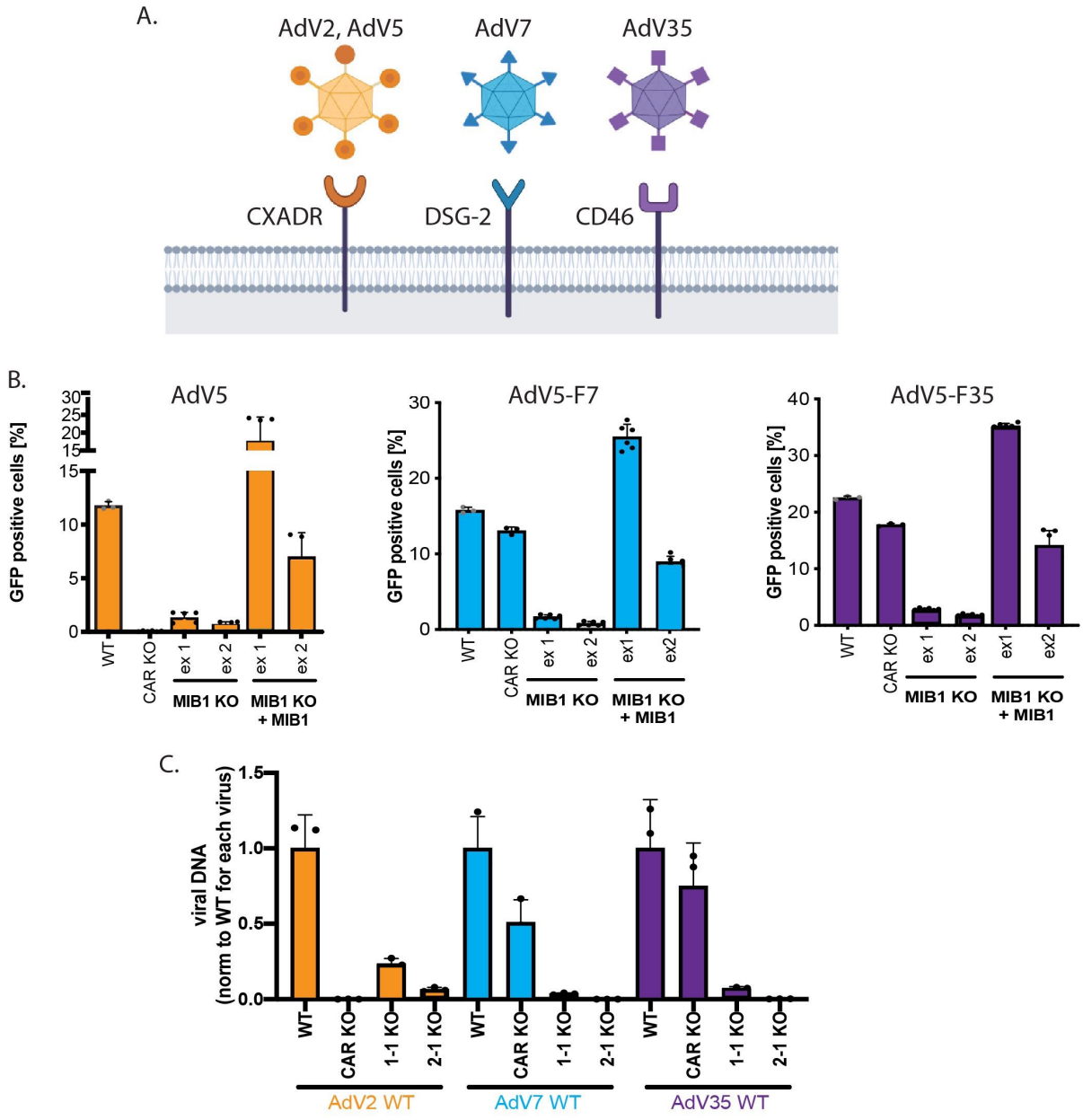

Figure 2.5 MIB1 is a host factor for multiple AdV serotypes independent of entry receptor. (A) Schematic showing utilization of distinct entry receptors among different AdV serotypes (AdV2/5: CAR, AdV7: DSG-2 and AdV35: CD46). (B) Hap1 WT cells, CAR KO clones, MIB1 KO clones and MIB1 KO clones reconstituted with WT MIB1 were infected with recombinant AdV5-GFP or AdV5-GFP expressing the fiber protein of either AdV7 or AdV 35 (MOI= 10000 p/cell). At 24 hpi, harvested cells were analyzed by flow cytometry and plotted as the percentage of GFP-positive cells averaged across the two selected clones for guide RNAs targeting either exon 1 (ex1: 1-1, 1-2) or exon 2 (ex 2: 2-1, 2-2). (C) Hap1 WT, CAR KO and select MIB1 KO clones (1-1 and 2-1) were infected with WT AdV2, AdV7 or AdV35 (MOI=10000 p/cell), harvested for viral DNA at 72 hpi and quantified by RT-qPCR (generously performed by Eric Lam from the Falck-Pedersen Lab).

Mining the haploid screen for additional AdV5 host factors

We have recently gone back and reexamined the Hap1 AdV5 loss-of-function screen for additional genes that displayed significant enrichment in number of insertions in the sense orientation albeit far below the levels observed for our strongest hits: CAR, ITGB5, and MIB1 **(Table 2.1)**. Regraphing the data with these top hits removed, revealed subtle enrichment in the population of a number of genes previously implicated in AdV infection. The emergence of these hits validated the strength of this screening approach but also revealed that its stringency and/or insufficient depth of coverage perhaps masked more subtle host factors **(Figure 2.1C)**. For example, although Nup214 mediates direct AdV capsid binding to the nuclear pore, its intimate binding partner RANBP2 (Nup358) has been implicated in efficient disassembly after docking (Strunze et al., 2011). NFIC is necessary for the efficient replication of AdV genomes via interaction with adenoviral DNA binding protein (DBP) (Cleat & Hay, 1989). ANP32 is a validated binding partner of not only the adenoviral ubiquitin ligase E1B55-E4orf6 complex but constitutively with CRM1, a pathway necessary both for AdV entry as well as late stage mRNA export (Higashino et al., 2005). ATXN1, is a well-validated interaction partner of ANP32, implicated together in neurodegenerative disease (Matilla et al., 1997; Sánchez et al., 2013). Although only represented by a small number of gene insertions, KLC1, the adaptor component of the plus-end directed motor kinesin, also emerged among these lower-stringency genes. Kinesin has been implicated in successful AdV trafficking both to and away from the nucleus although siRNA KD of KLC1 showed it was dispensable for the initial trafficking to the MTOC (J. Zhou et al., 2018). Another subset of these genes converged on MIB1-related pathways. NR1H4, for example, is implicated in the regulation of ciliogenesis. Knock-down of NR1H4 increases ciliogenesis via induction of autophagy similar to MIB1, a reported inhibitor of ciliogenesis (Z.-Q. Liu et al., 2018b). MAGED1 is a validated centrosome component.

Among the third tier of potential AdV5 host factors (blue in **Table 2.1** and classified as significantly enriched by number of gene insertions but with a sense orientation/total insertion ratio of <0.5), several genes caught our eye for their involvement in MT dynamics and vesicle trafficking. We chose to take note of significant genes in this category since insertion of the splice-acceptor cassette within an exon, even in the antisense orientation, could still act to functionally disrupt the gene by generating in-frame non-functional gene products or introducing frame-shift stop codons[14]. Here we observed MT motors, kinesins Kif22 and Kif11, as well as regulators of MT dynamics TBCD and AGBL1. AGBL1 (> 50 insertions), as a deglutamylase of tubulin, is particularly intriguing to us given the hypothesis that CRM1 may facilitate trafficking from MTOC to NPC by altering post-translational modification (such as glutamylation) of perinuclear MTs. We also observed a number of Golgi vesicle trafficking factors STX18 and NSF as well as more general vesicular transport factors VPS33A, CHMPB, EXOC4 and RAB8B. Of relevance to MIB1, CEP135, a component and regulator of centriollar satellites also appeared among these genes. Given the stringency of the haploid screening approach any of the genes presented above may pose exciting future avenues of study when probed individually. Taken together, they may illuminate broader functional pathways required for AdV infection that might even intersect with the mechanism by which MIB1 facilitates the viral lifecycle.

[14] although these events would inevitably be at lower frequency and depend on the accessibility of certain regions of DNA or the size of the gene and its relative proportion of exonic to intronic sequence

Table 2.1 Haploid genetic screen identifies candidate host factors for AdV5 infection. Hits from gene-trap screen (classified as those genes significantly enriched [p-value <0.05] following selection by AdV5 infection relative to an uninfected control population) broadly grouped by sense orientation insertions/total insertions ratio >0.5 (red, orange, yellow) or <0.5 (blue, purple) and then sorted by total number of insertions (red>75, orange/blue>=10, yellow/purple<10).

Gene	Sense insertions	Antisense insertions	p-value	FDR-adjusted p-value	Total Number of insertions	Sense/Total insertion ratio >0.5
CXADR	463	25	1.48E-105	1.44E-101	488	0.948770492
MIB1	370	34	1.79E-72	8.73E-69	404	0.915841584
ITGB5	69	7	6.42E-14	2.09E-10	76	0.907894737
PCDH9	28	14	0.043558522	1	42	0.666666667
NRP1	27	13	0.038477308	1	40	0.675
HMBOX1	27	12	0.023702702	1	39	0.692307692
GPM6A	18	4	0.00434351	1	22	0.818181818
ANP32A	16	5	0.026603699	1	21	0.761904762
PARN	16	5	0.026603699	1	21	0.761904762
NCOA3	17	2	0.000728607	0.789405399	19	0.894736842
CATSPERD	15	2	0.002349854	1	17	0.882352941
ATXN1	13	4	0.049041748	1	17	0.764705882
NFIC	13	4	0.049041748	1	17	0.764705882
IDH3A	12	2	0.012939453	1	14	0.857142857
NR1H4	12	2	0.012939453	1	14	0.857142857
RANBP2	12	0	0.000488281	0.632350922	12	1
DGKH	9	1	0.021484375	1	10	0.9
KCNMB2	9	1	0.021484375	1	10	0.9
MAGED1	9	1	0.021484375	1	10	0.9
VWA3B	9	1	0.021484375	1	10	0.9
ANO10	8	1	0.0390625	1	9	0.888888889
MAML3	8	1	0.0390625	1	9	0.888888889
PDE10A	8	1	0.0390625	1	9	0.888888889
ACSS3	7	0	0.015625	1	7	1
KLC1	7	0	0.015625	1	7	1
ZRANB3	7	0	0.015625	1	7	1
CACNA1D	6	0	0.03125	1	6	1
DOCK11	6	0	0.03125	1	6	1

Sense/Total integration ratio <0.5

DLGAP1	20	37	0.033143968	1	57	0.350877193
AGBL1	17	34	0.024092908	1	51	0.333333333
CNTNAP2	12	27	0.023702702	1	39	0.307692308
EPHA3	10	24	0.02430651	1	34	0.294117647
RAB8B	7	26	0.001318727	1	33	0.212121212
STX18	2	29	4.63E-07	0.001128355	31	0.064516129
MECOM	9	21	0.042773945	1	30	0.3
PBRM1	8	20	0.035698138	1	28	0.285714286
NXN	6	19	0.014633298	1	25	0.24
PDSS2	6	19	0.014633298	1	25	0.24
NARS2	3	22	0.000156522	0.305248809	25	0.12
EXOC4	5	18	0.010622025	1	23	0.217391304
FTO	5	15	0.041389465	1	20	0.25
MICU1	4	14	0.030883789	1	18	0.222222222
RNF157	3	14	0.01272583	1	17	0.176470588
ADGRG4	2	15	0.002349854	1	17	0.117647059
VPS13D	2	15	0.002349854	1	17	0.117647059
SAE1	1	15	0.000518799	0.632350922	16	0.0625
NELL2	3	12	0.03515625	1	15	0.2
NSF	3	12	0.03515625	1	15	0.2
ISYNA1	1	12	0.003417969	1	13	0.076923077
SUPT3H	1	12	0.003417969	1	13	0.076923077
NFATC3	2	10	0.038574219	1	12	0.166666667
PKM	2	10	0.038574219	1	12	0.166666667
KANSL1	1	11	0.006347656	1	12	0.083333333
TANGO6	0	12	0.000488281	0.632350922	12	0
CDON	1	9	0.021484375	1	10	0.1
TBCD	1	9	0.021484375	1	10	0.1
METTL16	1	8	0.0390625	1	9	0.111111111
SPTLC2	1	8	0.0390625	1	9	0.111111111
ATP9B	0	9	0.00390625	1	9	0
C7orf50	0	9	0.00390625	1	9	0
COL11A1	0	8	0.0078125	1	8	0
GART	0	8	0.0078125	1	8	0
GFPT1	0	8	0.0078125	1	8	0
INO80	0	8	0.0078125	1	8	0
SARS	0	8	0.0078125	1	8	0
C15orf41	0	7	0.015625	1	7	0
CDC73	0	7	0.015625	1	7	0
CNN2	0	7	0.015625	1	7	0
EFR3B	0	7	0.015625	1	7	0
GPATCH8	0	7	0.015625	1	7	0
KIF22	0	7	0.015625	1	7	0

SETD2	0	7	0.015625	1	7	0
YWHAE	0	7	0.015625	1	7	0
ATF1	0	6	0.03125	1	6	0
CEP135	0	6	0.03125	1	6	0
CHMP4B	0	6	0.03125	1	6	0
KIF11	0	6	0.03125	1	6	0
NUP210L	0	6	0.03125	1	6	0
ORC3	0	6	0.03125	1	6	0
PICALM	0	6	0.03125	1	6	0
RBPJ	0	6	0.03125	1	6	0
URGCP	0	6	0.03125	1	6	0
VPS33A	0	6	0.03125	1	6	0

MIB1 ubiquitination activity is required for AdV infection

Having confirmed MIB1 as a host factor for AdV infection, we were interested in characterizing the properties of MIB1 that mediate infection. In particular, we focused on MIB1's classification as an E3 ubiquitin ligase. E3 ubiquitin ligases are the effectors of ubiquitination, a post-translational modification (PTM) characterized by the attachment of ubiquitin to a target protein. Modification can result in that protein's subsequent degradation or changes in its localization and/or binding partners. There are several distinct classes of E3 ubiquitin ligases characterized by the organization of their ubiquitin transfer-mediating domains and mechanisms. For example, HECT and RBR E3 ligases carry out an intermediate step of transferring ubiquitin from the E2 to themselves and then to the substrate. Instead, RING E3 ligases (named for the domain Really Interesting New Gene) arrange the E2 and substrate relative to one another to facilitate direct transfer of ubiquitin between the two (Morreale & Walden, 2016).

MIB1 is a member of this abundant and diverse RING family of E3 ligases. However, while many E3 ligases such as the Cullin E3 ligases (CRLs), to which MIB1 bears resemblance, are multi-subunit complexes, MIB1 is remarkable in that it contains within a single polypeptide (of 1006 AA) all domains needed to carry out ubiquitination of a target protein (Guo et al., 2016). At the N-terminus of MIB1 are two distinct substrate-binding domains termed MZM and REP cumulatively designated the "MIB" domain, which serves as the primary determinant of target specificity. This substrate-recognition domain is then connected by a series of ankyrin repeats to a C-terminus comprised of three RING finger domains. These RING domains, the defining feature of these ligases, act by binding E2 conjugating-enzymes and facilitating the direct transfer of ubiquitin from E2 onto a specific target protein **(Figure 2.6A)**.

Our initial reconstitution of MIB1 KO cells with domain mutants of MIB1 demonstrated that only full-length MIB1 was capable of rescuing AdV infection **(Figure 2.6B)**. However, in order to more specifically determine whether MIB1's effect on AdV was dependent upon its ubiquitination activity, we next reconstituted MIB1 KO cells with a set of previously-characterized point mutants. These included single mutations to RING domains 1 and 2, three distinct mutations to RING domain 3 and a patient variant, V943F, associated with LVNC, which maps to the coiled-coil domain between RING domains 2 and 3 (Luxán et al., 2013). Consistent with previous literature reporting lack of function for RING domains 1 and 2, we observed that only those MIB1 constructs with mutations in RING3 failed to restore AdV infection **(Figure 2.6C)** (Choe et al., 2007; Itoh et al., 2003; L. Zhang & Gallagher, 2009). This verified that the ubiquitination activity of MIB1 is required for AdV infection in Hap1 cells, presumably via targeted modification of either a viral or host protein. We also noted that reconstitution with the V943F mutant showed slight enhancement of AdV infection over WT MIB1[15]. This was striking given that the V943F mutation abrogates ubiquitination of bona fide target Notch signaling protein Jagged (JAG1) resulting in impaired Notch pathway signaling and the observed LVNC disease phenotype (Luxán et al., 2013). While the V943F mutation was speculated by Guo et al. to impair homodimerization and thereby autoubiquitination and turnover given the role of parallel coiled-coil domains in other E3 ligases, Luxan et al. demonstrate that

[15] we point this out here as the V943F mutant will become important later on in both our reconstitution of non-Hap1 cell lines and in our proximity-labeling proteomics.

V934F is still dimerization-competent but distorted in its interaction site with JAG1. We therefore conclude that MIB1's role in AdV infection is independent of its Notch pathway targets. Instead we hypothesize that the inability to bind and modify a subset of its targets might increase the pool of protein available to modify the target protein relevant to virus infection.

The distinct MZM and REP subdomains comprising the "MIB" domain were shown by McMillan et al. to recognize and bind distinct epitopes on substrates opening up the potential for combinatorial substrate recognition (McMillan & Blacklow, 2015). The ability to recognize two different proteins simultaneously could allow MIB1 to ubiquitinate only upon formation of specific protein complexes or at specific subcellular sites. Alternatively, if only one or the other domains was necessary this could assist in our own experiments by facilitating the design of more targeted substrate identification strategies. MZM is a tripartite structure composed of two copies of the Mib-Herc2 subdomain separated by a ZZ Zinc Finger, while REP is a set of tandem repeats completely unique to MIB (Guo et al., 2016). We were curious then whether one or the other domain is required for the impact on AdV entry or whether they work in concert. As shown above and unsurprisingly, reconstituted cells expressing MIB1 lacking the entire MIB domain (aka all substrate-recognition capacity) were unable to rescue infection **(Figure 2.6B)**. However, reconstitution with constructs lacking either MZM or REP domains individually were similarly impaired **(Figure 2.6B)** suggesting that both the MZM and REP domains participate in substrate recognition of the target protein relevant to AdV infection. However, it is also possible that full domain deletion of either MZM or REP abrogates ubiquitination of the relevant target by altering MIB1's structure more broadly despite target binding to one or the other domains. Future studies will explore the contribution of the individual substrate recognition domains using more nuanced point mutants within each of these domains.

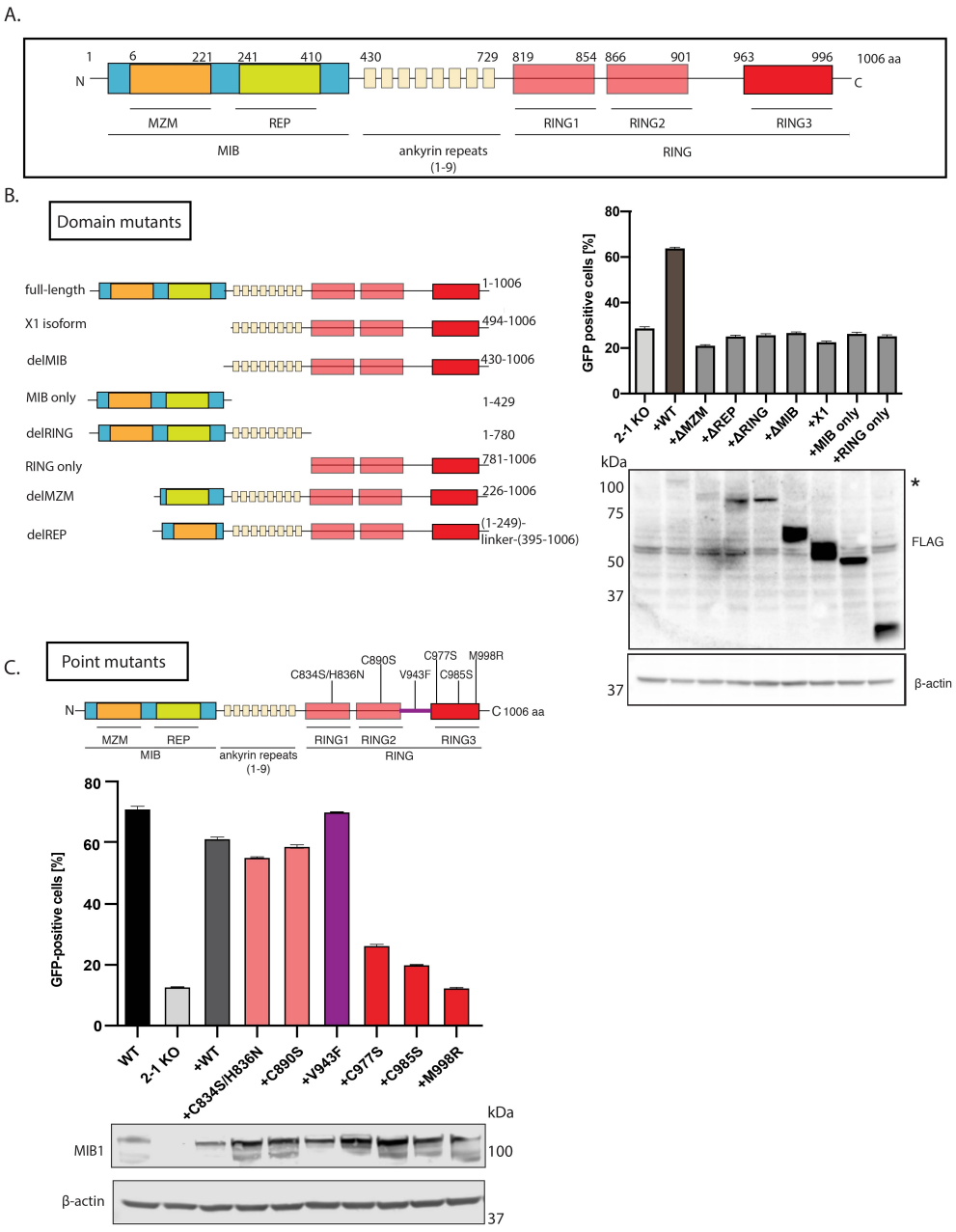

Figure 2.6 The ubiquitination activity of MIB1 is required for AdV infection. (A) Schematic of MIB1 architecture labeled with domain names. (B) Replication-competent AdV5-GFP infection (MOI =200 p/cell; 24hpi) of MIB1 KO clone 2-1 and KO 2-1 reconstituted with panel of domain mutants schematized on the left with accompanying Western blot confirming expression of various domain mutants (anti-FLAG) and b-actin (loading control) (*=full length WT MIB1. (C) Replication-competent AdV5-GFP infection (MOI=200p/cell; 24 hpi) of Hap1 WT cells, MIB1 KO clone 2-1 and KO 2-1 reconstituted with a panel of untagged point mutants (labeled on schematic above graph) with accompanying Western blot confirming expression of point mutants (anti-MIB1) and b-actin (loading control). Experiments were performed in triplicate and harvested cells were analyzed by flow cytometry and plotted as the percentage of GFP-positive cells (average of three technical replicates for single representative experiment).

Specificity of MIB1 as a host factor for virus infection

Given that the effects of MIB1 were independent of the AdV5 receptor, we were curious whether MIB1 might be a necessary host factor for other viruses as well. However, infection of Hap1 MIB1 KOs and reconstituted clones with a broad panel of viruses (predominantly GFP-reporter viruses) revealed the extreme specificity of MIB1-dependence for the adenovirus family (**Figure 2.7)**. This panel of viruses was chosen to include representative viruses for different virus classifications (ie. RNA vs DNA viruses, viruses with nuclear vs cytoplasmic replication steps). Interestingly, even those viruses which similarly possess a nuclear trafficking stage in their early lifecycle (the relevance of this shared feature will become more apparent in the following chapter) such as influenza, HSV-1 and lentiviruses, were unaffected by the presence or absence of MIB1 in this cell line. We found that in those cases where we did observe a defect (for example influenza) this reflected clone-to-clone variability as the defect was not rescued upon MIB1 reconstitution or was not reflected by the majority of clones. Furthermore, although MIB1 had been show to be antiviral to VSV infection, likely by enhancing innate immune responses (S. Li et al., 2011), we saw no major impact of MIB1 KO in our Hap1 cells upon infection with a panel of RNA viruses.

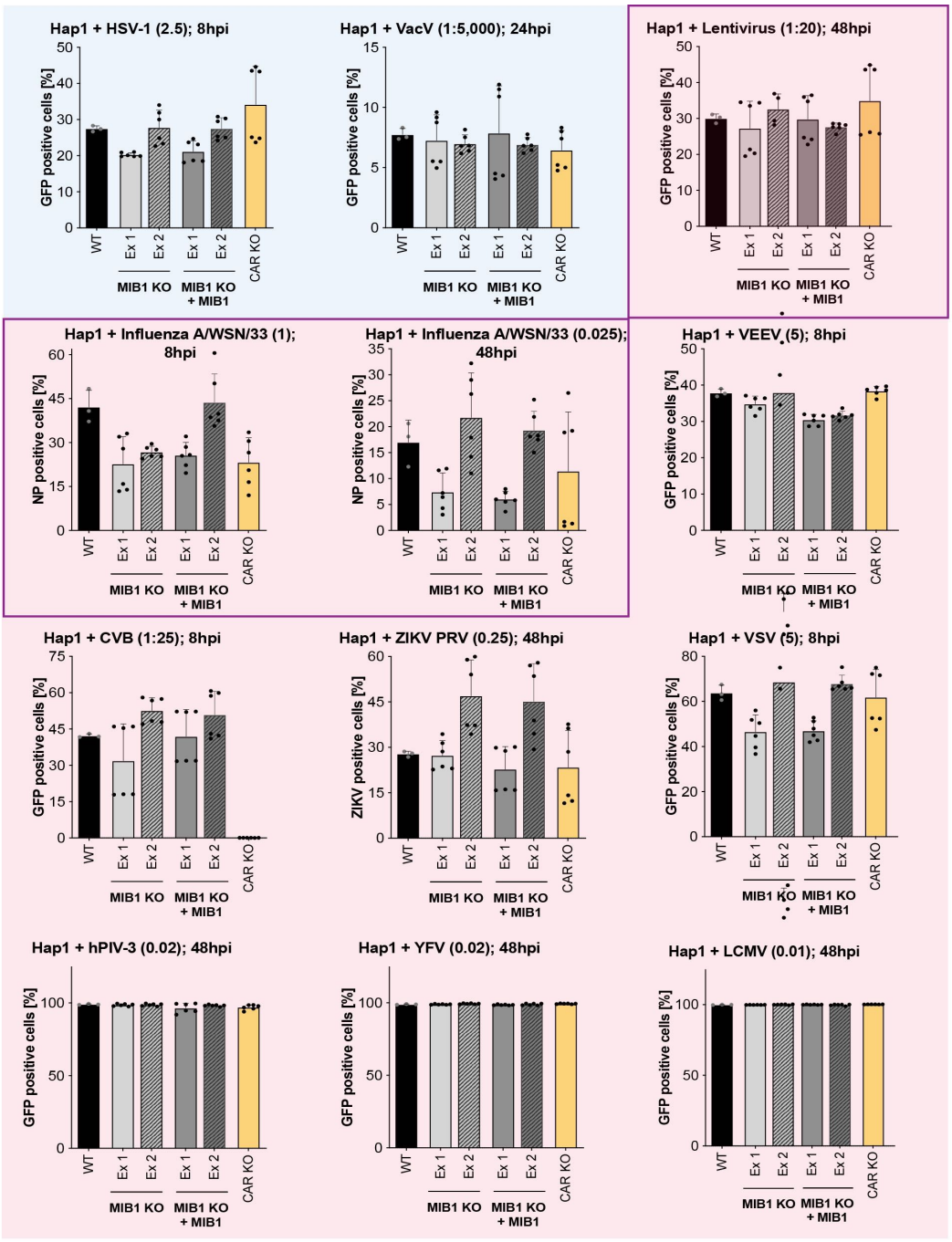

Figure 2.7 MIB1 is an AdV-specific host factor in Hap1 cells. Infection of Hap1 WT, MIB1 KO clones, MIB1 KO clones reconstituted with WT MIB1 and CAR KO clones with panel of viruses with diverse lifecycles: DNA (*blue*: HSV-1, VacV), RNA (*red*: VEEV, CVB, ZIKV PRV, VSV, hPIV-3, YFV, LCMV) or RNA virus with nuclear replication stage (*red with purple border*: lentivirus, influenza A/WSN/33) at stated dose and collected at stated timepoint. All cells infected with GFP-reporter viruses (with the exception of non-reporter influenza/WSN/33 virus which was processed by antibody-staining for viral NP prior to flow cytometry) were harvested and analyzed by flow-cytometry for percentage of GFP-positive cells averaged across the two selected MIB1 KO clones for sgRNAs targeting either exon 1 (Ex1) or exon 2 (Ex 2).

Despite preliminarily concluding that MIB1 was a host factor specific to AdV based on these results in Hap1 WT and MIB1 KO cells in which we saw no influence of MIB1 against any other virus, we were in fact unable to evaluate all viruses within this cell line. Of particular interest to us was Hepatitis B Virus (HBV), the focus of one major branch of the lab, and which incidentally shares certain key features of the AdV lifecycle. HBV, like adenovirus, is a DNA virus (technically DNA virus with RNA intermediate) that similarly traffics to the nucleus where it docks its capsid on the nuclear side of the NPC for subsequent disassembly and genome delivery (Rabe et al., 2003). Upon the initial round of viral infection, HBV capsids are assembled for enveloped release from the cell but can alternatively undergo a unique intracellular recycling through repeated capsid attachment and genome delivery at the NPC to enhance nuclear genome accumulation (Ko et al., 2018). HBV therefore uniquely undergoes capsid engagement at the NPC multiple times within the same cell beyond initial entry. In order to test HBV dependence on MIB1, we first generated MIB1 KO cells in HepG2-NTCP and Huh7.5-NTCP cells, both hepatoma cell lines engineered to stably overexpress the HBV receptor, NTCP. KOs were validated by Western blot and sequencing **(Figure 2.8A,C)**. Reassuringly, as in Hap1s, KO of MIB1 in HepG2-NTCP and Huh7.5-NTCP cells recapitulated the severe inhibition of AdV infection **(Figure 2.8B,D)**. We also decided to retest a more limited panel of other viruses in these additional cell lines. Similar to our results in the Hap1 cells, representative RNA viruses PIV and YFV showed no dependence on MIB1. The cytoplasm-replicating DNA virus vaccinia (VACV) displayed slightly enhanced replication in the absence of MIB1 in HepG2s **(Figure 2.8B,D)**.

Again we were particularly interested in testing those viruses that feature a nuclear genome delivery step given the parallels with the AdV lifecycle. In HepG2-NTCP cells, HSV-1 replication in MIB1 KO cells was impaired although in Huh7.5-NTCP cells this decrease was only observed for one MIB1 KO clone (and was enhanced in the other). We also chose to test two different types of retroviruses which differ in a key feature of their lifecycles. While lentiviruses dock at the nuclear pore to release their pre-integration complex into the nucleus, Moloney Leukemia Virus (MLV) requires the dissolution of the nuclear envelope which occurs upon mitosis to access the nuclear compartment. As a result, lentiviruses can replicate in all cell types while MLV can only infect dividing cells. Intriguingly, while lentivirus infection was inhibited across all HepG2- and Huh7.5-NTCP MIB1 KO clones, MLV (only tested in HepG2-NTCP cells) appeared to be independent of MIB1 (in fact, HepG2 clone 1-4-1 showed enhanced infectivity). This served as a preliminary indication that MIB1 may act at the parallel step in the lentivirus lifecycle as well while requiring further mechanistic follow-up. Unfortunately, these observations conflicted with the data from our Hap1 cells in which no clear phenotype for HSV-1 or lentiviruses were observed. Understanding this discrepancy will be the focus of future studies.

We had originally generated these cell lines for the express purpose of testing HBV. HBV infection of both HepG2-NTCP and Huh7.5-NTCP MIB1 KO cells was significantly reduced relative to WT infection as assayed by percentage of cells expressing HBV core protein **(Figure 2.9A)** and HBV S antigen release (data not shown). However, to conclusively validate MIB1 as a host factor for HBV (as well as potentially lentiviruses and HSV-1 in this particular cell line), we sought to reconstitute with WT MIB1 and rescue infection in these clones. HepG2-

NTCP KO clones 1-4-1 and 2-2-2 were stably reconstituted with WT or C985S MIB1 as well as WT and C985S in the background of the V943F mutation (MIBV9 and C9V9 respectively, which we had shown using our mutagenesis studies further boosted virus infection in Hap1 cells) **(Figure 2.9B)**. Checking for expression level by Western blot we observed that reconstituted WT MIB1 expression was almost negligible in both clones while the C985S mutant was expressed substantially hinting at autoubiquitination and turnover or toxicity upon reintroduction of a ubiquitination-competent MIB1 in these cells. Although unclear if the V943F mutant acts by abrogating autoubiquitination, by contrast, MIBV9 was appreciably expressed. Subsequent infection, however, with AdV5 revealed that while replication-competent AdV5-GFP could be rescued in WT MIB1-reconstituted cells, rescue of replication-incompetent AdV5-GFP was almost negligible (with the exception of MIBV9-reconstituted clone 2-2-2) despite restored MFI in those cells that were infected **(Figure 2.9C)**.[16] Subsequent infection of the HepG2 MIB1 KO clone 2-2-2 and the corresponding MIBV9 and C9V9-reconstituted cells (which had at least afforded some rescue of replication-competent AdV5) with HBV showed no rescue of HBV infection (rather infection was further suppressed) **(Figure 2.9D)**. However, ultimately, concluding that MIB1 is not a host factor for HBV on this basis seemed premature given the complications of rescuing even our typically robust AdV infection phenotype in this context. Staining of HBV capsids and DNA genomes (as described in Rabe et al. 2003—a parallel to the JR34 assay for AdV genome release to be described in the next chapter) to confirm whether HBV capsids similarly journey to the nucleus but fail to release their genomes or whether MIB1 exerts its influence on HBV through another independent step of the HBV lifecycle could give us greater confidence in the HBV defect even in the comparison between WT and KO cells. This would also allow us to assay the HBV phenotype within hours after infection and avoid the indirect impact of differential growth kinetics between clones and their reconstituted counterparts for collection at two weeks post-infection.

[16] Of note, we also reconstituted A549 and Huh7.5-NTCP KO clones with WT MIB1 to rescue AdV5 infection in MIB1 KO cells in these contexts. However, in all cases despite detection of the protein (to endogenous levels), poor rescue of infection was observed particularly for replication-incompetent AdV5. The disparity in rescue between replication-competent and replication-incompetent AdV5-GFP is also something we still don't understand given that there should be no difference in these viruses and their capsids at this stage of infection.

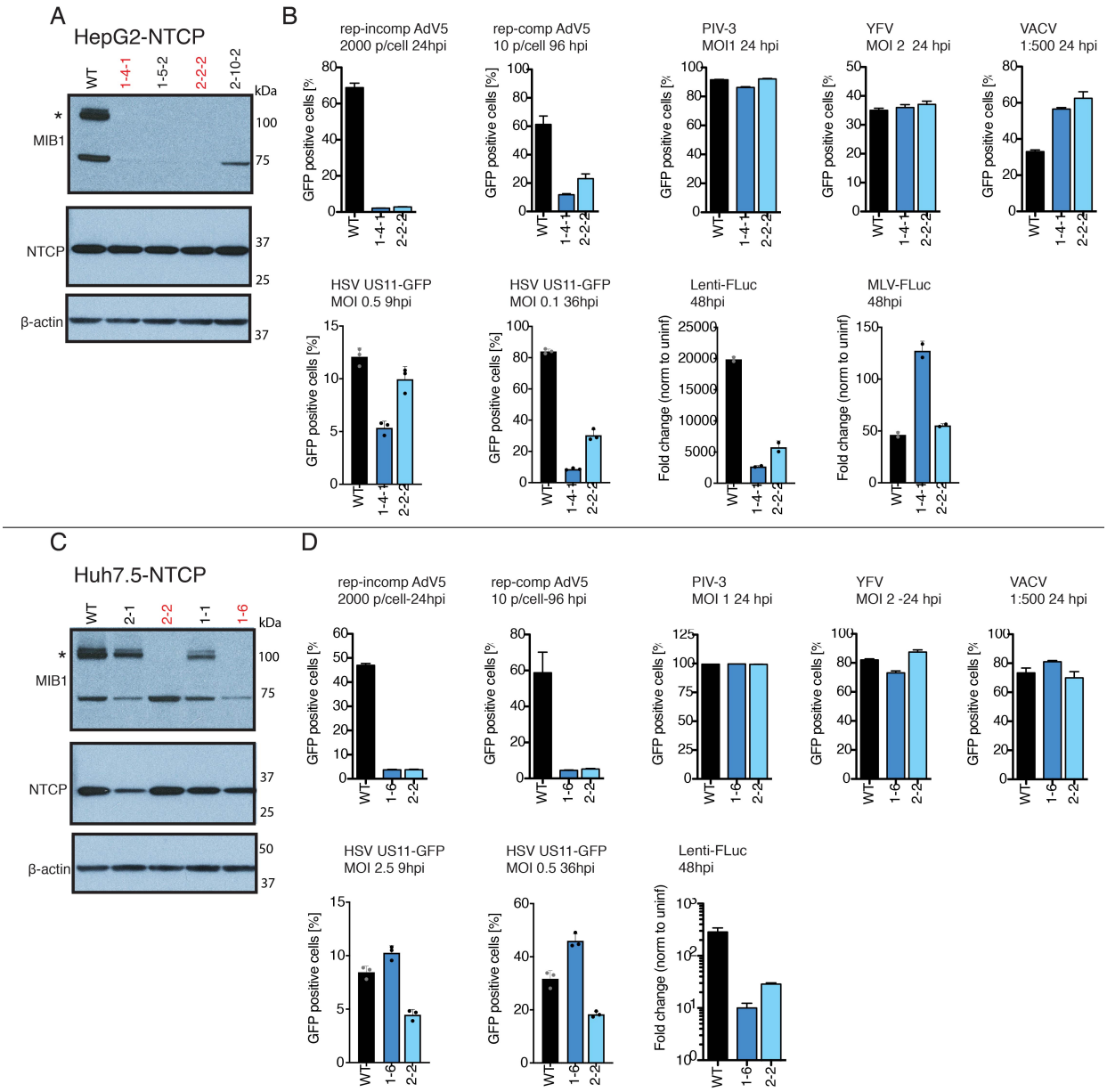

Figure 2.8 MIB1 KOs in hepatoma cell lines recapitulate MIB1-dependence for AdV infection but display variable MIB1-dependence for other nuclear targeting viruses. A) MIB1 KO clones were generated in HepG2-NTCP cells by CRISPR-Cas9 editing using guide RNAs targeting exon 1 or exon 2 and screened for MIB1 expression level via Western blot (* indicates full-length MIB1, lower band suspected MIB1isoform [unreported]). (B) HepG2-NTCP WT cells, and selected KO clones 1-4-1 and 2-2-2 (indicated in red on western) were infected with a panel of viruses (rep-incompetent and -competent AdV5-GFP, PIV-3, YFV, VacV, HSV-1, Lenti-FLuc and MLV-FLuc) at stated dose. At indicated timepoint, cells were harvested and analyzed by flow-cytometry for percentage of GFP-positive cells with the exception of Lenti-FLuc and MLV-FLUC for which cells were lysed and luminescence assayed as described. (C) Verification of MIB1 KO clones in Huh7.5-NTCP cells by Western blot as in (A). (D) Infection of Huh7.5-NTCPs with panel of viruses as in (B).

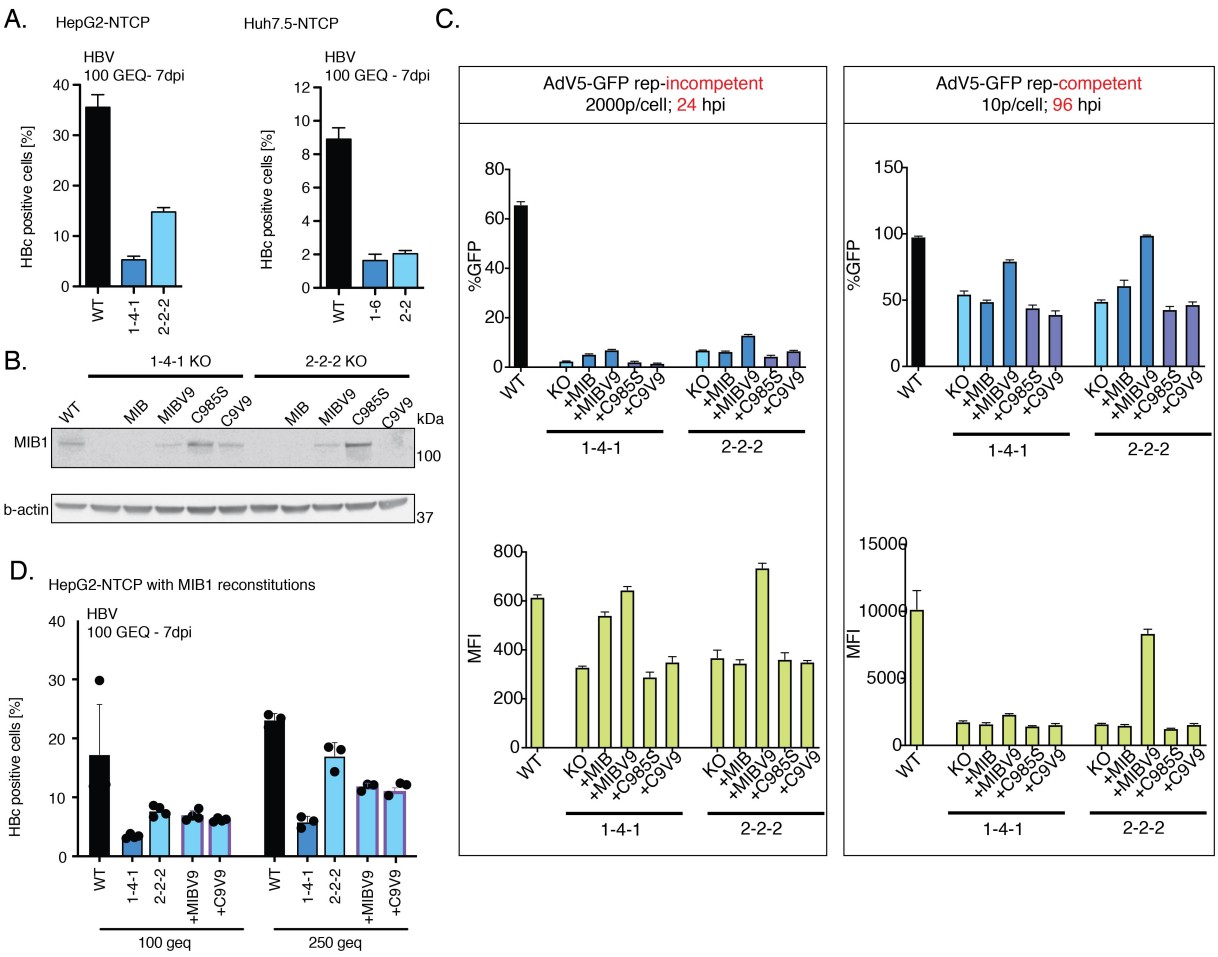

Figure 2.9 MIB1 KO in hepatoma cell lines reduces HBV infection but cannot be rescued by MIB1 reconstitution. (A) HBV infection (100 genome equivalents [GEQ]) of HepG2-NTCP and Huh7.5-NTCP WT and MIB1 KO clones, fixed at 7 dpi and assayed for % of infected cells by HBV core (HBc) staining and high-throughput imaging analysis. (B) Western blot assessing expression of MIB1 and b-actin (loading control) in WT HepG2 cells and MIB1 KO clones 1-4-1 and 2-2-2 stably reconstituted with WT MIB1, C985S or corresponding V943F mutants. (C) Infection of panel of HepG2 cell lines in (B) with either replication-incompetent (2000 p/cell) or replication-competent (10 p/cell) AdV5-GFP. Cells were harvested at 24 or 72 hpi respectively, analyzed by flow cytometry and plotted as the percentage of GFP-positive cells and the mean fluorescence intensity (MFI). (D) HBV infection (100 GEQ or 250 GEQ as indicated) of HepG2-NTCP WT, and MIB1 KO clones 1-4-1 and 2-2-2 with inclusion of MIBV9- and C9V9-reconstituted clone 2-2-2 counterparts assayed for % of HBc-positive cells as in (A).

In summary, it remains unclear why all cell lines besides Hap1 are refractory to MIB reconstitution in our hands. While expression of MIB1 in transduced cells was verified by Western blot, perhaps prolonged stable cell line selection and passage results in gradual silencing of MIB1 expression since the cells seem very sensitive to MIB1 levels. Alternatively, perhaps low-level truncation mutants of MIB1 generated by CRISPR editing and alternative start sites, although not detected by Western, could act in a dominant negative fashion in these cell lines in the presence of reintroduced WT MIB1. Future efforts to reconstitute these other cell lines will center around either introducing doxycycline-inducible MIB1 constructs into these cells and performing transient induction only encompassing the length of infection or cloning MIB1 into a different lentivirus vector less subject to cassette silencing. These are both strategies that have been effectively employed by Bauer et al. to study MIB1's role in AdV in HeLa cells (Bauer et al., 2019). Solving this issue of reconstitution in the non-Hap1 cell lines will be important for future work to conclusively examine MIB1's possible role in diverse virus lifecycles.

Chapter III. Elucidating the role of MIB1 in the AdV lifecycle --- A microscopy approach

MIB1 is necessary for AdV5 genome delivery

Having validated MIB1 as a potent host factor for AdV, our next task was to narrow in upon precisely which facet of the complex AdV lifecycle intersected with the action of this E3 ligase. Fortunately, we already had some clues. The inhibition of both replication-competent *and* incompetent AdV5 infection in the absence of MIB1 restricted the role of MIB1 to the early stage of the viral lifecycle. This early phase, however, still encompasses a series of discrete steps as the virus traverses the cytosol from plasma membrane to nuclear pore, releases its DNA and begins early transcription. To pinpoint the specific step at which MIB1 functions, we utilized a recombinant AdV5, JR34, modified to express a FLAG-tagged pVII protein (Smith et al., 2009). The pVII protein is a component of the incoming capsid and arranged in tight complex to the viral genomic DNA. When contained within the intact capsid the FLAG-tagged pVII is obscured from recognition by the anti-FLAG antibody. However, upon release of the viral DNA into the nucleus, the DNA-associated FLAG-tagged pVII may now be accessed by anti-FLAG antibodies and visualized by immunofluorescence (IF) microscopy (**Figure 3.1A)**. While some groups have developed click chemistry methods to visualize the released vDNA directly, this pVII approach has been widely used as a proxy for DNA at this step since pVII remains in complex with the DNA in "nuclear dot structures" even through the beginning of DNA replication (Chen et al., 2007; Komatsu et al., 2015; Xue et al., 2005).

Hap1 MIB1 KO clone 2-1 cells and clone 2-1 KO cells reconstituted with WT MIB1[17] were infected with AdV5-JR34 and stained for both capsid (anti-hexon) and released FLAG-pVII (anti-Flag) at 1.25 hpi. Strikingly, while MIB1 KO and WT MIB1-reconstituted cells displayed a similar quantity of viral particles in the cytoplasm, the appearance of viral DNA (quantified as pVII "particles") in the nucleus was severely compromised in the MIB1 KO cells (**Figure 3.1B,C,D)**. This block in DNA release in MIB1 KO cells persisted even up to 4hpi suggesting that the lack of pVII signal is not merely a kinetic delay in MIB1 KO cells (data not shown). Additionally, the block on DNA delivery in the absence of MIB1 was similarly observed upon AdV5-JR34 infection of HepG2-NTCP cells confirming the robustness of the phenotype in diverse cellular contexts. FLAG-pVII "particle" staining in HepG2-NTCP KO clone 2-2-2 or the KO clone reconstituted with the C985S mutant was markedly reduced relative to HepG2-NTCP WT cells or upon reconstitution of KO clone 2-2-2 with WT MIB1 (**Figure 3.1E)**. In most experiments, a timepoint of 1 hour and 15 mins post-infection for assaying DNA virus release was chosen based on a timecourse of pVII-DNA release which was consistent with existing literature and which placed arrival at the centrosome and nuclear pores around 1 hpi (Leopold et al., 2000; Suomalainen et al., 1999). Synchronization on ice allowing adsorption of added virus prior to internalization (the start of "infection" marked by inoculum removal and addition of prewarmed media) was used to homogenize the population of viral capsids captured along their trajectory from plasma membrane to nucleus.

[17] The 2-1KO clone reconstituted with WT MIB1 was our comparative "WT" for all microscopy experiments in order to ensure a more morphologically homogenous population derived from the same single cell clonal population.

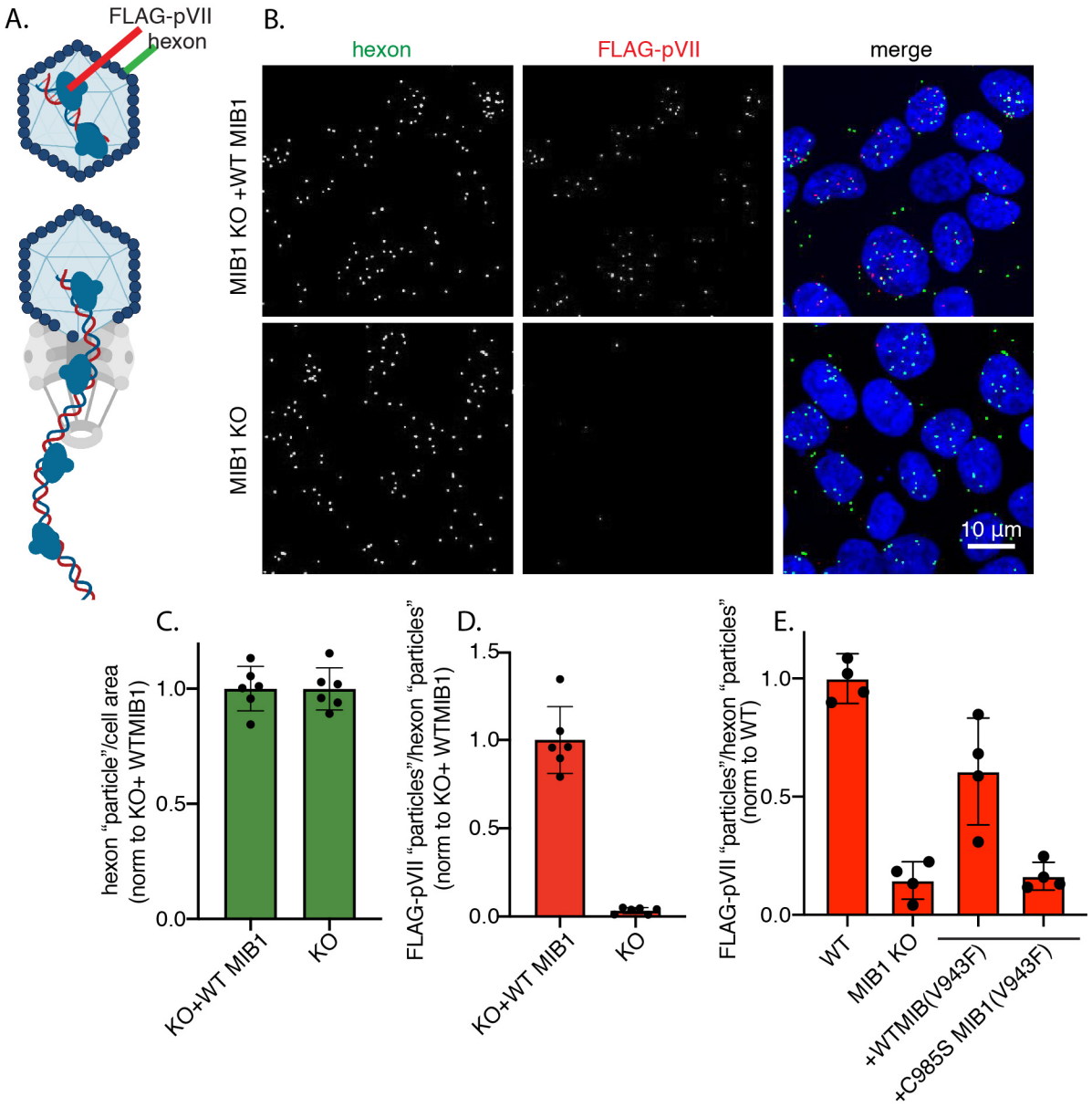

Figure 3.1 MIB1 is required for delivery of AdV5 DNA into the nucleus. (A) Schematic of recombinant AdV5-JR34 expressing FLAG-tagged pVII protein in complex with adenoviral DNA. The FLAG epitope is inaccessible to antibody binding within the capsid but becomes accessible upon DNA release at the nuclear pore (image generated using biorender.com). (B) Representative images of Hap1 MIB1 KO clone 2-1 and its WT MIB1-reconstituted counterpart infected with AdV5-JR34 (MOI=2000 p/cell; 1.25 hpi) stained for capsid (anti-hexon) and pVII (anti-FLAG) shown in individual channels (maximum-projected Z-stack) and as merged images (green: hexon, red: FLAG-pVII, blue: nucleus) Scale bar= 10 µm. (C) Quantification of hexon "particles" and (D) FLAG-pVII "particles" as seen in (B) by Fiji 3D Objects Counter normalized by cell area per field of view (FOV) and number of hexon "particles" respectively and averaged across 6 FOV. (E) Quantification of FLAG-pVII "particles" (as above) following JR34 infection (MOI=2000 p/cell) of HepG2 WT, HepG2 KO clone 2-2-2 and KO clone 2-2-2 reconstituted with WT MIB1 or C985S MIB (both in the background of the V943F mutation).

MIB1 mediates genome delivery downstream of MTOC arrival

Mutations in RING domain 3 of MIB1 demonstrated that the ubiquitination activity of MIB1 was necessary for AdV infection. While post-translational modification by ubiquitin can lead to diverse outcomes for the target protein depending on the nature of the lysine linkage, one well-characterized consequence is the targeting of the modified protein to the proteasome for degradation. A functional UPS is critical for the entry of several viruses that like AdV require nuclear trafficking. Inhibition of the proteasome, for example, resulted in sequestration of IAV particles in endocytic compartments and inability of HSV capsids to traffic to the nuclear pore. We were therefore curious whether the ubiquitin-proteasome system more broadly impacts AdV genome delivery. A role for the UPS would be in line with a role for MIB1 in marking its target protein for degradation. MG132 is a widely used inhibitor of proteasome-mediated degradation. Brief pre-treatment of WT cells with MG132 before and throughout AdV5-JR34 infection significantly reduced (4-5 fold) the appearance of pVII foci albeit not quite to the degree observed upon MIB1 KO (**Figure 3.2A**). Blocking proteasomal degradation in WT cells thus mildly phenocopied the impact of not having MIB1 present at all hinting in both cases at the aberrant stabilization of some target protein relevant to virus infection. However, this effect could also be due to the overwhelming impact complete shut-down of proteasomal degradation could be having on the cell independent of the contribution of any specific MIB1-dependent ubiquitination event(s).

Recent studies of AdV entry conducted by Wang et al. have reported that inhibition of CRM1-mediated export by inhibitor leptomycin B (LMB) boosts virion association with MT motors leading to the dramatic aggregation of virions directly at the MTOC (I.-H. Wang et al., 2017). Indeed, treatment of our WT MIB1-reconstituted KO cells with LMB prior to and throughout AdV5-JR34 infection resulted in capsid aggregation at the MTOC visible as enhanced clustering of AdV hexon foci around pericentrin (a defining structural component of the MTOC) (**Figure 3.2B**). Treatment with LMB also blocked DNA release into the nucleus as quantified by pVII staining, in line with arrest of capsids prior to NPC arrival (**Figure 3.2A**). To further resolve the MIB1-dependent step in viral genome delivery we next characterized the spatial distribution of AdV5-JR34 virus particles in (1) KO cells treated with LMB and (2) WT cells treated with LMB and MG132 simultaneously. We hypothesized that if the block in virus infection mediated by MIB1 occurs before reaching the MTOC then the characteristic aggregates upon LMB treatment should not be observed in MIB1 KO cells. In fact, we observed that both MIB1 KO cells treated with LMB and WT cells co-treated with both MG132 and LMB showed characteristic MTOC particle aggregation comparable with WT cells treated with LMB alone (**Figure 3.2C**). We therefore concluded that both MIB1 and the proteasome (either independently or consecutively) mediate some critical step *downstream* of MTOC arrival to facilitate the coordinated release of vDNA into the nucleus.

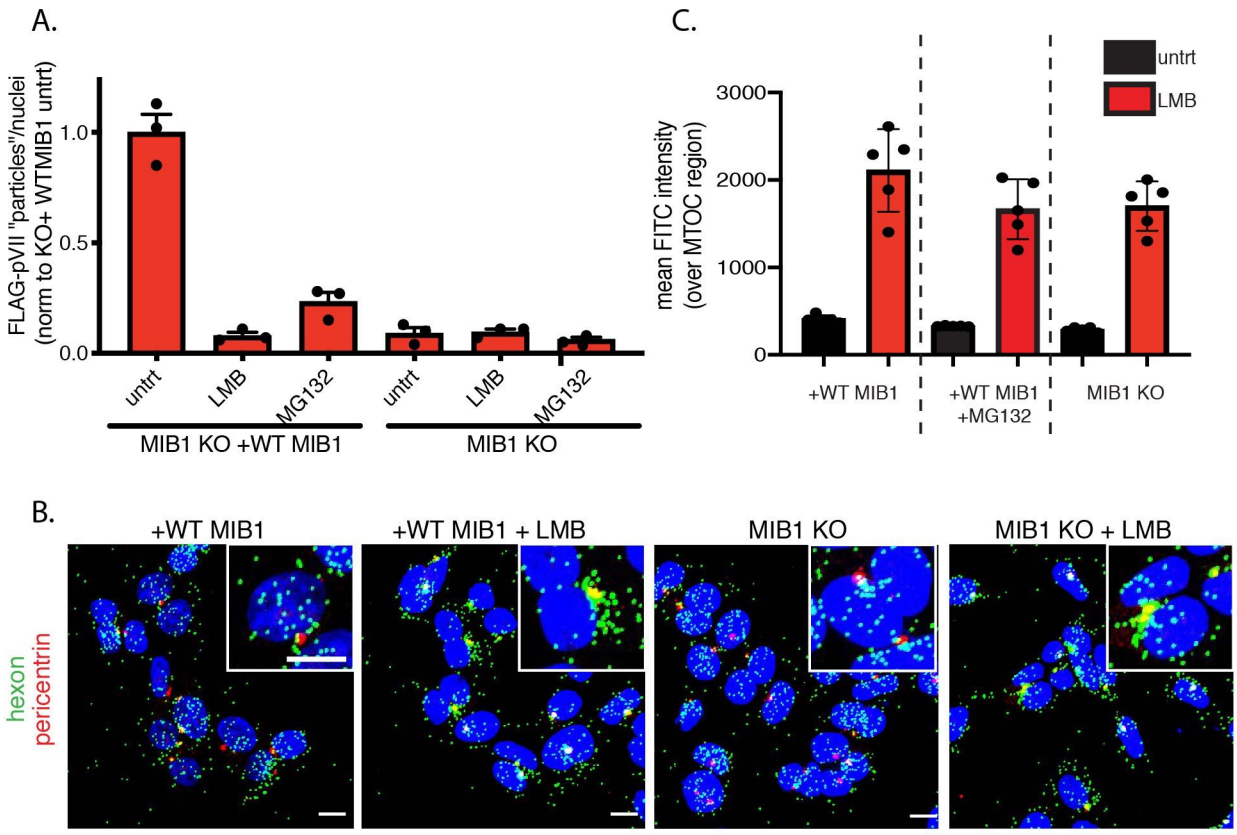

Figure 3.2 MIB1 mediates delivery of AdV5 DNA into the nucleus at a step downstream of arrival at the MTOC. (A) Quantification of FLAG-pVII "particle" number by Fiji 3D Objects Counter of images collected upon infection of untreated, LMB- or MG132-treated (20 nM and 30 µM respectively) MIB1 KO clone 2-1 and its WT MIB1-reconstituted counterpart with AdV5-JR34 (MOI=2000 p/cell; 1.25 hpi). FLAG-pVII "particle" number normalized to number of nuclei per FOV across 3 FOV. (B) Representative IF images showing distribution of AdV capsids (green: anti-hexon) relative to centrosome (red: anti-pericentrin) in MIB1 KO clone 2-1 and its WT MIB1-reconstituted counterpart infected with AdV5-JR34 (as above) in the presence or absence of LMB (20 nM) (C) Quantification of distribution of adenoviral capsids relative to MTOC depicted in (B) as the mean FITC intensity (anti-hexon) over MTOC region (anti-pericentrin stain). MIB1 KO clone 2-1 or its WT MIB1-reconstituted counterpart were treated as indicated with LMB (20 nM), MG132 (30 µM) or both in combination and infected with AdV5-JR34 (as above) averaged across 5 FOV. (Scale bar: 10 µm).

The window between MTOC departure and genome delivery was the extent of our resolution on MIB1's intersection with the virus. We therefore reached out to Dr. Urs Greber, who has a long history studying adenoviral entry and who commonly performs particle tracking and electron microscopy on capsids in this window, to ask for his assistance in gaining further resolution into the specific localization of the block on DNA release following MTOC arrival. Instead, we learned that his group had also identified the MIB1 host factor and had performed precisely those assays. Their work, now published in Bauer et al. 2019, confirmed by both confocal and TEM, that in MIB1 KO cells the AdV particles even successfully arrive at the nuclear pore but remain stuck there, unable to release their genomic cargo (Bauer et al., 2019). While we had struggled to definitively show that the particles were in fact still reaching the nuclear membrane in MIB1 KO cells, we had observed the apparent distribution of particles along the curved rim of the nucleus in these cells (this was also observed for WT MIB-reconstituted cells treated with MG132). In looking back, we indeed noted that while at later timepoints such as 4 hpi, in WT MIB1-reconstituted cells capsid stain was visualized in the cytosolic space in between cells, in KO cells the capsid signal remained tightly localized to the edge of the nucleus (**Figure 3.3**). Taken together, these observations are consistent with a model in which capsids are stuck on nuclear pores and therefore distributed more evenly and discretely along this surface in MIB1 KO cells but pushed away again in WT MIB1-reconstituted cells into larger cytoplasmic aggregates of empty capsid shells as described (Strunze et al., 2011). These observations were in line with the work from Greber's group concluding that in MIB1 KO cells, virus particles reach the NPC and yet the genome is never released into the nucleus.

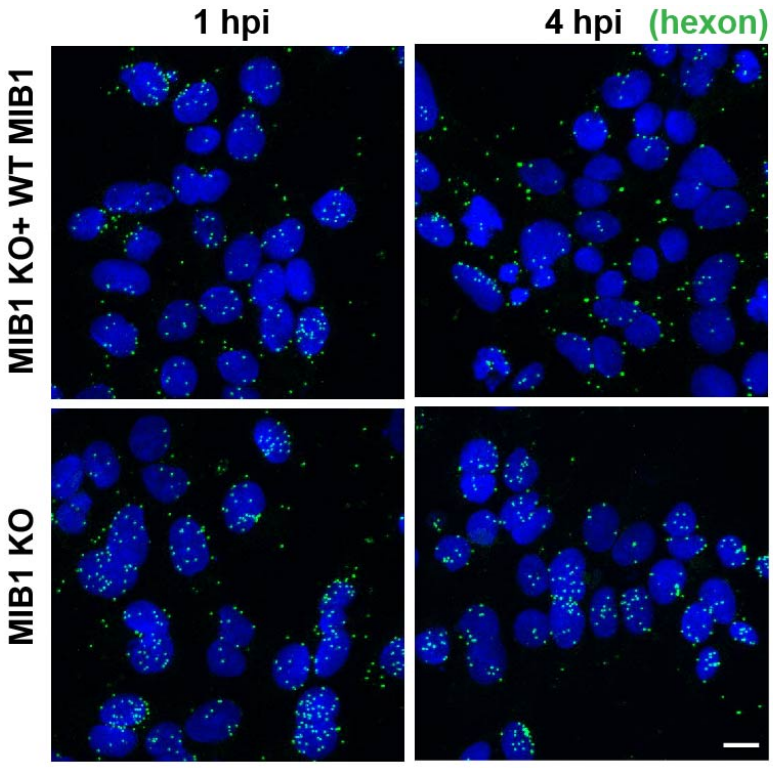

Figure 3.3 AdV5 capsids are arrested at NPC in MIB1 KOs. Infection of MIB1 KO clone 2-1 and its WT MIB1-reconstituted counterpart with AdV5-JR34 (MOI=2000 p/cell) fixed at 1 and 4 hpi and stained for capsid (anti-hexon). (Scale bar = 10 μm)

Microtubule dynamics: MIB1-dependence and AdV genome delivery

We had narrowed the window of MIB1's action to the immediate vicinity of the nucleus downstream of the MTOC. Reassuringly, this put MIB1's AdV-centric role in precisely the same region as MIB1's reported role as a component of centriollar satellites involved in the homeostasis of centrosomes. Centrosomes act as dominant sites of MT nucleation—we therefore wondered whether MIB1 facilitated virus infection through MT regulation. In HeLa and TC7 cells, untreated or taxol-stabilized MTs facilitate Ad2 and Ad5 capsid plus-end motility while collapse of MTs by nocodazole inhibits this directed motion (Mabit et al., 2002; Suomalainen et al., 1999). However, we had previously shown (**Figure 3.2C**) that capsids at least successfully arrived at the MTOC suggesting any impact on these long-range dynamics would be independent of the AdV phenotype. Therefore, any relevant involvement of MTs would need to lie downstream of the MTOC. Recently, it had been shown that knocking-down GTPase DNM2[18] boosts nuclear delivery of Ad37 vDNA through a mechanism attributed in part to enrichment of perinuclear acetylated tubulin in DNM2 KD cells (Lee et al., 2019). This study linked AdV trafficking in the immediate vicinity of the nucleus to the dynamics of a specific subpopulation of MTs. Acetylated MTs are post-translationally modified on a luminal lysine of alpha-tubulin and are often indicative of more stable and longer-lived populations. However, this population can also be dynamically regulated. HDAC6, for example, removes acetylation from MTs and its activity may be regulated by its interaction with centriollar satellites (Hubbert et al., 2002; Lecland & Merdes, 2018). Acetylation also increases the flexibility of MTs to bending and may therefore be particularly conducive to regulation of MT dynamics along the curved surface of the nuclear membrane where viral capsids arrive (Perdiz et al., 2011).

To assess the impact of MTs on AdV5 DNA release in Hap1 cells, we treated both MIB1 KO and WT MIB1-reconstituted cells with various drugs known to manipulate MT populations and infected them with AdV5-JR34. We tested three MT-manipulating drugs: nocodazole which depolymerizes MTs, taxol which stabilizes them and vinblastine B which depolymerizes the more stabilized acetylated-tubulin pool which has been shown to be nocodazole-resistant. We anticipated that depolymerization of MTs would likely inhibit AdV DNA delivery in WT MIB1-reconstituted cells but also considered that it might alternatively rescue DNA delivery in MIB1 KO cells. This would be the case if the inhibition of DNA release was due to the aberrant overstabilization or instability of certain MT populations in the vicinity of the nucleus. Rather surprisingly, MT drug treatments in WT MIB1-reconstituted cells had minimal effect on AdV5 DNA release as assayed by FLAG-pVII foci although all drugs reduced DNA release slightly relative to untreated cells **(Figure 3.4A)**. MT drug treatments also had no effect on the block on DNA release in MIB1 KO cells. Staining with antibodies to α-tubulin and acetylated α-tubulin confirmed the effectiveness of the various drug treatments on their intended MT populations **(Figure 3.4B)**.

The minimal impact of these drugs on DNA release was puzzling given both the expansive literature on the contribution of MT in transport of AdV capsids to the nucleus and our own detection of a number of MT motor and modifying proteins among our weaker Hap1 screen candidates. We concluded that this relative MT-independence of DNA delivery in Hap1s reflected cell-type specific differences (perhaps due to their relatively small size approx. 11 μm)

[18] A gene that will make another interesting appearance in our proteomics in Chapter 4.

compared to more classically-employed cell lines for AdV study (HeLa, A549). Indeed, there is precedent for MT-independence in other cell lines such as HEK293s (Yea et al., 2007). Viewed positively, this meant that evaluating the role of MIB1 in these cells could be decoupled from any secondary influence of MIB1 KO on MT dynamics upstream of arrival at the MTOC which had been one hypothesis given its known roles in primary cilia formation/centrosomal regulation. However, the seeming independence from MT is especially curious given that the AdV capsids in Hap1 cells are still susceptible to LMB treatment. LMB-treated cells show the characteristic aggregation of capsids at the MTOC that was presumed to reflect first directed trafficking to the hub of MT growth as well as an inability to decouple from those microtubules upon arriving there[19]. We posit that Hap1s may not *require* microtubules for this first delivery step but that some of the factors identified by the screen (Kif22, Kif11, KLC1) may be necessary after delivery to the nuclear pore, and allow the exploration of phenotypes normally masked by these upstream contributions. It is also possible that while we validated global alteration of MT networks with the various drug treatments, these treatments 1) may still not be reaching the relevant pool of MTs or 2) by acting so globally, may not be able to capture more dynamic or nuanced regulation of MTs in the immediate vicinity of the nucleus.

We additionally attempted treating MIB1 KO cells with the MT-manipulating drugs only *after* untreated infection was allowed to proceed for 1.25 hrs **(Figure 3.4C)**. This experiment was motivated by the Greber group's observation that in MIB1 KO cells the viral capsid does in fact arrive at the NPC but is fixed there, unable to release its genome while in WT cells the capsid is rapidly disassembled, emptied and pushed away again. We hypothesized that perhaps stabilizing or destabilizing certain populations of MTs in the vicinity of the nucleus *after* first giving the capsids the chance to dock at the NPC in KO cells might somehow serve to rescue infection. However, the block on DNA release in KO cells persisted in all cases.

Imaging of alpha-tubulin and acetylated-alpha tubulin in untreated MIB1 WT or KO cells in the presence or absence of infection also allowed us to assess broader morphological differences in these MT populations for their dependence on MIB1 **(Figure 3.4B)**. We tentatively observed that the MIB1 KO cells display denser networks of MTs (anti-alpha-tubulin) than WT MIB1-reconstituted cells in both infected and uninfected conditions. However, we have struggled to find a way to quantify MT staining due to their dense filamentous appearance as well as variability between cells. In the future perhaps cell cycle synchronization prior to treatment and infection would help homogenize the morphologies of these different MTs during interphase making them more compatible with downstream quantification. However, assessing subtle differences in morphology of MTs in MIB1 WT vs KO cells may also not be the direction to focus given the minimal impact crude manipulation of these structures had on AdV infection generally in our Hap1 cells. We therefore, moved towards characterizing other cellular structures that might be impacted by the presence or absence of MIB1 with more relevance to our AdV DNA release phenotype.

[19] In the future we would like to treat with LMB and nocodazole in combination and see if this would abrogate MTOC aggregation of capsids as expected.

Figure 3.4 Manipulation of MTs has minimal impact on AdV5 DNA delivery in Hap1 cells. AdV5-JR34 infection (MOI= 2000 p/cell; 1.25 hpi) of MIB1 KO clone 2-1 and its WT MIB1-reconstituted counterpart treated with nocodazole (10 μM), paclitaxel (10 μM) or vinblastine (10 μM) for 30 minutes prior to infection, and throughout synchronization on ice and infection. (A) Cells were stained for FLAG-pVII "particles" (anti-FLAG) and hexon "particles" (anti-hexon) and plotted as the average across three independent experiments (5 FOV each). Significance determined using unpaired parametric t-tests between indicated conditions (*= $p<0.05$, ***= $p<0.001$). (B) Same as (A) except that MIB1 KO cells only were treated with MT-manipulating drugs for 30 mins beginning at 1.25 hpi ("POST" treatment) and plotted as the average of 5 FOV. Significance determined using unpaired parametric t-tests between indicated conditions (*= $p<0.05$, ***= $p<0.001$). (C) Representative IF images (a maximum projection of all Z-stacks) examining morphology of alpha-tubulin and acetylated-alpha tubulin in MIB1 KO and WT MIB1-reconstituted cells both in untreated cells and AdV5-infected cells and in WT MIB1-reconstituted cells upon treatment with MT-altering drugs. (Scale bar=10 μm.)

Figure 3.4

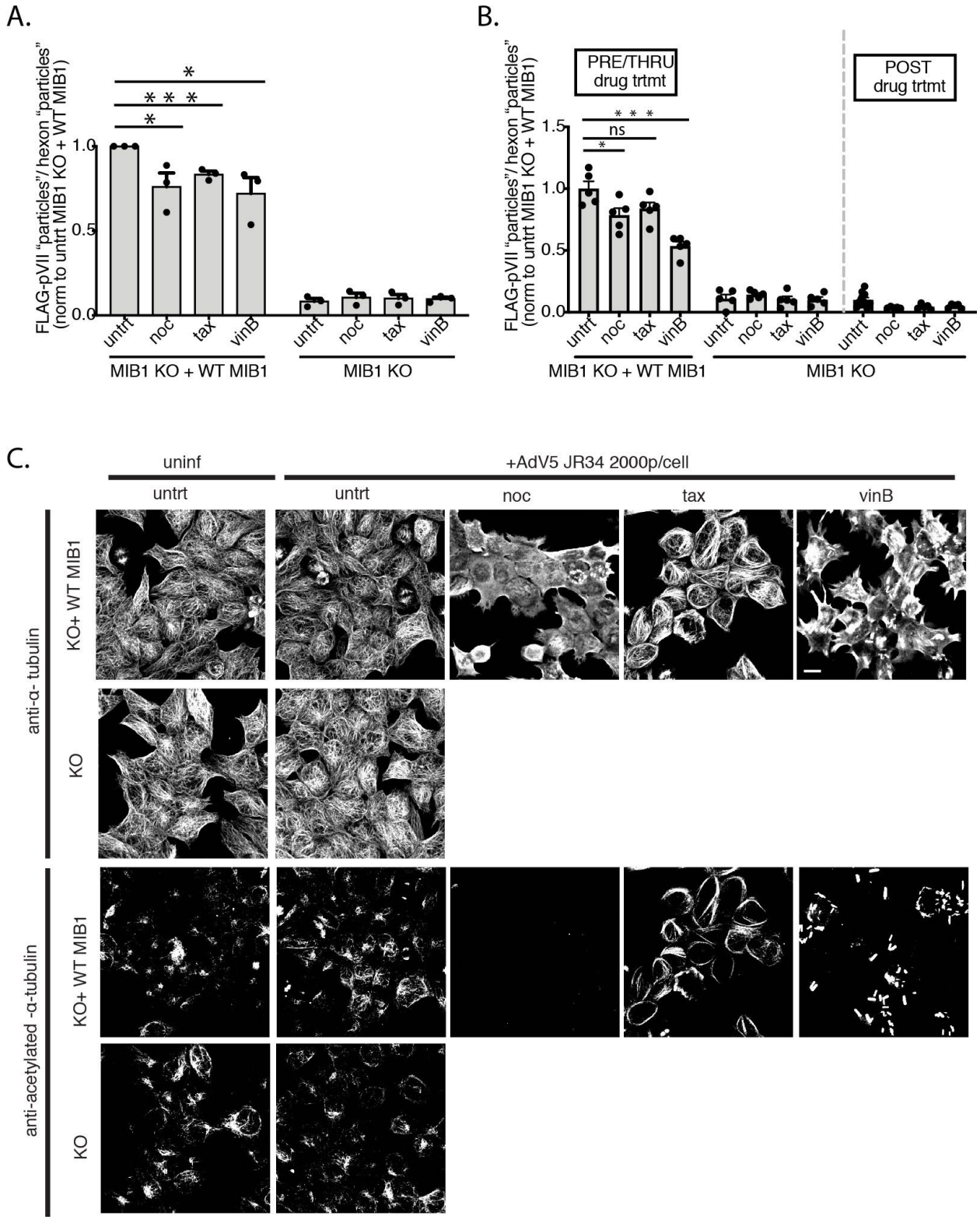
A.
FLAG-pVII "particles"/ hexon "particles" (norm to untrt MIB1 KO + WT MIB1)
1.0
0.5
0.0
* * * *
untrt noc tax vinB
MIB1 KO + WT MIB1
MIB1 KO
B.
PRE/THRU drug trtmt
POST drug trtmt
* * *
ns
*
1.5
C.
uninf
+AdV5 JR34 2000p/cell
untrt
noc
tax
vinB
anti-α- tubulin
KO+ WT MIB1
KO
anti-acetylated -α-tubulin

Centriollar satellite dynamics: MIB1-dependence and AdV genome delivery

MIB1 is a core component of centriollar satellites, 70-100 nm granules that cluster around the centrosome through association with centrosome-proximal MTs (**Figure 1.6C).** MIB1 had also been closely linked to regulation of centriollar satellites via direct ubiquitination of PCM1 and CEP131 (which is inhibited upon certain types of stresses)[20] (Villumsen et al., 2013). We were curious whether we might observe differences in the organization of centriollar satellites in MIB1 WT vs KO cells that could have implications for virus infection. In particular, we wondered whether the block on infection in the absence of MIB1 might result from impaired centriollar satellite dynamics normally required for genome delivery. Among its many functions, the centrosome is a sensing organelle that can respond to diverse environmental stressors and integrate a response involving MT-mediated transport and signal transduction to the nucleus. Osmotic stress, for example, triggers p38 MAP kinase signaling and results in the rearrangement of centriollar satellites albeit in distinct trigger-dependent ways (Nielsen et al., 2018). Anisomycin treatment induces dispersal of centriollar satellites, while treatment with sorbitol induces their paralysis and aggregation in tighter proximity to the centrosome. Interestingly, AdV entry itself is reported to activate the p38 MAP kinase signaling pathway, an event which enhances infection by boosting MT minus-end directed migration of AdV capsids towards the nucleus (Suomalainen et al., 2001). However the corresponding impact of AdV entry on these specific centriollar satellite structures and their distribution was unexplored. Recently, ZIKV infection was shown to increase levels of MIB1 leading to the dispersal of satellites around the centrosome although the implications for the viral lifecycle remain unclear (Wen et al., 2019).

We hypothesized that in WT MIB1-expressing cells we might observe a change in centriollar satellite distribution upon infection similar to that observed by either anisomycin or sorbitol treatment. To determine if AdV infection induced changes in centriollar satellite distribution and whether this distribution was dependent on MIB1, we infected MIB1 KO and WT MIB1-reconstituted cells with AdV5-JR34 and stained for centriollar satellites (anti-PCM1) and the centrosome (anti-pericentrin) at 1.25 hpi (**Figure 3.5A)**. Treatment with anisomycin and sorbitol indeed induced the stereotyped dispersal or centrosomal clustering of satellites respectively in both uninfected and AdV-infected WT and KO cell. This was quantified by the intensity of the PCM1 stain in the vicinity of pericentrin. This indicated that the absence of MIB1 does not impact the gross responsiveness of satellites to known manipulators (**Figure 3.5B)**. In contrast to these pharmacological manipulations, AdV infection alone (at least at our dose of 2000p/cell) had no impact on the distribution of centriollar satellites in untreated WT MIB1-reconstituted or MIB1 KO cells.[21] However, we did notice that MIB1 KO cells showed a small but significant increase in centriollar satellite signal over the centrosome when compared to WT MIB1-reconstituted cells under both uninfected and infected conditions (**Figure 3.5C)**. In addition we noted that MIB1 KO cells appeared slightly more refractory to anisomycin-induced satellite dispersal than WT MIB-reconstituted cells particularly upon AdV infection. Infection of WT MIB1-reconstituted cells further enhanced the dispersal of satellites in anisomycin-treated cells whereas in MIB1 KO cells infection decreased the degree of satellite dispersal. While seen across multiple experiments, this effect is very subtle and it is unclear what the implication

[20] If certain stresses result in inactivation of MIB1 ubiquitination activity then this would be functionally equivalent to the scenario in our MIB1 KO cells

[21] despite being reported to trigger the p38 signaling pathway

would be. We propose that in MIB1 KO cells centriollar satellites are more tightly associated with the centrosome than in WT MIB1-reconstituted cells which becomes more apparent upon their refractoriness to induced satellite dispersal by anisomycin. Alternatively, MIB1 KO cells may just express higher levels of PCM1 overall due to lack of PCM1 degradation by MIB1.

While AdV infection demonstrated no major impact on satellite morphology, we wondered whether, conversely, these dramatic reorganizations of centriollar satellites (and the MIB1 that they are reported to contain) would influence the success of AdV genome delivery.[22] Cells were pretreated with anisomycin and sorbitol and infected with AdV5-JR34 but now stained for viral capsids (anti-hexon) and FLAG-pVII DNA release (anti-FLAG). Dispersal of satellites by anisomycin showed little to no decrease in FLAG-pVII foci. By contrast, paralysis/aggregation of satellites by sorbitol resulted in almost complete abrogation of FLAG-pVII detection (**Figure 3.5D)**. We therefore speculated that the ability of centriollar satellites to traffic away from the centrosome on MT, which is paralyzed by sorbitol treatment, is essential for successful adenoviral DNA delivery to the nucleus. The aggregation of centriollar satellites over the MTOC upon sorbitol treatment was also reminiscent to us of the aggregation of adenoviral capsids over the MTOC upon LMB treatment leading us to wonder if capsids may traffic in association with MIB1-containing centriollar satellites under these conditions. However, sorbitol treatment did not result in the aggregation of AdV particles at the MTOC observed for LMB treatment (**Figure 3.5E)**. More tellingly, co-treatment of MIB1 WT cells with LMB and sorbitol (similar to the experiments we'd performed to localize the block on DNA release upon MG132 treatment) did not lead to capsid aggregation at the MTOC. We therefore concluded that the block on DNA delivery in the presence of sorbitol lay *upstream* of the arrival at the MTOC and would therefore obfuscate any additional impact of this drug on DNA delivery due to centriollar satellite dynamics. Indeed, sorbitol treatment, a harsh osmotic stress agent could be having a number of other effects on these cells (for example stress granule formation).

[22] Given their trafficking along MTs, our disruption of MT populations should also have resulted in reorganization of centriollar satellites (although we did not monitor satellites upon treatment with noc, tax, vinB) and yet we saw no dramatic effect of MT manipulation on adenoviral DNA delivery in Hap1 cells.

Figure 3.5 Centriollar satellite morphology/dynamics upon AdV5 infection in MIB1 KO and MIB1 WT-reconstituted cells. (A) Representative images of MIB1 KO and WT MIB1-reconstituted KO cells infected with AdV5-JR34 (MOI =2000 p/cell) and treated with osmotic stress-inducing drugs anisomycin (1ug/ml) and sorbitol (500 mM) and fixed at 1.25 hpi to assess the impact on centriollar satellite (green: anti-PCM1) distribution relative to the centrosome (red: anti-pericentrin). Each image is a single representative plane of a Z-stack displayed as individual channels, the merged image and an enlarged merged image (region within white box). (B) Quantification of the images in (A) plotting the log of the mean intensity of PCM1 signal in the twice-dilated region in and around the pericentrin signal (performed in 2D on maximum projections of Z-stacks and averaged across 5 FOV. (C) Same as in (B) but only showing untreated and anisomycin treated conditions plotted in linear scale. Significance determined using unpaired parametric t-tests between indicated conditions (*= $p<0.05$, ****= $p<0.0001$). (D) MIB1 KO and WT MIB1-reconstituted KO cells were infected with AdV5-JR34 (MOI =2000 p/cell) and treated with osmotic stress-inducing drugs anisomycin and sorbitol and assayed for AdV5 DNA release quantified as FLAG-pVII "particle" number normalized to hexon "particles" as in **Figure 3.1C** and averaged across 8 FOV. (E) Quantification of distribution of adenoviral capsids relative to MTOC as the mean hexon intensity (anti-hexon stain) over MTOC region (anti-pericentrin stain) as in **Figure 3.2C** in WT MIB1-reconstituted cells only and averaged across 5 FOV.

Figure 3.5

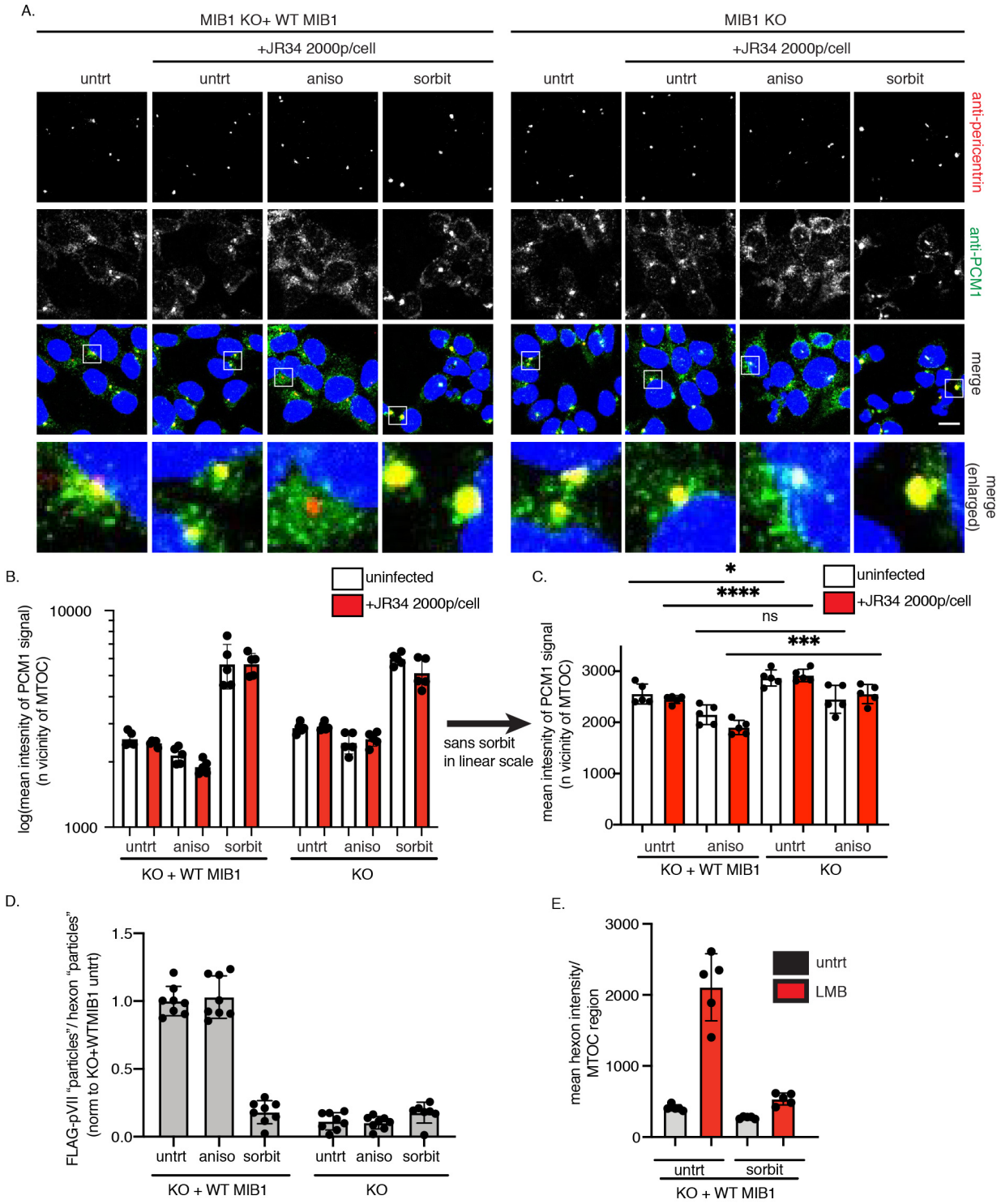
A.
MIB1 KO+ WT MIB1
MIB1 KO
+JR34 2000p/cell
untrt
untrt
aniso
sorbit
anti-pericentrin
anti-PCM1
merge
merge (enlarged)
B.
uninfected
+JR34 2000p/cell
log(mean intesnity of PCM1 signal (n vicinity of MTOC)
10000
1000
KO + WT MIB1
KO
sans sorbit in linear scale
C.
*
****
ns
***
mean intesnity of PCM1 signal (n vicinity of MTOC)
3000
2000
1000
0
D.
FLAG-pVII "particles" / hexon "particles" (norm to KO+WTMIB1 untrt)
1.5
1.0
0.5
0.0
E.
mean hexon intensity/ MTOC region
untrt
LMB

While this set of experiments sought to better characterize the relationship between virus infection and centriollar satellite dynamics there are a number of caveats. It is important to keep in mind that the composition and heterogeneity between centriollar satellites particularly in response to stress is still very poorly understood although an appreciation for distinct compositions and functions for centriollar satellites are emerging (largely through new data from proximity-labeling approaches) (Gheiratmand et al., 2019). Although PCM1 seems to be the dominant structural/scaffolding component of the satellites it is also possible the certain subpopulations of satellites lack PCM1 and would therefore not be detected using our current methods. Alternatively, certain types of stresses alter the localization of PCM1 independent of other centriolar satellite components. For example, upon UV treatment, CEP131 and CEP290 have been shown to reassociate with the centrosome while PCM1 disperses. While the literature (and our proximity labeling data to be discussed in the next chapter) gave us confidence that PCM1 is intimately associated with MIB1, future work, labeling MIB1 directly with GFP, will obviate the need for other proteins as proxies for these structures by allowing us to focus on only the relevant satellite structures (or independent activities) of which MIB1 is a part. Tracking MIB1 relative to AdV particles as in Bauer et al. would have allowed us to determine better whether the impact of MIB1 on the capsid was direct or indirect. In their work they track MIB1 directly and observe cases of a rapid and transient interaction with capsids docked at the NPC prior to genome release. Whether this is performed as a component of centriollar satellite complexes or through an independent localization of MIB1 however was not demonstrated.

Chapter IV: Proteomic approaches towards a MIB1 mechanism

Rationale for a proteomics approach

Having demonstrated that MIB1 and its ubiquitination activity are necessary for the successful delivery of the AdV genome at a step downstream of arrival at the MTOC[23], we next sought to elucidate the precise role of MIB1 within this narrow window. We hypothesized that AdV DNA release required MIB1 to ubiquitinate some unknown target protein or proteins for degradation. Given previous reports of direct ubiquitination of the capsid as well as the requirement for structural disruption of the capsid at the nuclear pore, we felt it was certainly plausible that MIB1 could be necessary for direct ubiquitination of a capsid protein resulting in its degradation to mediate genome release. Interestingly, a similar phenotype of capsid docking, paralysis and inhibited DNA release had been observed for HSV-1 expressing a truncated mutant of capsid protein pUL25 and is dependent upon proteolytic cleavage of pUL36 upon docking at the nuclear pore. This observation provides precedent for direct capsid modification/regulation at this site (Huffman et al., 2017; Jovasevic et al., 2008).

Given the reported ubiquitination of AdV pVI during entry, we began by focusing on the AdV capsid proteins as potential direct ubiquitination targets of MIB1. There are limited candidates for ubiquitination at this stage. By the time the virus has traversed endosomes and cytosol and arrived at the nucleus, it has shed most incoming capsid components with the exception of V, VII, mu, and TP contained within the partially-degraded hexon shell (**Figure 1.3)** (Greber et al., 1993). However, our early efforts to assay incoming capsid components using antibodies to these components by Western blot were unsuccessful due to insufficient detection of input virions as well as non-specific detection of cellular proteins. We therefore turned to more classical S^{35}-labeling of AdV particles to ask most preliminarily whether the stability of specific capsid components was altered in MIB1 WT vs KO cells. An AdV5 stock grown in the presence of [S^{35}]-Met/Cys was used to infect MIB1 WT and KO cells and collected across a timecourse of early infection.[24] While this classical approach finally permitted specific detection of several of the more abundant capsid proteins, we observed little difference in banding pattern between WT and KO cells or their stability out to 4 hpi (although signal was slightly weaker in MIB1 KO cells) and were also unable to visualize the less abundant capsid-associated proteins **(Figure 4.1)**. It became clear that this approach would be too low-throughput and too narrow in its scope given that MIB1 might not act directly on a virion component.

We had reason to suspect that MIB1 might mediate AdV infection by targeting a cellular protein. Based on our preliminary work at the time, MIB1 appeared to be a host factor for other DNA viruses such as lentiviruses, HSV and HBV that all release their genomes at the pore. We had also confirmed MIB1-dependence across several distinct AdV serotypes. While the possibility that MIB1 acted through a conserved motif across these viruses could not be excluded, the sequence and structure diversity of capsid proteins between these virus families and even among AdV serotypes led us to consider a cellular substrate for MIB1 ubiquitination

[23] retrospectively (with Bauer et al.'s observations) directly at the NPC

[24] This experiment was conducted in A549 WT and 2-1 KO clone since at the time we had intended to switch to this system.

during infection.

To generate an unbiased list of MIB1 target candidates capable of capturing potential targets on either viral or host proteins we turned to two complementary proteomic approaches. The first of these identified proteins in the immediate vicinity of MIB1 using APEX2 proximity labeling. However, while we anticipated that the relevant target protein would be enriched in proximity to MIB1, this approach could obviously not provide insight into which of these neighboring proteins is directly modified by MIB1. Therefore, to identify those proteins whose ubiquitination upon AdV infection was mediated by MIB1, we performed immunoprecipitation for endogenous ubiquitinated proteins using Tandem Ubiquitin Binding Entities (or TUBEs). The implementation, analysis and mechanistic follow-up based on these two approaches is discussed in further detail below.

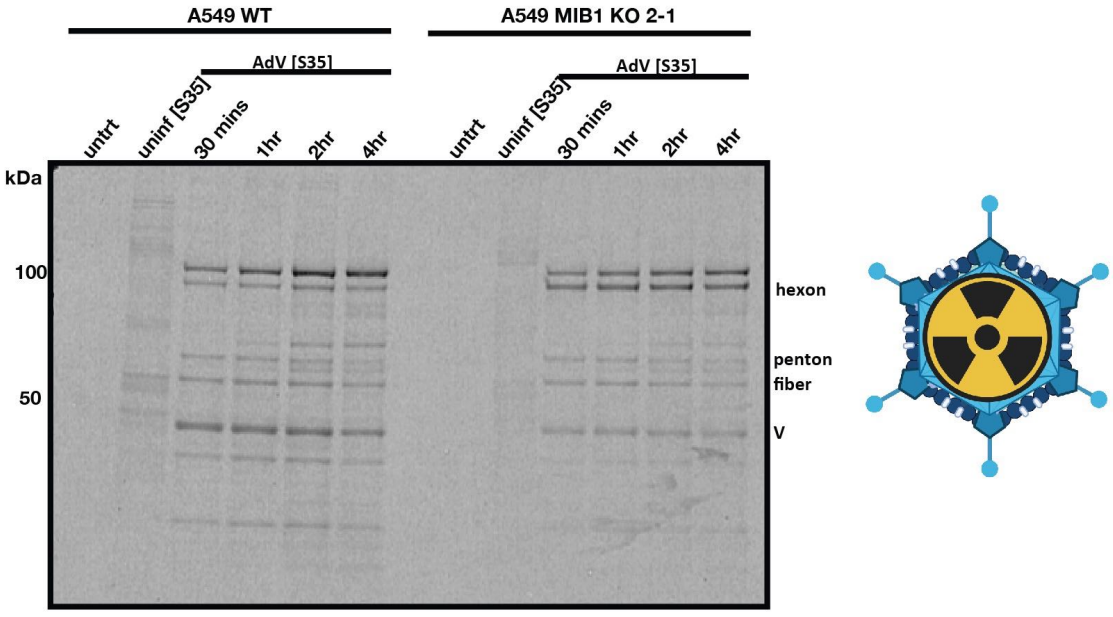

Figure 4.1 Radiolabeling of AdV5 particles monitors incoming capsid components in MIB1 WT and KO cells. Western blot of MIB1 WT and KO A549s collected at early timepoints following infection with [S^{35}]-Met/Cys replication-incompetent AdV5-GFP. [S^{35}]-Met/Cys-labeled replication-incompetent AdV5-GFP was prepared by addition of [S^{35}]-Met/Cys to growth media during the late-stage of adenovirus infection (16-72hpi). Uninfected cells incubated with [S^{35}]-Met/Cys were prepared in parallel. Clarified supernatants from uninfected or AdV5-infected freeze-thawed cells were added to either WT A549 or MIB1 KO A549 cells and prepared as lysates at indicated timepoints.

Characterization of MIB1-proximal proteome upon AdV5 infection

Proximity labeling: An Introduction

For most biological processes, physical proximity is a prerequisite for functional interaction. In recent years, chemical labeling of a proteome proximal to a given protein of interest has become a powerful strategy for elucidating the functional connections between proteins. These approaches utilize chemical biology tools to enable orthogonal labeling in situ followed by subsequent isolation and mass spectrometry. Among the first of these tools was Bio-ID (Roux et al., 2012). A mutation of this *E.Coli* biotin ligase referred to as BirA R118G or BirA* allows the enzyme to convert free biotin to a reactive intermediate. A cloud of reactive biotin is generated around the enzyme capable of non-specifically attaching to lysine residues of other proteins in the immediate vicinity. However, this approach requires long labeling times on the scale of hours (although more recent re-engineered versions, such as Turbo-ID, have significantly reduced the labeling times down to minutes) (Branon et al., 2018).

An alternate proximity labeling approach relies on an engineered version of soybean ascorbate peroxidase, APEX2 **(Figure 4.2)** (Hung et al., 2016). In the presence of a short hydrogen peroxide pulse, APEX2 generates biotin-phenoxyl radicals which react with electron-rich amino acids on adjacent proteins resulting in covalent addition of the biotin moiety.[25] The short lifetime of the radical limits labeling to a tight radius of approximately 10-20 nm around the APEX2-tagged protein. The labeling is also rapid, taking place in a single minute upon addition of H_2O_2. These kinetics were therefore compatible with the timescale of not only virus entry but the specific step of the capsid arrival in the vicinity of the nuclear pore and DNA release. We therefore proceeded with this APEX2 proximity labeling approach to probe the MIB1-proximal proteome upon AdV5 infection.

[25] In a recent lecture on campus Dr. Alice Ting likened this process to “molecular spray painting”!

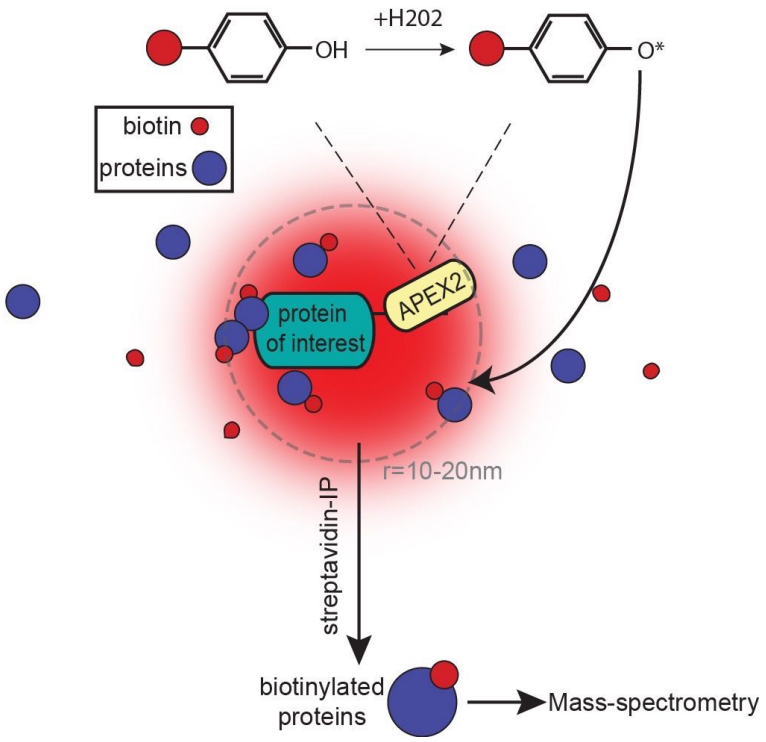

Figure 4.2 Schematic of APEX2 proximity labeling. A protein-of-interest is tagged with APEX2. When cells (preloaded with biotin-phenol) receive a pulse of H_2O_2, APEX2 converts the biotin-phenol to a biotin-phenoxyl radical which covalently labels electron-rich amino acids on proteins within a radius of 10-20 nm. These biotinylated proteins can then be immunoprecipitated by streptavidin and submitted for LC-MS/MS to identify the proximal proteome of the protein-of-interest.

Proximity labeling: Preparation and validation of technique

Our microscopy studies had placed the block on infection in MIB1 KO cells to some point after departure from the MTOC but prior to successful vDNA delivery at the NPC. We were therefore curious where MIB1 itself localized in Hap1 cells and whether that localization was altered upon AdV infection. MIB1 has been widely studied in the context of neuronal morphogenesis where it was found to localize to the post-synaptic density in neurons (Choe et al., 2007). Yeast two-hybrid screens in zebrafish and sequential elution of MIB1 binding partners from rat brain linked MIB1 to trafficking, cytoskeleton and vesicular transport, all pathways that could have relevance for viral endocytosis and dynein-mediated transport (Mertz et al., 2015; Tseng et al., 2014). More recently, however, MIB1 has emerged as a core component of centriollar satellites (substructures in vicinity of centrosome) involved in regulation of centriole homeostasis and ciliogenesis (Čajánek et al., 2015) (Villumsen et al., 2013). This latter locale would place MIB1 precisely in the region between the centrosome and nuclear pore where the transfer of viral capsids and the observed block in infection in MIB1 KO cells occurs.

Our initial efforts to image endogenous MIB1 were stymied by the extremely low levels of

MIB1, perhaps maintained by its autoubiquitination activity. The APEX2 proximity labeling method to biochemically characterize proteins proximal to MIB1 therefore offered an ideal approach to capture the cellular context of this protein upon virus infection. We reasoned that proximity labeling might also capture potential ubiquitination targets that might even escape detection by direct immunoprecipitation of MIB1 given the rapid dissociation typical of E3 ligases with their substrates. We began by adding FLAG-APEX2 at either the N- or C-terminus of WT MIB1 or its C985S mutant. Again, the consideration of the rapid dissociation of ubiquitin ligase substrates upon ubiquitination motivated our inclusion of the C985S mutant which on the one hand we thought might show further enrichment of proteins no longer targeted for degradation by MIB1 ubiquitination but could conversely serve as a useful comparison for whether the overall localization of MIB1 is in fact dependent on its ability to ubiquitinate some target protein(s).

Stable cell lines expressing either N or C-terminal FLAG-APEX2-tagged WT MIB1 and C985S MIB1 were generated by lentiviral transduction into Hap1 MIB1 KO clone 2-1 and assayed for their capacity to restore AdV infection. While KO cells reconstituted with either N- or C- terminally APEX-tagged WT MIB1 were able to rescue AdV5 infection, infection was notably reduced relative to untagged MIB1 (**Figure 4.3A)**. Furthermore, treatment with H_2O_2 resulted in no appreciable biotin-labeling in MIB1-WT cells while strong labeling was observed for the APEX-tagged C985S mutant (data not shown). We therefore attributed the very low levels of functional protein to autoubiquitination and turnover of WT MIB1 perhaps further exacerbated by the addition of APEX2. In order to increase WT MIB1 activity and subsequently both AdV infection and APEX2 labeling efficiency, we introduced the V943F homodimerization mutant (tested in our mutant panel **Figure 2.6**) into both WT MIB1 and C985S APEX constructs given that it had proven effective at enhancing AdV infection in these assays. Indeed, the V943F mutation restored the capacity of APEX2-tagged WT MIB1 to rescue virus infection (**Figure 4.3A)** (and showed appreciable labeling [data not shown]). The C-terminally APEX2-tagged constructs with the V943F mutation[26] were chosen for all subsequent proximity-labeling experiments. In parallel, we also generated MIB1 KO cells expressing the fluorescent protein mKate fused to APEX2. As a ubiquitously-localized cytoplasmic protein, this construct served as a generic baseline control over which enrichment for specific proximal partners of MIB1 could be determined.

In preparation for the large-scale proteomics experiment, we confirmed expression of each FLAG-APEX2-tagged construct and its H_2O_2-dependent labeling specificity by Western blot for the APEX2-tagged protein (green: anti-FLAG) and all biotinylated proteins (red: streptavidin) **(Figure 4.3B)**. We also validated the labeling specificity of our three different constructs by IF which gave us our first glimpse into the spatial organization of MIB1 and its proximal proteome in Hap1 cells. Uninfected parental MIB1 KO cells, and KO cells reconstituted with WT MIB1-APEX2, C985S-APEX2 and APEX2-mKATE were pre-incubated with biotin, pulse-labeled with H_2O_2 and immediately fixed. Staining for the introduced APEX2-tagged protein (anti-FLAG) revealed that both WT MIB1-APEX2 and C985S-APEX2 localized predominantly to singular puncta within each cell **(Figure 4.3C)**. This distribution was corroborated by strong streptavidin stain tightly localized to the area surrounding the APEX2-

[26] although they will referenced throughout this section as simply WT MIB1 or C985S MIB1 from this point on including in Figure 4.3B and C.

tagged protein. The observation of this singular puncta per cell (at times surrounded by other bright smaller puncta) was compatible with our anticipated association with the centrosome (and centriollar satellites) although we had not yet validated by co-staining with the centrosomal marker pericentrin. Indeed, by contrast, the APEX2-mKate protein and its biotinylated proximal proteome were diffusely spread throughout the cell **(Figure 4.3C)**. Labeling was again clearly dependent on H_2O_2 addition. Of note, however, for all constructs, we noticed that there were also a number of cells in the population that did not express the APEX-tagged protein (perhaps due to silencing of our lentivirus cassette in some proportion of cells).

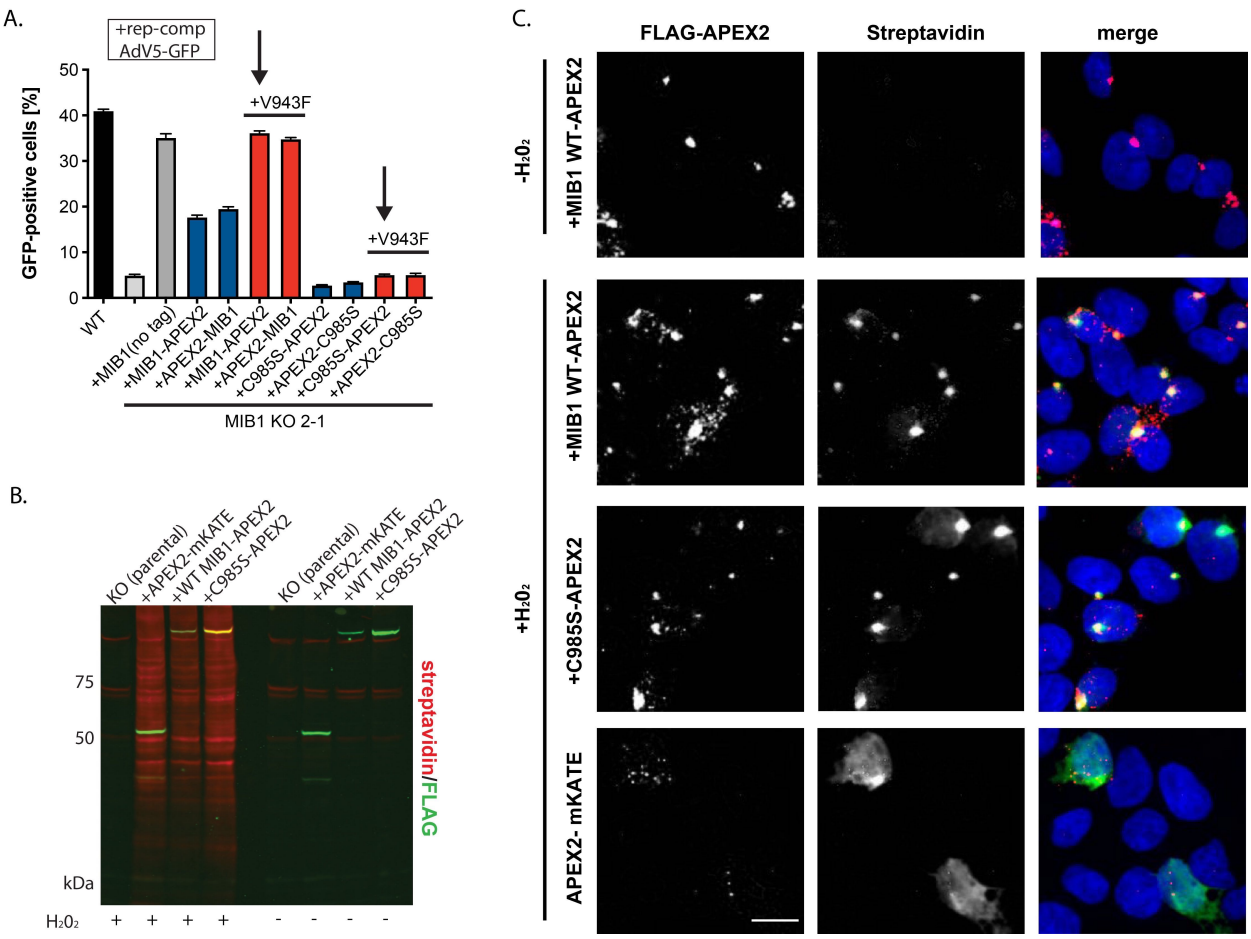

Figure 4.3 Generation and characterization of APEX2-tagged WT MIB1-, C985S MIB1- and mKATE-reconstituted MIB1 KO cells. (A) replication-competent AdV5-GFP infection (MOI =200p/cell; 24hpi) of Hap1 WT cells, MIB1 KO clone 2-1 and its reconstituted counterparts expressing untagged WT MIB1, N- and C-terminally APEX2-tagged WT or C985S MIB1 and upon additional V943F mutation. Experiments were performed in triplicate and harvested cells were analyzed by flow cytometry and plotted as the percentage of GFP-positive cells to assess the capacity of each construct to rescue AdV5 infection. Arrows delineate the C-terminal APEX2-tagged WT MIB1 (+V943F)- and C985S (+V943F)-reconstituted cells chosen for downstream proximity labeling experiments and mass spectrometry sample preparation. (B) Western blot confirming expression of MIB1 KO clone 2-1 parental cells and KO cells reconstituted with WT MIB1-APEX2, C985S-APEX2 or FLAG-APEX2 fused to mKate following pre-incubation with biotin with or without H_2O_2 pulse-labeling and stained for the APEX2-tagged construct (green: anti-FLAG) and biotin (red: streptavidin). (C) Representative IF images (maximum—projected Z-stacks) of uninfected MIB1 KO clone 2-1 reconstituted with WT MIB1 or C985S MIB1 or FLAG-APEX2 fused to mKate upon APEX labeling as in (B) followed by fixation and staining for the APEX2-tagged construct (red: anti-FLAG) and for biotinylated proteins (green: AF488-coupled streptavidin) and DRAQ5 nuclear stain (blue). (Scale bar: 10 µm)

Determining AdV5 infection parameters

Based on our mechanistic microscopy studies of MIB1 using the AdV5-JR34 virus as well as work by Bauer et al., we knew that in MIB1 KO cells, the virus arrives at the nuclear pore but fails to release its DNA into the nucleus. MIB1 therefore must mediate a very specific and potentially highly spatiotemporally-regulated event in the AdV lifecycle. While the MIB1 ubiquitination target(s) relevant to AdV entry might be subject to constitutive ubiquitination and turnover that is then lost in MIB1 KO cells, we also envisioned that virus infection may in fact trigger the relevant ubiquitination event whose detection would then be very dependent on the percentage of infected cells and the specific timepoint assessed after entry. To determine the optimal parameters (mainly incoming particle number and collection timepoint) for AdV infection in our proteomics experiments, we first titrated both our rep-competent and rep-incompetent AdV5-GFP viruses on WT Hap1 cells, MIB1 KO clone 2-1 and its WT MIB1-reconstituted counterpart **(Figure 4.4A,B)**. Specifically, we sought a virus dose that would maximize the dynamic range between MIB1 KO and WT MIB1-reconstituted cells while infecting the maximum percentage of cells. Based on these criteria we chose the replication-competent AdV5-GFP virus at a dose of 200 p/cell for which approximately 52% of cells were infected in the KO reconstituted with WT MIB1 relative to only 8% in the KO, a dynamic range of about 6-fold.[27] We then used the kinetics of FLAG-pVII release upon AdV5-JR34 virus infection to determine the appropriate window for labeling and collection— specifically when a population of viruses would be arriving at the nuclear envelope for docking and rapid genome release. A timecourse of infection with AdV5-JR34 showed that DNA release began around 45 mins post-infection but rose rapidly between 45 mins and 80 mins after synchronized infection **(Figure 4.4C)**. We therefore selected 1 hr to 1 hr 10 mins post-synchronized infection as our collection timepoint for all subsequent proteomic experiments.

[27] While infection with rep-incompetent AdV-GFP at 25000 p/cell showed similar dynamic range and % infection, this dose was toxic to the cells. We also preferred to use the replication-competent virus as it showed better capacity for rescue in other cell lines like HepG2-NTCP when reconstituted with WT MIB1.

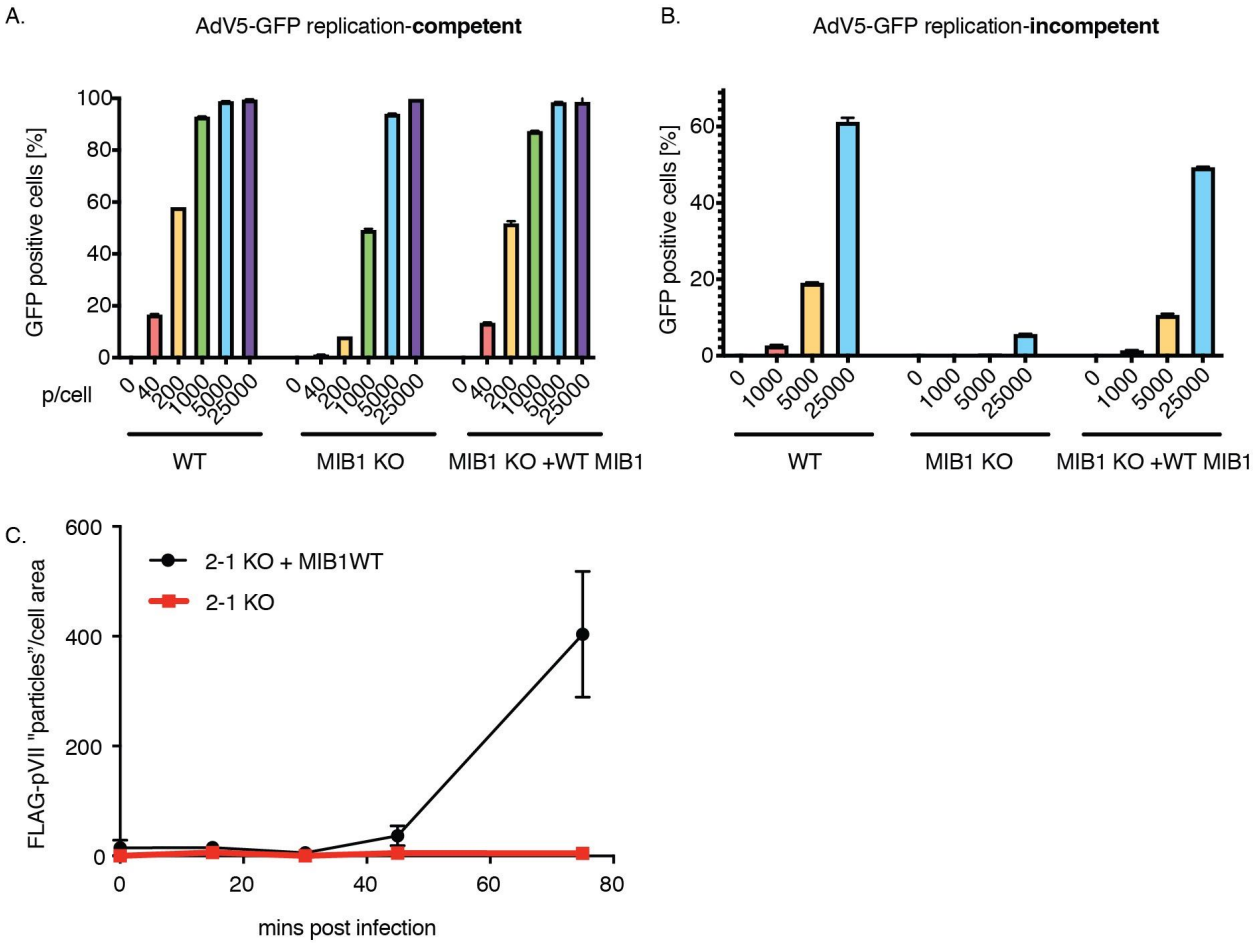

Figure 4.4 Selection of AdV5-GFP infectious dose and timepoint for sample collection in proteomic experiments. Titration of recombinant (A) replication-competent AdV5-GFP or (B) replication-incompetent AdV5-GFP on Hap1 WT cells, MIB1 KO clone 2-1 and its WT MIB-reconstituted counterpart harvested at 24 hpi, analyzed by flow cytometry and plotted as the percentage of GFP-positive cells. (C) To determine kinetics of AdV5 DNA release in Hap1 cells, at 15-minute intervals following synchronized AdV5-JR34 infection (MOI=2000 p/cell), MIB1 KO and WT MIB1-reconstituted cells were fixed in 4% PFA, stained for FLAG-pVII (anti-FLAG) and normalized to cell area/FOV (averaged across 5 FOV).

Proximity labeling confirms MIB1 localization to centriollar satellites

MIB1 KO clone 2-1 reconstituted with either WTMIB1-APEX2, C985S-APEX2 or APEX2-mKate were infected with replication-competent AdV5-GFP (200 p/cell) for 1 hr and 10 mins followed by 1 min pulse-labeling with H_2O_2, lysate collection and IP of biotinylated proteins **(Figure 4.5A)**. Prior to mass spectrometry submission, a diagnostic sample of pre- and post-IP lysates taken from each condition were assayed by Western blot to confirm H_2O_2-dependent labeling and validate subsequent depletion upon streptavidin-IP **(Figure 4.5B)**. Comparable labeling was observed for WT MIB1 and C985S-APEX2 expressing cells with stronger labeling observed for the APEX2-mKate control (likely due to its proximity to a broad spectrum of cytoplasmic proteins).

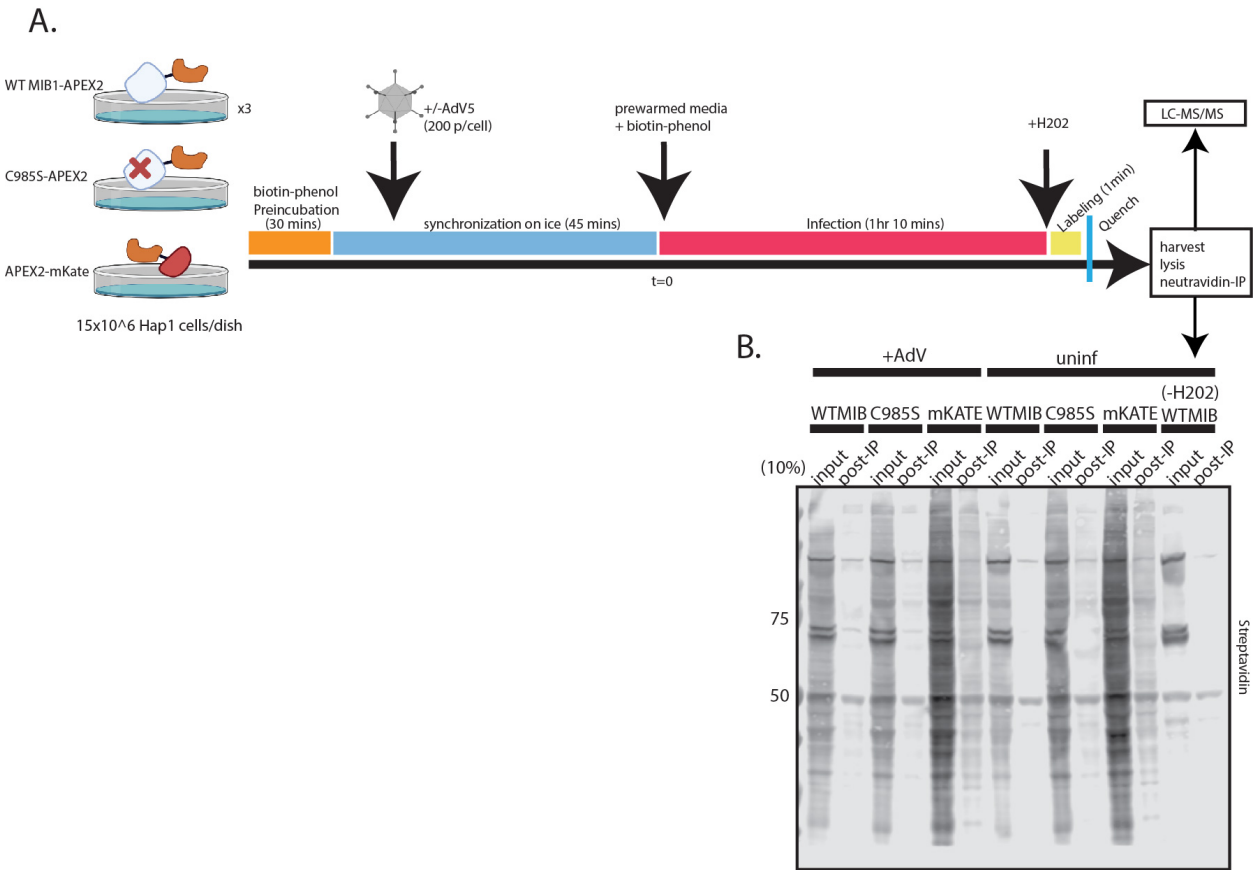

Figure 4.5 Schematic of APEX2 proximity labeling experiment to determine MIB1-proximal proteome upon AdV5 infection. (A) APEX2 proximity labeling experiment of MIB1 KO clone 2-1 reconstituted with either WT MIB1-APEX2, C985S-APEX2 or APEX2-mKate carried out as depicted above as described in Methods and submitted for LC-MS/MS following (B) diagnostic western blot across all collected conditions to confirm biotin labeling (streptavidin-680) in samples prepared from 10% input lysate and 10% of input lysate after incubation with neutravidin-agarose beads ("post-IP").

Analysis of the proximal proteomes of both WT-MIB1 and C985S MIB1 relative to cytoplasmic mKate showed strong correlation. As perhaps anticipated by previous literature and our own IF in uninfected cells, those genes enriched (>=2-fold; p-value <0.05) in proximity to both WT-MIB1 and C985S MIB1 relative to mKate during AdV infection showed functional enrichment for centrosome and even more specifically, centriollar satellite components by gene ontology (GO) terms analysis **(Figure 4.6A,B,C) (Table 4.1)**. Other GO term categories enriched in both the independent and overlapping WT and C985S MIB1 proximal proteomes included "microtubule cytoskeleton" (encompassing the centrosomal proteins), "vesicle/coated vesicle" and somewhat unexpectedly "Golgi subcompartment" [28] **(Figure 4.6C) (Table 4.1)**. Localization of both APEX2-tagged WT and C985S MIB1 to the centrosome in AdV-infected cells was then confirmed by IF revealing strong colocalization of proximity-labeled biotinylated proteins and pericentrin, a marker of the centrosome **(Figure 4.6D)**. Proteomic detection of the enriched association of both WT and C985S MIB1 with centriollar satellites demonstrated the power of the proximity labeling approach to capture association with discrete substructures beyond those immediately apparent by eye. Interestingly, while a number of centrosomal components were indeed enriched in proximity to either WT- or C985S- MIB1 over mKate, there were still a number of centrosomal and centriollar satellite components that were unenriched or even deenriched **(Figure 4.6E)**. This may similarly reflect the sensitivity of proximity labeling and proteomics observed by other groups for proteins functionally classified as "centrosomal" or visualized as "centrosomal" by confocal imaging that nevertheless reflect unique proximal proteomes when assayed by BioID (Gheiratmand et al., 2019).

[28] this may also account for the enrichment of endogenously biotinylated proteins observed over mKate given the localization of endogenously biotinylated proteins to the Golgi.

Figure 4.6 WT and C985S MIB1 localize to centrosome and centriollar satellites in AdV5-infected Hap1 cells. (A) Proximal proteomes of WT MIB1 and C985S over mKate (filtered for unique peptides ≥2) are plotted as $\log_2$ of the ratio of protein abundance of WT MIB1/mKate (x-axis) and C985S MIB1/mKate (y-axis). Colors denote genes enriched (≥2-fold; p-value <0.05) in the WT MIB1/mKate (red), C985S/mKate (yellow) and in both (orange). (B) Venn diagram comparing proteins enriched (>=2-fold, p-value <0.05) in WT MIB1/mKate versus C985S/mKate proximal proteomes as in (A) with corresponding gene lists for each category: WT MIB1/mKate only (red), C9985S/mKate only (yellow), both WT MIB1 and C985S/mKate (orange). (D) STRING network map of genes enriched (>=2-fold, p-value <0.05) in WT and C985S over mKate (orange box in (C)) labeled by color for enrichment of GO term categories centriollar satellite (red), centrosome (blue), golgi stack (green), microtubule cytoskeleton (yellow) along with corresponding adjusted p-value. (D) Immunofluorescence staining for biotinylated proteins (green: streptavidin) and centrosome (red: anti-pericentrin) upon infection with rep-comp AdV5-GFP (MOI=200 p/cell; 1.25 hpi) and H_2O_2 pulse-labeling verifies WT MIB1 and C985S localization to centrosome in AdV-infected cells. (E) Proximal proteomes of WT MIB1 and C985S over mKate as in (A) displaying all GO category "centrosome" components (blue) and all GO category "centriollar satellite" components (red).

Figure 4.6

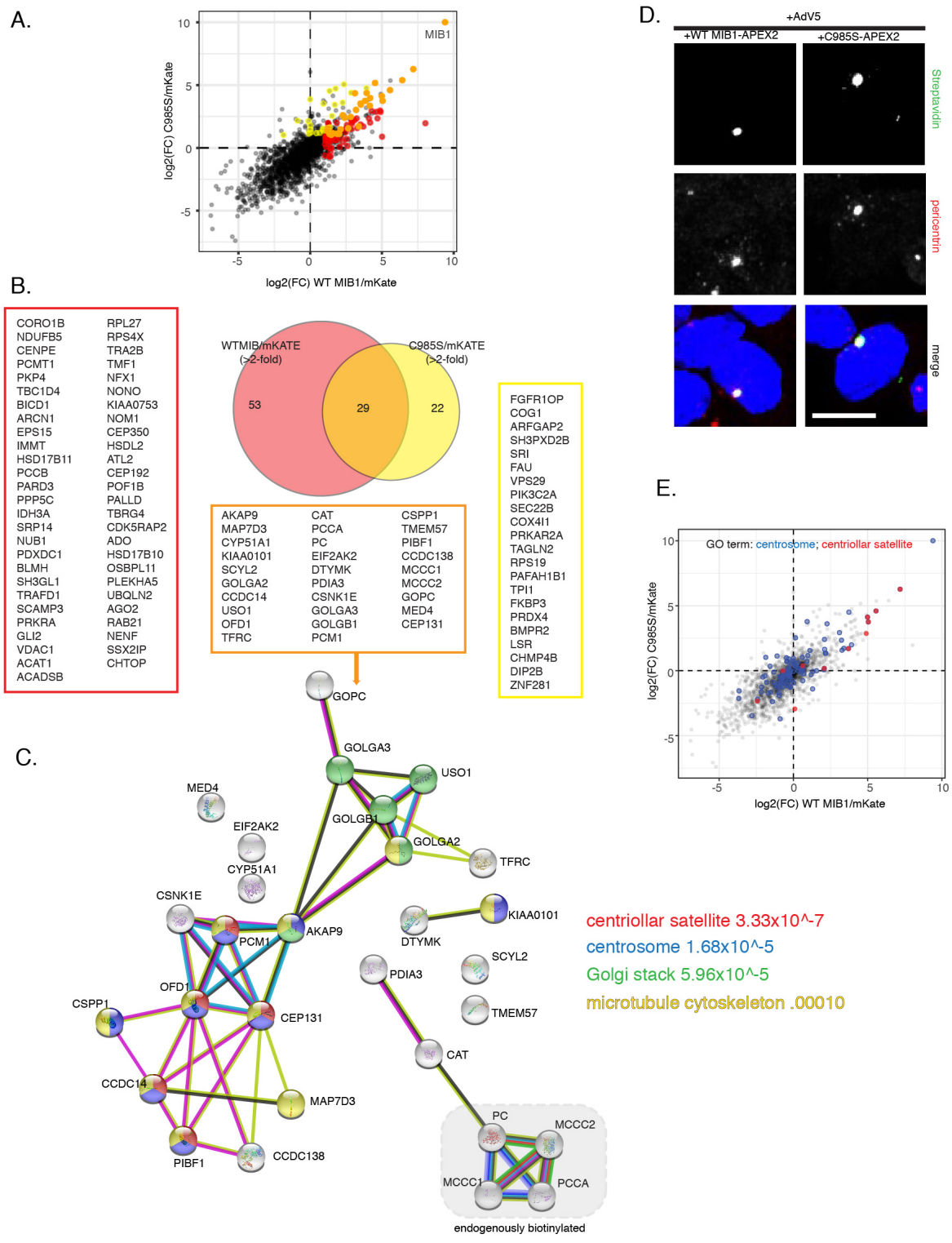
A.
MIB1
log2(FC) C985S/mKate
log2(FC) WT MIB1/mKate
B.
CORO1B
NDUFB5
CENPE
PCMT1
PKP4
TBC1D4
BICD1
ARCN1
EPS15
IMMT
HSD17B11
PCCB
PARD3
PPP5C
IDH3A
SRP14
NUB1
PDXDC1
BLMH
SH3GL1
TRAFD1
SCAMP3
PRKRA
GLI2
VDAC1
ACAT1
ACADSB
RPL27
RPS4X
TRA2B
TMF1
NFX1
NONO
KIAA0753
NOM1
CEP350
HSDL2
ATL2
CEP192
POF1B
PALLD
TBRG4
CDK5RAP2
ADO
HSD17B10
OSBPL11
PLEKHA5
UBQLN2
AGO2
RAB21
NENF
SSX2IP
CHTOP
WTMIB/mKATE (>2-fold)
C985S/mKATE (>2-fold)
53
29
22
AKAP9
MAP7D3
CYP51A1
KIAA0101
SCYL2
GOLGA2
CCDC14
USO1
OFD1
TFRC
CAT
PCCA
PC
EIF2AK2
DTYMK
PDIA3
CSNK1E
GOLGA3
GOLGB1
PCM1
CSPP1
TMEM57
PIBF1
CCDC138
MCCC1
MCCC2
MED4
GOPC
FGFR1OP
COG1
ARFGAP2
SH3PXD2B
SRI
FAU
VPS29
PIK3C2A
SEC22B
COX4I1
PRKAR2A
TAGLN2
RPS19
PAFAH1B1
TPI1
FKBP3
PRDX4
BMPR2
LSR
CHMP4B
DIP2B
ZNF281
C.
GOPC
GOLGA3
USO1
MED4
GOLGB1
EIF2AK2
GOLGA2
TFRC
CYP51A1
CSNK1E
KIAA0101
AKAP9
DTYMK
PCM1
SCYL2
PDIA3
OFD1
TMEM57
CSPP1
CEP131
CAT
CCDC14
MAP7D3
PC
MCCC2
PIBF1
CCDC138
MCCC1
PCCA
endogenously biotinylated
centriollar satellite 3.33x10^-7
centrosome 1.68x10^-5
Golgi stack 5.96x10^-5
microtubule cytoskeleton .00010
D.
+AdV5
+WT MIB1-APEX2
+C985S-APEX2
Streptavidin
pericentrin
merge
E.
GO term: centrosome; centriollar satellite
log2(FC) C985S/mKate
log2(FC) WT MIB1/mKate

Table 4.1 Select GO terms categories enriched in WT MIB1 and/or C985S proximal proteomes relative to mKate control. Table displays total number of genes within the given GO classification and the number of genes ascribed to that category among those genes "enriched" (>=2-fold) in comparison between WT MIB1 over mKate and C985S MIB1 over mKate with corresponding adjusted p-value. Note: these categories are only a select subset of the significant (adjusted p-value <0.05) GO terms identified for each comparison.

			WT MIB1/mKATE		C985S/mKATE	
GO term ID	term description	# genes in GO category	gene count	adj. p-value	gene count	adj. p-value
GO:0034451	centriolar satellite	30	7	9.57E-09	5	2.29E-06
GO:0005813	centrosome	468	15	6.62E-08	12	1.10E-06
GO:0015630	microtubule cytoskeleton	1118	19	5.43E-06	14	4.11E-05
GO:0044430	cytoskeletal part	1547	24	5.75E-07	15	0.00019
GO:0030135	coated vesicle	255	7	0.0017	7	0.00016
GO:0031982	vesicle	2318	19	0.0255	15	0.0074
GO:0005759	mitochondrial matrix	463	12	1.58E-05	5	0.0442
GO:0044429	mitochondrial part	1015	15	0.0004	n/a	n/a
GO:0098791	Golgi subcompartment	801	11	0.0065	10	0.0007

As non-membrane-bound and fairly insoluble organelles within the cell (previously only isolated via elaborate fractionation methods), the centrosome and its associated substructures like centriollar satellites, are ideal objects for study using proximity labeling. Our proximal proteome for MIB1 in Hap1 cells therefore joins a number of published proximal proteomes carried out for centrosome-and centriollar satellite proteins (Conkar et al., 2017; Firat-Karalar & Stearns, 2015; Firat-Karalar et al., 2014; Gupta et al., 2015). Several recent studies have even tagged MIB1 directly (Dho et al., 2019; Gheiratmand et al., 2019). Using this approach,[29] this latest work by Gheiratmand et al. demonstrated that despite the interaction of centriollar satellites with MTs in trafficking to and from the centrosome, centriollar satellite composition and integrity is in fact independent of MT/centrosome disruption. Comparison of the high-confidence hits from these previous publications using the Bio-ID approach with Tet-inducible BirA*-Flag-tagged MIB1 bait with our own proximal proteome for WT MIB1 revealed partial overlap particularly for centriollar satellite components **(Figure 4.7)**. Reassuringly, we also identified CCDC14 and EPS15, two of the stronger proximal targets that Dho et al. went on to validate as ubiquitinated by MIB1 but not targeted for degradation. Gheiratmand et al. note that among centriollar satellite proteins, MIB1 shows additional unique interaction with AP-2 adaptor complex proteins (AP2A1, AP2A2 and AP2M1). While these were not detected in our dataset, we did detect AP-2 subunit SCYL2. The remaining numerous differences between these datasets could be attributable to cell line, the stringency set for calling enrichment, and also that our analysis included infection with AdV. Unfortunately, we did not have the uninfected WT MIB1-APEX2 condition to compare with these datasets. The WT MIB1-APEX2 samples did not fly properly by mass spectrometry, making identification of infection-specific changes in the proximal-proteome of MIB1 impossible to assess.

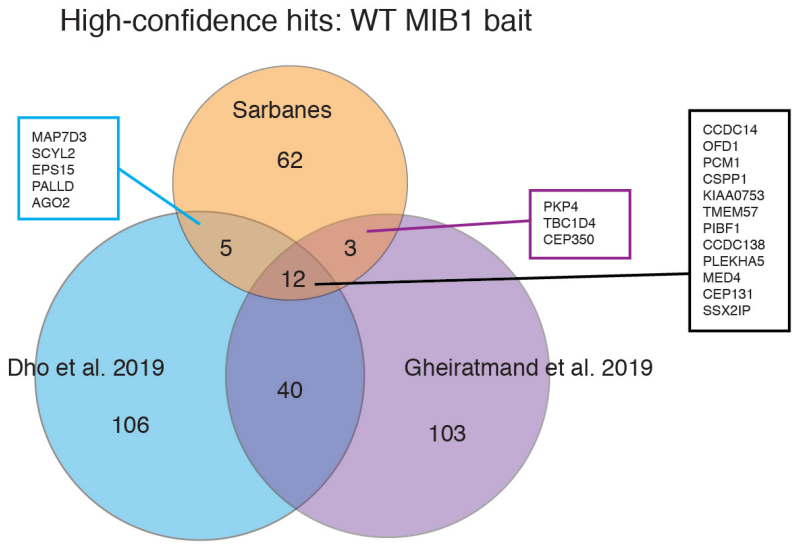

Figure 4.7 Cross-comparison with other MIB1 proximity labeling datasets. Venn diagram comparing high-confidence hits identified in our proximal proteome prepared using APEX2-labeled WT MIB1 in Hap1 cells relative to proximal proteomes of WT MIB1 in previous publications using the Bio-ID approach— tet-inducible BirA* Flag-tagged MIB1 bait in either HEK293 (Dho et al.) or Flp-IN T-REX 293 (Gheiratmand et al.) cells.

[29] and relevant given the minimal impact of MT manipulation on adenoviral DNA release observed in Hap1 cells

Proximity labeling reveals Ub-dependent association with RNPs

Our proximity labeling analysis against the cytoplasmic mKate control had validated an overarching localization of both the WT and C985S MIB1 to centriollar satellite structures. However, we had also intended to use this sensitive proteomic approach to parse out a more nuanced picture of protein partners and localization dependent upon either MIB1 ubiquitination activity or upon virus infection. In the absence of a WT MIB1-uninfected sample, we began by looking for Ub-dependent, proximal protein partners by comparing the proximal proteomes of WT MIB1 and C985S in AdV-infected cells. We had hypothesized that in WT MIB1-expressing cells, rapid release kinetics and/or subsequent degradation of targets by the proteasome may result in a depletion of direct targets in the vicinity of WT MIB1. Direct targets might then be enriched in proximity to the C985S mutant that retains the capacity to bind substrates but is unable to carry out ubiquitination. We also considered the possibility that MIB1's protein partners and localization might depend upon its ability to carry out ubiquitination of its target proteins. As shown above, many enriched proximal partners and functional gene categories were shared between WT and C985S MIB1. Nevertheless, analysis of the MS data directly comparing these two conditions exposed significant ubiquitin-dependent differences in their proximal proteomes (**Figure 4.8A)**. Most striking was the instant recognition of a number of RNA-binding proteins characteristic of stress granules—a class of ribonucleoprotein (RNP) granules that can be induced by virus infection. Indeed, GO term enrichment analysis of those genes enriched (>=2-fold; p-value <0.05) in proximity to WT MIB1 versus C985S revealed RNA-binding (adj p-value =0.005), RNA localization (adj p-value= 0.0165) and cytoplasmic ribonucleoprotein granule (adj p-value= 0.012). There was also further enrichment of a subset of centrosome components (KIF2A, C2CD3,CCDC14, FLOT1,SKI,CSPP1, and CEP192) (adj p-value=0.0038). By contrast, the C985S MIB1 mutant showed greater proximity to MT cytoskeleton (adj p-value= .0070), cytoskeleton (adj. p-value= .0201), nucleoplasm (adj p-value=.0043) and a distinct set of centrosomal proteins (adj. p-value=0.0232). Strong enrichment of cadherin-binding genes (SH3GLB1, ABI1, SLC3A2, TAGLN2, BMPR2 and BAIAP2L1) was identified (adj. p-value 0.0247) when assessed for enrichment by an alternate functional mapping program gProfiler. In particular, we noted a strong relative enrichment of C985S MIB1 to NUP85 more commonly referred to as pericentrin which we had used as a marker for the centrosome in our IF experiments[30]. Therefore, MIB1 WT and C985S have distinct proximal proteomes—with WT MIB1 associating preferentially with RNPs while the C985S mutant remains more tightly associated with certain cytoskeletal components and perhaps the centrosome itself— despite a shared dominating localization to the centrosome and centriollar satellites when compared against APEX2-mKate.

Characterization of potential MIB1-associated RNP granules

We were motivated to explore the emerging relationship between MIB1 and RNP granules further. There are several well-known types of cellular RNP granules found within the cytoplasm which are delineated by specific factors despite sharing many constituent RNA-binding proteins and other factors. The most thoroughly explored of these in the context of virus

[30] This was in line with the subtle phenotype we had observed in our centriollar satellite IF experiments in which centriollar satellites in MIB1 KO cells appeared more densely clustered at the centrosome, particularly apparent in their slight refractoriness to anisomycin-induced satellite dispersal relative to MIB1 WT cells.

infection (as mentioned above) are stress granules, cytoplasmic aggregates of stalled translational machinery that form transiently in response to a number of cellular stresses. Stress granule formation is typically associated with the later stage of many different virus infections when large-scale production of viral transcripts or cytoplasmic RNA genomes trigger host translational shut-off [31] (also leading many viruses to develop mechanisms to bypass normal translation) (Zhang et al., 2019). CAPRIN1, ATXN2 and MSI2 which all appeared more enriched in proximity to WT MIB1 relative to C985S MIB1 are reported components of these stress granules. Interestingly, UBQL2, also enriched in proximity to WT MIB1, although not an RNA-binding protein itself, has also been shown to associate with stress granules and serve as a bridge between stress granules and the ubiquitin-proteasome pathway (Dao et al., 2018).

Based on the identification of these proteins, we hypothesized that perhaps transient stress granule formation might be triggered by AdV entry alone and be regulated by MIB1 with consequences for AdV DNA delivery. Recent studies of neurodegenerative disease ALS and fronts-temporal dementia (FTD) have directly linked aberrant stress granule formation to disruption of nucleocytoplasmic transport by relocalizing nuclear pore components (including CRM1 and POM121) to these granules (K. Zhang et al., 2018). Nucleocytoplasmic transport can be rescued by KD of ATXN2 to inhibit stress granule formation. We hypothesized that WT MIB1 given its proximal association with ATXN2 might promote AdV DNA delivery by inhibiting stress granule formation and thereby preventing dysregulated nucleocytoplasmic transport. However, infection with AdV5-JR34 (2000 p/cell) in either MIB1 KO or WT MIB1-reconstituted cells at 1 hr 15 min pi showed no induction of stress granule formation (anti-MSI2) **(Figure 4.8B)**. By contrast, treatment with sorbitol resulted in robust and dose-dependent stress granule formation (at higher concentration appearing more as short filaments than stereotyped puncta) in both MIB1 KO and WT MIB1-reconstituted cells indicating that MIB1 does not play a role in the formation or the appearance of stress granules when induced by other means. Furthermore, staining for centriollar satellites (anti-PCM1) upon sorbitol treatment showed no clear colocalization of satellites with stress granule puncta (although recall that sorbitol treatment simultaneously aggregates and paralyzes satellites at the centrosome).

[31] there is no explicit study of stress granule formation in AdV late-stage infection even though this host shut-off is known to occur.

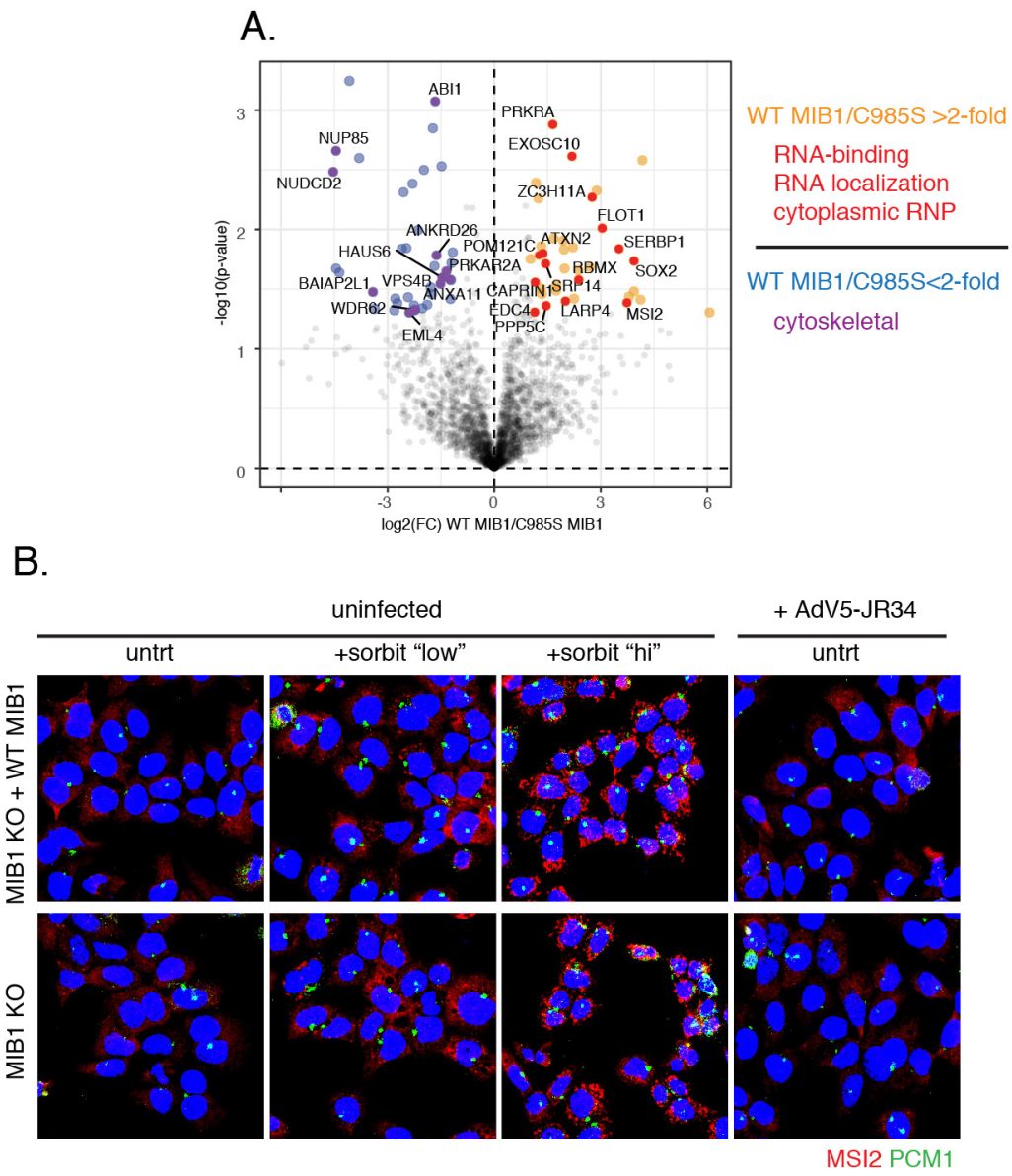

Figure 4.8 RNA-binding and RNP-associated proteins are enriched in the WT MIB1 ubiquitination-dependent proximal proteome. (A) MIB1 ubiquitination-dependent enrichment based on direct comparison of proximal proteomes of APEX2-tagged WT MIB1 and the C985S MIB1 (filtered for unique peptides >=1) plotted as $\log_2$ of the ratio of WT MIB1/ C985S MIB1 (x-axis) and –log(p-value) (y-axis) indicating proteins enriched (≥2-fold; p-value <0.05 : orange) and deenriched (<=-2-fold; p-value <0.05: blue). GO terms enrichment (≥2-fold; p-value <0.05) of "RNA-binding" "RNA localization" and "cytoplasmic ribonucleoprotein particle" components (red with gene names labeled) in proximity to WT MIB1 relative to the C985S MIB1 mutant and a de-enrichment for "cytoskeletal" components (purple with gene names labeled). (B) IF images (maximum-projection of Z-stacks) of MIB1 KO and WT MIB1-reconstituted cells either treated with sorbitol (100 mM "lo" and 500 mM "hi") or infected with AdV5-JR34 (2000 p/cell) for 1.25 h and stained for stress granules (red: anti-MSI2) and centriollar satellites (green: anti-PCM1).

Another discrete class of RNP granules found constitutively within the cytoplasm are RNA processing bodies or P-bodies. P-bodies are sites of RNA storage and degradation mediated by miRNAs and the RISC complex (Q. Zhang et al., 2019). Among the different species of cytoplasmic RNP granules potentially alluded to in the abundance of RNA-binding proteins enriched in proximity to WT MIB1, we were particularly interested in P-bodies for a number of reasons. First, P-bodies have been shown to traffic along MTs and associate with the centrosome—properties they would share with MIB1-containing centriollar satellites (Aizer et al., 2008). EDC4, a defining component of P-bodies, was one of the proteins enriched in proximity to WT MIB1 relative to C985S. Comparison of proteins proximal to WT MIB1 relative to mKate showed enrichment of AGO2, the primary component of the RISC complex that mediates miRNA-mediated translational repression within these granules. Furthermore, recent proximity labeling studies corroborate an emerging connection between centrosome/centriollar satellites and P-bodies. AGO2 was similarly detected in MIB1's proximity by Dho et al. and Gheiratmand et al. Conversely, a recent Bio-ID study using P-body proteins as baits revealed an association with CEP85, a centrosomal protein, again linking P-bodies and RNA regulation to centrosome biology (Y. Liu et al., 2018a). However this intersection has not been validated experimentally.

Staining for both centriollar satellites (anti-PCM1) and P-bodies (anti-EDC4) in WT MIB1-expressing cells visually corroborated the emerging proteomic data linking these two cytoplasmic granules. More specifically, a subset of centriollar satellites could be observed as dense nucleating foci encompassed within a subset of P-body particles **(Fig 4.9A)**. These examples of P-body-ensconced centriollar satellites were observed in both the presence and absence of functional MIB1 despite the suggestion by proximity labeling that association with RNPs was more greatly enriched in proximity to WT MIB1[32]. However, P-bodies in MIB1 KO and C985S-reconstituted cells did display differences in appearance when compared to WT MIB1-reconstituted cells, appearing larger and more globular. Centriollar satellite staining was frequently but not always observed at the center of these enlarged foci. Examining P-bodies across a timecourse of AdV infection revealed that this differential appearance was in fact both infection- and MIB1-dependent **(Fig 4.9B,C)**. A predominance of smaller perinuclear P-bodies were observed similarly across WT MIB1-reconstituted, C985S-reconstituted and MIB1 KO cells at 45 min pi. However, by 1 hpi and even more apparent by 1.25 hpi, while WT MIB1-reconstituted cells retained this perinuclear P-body distribution, C985S-reconstituted and MIB1 KO cells displayed enlarged P-body foci dispersed throughout the cytoplasm. In addition, somewhat surprisingly, tighter perinuclear P-body distribution was also observed more strongly across all conditions at 45 min post-infection relative to even uninfected cells suggesting that infection might first enhance trafficking of P-body to the perinuclear region before becoming dysregulated in the absence of MIB1. Of note, across all conditions little to no P-body localized to the centrosome (indicated by sites of intense PCM-1 stain). We also noted that the difference in appearance and localization was most dramatically observed in the C985S-reconstituted even relative to the MIB1 KO cells. This perhaps suggests that C985S MIB1 may nevertheless play a structural role in centriollar satellite integrity or localization independent of its ubiquitination activity that might exacerbate the observation of this phenotype relative to cells that do not express MIB1 at all.

[32] Although of course we are staining here for PCM-1 as a proxy for the broadly MIB1-localized centriollar satellites. In the future these experiments would need to be corroborated by imaging MIB1 directly.

Overall, these observations suggest that in the absence of functional MIB1 and by 1 hpi, P-bodies are aberrantly mislocalized into the cytoplasm and away from the immediate vicinity of the nucleus **(Fig 4.9C)**. We hypothesize that the larger particles observed may be a result of the accumulation and fusion of smaller P-body granules at these sites. We also hypothesize that AdV infection (specifically an event taking place in the window between 45 min pi and 1 hpi[33]) triggers a retrafficking of these RNP granules that is normally suppressed by the ubiquitination activity of MIB1. However, the functional significance of 1) the interaction between centriollar satellites and P-bodies in WT MIB1-reconstituted cells generally and 2) their altered distribution in infected MIB1 KO or C985S MIB1 cells to AdV DNA release remains unclear (although will be explored extensively in **Chapter 6: Discussion**). We speculate that regulated concentration of P-bodies at the nuclear envelope may somehow facilitate AdV DNA release.

[33] when virus particles arrive at the nucleus

Figure 4.9. P-bodies colocalize with centriollar satellites and display MIB1-dependent dynamics across a timecourse of AdV infection. (A) IF images (single Z-plane) of WT MIB1-reconstituted, C985S-reconstituted and MIB1 KO cells infected with AdV5 JR34 (2000 p/cell) for 75 mins and stained for P-bodies (red: anti-EDC4) and centriollar satellites (green: anti-PCM1) displayed as individual channels and as merged images. (B) IF images (maximum-projection of Z-stacks) of WT MIB1-reconstituted, C985S-reconstituted and MIB1 KO cells fixed across a timecourse of infection with AdV5 JR34 (uninfected, 45, 60 and 75 minutes post-infection; 2000 p/cell) and stained as in (A) for P-bodies (red) and centriollar satellites (green). Scale bar =10 μm. (C) Quantification of P-body stain within perinuclear region in images obtained as in (B) at 1.25 hpi and in uninfected cells. Values calculated as the total area of thresholded TR (anti-EDC4) signal within a mask of the perinuclear region generated by four dilations of nucleus and subtraction of undilated nucleus for the Z-plane representing the widest cross-section of the nucleus. The area of the TR signal was then normalized to the total perinuclear area per FOV and averaged across 3 FOV.

Figure 4.9

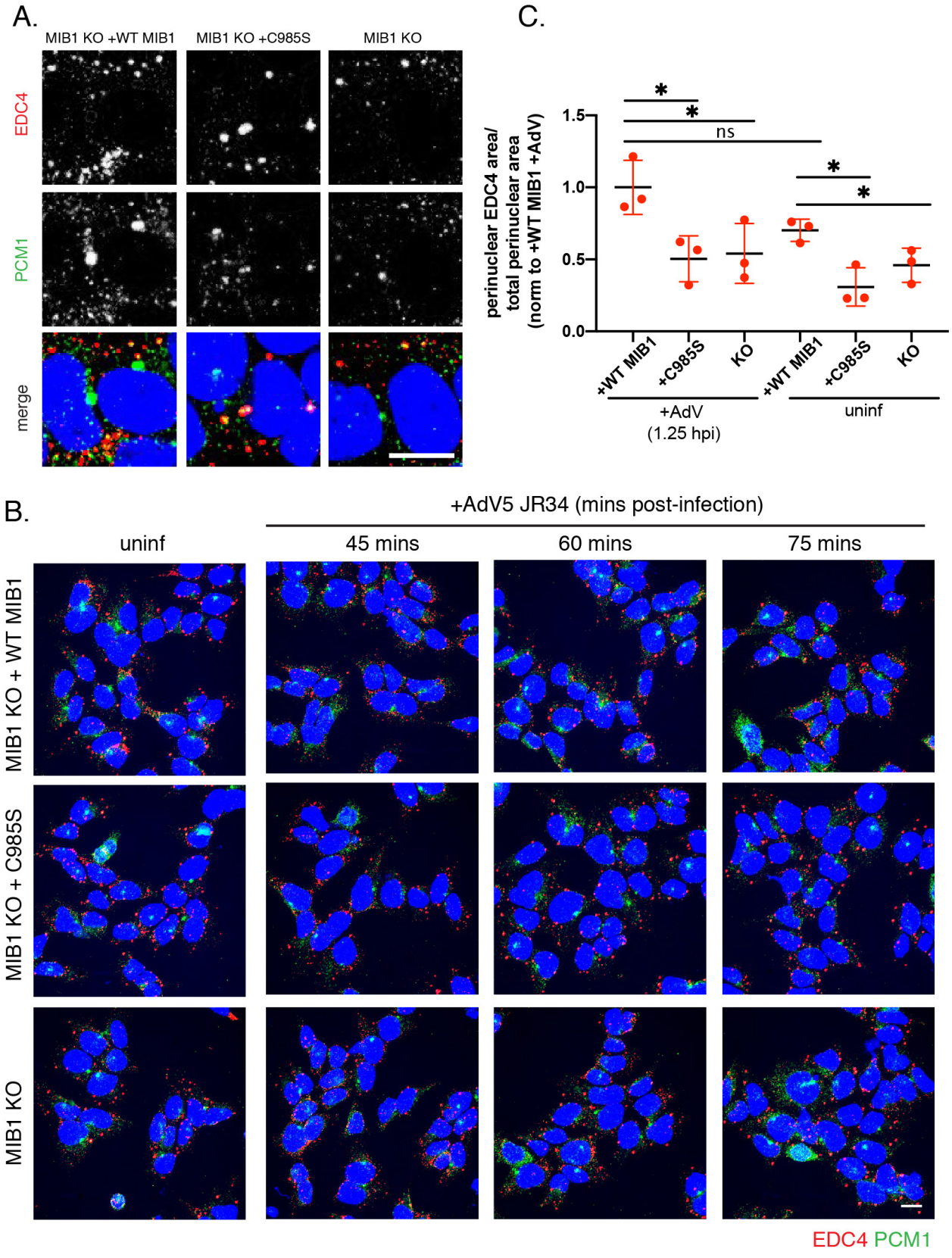
A.
MIB1 KO +WT MIB1
MIB1 KO +C985S
MIB1 KO
EDC4
PCM1
merge
C.
perinuclear EDC4 area/
total perinuclear area
(norm to +WT MIB1 +AdV)
1.5
1.0
0.5
0.0
*
*
ns
*
*
+WT MIB1
+C985S
KO
+WT MIB1
+C985S
KO
+AdV
(1.25 hpi)
uninf
B.
+AdV5 JR34 (mins post-infection)
uninf
45 mins
60 mins
75 mins
MIB1 KO + WT MIB1
MIB1 KO + C985S
MIB1 KO
EDC4 PCM1

Discussion of proximity labeling results

Physical proximity between proteins is typically a prerequisite for functional intersection. Identification of specific genes enriched in proximity to WT MIB1 both relative to the broader but more arbitrary mKate control and the more directly comparable ubiquitination-defective mutant C985S provided us with valuable information about the functional networks MIB1 participates in during AdV5 infection.

Using this approach, we identified an interesting intersection with RNP granules and subsequently demonstrated that centriollar satellites (likely containing MIB1) localize with a subset of P-bodies. Our subsequent IF of centriollar satellites and P-bodies marked the first non-proteomic validation of an emerging relationship between these two phase-separated granules. We are currently reconstituting MIB1 KO and WT cells with GFP-tagged P-body protein DCP1a to facilitate live-cell particle tracking of P-bodies upon infection. Specifically, we hope to collaborate with the Greber Lab to image these labeled P-bodies in conjunction with both their fluorescently-tagged MIB1 and fluorescently-labeled AdV5 particles. These studies will help to connect the interaction of the satellites and P-bodies back to AdV DNA release at the NPC[34]. Experimental manipulation/reduction of P-bodies either through treatment with drugs that reduce P-body formation (such as HSP90 inhibitor geldanamycin) or by KD of core P-body components such as DDX6 by siRNA will also be future directions that will help determine the relevance of P-body integrity to the AdV DNA release inhibition phenotype in MIB1 KO cells (Ayache et al., 2015; Matsumoto et al., 2011). Lastly, it is also possible that MIB1 interacts with other classes of RNP granules such as GW182-bodies (distinct from P-bodies but that also contain AGO2 and RISC components) or even smaller less discrete RNPs. Probing other RNPs and their implications for AdV infection will help determine the specificity and subsequent significance of the observed P-body interaction. We can assess more generally the nature and contribution of RNP granules to AdV5 genome release by treating MIB1 WT and KO cells with 1-6-hexanediol. 1-6 hexanediol is widely-used to dissolve liquid-like membraneless compartments such as RNP granules (although its impact on the membraneless centriollar satellites and nuclear pore integrity will need to be assessed in tandem) (Kroschwald et al. 2017).

We were also intrigued by the identification of CDK5RAP2, a bona fide centrosomal protein, which emerged as highly enriched in proximity to WT MIB1 over mKate. This protein represents the human counterpart to the Mto1/2 complex in yeast sharing the same domain (CM1-centrosome motif 1) that binds the gamma-tubulin complex (Bao et al., 2018). We were intrigued to see its enrichment almost to the level of centriollar satellite proteins in more intimate complex with MIB1 given the connection of Mto1 with the generation of MTOCs directly at the NPC in yeast (Bro) by binding directly to CRM1. Perhaps CDK5RAP2 similarly acts as an adaptor between centriollar satellites (containing MIB1) and nuclear pore complexes through interaction with CRM1 in our mammalian cells.

We are currently repeating the proximity-labeling proteomics to capture the WT MIB1

[34] Preliminary costaining of P-bodies and AdV capsids did reveal some colocalization events near the nuclear rim (data not shown) but this were extremely rare events and with fixed samples we are only ever capturing a subset of these potentially fleeting events at that given moment.

infected/uninfected comparison. Bauer et al. report that the dynamics/localization of MIB1 appear unaltered by infection (Bauer et al., 2019). Even if this is the case, MIB1's proximal proteome could certainly change upon infection due to broader changes within the perinuclear environment that could alter the accessibility of its interaction-partners and ubiquitination targets. We did note interesting infection-dependent differences in the proximal proteome of the C985S MIB1 mutant alluding to increased nuclear proximity upon AdV infection **(Figure 4.10)**. Enrichment of components of the nuclear lumen, nucleocytoplasmic transport and nuclear mRNA metabolic processes were observed. Of particular note was a strong enrichment of LMNB, a scaffolding component on the inner face of the nuclear envelope and presumably only accessible to cytoplasmic proteins through the NPC. Therefore, while it is possible that upon infection proteins normally localized to the nuclear pore or nuclear compartment become relocalized to the cytoplasm/centrosome (as reported in the context of ALS and FTD), we find it more likely that C985S MIB1-APEX2 itself shifts towards the nucleus (K. Zhang et al., 2018). Given the subtle differences in proximal proteomes between WT and C985S MIB1, it is unclear to what extent this suggested shift towards the nucleus upon AdV5 infection hinted at by the C985S infected versus uninfected comparison could be extrapolated to WT MIB1. Work by Bauer et al. using live-cell particle tracking of GFP-tagged MIB1 during infection suggests that MIB1 association at the nuclear pore is a fleeting hit-and-run event rather than an extended interaction with this site. However, they do not present particle-tracking data comparing the dynamics of WT MIB1 to its ubiquitination-defective counterpart.

In the future, additional modification of certain experimental parameters may help yield more insight into MIB1's role in AdV infection. For example, we chose to label at a timepoint of 1 hr and 15 mins post-infection consistent with our observation of nuclear pore arrival and DNA release in our microscopy studies of JR34 infected with 2000 p/cell. Given that the relevant ubiquitination event by MIB1 may be a transient and fleeting event triggered by virus infection it was important to us to catch the window when appreciable DNA release was observed but was not yet saturated. However, in the future it might be useful to conduct a timecourse of H_2O_2 labeling and collection at 30 mins, 45 mins, 1hr, 1 hr 15 mins and 1 hr 30 mins after infection which would guarantee capturing the relevant window and also follow any shifts in the the association partners of MIB1 WT that occur as a result of the relevant ubiquitination event having occurred that would not be observed in the C985S mutant which we might expect to give a more static picture[35]. Alternatively, further engineering of the APEX labeling system has led to the development of split-APEX constructs that allow one to capture the proximal proteome of a subset of the protein of interest only at certain specific interfaces or compartments or upon certain interactions(Y. Han et al., 2019). This approach could prevent the proteome from being dominated by a majority of the protein localizing to the centrosome when it is suggested by Bauer et al. that the relevant ubiquitination event(s) takes place at the NPC. In the future, we could design a split-APEX system to label proximal partners of MIB1 exclusively at the cytoplasmic face of the NPC.

We chose to use our replication-competent AdV5-GFP for the proteomics experiments at 200 p/cell which maximized the dynamic range using this virus between KO cells and KO cells reconstituted with WT MIB1. Given the somewhat surprising lack of adenoviral protein detection in either the proximity labeling (or Ub-IP proteome discussed below) with this

[35] Or may alternatively be aberrantly localized

relatively low input, in the future we might instead elect to perform the proteomics experiments using the JR34 virus for which I could also directly confirm the amount of capsid delivery and DNA release within the same experiment and at the higher dose of 2000 p/cell for which we still observed a complete block at the level of DNA release in KO cells. Lastly, although we elected here to probe the full proximal proteome rather than direct binding partners of MIB1, the inclusion of a FLAG tag in addition to the APEX2 tag, preserves the possibility of more traditional crosslinking and IP for proteomic identification of direct MIB1 binding partners.

While employed here in the very specific context of MIB1's contribution to AdV infection, proximity labeling applied more broadly has the potential to yield exciting new insights into viral infection and entry. In the future, infection with AdV (or even other viruses!) whose capsid proteins have been tagged with APEX2, with labeling at frequent timepoints following entry could help dissect shifts in proximal partners as the capsid traverses the cytosol, reaches the centrosome and docks at the nuclear pore.

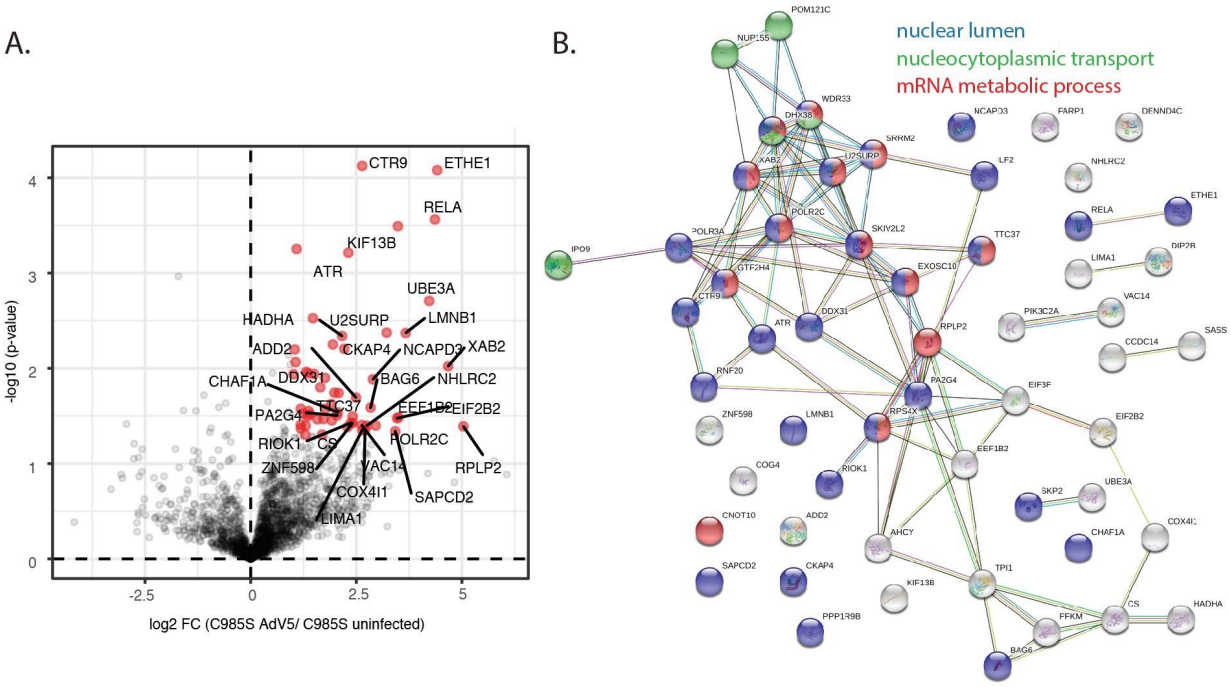

Figure 4.10 C985S MIB1 proximal proteome reveals infection-dependent enrichment of nuclear proteins. (A) AdV5 infection-dependent enrichment based on comparison of proximal proteomes of APEX2-tagged C985S MIB1 in AdV5-infected and uninfected cells plotted as $\log_2$ of the ratio of C985S+AdV5/ C985S uninfected (x-axis) and –log(p-value) (y-axis). Proteins enriched upon infection by >2-fold (p-value <0.05) labeled in red, proteins enriched by >4-fold labeled by gene name. (B) STRING map of proteins enriched upon infection by >2-fold (red in (A)) colored to highlight select enriched GO term categories: nuclear lumen (blue; adjusted p-value = 1.73x10^-5), nucleocytoplasmic transport (green; adjusted p-value = 0.0240) and mRNA metabolic process (red; adjusted p-value = 8.24x10^-5).

Characterization of MIB1-dependent ubiquitinated proteome upon AdV5 infection

Ubiquitin-IP: An Introduction

Proximity labeling proteomics allowed us to characterize MIB1's cellular context during AdV infection. However, proximity labeling was unable to clarify which out of these proximal proteins are functionally linked to MIB1 as substrates of its ubiquitin ligase activity. To more directly identify candidates for the ubiquitination target of MIB1 relevant to virus infection, we therefore turned to a complementary proteomic approach that would examine ubiquitination events directly.

Historically, identifying and validating ubiquitination targets of a particular E3 ubiquitin ligase is no small feat. A full appreciation of the role of numerous PTMs to both viral infection and cell homeostasis has been hindered by the technical challenge of characterizing these events. Rapid proteasomal degradation as an outcome for ubiquitinated proteins or the dynamic counter-action of DUBs can make capturing these events particularly difficult (Iconomou & Saunders, 2016). Furthermore, modification at a specific site (such as the nuclear pore) or upon a specific trigger may only occur on a small fraction of the total pool of a given protein. Proteins may also undergo multiple ubiquitination events mediated by distinct E3 ligases that mask the contribution of individual ligases (Iconomou & Saunders, 2016).

Several different proteomic approaches have emerged in recent years to aid in the quantitative and sensitive detection of ubiquitination events. HA-tagged ubiquitin constructs can be transfected into cells and then immunoprecipitated for incorporation into ubiquitinated proteins. However, this approach requires first subjecting the cells to transfection (which can stress cells and have variable efficiency). Furthermore, the exogenous HA-tagged ubiquitin can introduce artifacts as they may alter the dynamics of ubiquitination by not being incorporated or removed by E3 ligases and DUBs in a physiological way (Emmerich & Cohen, 2015). Mutant constructs of the HA-tagged ubiquitin unable to perform K48 or K63 linkage respectively allows one to proteomically distinguish between different ubiquitin linkage-types and their anticipated fates but can similarly skew the endogenous view of ubiquitination events. These constructs are therefore more conducive to downstream validations once a specific target of interest has been identified by other means.

Fortunately, there are a number of approaches capable of characterizing endogenous ubiquitination profiles. One of these is an immunoprecipitation strategy using an antibody that detects a unique signature left by ubiquitin on its conjugated peptide following trypsin digestion (Xu et al., 2014). Ubiquitin covalently attaches to the ε-amino group of the target lysine through its C-terminal glycine, an initiating linkage that is the same regardless of downstream poly-ubiquitinated linkage type. Trypsin digestion which cleaves between the R/GG of ubiquitin preceding this linkage therefore generates a "di-Gly" motif which can be specifically immunoprecipitated and recognized upon LC/MS-MS analysis as a 114.1 Da signature.[36] One drawback of this approach is that ubiquitin-like PTMs such as neddylation also leave this di-Gly

[36] Recall from the introduction: it was this very same tryptic digestion remnant detected by Goldknopf and Busch as a second "head" (or N-terminus) on histone H2A that marked the initial discovery of ubiquitination.

signature on their target proteins upon cleavage resulting in “false positives”. However, the power of this approach is that it allows for site-specific ubiquitin identification by immunoprecipitating the specific peptide that is ubiquitinated rather than the whole protein. This may be especially valuable in identifying the contributions of individual E3 ligases to proteins that are multiply ubiquitinated by distinct E3 ligases that would be masked by IP of the entire protein. It may also allow for identification of very low-level ubiquitination events through enrichment of ubiquitinated peptide alone without having to compete with peptides across the whole protein for detection.

Another approach for isolating the endogenous ubiquitinated proteome is through the use of Tandem Ubiquitin Binding Entities (TUBEs). These TUBEs are made up of four ubiquitin binding domains (UBDs) taken from two different proteins, ubiquilin-1 and HR23A, connected by flexible linkers (Hjerpe et al., 2009). These domains make them very specific to the binding of ubiquitin rather than the similar post-translational modifications sumoylation and neddylation. At the same time, their combination facilitates high-affinity binding to broad types of ubiquitin chains as well as monoubiquitin (although at lower efficiency) allowing for an all-encompassing look at cellular ubiquitination (Y. Shi et al., 2011). Encouragingly, ubiquitinated proteins isolated using this method show strong overlap with those proteins isolated by the di-Gly approach under similar conditions (Lopitz-Otsoa et al., 2012).

Weighing the pros and cons of each of these approaches we ultimately decided upon the TUBEs for the detection of MIB1-specific ubiquitination targets given the ability to detect endogenous ubiquitination events that discriminate ubiquitin from other UBL-modifiers. While forgoing site-specific resolution, we also hoped that the immunoprecipitation of the entire ubiquitinated *protein* rather than *peptide* would increase detection and ensure capture of all relevant ubiquitination targets even if the particular modified peptide did not fly well by LC-MS/MS. From this point on, we will refer to the application of these TUBEs as our ubiquitin-immunoprecipitation (Ub-IP) experiments.

Ub-IP: Preparation and Experimental Design

We first validated the ability of the TUBEs to enrich the ubiquitinated proteome and titrated the protein input to a fixed number of beads to choose an appropriate ratio. A ratio of 200 mg of input lysate to 100 ul of beads was selected due to greatest depletion by post-IP and enrichment upon elution relative to the 10% input **(Figure 4.11A).** Treatment with MG132 to block proteasomal degradation confirmed enrichment of ubiquitinated proteins by the TUBEs, as this treatment resulted in enhanced detection of ubiquitinated proteins.

In proceeding to the large-scale mass spectrometry experiment **(Figure 4.11B)**, MIB1 KO clone 2-1 and MIB1 KO cells reconstituted with either WT MIB1 or the C985S mutant were infected with 200 p/cell of replication-competent AdV5-GFP. Additionally, uninfected samples of WT MIB1-reconstituted cells were prepared in parallel for identification of infection-dependent ubiquitination events. At 1 hpi, cells were lysed in TUBE lysis buffer supplemented with protease inhibitors and most importantly a DUB inhibitor PR-619 to prevent the rapid de-ubiqiuitination of ubiquitinated proteins upon lysis. The lysates were then incubated with TUBE-Dynabeads to immunoprecipitate all endogenously ubiquitinated proteins and the isolated proteins were submitted for processing by LC-MS/MS and subsequent analysis. Around 1000

unique proteins were detected per condition and initial principal components analysis (PCA) confirmed distinct separation between all submitted categories: MIB1 KO + AdV5, C985S +AdV5 WT MIB1+AdV5 and WT MIB1 without infection **(Figure 4.11C)**. In addition, subsequent heat map hierarchies based on iBAQ values accurately rederived all submitted conditions and suggested that the presence or absence of MIB1 rather than AdV infection was the dominant influence on the differential protein detection **(Figure 4.11D)**.

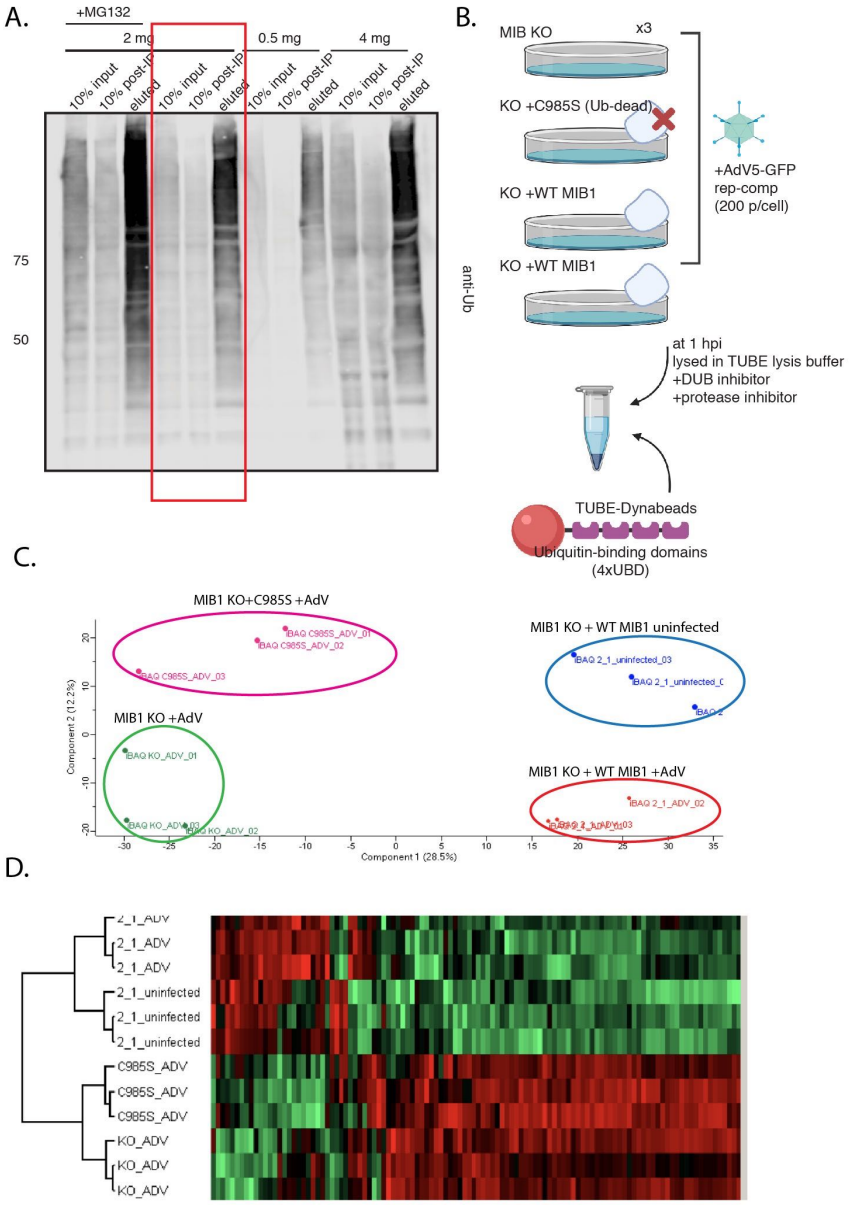

Figure 4.11 Isolation of ubiquitinated proteomes from AdV5-infected MIB1 KO and WT or C985S MIB1-reconstituted cells using Tandem Ubiquitin Binding Entities (TUBEs) (A) Hap1 lysate to TUBE-Dynabead slurry ratio optimization using 0.5 mg, 2mg or 4 mg of input lysate from Hap1 WT cells in 500 ul TUBE lysis buffer relative to a fixed 100 ul of TUBE-Dynabead slurry. Western blot (anti-Ub) of 10% of the input, 10% of the post-IP supernatant following incubation with TUBE-Dynabeads, and total eluant directly from the beads into sample loading buffer to detect all ubiquitinated proteins. (B) Simplified schematic of Ub-IP experiment using TUBE-Dynabeads for LC-MS/MS submission. (C) Principal Components Analysis (PCA) plot of infected MIB1 KO and KO reconstituted with C985S MIB1 or WT MIB1, and uninfected WT MIB1-reconstituted cells. (D) Hierarchical clustering heat map based on iBAQ values showing clean segregation of replicates displaying relative up-regulation (red) or down-regulation (green) of individual genes arranged into functional clusters.

MIB1-dependent ubiquitinated proteome is enriched for RNA-associated proteins

Our mutagenesis experiments had suggested that MIB1 mediates AdV5 infection through ubiquitination of a specific target protein (or proteins). We were therefore interested in identifying those proteins enriched upon IP of ubiquitinated proteins in WT MIB1-expressing cells over either MIB1 KO cells or cells reconstituted with the C985S mutant MIB1 during infection. These proteins would reflect "MIB1-dependent" ubiquitination events and in theory encompass the target protein relevant to AdV infection. The identified proteins could then serve as a "short-list" of candidates for mechanistic follow-up to probe their impact on AdV infectivity. Examining those proteins significantly enriched (>2-fold; p-value <0.05) in WT MIB1-reconstituted cells relative to *both* the MIB1 KO and C985S-reconstituted cells during AdV infection yielded a list of nine genes (DRG1, EIF3C, FHL1, FMR1, RNF25, SRPK1, UPF1, YY1 and STAU2) that represented the most stringent MIB1 ubiquitination target candidates **(**red, **Figure 4.12A,B)**. Interestingly, several of these MIB1 target candidates, including STAU2 and DRG1, have been reported to localize to the spindle or centrosome through microtubule-binding domains. This increased our confidence in the capacity of a localization-blind mass spectrometry approach to nevertheless detect plausible targets of our centrosome- and satellite- localized MIB1. Recognizing the inherent "noisiness" of mass spectrometry data, we also defined a set of less stringent MIB1-ubiquitination candidates to include those genes significant (p<0.05) in *either* the WT MIB1/KO or WT MIB1/C985S comparison but enriched by > 2-fold in both **(**orange, **Figure 4.12B**). This encompassed an additional 19 genes. GO terms analysis of this expanded set of MIB1 target candidates **(Table 4.2)** revealed a striking enrichment of ribonucleoprotein complexes (adj. p value= 4.12x10^-5), RNA-binding proteins (adj. p value= 0.0028) and RNA localization genes (adj. p-value=0.001) (**Figure 4.12C**). Many of these are well-characterized components of specific RNPs like the b-actin mRNA interactome or neuronal transport RNPs (to be discussed in further detail below in regards to STAU2) (Mukherjee et al., 2019). The emergence of these functional categories independently corroborated the finding from our proximity-labeling dataset which had identified a MIB1 ubiquitination-dependent enrichment of RNP-related proteins in proximity to WT MIB1 relative to the C985S mutant. We were also interested in the appearance within our candidate list of proteins like RAN, which had been previously implicated in AdV infection due to its role in nucleocytoplasmic transport as a direct binding partner of CRM1. Recall, the inhibition of CRM1 by LMB precludes binding to NES-cargo and RAN and results in a strong block in adenoviral capsid trafficking away from the MTOC (I.-H. Wang et al., 2017).

Out of curiosity, we also looked at all additional genes enriched by greater than two-fold even if they did not quite meet the significance threshold in either the WT MIB1/KO or WT MIB1/C985S comparison (gray box, **Figure 4.12B**). These 48 "low quality" Ub-IP genes were also enriched for RNA-related processes with 15 genes falling under "mRNA metabolic process" (FDR 0.0063), "regulation of mRNA metabolic process" (FDR 0.0338) or "RNA transport" (FDR 0.0338) by GO terms analysis. Several of these in particular caught our eye. NXF1 is a mRNA export factor associated with microtubules for the trafficking of cytoplasmic RNA granules (Mamon et al., 2017). Serrate (SRRT) is involved in miRNA processing likely within P-bodies. RANBP1 is involved in the RAN-GDP/RAN-GTP cycle necessary for CRM1-mediated transport and is itself a bona fide substrate of CRM1 export (Thakar et al., 2013).

Figure 4.12 RNA-binding and RNP-associated proteins enriched among MIB1-ubiquitination target candidates identified by Ub-IP from AdV5-infected WT MIB1 relative to KO or C985S-reconstituted cells (A) Enrichment of ubiquitinated proteins in WT MIB1-reconstituted compared with MIB1 KO cells (orange outline), WT MIB1-reconstituted compared with C985S-reconstituted cells (purple outline) and WT MIB1-reconstituted cells infected with AdV5 compared with uninfected cells (gray outline) plotted as a volcano plot of $\log_2$ fold change in protein abundance between the two conditions (x-axis) and –log10 of the t-test p-value (y-axis). Red circles are those proteins enriched ≥2-fold (p-value <0.05). (B) Venn Diagram and associated gene lists of the enriched proteins (red circles) from each of the comparisons in (A) identifies 9 high stringency MIB1 ubiquitination target candidates enriched (≥2-fold; p-value<0.05) in both the WT MIB1/MIB1 KO and the WT MIB1/C985S comparison (gene names in red) and 22 lower stringency candidates significant (p-value <0.05) in either the WT MIB1/MIB1 KO or WT MIB1/C985S comparison but enriched (≥2-fold) in both (genes names in orange). Those genes enriched (≥2-fold) in both WT MIB1/MIB1 KO or WT MIB1/C985S but not significant (p-value >0.05) listed in gray in the box on the right. (C) STRING network map of the 31 MIB1 ubiquitination target candidates genes (orange and red in (B)) labeled by color for enrichment of GO term categories: ribonucleoprotein complex (green), RNA-binding (red) and RNA localization (blue) along with number of genes identified in each category and corresponding adjusted p-value.

Figure 4.12

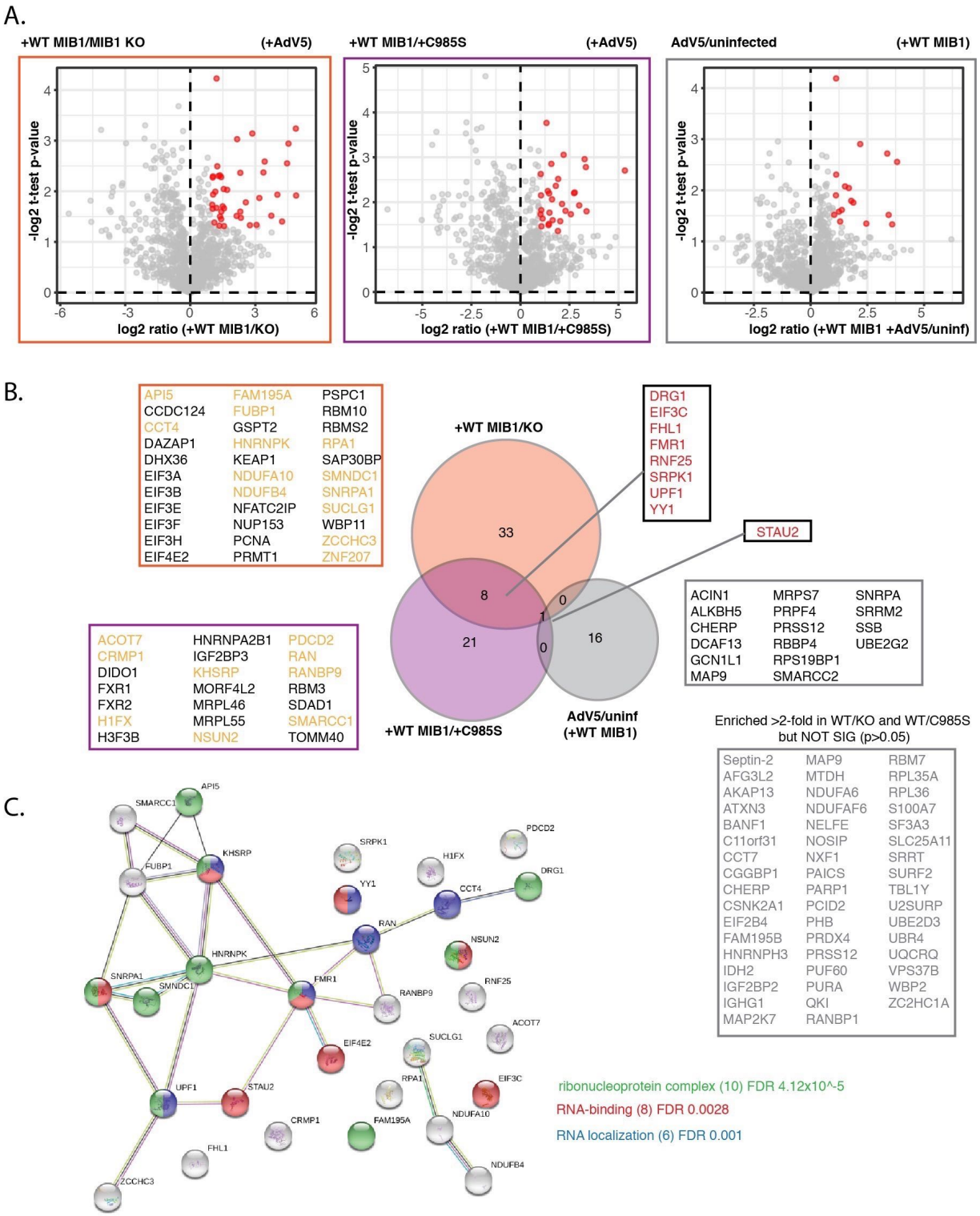
A.
+WT MIB1/MIB1 KO
(+AdV5)
+WT MIB1/+C985S
(+AdV5)
AdV5/uninfected
(+WT MIB1)
-log2 t-test p-value
log2 ratio (+WT MIB1/KO)
log2 ratio (+WT MIB1/+C985S)
log2 ratio (+WT MIB1 +AdV5/uninf)
B.
API5 FAM195A PSPC1
CCDC124 FUBP1 RBM10
CCT4 GSPT2 RBMS2
DAZAP1 HNRNPK RPA1
DHX36 KEAP1 SAP30BP
EIF3A NDUFA10 SMNDC1
EIF3B NDUFB4 SNRPA1
EIF3E NFATC2IP SUCLG1
EIF3F NUP153 WBP11
EIF3H PCNA ZCCHC3
EIF4E2 PRMT1 ZNF207
+WT MIB1/KO
33
8
21
0
1
0
16
+WT MIB1/+C985S
AdV5/uninf
(+WT MIB1)
DRG1
EIF3C
FHL1
FMR1
RNF25
SRPK1
UPF1
YY1
STAU2
ACIN1 MRPS7 SNRPA
ALKBH5 PRPF4 SRRM2
CHERP PRSS12 SSB
DCAF13 RBBP4 UBE2G2
GCN1L1 RPS19BP1
MAP9 SMARCC2
ACOT7 HNRNPA2B1 PDCD2
CRMP1 IGF2BP3 RAN
DIDO1 KHSRP RANBP9
FXR1 MORF4L2 RBM3
FXR2 MRPL46 SDAD1
H1FX MRPL55 SMARCC1
H3F3B NSUN2 TOMM40
Enriched >2-fold in WT/KO and WT/C985S but NOT SIG (p>0.05)
Septin-2 MAP9 RBM7
AFG3L2 MTDH RPL35A
AKAP13 NDUFA6 RPL36
ATXN3 NDUFAF6 S100A7
BANF1 NELFE SF3A3
C11orf31 NOSIP SLC25A11
CCT7 NXF1 SRRT
CGGBP1 PAICS SURF2
CHERP PARP1 TBL1Y
CSNK2A1 PCID2 U2SURP
EIF2B4 PHB UBE2D3
FAM195B PRDX4 UBR4
HNRNPH3 PRSS12 UQCRQ
IDH2 PUF60 VPS37B
IGF2BP2 PURA WBP2
IGHG1 QKI ZC2HC1A
MAP2K7 RANBP1
C.
API5
SMARCC1
KHSRP
FUBP1
SRPK1
PDCD2
H1FX
DRG1
YY1
CCT4
RAN
NSUN2
HNRNPK
SNRPA1
SMNDC1
FMR1
RANBP9
RNF25
ACOT7
SUCLG1
EIF4E2
RPA1
EIF3C
UPF1
STAU2
NDUFA10
CRMP1
FAM195A
FHL1
NDUFB4
ZCCHC3
ribonucleoprotein complex (10) FDR 4.12x10^-5
RNA-binding (8) FDR 0.0028
RNA localization (6) FDR 0.001

Table 4.2 Genes enriched (>2-fold) by Ub-IP in both WT MIB1-reconstituted cells over MIB1 KO and WT MIB1-reconstituted cells over C985S-reconstituted cells with significance (p<0.05) in either comparison. Table displays log2(FC) and corresponding significance status for each of the listed comparisons (WT/KO, WT/C985S and WT AdV5/uninf) sorted by log2(FC) for WT MIB1-reconstituted over MIB1 KO and shaded in heat map ranging from highest (red) to lowest (blue) log2(FC) value represented.

	log2(FC)			Significance?		
Gene Name	WT/KO	WT/C985S	AdV/uninf (in WT)	WT/KO	WT/C985S	AdV/uninf (in WT)
RNF25	5.25095	3.27142	0.454898	+	+	
FHL1	4.88033	5.32509	0.394771	+	+	
NDUFA10	4.86619	3.07838	0.159844	+		
STAU2	4.52864	2.99644	3.8109	+	+	+
SMNDC1	4.46235	2.98544	0.126607	+		
HNRNPK	4.23285	4.85498	2.62115	+		
FAM195A	4.01555	1.50106	-0.606332	+		+
SNRPA1	3.73707	2.44455	0.175936	+		
YY1	3.37251	1.04942	0.293828	+	+	
SUCLG1	3.18403	2.66337	-0.842204	+		
FUBP1	2.86084	1.68101	2.71338	+		
ACOT7	2.8018	3.37031	-0.200792		+	
API5	2.74803	1.0295	-0.905067	+		
ZCCHC3	2.5609	2.30434	-0.010252	+		
RAN	2.49088	1.91163	0.717539		+	
EIF4E2	2.30641	1.12844	0.373086	+		
SRPK1	2.30507	2.57014	1.63958	+	+	
NSUN2	2.21459	2.2978	1.76685		+	
NDUFB4	2.15967	3.0419	-0.0778796	+		
EIF3C	2.13606	1.46326	0.672617	+	+	
RANBP9	1.7117	3.3362	0.886613		+	
DRG1	1.69905	1.92325	0.167866	+	+	
CCT4	1.55511	1.48964	-0.289843	+		
RPA1	1.54045	1.36601	1.33456	+		
PDCD2	1.43336	2.73228	0.0540504		+	
KHSRP	1.2171	1.6433	0.512241		+	+
UPF1	1.15263	1.32829	0.646434	+	+	+
H1FX	1.15218	2.02931	-0.887847		+	
SMARCC1	1.13495	1.06116	1.0701		+	
FMR1	1.11109	2.76836	0.44407	+	+	
CRMP1	1.10794	2.12194	-0.438966		+	

MIB1-dependent ubiquitinated proteome shows depletion of cytoskeletal factors

Proteins enriched by Ub-IP only in the presence of functional WT MIB1 represented intuitive potential targets of direct ubiquitination by this E3 ubiquitin ligase. However, during our analyses, we also noted a larger group of 43 genes that were significantly depleted by Ub-IP by >2-fold in both the comparison between WT MIB1 and MIB1 KO or C985S-reconstituted cells (**Figure 4.13A,B**) **(Table 4.3)**. How these depleted proteins might reflect MIB1 ubiquitination activity is less intuitive, however, their differential detection in WT MIB1 relative to both KO and C985S cells suggested a functional connection with MIB1 worth investigating further[37]. Intriguingly, GO term analysis of this particular set of genes revealed enrichment of functional clusters corresponding to either MT-based processes, cytoskeleton organization or proteasome-mediated ubiquitin-dependent protein catabolism (**Figure 4.13C**). Vesicle-mediated transport also emerged as an enriched functional category when MIB1 was included among the gene set. Our proximity labeling dataset had confirmed that while both WT and mutant MIB1 localized generally to centriollar satellites, in the absence of MIB1 ubiquitination activity the mutant C985S showed enhanced proximity to a subset of MT/cytoskeletal proteins. The fact that this independent dataset of proteins differentially ubiquitinated in the presence or absence of MIB1 now similarly identified both RNP-related proteins enriched in the WT MIB1 condition and cytoskeletal proteins enriched for the C985S mutant (and even additionally the MIB1 KO) condition was validating and more definitively implicated MIB1 in an emerging balance between RNPs and cytoskeleton with possible relevance to AdV infection.

[37] how/why we might observe this depletion will be discussed in more detail below

Figure 4.13 Cytoskeleton-associated factors depleted among proteins isolated by Ub-IP from AdV5-infected WT MIB1 relative to KO or C985S-reconstituted cells. (A) Proteins depleted upon Ub-IP in WT MIB1-reconstituted compared with MIB1 KO cells (orange outline), WT MIB1-reconstituted compared with C985S-reconstituted cells (purple outline) and WT MIB1-reconstituted cells infected with AdV5 compared with uninfected cells (gray outline) plotted as a volcano plot of $\log_2$ fold change in protein abundance between the two conditions (x-axis) and -log of the t-test p-value (y-axis). Blue circles are those proteins de-enriched ≥2-fold (p-value <0.05). (B) Venn Diagram and associated gene lists of the enriched proteins (blue circles) from each of the comparisons in (A). (C) STRING network map of the 41 MIB1 ubiquitination target candidates genes (blue text in (B)) labeled by color for enrichment of GO term categories: microtubule-based process (green), cytoskeleton organization (red) and proteasome-mediated ubiquitin-dependent protein catabolism (blue) along with number of genes identified in each category and corresponding adjusted p-value.

Figure 4.13

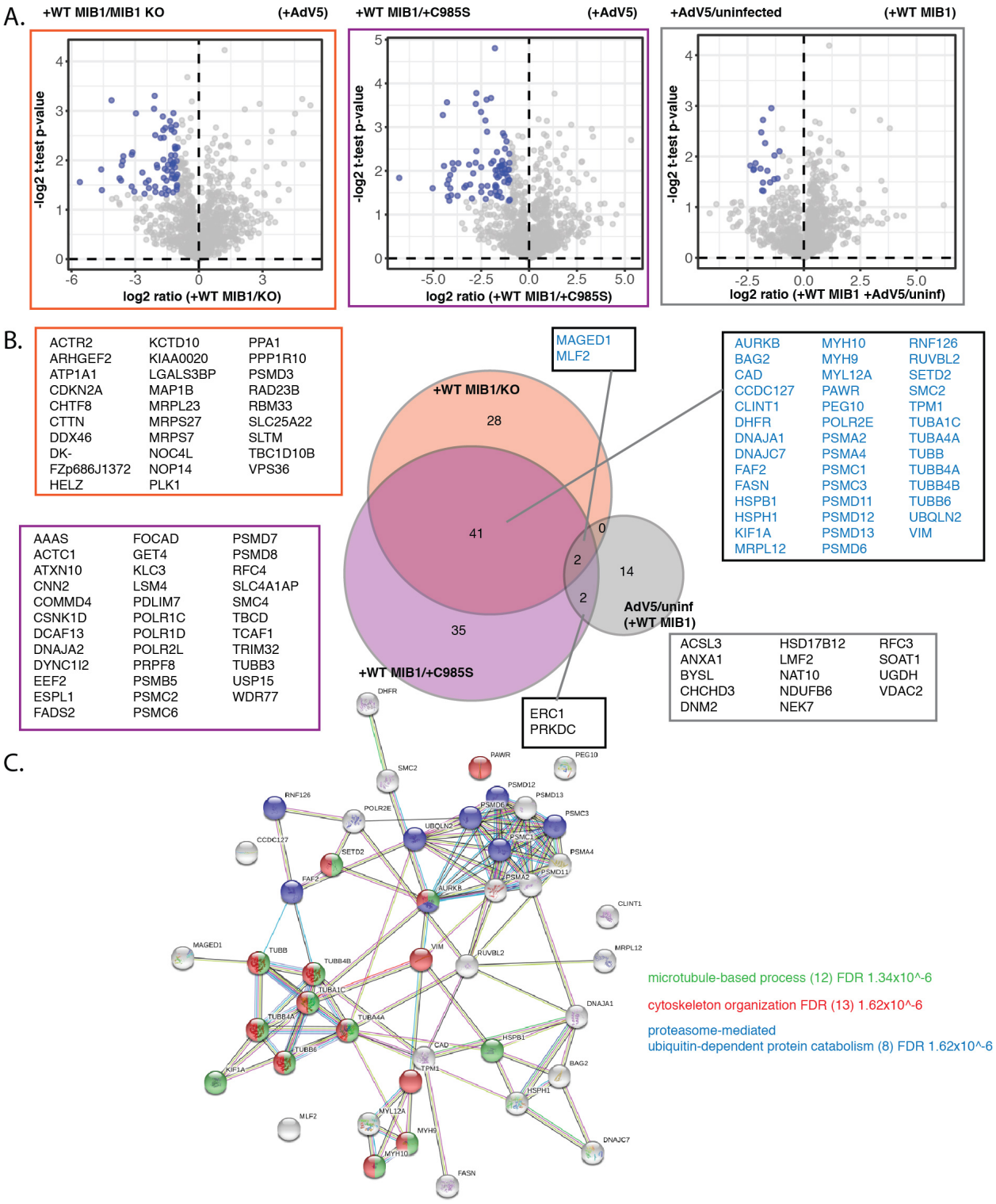
A.
+WT MIB1/MIB1 KO
(+AdV5)
+WT MIB1/+C985S
(+AdV5)
+AdV5/uninfected
(+WT MIB1)
-log2 t-test p-value
log2 ratio (+WT MIB1/KO)
log2 ratio (+WT MIB1/+C985S)
log2 ratio (+WT MIB1 +AdV5/uninf)
B.
ACTR2 ARHGEF2 ATP1A1 CDKN2A CHTF8 CTTN DDX46 DK- FZp686J1372 HELZ
KCTD10 KIAA0020 LGALS3BP MAP1B MRPL23 MRPS27 MRPS7 NOC4L NOP14 PLK1
PPA1 PPP1R10 PSMD3 RAD23B RBM33 SLC25A22 SLTM TBC1D10B VPS36
MAGED1 MLF2
+WT MIB1/KO
28
41
0
2
14
2
35
AdV5/uninf (+WT MIB1)
+WT MIB1/+C985S
ERC1 PRKDC
AURKB BAG2 CAD CCDC127 CLINT1 DHFR DNAJA1 DNAJC7 FAF2 FASN HSPB1 HSPH1 KIF1A MRPL12
MYH10 MYH9 MYL12A PAWR PEG10 POLR2E PSMA2 PSMA4 PSMC1 PSMC3 PSMD11 PSMD12 PSMD13 PSMD6
RNF126 RUVBL2 SETD2 SMC2 TPM1 TUBA1C TUBA4A TUBB TUBB4A TUBB4B TUBB6 UBQLN2 VIM
AAAS ACTC1 ATXN10 CNN2 COMMD4 CSNK1D DCAF13 DNAJA2 DYNC1I2 EEF2 ESPL1 FADS2
FOCAD GET4 KLC3 LSM4 PDLIM7 POLR1C POLR1D POLR2L PRPF8 PSMB5 PSMC2 PSMC6
PSMD7 PSMD8 RFC4 SLC4A1AP SMC4 TBCD TCAF1 TRIM32 TUBB3 USP15 WDR77
ACSL3 ANXA1 BYSL CHCHD3 DNM2
HSD17B12 LMF2 NAT10 NDUFB6 NEK7
RFC3 SOAT1 UGDH VDAC2
C.
microtubule-based process (12) FDR 1.34x10^-6
cytoskeleton organization FDR (13) 1.62x10^-6
proteasome-mediated ubiquitin-dependent protein catabolism (8) FDR 1.62x10^-6

Table 4.3 Genes significantly depleted (<-2-fold, p-value <0.05) by Ub-IP in both WT MIB1-reconstituted cells over MIB1 KO and WT MIB1-reconstituted cells over C985S-reconstituted cells. Table displays log2(FC) and corresponding significance status for each of the listed comparisons (WT/KO, WT/C985S and WT AdV5/uninf) sorted by log2(FC) for WT MIB1-reconstituted over MIB1 KO and shaded in heat map ranging from lowest (blue) to highest (red) log2(FC) value represented.

	log2(FC)			Significance?		
Gene Name	WT/KO	WT/C985S	AdV/uninf	WT/KO	WT/C985S	AdV/uninf
HSPB1	-5.6058	-6.77723	-1.67849	+	+	
CCDC127	-4.59948	-4.23803	-3.24623	+	+	
MLF2	-4.11423	-4.49965	-1.9226	+	+	+
DNAJC7	-3.73521	-4.19429	-1.3904	+	+	
PAWR	-3.66759	-4.11144	-3.13773	+	+	
CAD	-3.63426	-4.43943	-0.364127	+	+	
TUBA4A	-3.58568	-3.6901	-0.737189	+	+	
DHFR	-3.15949	-4.28448	0	+	+	
FAF2	-3.12901	-3.12707	-1.16457	+	+	
AURKB	-2.55925	-2.91538	-0.272946	+	+	
TUBA1C	-2.35361	-3.07623	0.471373	+	+	
BAG2	-2.11175	-2.50782	-0.408145	+	+	
KIF1A	-2.05521	-1.61594	0.827648	+	+	
TPM1	-2.02682	-1.90766	-0.948942	+	+	
TUBB4A	-1.98077	-2.75067	0.551711	+	+	
CLINT1	-1.95862	-1.43912	-0.488649	+	+	
SMC2	-1.80128	-2.49863	-0.846722	+	+	
TUBB	-1.69682	-2.21486	-0.0968596	+	+	
TUBB6	-1.67627	-2.1911	-0.200984	+	+	
POLR2E	-1.66864	-1.70038	-0.0947227	+	+	
TUBB4B	-1.65283	-2.27962	-0.170329	+	+	
MRPL12	-1.65228	-1.48014	0.264768	+	+	
UBQLN2	-1.6053	-1.86171	0.02403	+	+	
VIM	-1.58118	-2.75268	0.324141	+	+	
MAGED1	-1.49146	-1.7496	-1.16542	+	+	+
PSMD6	-1.3348	-1.40506	0.131222	+	+	
FASN	-1.28492	-2.78218	-0.212423	+	+	
PSMD13	-1.28254	-1.45853	0.0142053	+	+	
MYH9	-1.26259	-1.7196	-0.0794048	+	+	
RUVBL2	-1.24596	-1.40501	-0.364129	+	+	
RNF126	-1.24372	-1.10185	0.264431	+	+	
SETD2	-1.22984	-1.64223	-0.117932	+	+	
DNAJA1	-1.20023	-1.98571	-0.0149682	+	+	

PSMD12	-1.17308	-1.5577	0.272655	+	+		
HSPH1	-1.16139	-1.25472	-0.0397949	+	+		
MYL12A	-1.11924	-1.27201	-0.263995	+	+		
PSMA4	-1.11569	-1.28996	0.2324	+	+		
PSMA2	-1.09759	-1.21458	0.877542	+	+		
PSMD11	-1.08772	-1.35973	0.441095	+	+		
PSMC1	-1.07779	-1.04169	0.433369	+	+	+	
MYH10	-1.04429	-1.39066	-0.0397237	+	+		
PEG10	-1.00688	-1.97024	0.301464	+	+		

Identification of AdV5 infection-specific ubiquitination events

Work by Suomalainen et al. demonstrated that even the earliest steps in AdV entry are capable of triggering PTMs in ways that rapidly alter the cellular environment and in some cases enhance infectivity (Suomalainen et al., 2001). Therefore, we were also interested in identifying "infection-dependent" changes in the ubiquitinated proteome by comparing ubiquitinated proteins between AdV5-infected versus uninfected WT MIB1-expressing cells. We reasoned that MIB1-dependent ubiquitinated proteins (presented above) whose ubiquitination was also enriched only upon AdV infection in WT MIB1 cells would represent the most intriguing candidates for follow-up. This cross-comparison yielded a single overlapping gene, STAU2 (one of the classified RNA-binding proteins) (**Figure 4.12B**). However, of this infection-induced set, CHERP, PRSS12 and MAP9 were dramatically enriched (greater than 4-fold although not significant) in both WT/KO and WT/C985S comparisons (gray box, **Figure 4.12B**). Of these, MAP9 associates with the spindle and has been implicated in stabilization of interphase microtubules making it a particularly interesting candidate. Conversely, a number of the MIB1-dependent candidates were notably enriched upon AdV infection despite not making the significance cut-off (ex. FMR1, HNRNPK, NSUN2, SRPK1) **(Table 4.2)**. While inevitably intrigued by candidates with the added distinction of being infection-specific, we also considered the possibility that the MIB1-ubiquitination target relevant to virus infection may be constitutively ubiquitinated by MIB1, the significance of which is only appreciated upon AdV infection. Therefore, the lack of further enrichment upon infection was not a basis for exclusion from downstream study.

We also took note of those proteins depleted by Ub-IP upon infection with AdV5 (**Figure 4.13A,B**) and were struck by the appearance of dynamin 2 (DNM2). DNM2 is a MT-binding protein with well-characterized roles in endocytosis and MT stabilization and has been connected independently in the literature to both AdV genome delivery and MIB1 function (Shpetner & Vallee, 1989; 1992). A recent study of AdV37 in keratocytes showed that siRNA KD of DNM2 enhanced nuclear targeting and AdV genome release by increasing perinuclear accumulation of acetylated tubulin and decreasing the distance between MTOC and nuclear envelope although the mechanism remains unclear (Lee et al., 2019).[38] In addition, there is an existing link in the literature between MIB1 and DNM2, not in regards to MTs in the vicinity of the nuclear envelope, but at the plasma membrane in Notch signaling. Here the ubiquitination activity of MIB1 mediated increased interaction between DNM2 and SNX18 to promote Delta ligand endocytosis. While the direct target of MIB1 ubiquitination in this context remains unknown it was notably not DNM2 itself (Okano et al., 2016). The depletion of DNM2 in the WT MIB1 infected condition by Ub-IP alludes to a shift in DNM2-binding partners triggered by AdV infection. However, whether this is mediated by MIB1 ubiquitination, as in the endocytic pathway, and whether it has implications for AdV delivery to the NPC will be interesting avenues to explore in the future. We speculate that ubiquitin-mediated decoupling of one of our MIB1 Ub-IP-enriched target candidates from DNM2 could perhaps be a requisite step in adenovirus DNA delivery and explain the MIB1-dependent depletion of MT-associated factors observed more broadly in infected cells by both Ub-IP and proximity labeling.

[38] Although the effect on the AdV5 serotype was not tested by Lee in the keratocytes, we subsequently performed siRNA KD of DNM2 in WT MIB1 and KO cells and observed slight enhancement of AdV5 infection in both conditions (although with associated toxicity) preliminarily corroborating their findings (data not shown).

Intersection of proteomic datasets: Ub-IP and proximity labeling

Our Ub-IP dataset had identified a list of protein candidates for the AdV-relevant target of MIB1 ubiquitination. Since proximity to MIB1 would be a necessary prerequisite to direct binding and ubiquitination, we reasoned that cross-comparison of our Ub-IP and proximity labeling proteomic datasets could perhaps corroborate or even serve to narrow our search among these candidates. We had already observed that our two independent proteomic approaches had converged upon similar functional pathways dependent upon MIB1-ubiquitination (although there was little to no overlap in the specific genes deriving these GO categories between datasets). We were therefore curious where the Ub-IP hits fell within our proximity labeling data, both in the broader comparison of WT MIB1 or C985S versus mKate or the more subtle comparison between WT and C985S MIB1. Although not representing direct ubiquitination candidates of MIB1 we also similarly assessed the distribution within the proximity labeling data of the genes depleted in WT MIB1 cells versus KO and C985S by Ub-IP. Somewhat discouragingly, highlighting the Ub-IP hits among the mKATE enrichment comparisons revealed either no enrichment or exclusive deenrichment of potential MIB1-ubiquitinated candidates in the proximity of both WT and C985S MIB1 relative to the mKate construct (**Figure 4.14A)**. The Ub-IP "deenriched" genes showed no correlation when graphed onto the proximity-labeling mKate comparison. However, these observations might reflect the arbitrary nature of the mKate control which, while sufficient to reveal enrichment of overarching structures such as centriollar satellites, may not be a useful comparison for assessing MIB1's relationship with more heterogenous or ubiquitously localized proteins. Overlay of the Ub-IP "enriched" or "deenriched" genes onto the proximity-labeling comparison between WT and C985S MIB1 also showed very little correlation with a few exceptions (**Figure 4.14B)**. FMR1 and SRPK1 appeared among the proteins enriched (although not significantly) in proximity to WT MIB1. The Ub-IP depleted CLINT1 was also strongly deenriched in proximity to the WT MIB1 relative to the C985S mutant. Ultimately, however, intersection of the two proteomic datasets was unable to clarify which among MIB1 target candidates would warrant functional follow-up.

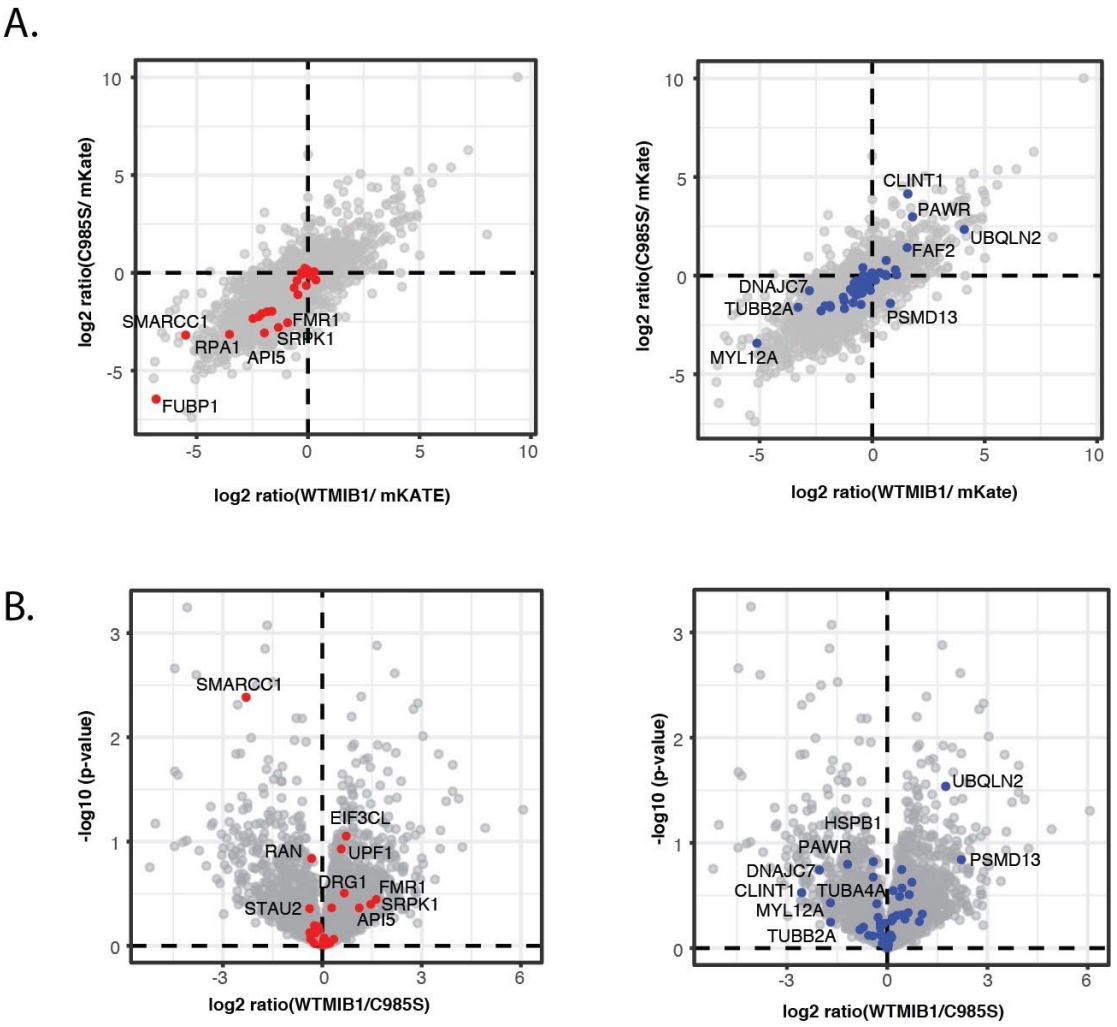

Figure 4.14 Intersection of Ub-IP and proximity labeling proteomic datasets. Proteins enriched (red circles) or depleted (blue circles) by Ub-IP (see **Figure 4.11** and **Figure 4.12**) highlighted among proteins identified in proximity labeling comparisons between (A) WT or C985S MIB1 and mKate (see **Figure 4.6)** plotted as the log2 fold-change of protein abundance between WT MIB1 and mKate (x-axis) and the log2 fold-change of protein abundance between C985S MIB1 and mKate (y-axis) or (B) WT MIB1 compared to C985S MIB1 (see **Figure 4.7A)** plotted as volcano plot of log2 fold-change of protein abundance between WT MIB1 and C985S MIB1 (x-axis) and -log10 of the t-test p-value (y-axis). Select proteins labeled by gene name.

Discussion of Ub-IP Results

In summary, mass spectrometry of ubiquitinated proteins from WT MIB1-reconstituted cells relative to the MIB1 KO and C985S mutant identified specific protein candidates of MIB1-mediated ubiquitination. More broadly, however, it revealed the differential regulation of certain functional pathways in a MIB1-dependent manner upon AdV infection. The reemergence via a spatially-blind method of two inverse functional categories (RNA-binding versus cytoskeletal proteins) exposed one of the unintended benefits of using the TUBE approach for isolation of ubiquitinated proteins. Due to the non-denaturing (and relatively low salt washing conditions

[150 mM NaCl]) required for binding by the TUBE ubiquitin-binding domains, our IP likely also captures many of the binding partners of any directly-bound differentially-ubiquitinated proteins. Indeed, the capture of binding partners/complexes in addition to actual ubiquitinated proteins was explicitly recognized in the initial descriptions of the TUBE technique (Hjerpe et al., 2009). This then provides a glimpse into ubiquitination-dependent changes in physical association of proteins/complexes that can yield mechanistic insight. In the case of MIB1, it appears that ubiquitination of one or more of the candidate genes enriched in WT MIB1 over KO or C985S either enhances association with RNA-binding proteins, promotes disassociation from cytoskeletal components or both. An approach intended to narrow in on proteins and then peptides instead again pointed us towards pathways. The obvious downside of this approach, then, is that it then requires other methods to validate which of the IP'd proteins was the direct ubiquitinated protein of interest rather than merely an associated factor. One powerful cross-validation strategy could be the more stringent IP of directly ubiquitinated proteins using the covalently bound HA-tagged Ub incorporation approach which should isolate only a subset of those MIB1-dependent enriched genes from our TUBE approach.[39] However, narrowing in on the direct MIB1 target from this now abbreviated list could also be accomplished using a functional readout, in our case AdV infection, upon manipulation of these genes. Our employment of this latter approach will be discussed in the upcoming section.

We suspected that MIB1's role in infection might be mediated through the UPS since inhibition of the proteasome with MG132 similarly blocked genome release downstream of the MTOC. One major challenge in identifying targets of E3 ubiquitin ligases is the rapid degradation of those proteins of interest by the proteasome. We therefore, also performed the Ub-IP with samples prepped in the presence of MG132. While intended to boost sensitivity and enrich detection of proteasome-fated targets of MIB1, comparison between WT MIB1 versus KO and C985S upon infection in these conditions, showed almost no significant differential protein enrichment between conditions (data not shown). We suspect that the MG132 treatment, acting globally to block degradation of all ubiquitinated proteins in the cell may have instead drowned out signal coming from MIB1 targets alone—likely low abundance and spatially-restricted events. This dataset was therefore disregarded in our pursuit of potential MIB1-dependent ubiquitination targets.

In the future, we also propose performing mass-spectrometry on collected lysates at 1 hpi for direct proteomic submission *sans* any enrichment strategy. If we hypothesize that MIB1 leads to the degradation of some target protein necessary for DNA release that is aberrantly overstabilized in MIB1 KO cells, then ubiquitinated proteins normally targeted for proteasomal degradation should be enriched in whole cell lysates from MIB1 KO cells relative to WT MIB1-expressing cells. By contrast, no change at the whole cell level might point instead at a non-degradative outcome for ubiquitination, an approach that has been successfully employed by other groups to distinguish between degradative and non-degradative ubiquitination events.

[39] Of note, the Greber group similarly performed Ub-IP using the alternate di-Gly approach to isolate ubiquitinated peptides from either MIB1 KO or WT HeLa cells. We therefore thought that crossing our lists would help to further narrow our candidates. Instead, soberingly, there were only two proteins that overlapped between each of our identified target candidate lists (PURA and H1FX) and testing these two individually by siRNA KD (discussed below) showed no impact on virus infection (personal correspondence).

Chapter V: Functional Evaluation of MIB1-ubiquitination candidates in AdV infection

Impact of siRNA KD of MIB1-ubiquitination candidates on AdV5 infection

Ub-IP using TUBEs allowed us to generate a list of putative MIB1 ubiquitination targets, however, the daunting task of validating these targets and, in particular, isolating the specific target(s) relevant to virus infection remained. To tackle this we returned to the functional read-out of AdV infection. While ubiquitination can have diverse consequences for protein fate ranging from relocalization/signaling to proteasome degradation, our observation that treatment with the proteasome inhibitor similarly blocked AdV DNA delivery led us to favor proteasomal degradation as the likely fate of the MIB1-target affecting AdV infection. Specifically, then, our working hypothesis was that in WT cells, MIB1 mediates the degradation of some target protein, removing its block on AdV genome release. Inversely, in the absence of functional MIB1 (in MIB1 KO or C985S-reconstituted cells), this target protein becomes aberrantly overstabilized and its presence blocks AdV DNA delivery. We reasoned that artificially reducing the expression of the relevant target protein in MIB1 KO cells should serve to rescue AdV infection. To accomplish this experimentally we turned to a siRNA KD screening approach. Our interrogation of candidates was divided into three class of genes based on the nature of their identification by Ub-IP: (1) high-stringency "enriched" (significantly enriched ≥2-fold in the comparison of both WT MIB1/KO and WT MIB1/C985S) (2) low-stringency "enriched" (enriched ≥2-fold in the comparison of both WT MIB1/KO and WT MIB1/C985S but only significant in one or the other) and (3) "de-enriched" (a curated subset of genes significantly depleted ≥2-fold in the comparison of both WT MIB1/KO and WT MIB1/C985S. [40]

MIB1 KO cells and WT MIB1-reconstituted cells were transfected with ONTARGETplus siRNA SMARTpools targeting each of these genes. At 48 hrs after siRNA transfection, cells were infected with replication-competent AdV5-GFP (75 p/cell) and collected at 24 hpi to assess AdV infection (%GFP) (**Figure 5.1)**. In all cases, reduction of infection upon KD of MIB1 (and either CXADR [the receptor] or Nup214 [the nuclear pore docking site for the capsid] were used as positive controls for siRNA transfection efficiency/dynamic range expectations. While varying slightly among the different candidate sets, MIB1 siRNA KD in MIB1 WT cells reduced infection by about 30-50% relative to a non-targeting siRNA control pool (IRR). As anticipated, KD of the majority of Ub-MS candidates displayed minimal to no impact on AdV infection. There were, however, several intriguing exceptions. Given our hypothesis that the block on AdV DNA release in MIB1 KOs was due to the aberrant overstabilization of some target protein, we were looking first for those genes that upon siRNA KD increased AdV infection in MIB1 KO cells. While none of the knocked-down genes came close to rescuing infection in MIB1 KOs to the level of infection in WT-MIB1 expressing cells, KD of HNRNPK showed slight increase in AdV infection in MIB1 KO cells. KD of vimentin (VIM) and RUVBL2 among those genes depleted in WT MIB1-expressing cells by Ub-IP also

[40] Given that the depletion of these genes by Ub-IP in WT MIB1 relative to KO and C985S could be interpreted as a physical decoupling of these proteins mediated by ubiquitination of the true MIB1 target, we hypothesized that siRNA KD could similarly recapitulate the effect of WT MIB1 by mimicking reduction of interaction with this protein.

boosted AdV infection in MIB1 KOs. And yet, in each of those three cases enhanced infection was also observed in WT MIB1-reconstituted cells. Therefore, it is possible and likely that the increase in infection is MIB1-independent. The relatively weak contribution of individual KD of genes to AdV rescue in MIB1 KO cells could also reflect that ubiquitination of multiple targets by MIB1 in combination is necessary for AdV genome delivery. It could also be a consequence of the blunt nature of global reduction of a given protein for a process that might require spatio-temporal regulation of a small subset in the vicinity of the nuclear pore.

While we had set out to identify genes whose KD boosted AdV infection in MIB1 KO cells, we also became intrigued by two genes, STAU2 and YY1, from among the high-stringency candidates enriched by Ub-IP in WT MIB1-expressing cells, whose knockdown had the opposite effect. In fact, STAU2 and YY1 KD decreased infection in MIB1 WT cells to levels comparable to MIB1 siRNA KD and further reduced infection even in MIB1 KO cells (other genes that showed a reduction in AdV infection [EIF3C, RAN, SNRPA1 and XPO1 (aka CRM1)] were visibly toxic to the cells). We hypothesized that these genes might reflect an alternate scenario in which the MIB1 target protein is both necessary for infection but must be subsequently degraded upon spatiotemporal cues in the vicinity of the NPC. Alternatively, these proteins could be ubiquitinated by MIB1 but have non-degradative functions necessary for mediating AdV DNA delivery such as signaling, relocalization or altered binding partners. In either of these cases KD of the gene would inhibit AdV infection. However, in theory, those genes should have emerged from the original haploid screen with MIB1 as requisite factors for AdV infection in WT cells (unless full KO of the gene inhibited cell viability and expansion).

To summarize our siRNA candidate screening, five genes, HNRNPK, VIM and RUVBL2 (which enhanced AdV infection in MIB1 KO cells) and STAU2 and YY1 (which reduced AdV infection in WT MIB1-reconstituted cells) were short-listed for further mechanistic follow-up. Follow-up on two of these factors VIM and STAU2 will be discussed in further detail below. While siRNA KD of our candidates genes presented a tractable strategy for identifying the MIB1-dependent ubiquitination target relevant to AdV infection there are certainly a number of caveats to this approach. First, it assumes that the relevant consequence of MIB1 ubiquitination is proteasomal degradation of the target which may not be the case. In addition, there were several instances in which our proteomics studies captured differential ubiquitination among isoforms of specific proteins. This was observed for HNRNPK and FMR1 (which appeared in multiple distinct entries within our MS data). In this scenario siRNA KD of all isoforms of these genes, insufficient targeting, or differential turnover of the relevant isoforms could mask the more nuanced contribution of individual isoforms to virus infection. Our proximity labeling data had also suggested to us that MIB1 might interact with P-bodies. As sites of RNA decay associated with the RISC complex that mediates siRNA gene-silencing, manipulations of P-body factors to determine their relevance to the MIB1-mediated phenotype in AdV infection might circularly influence KD efficiency itself making individual western blot validation of knock-down efficiency of these genes critical. Similarly, AdV infection may be extremely sensitive to the level of this target protein, meaning that any residual levels of the protein within the vicinity of the pore are sufficient to maintain the block on DNA release. In this case, KD even if efficient, could be insufficient for AdV rescue. It is also a very real possibility that the ubiquitination target of MIB1 relevant to AdV infection was merely not assayed within our limited siRNA screening criteria based on identification by Ub-IP.

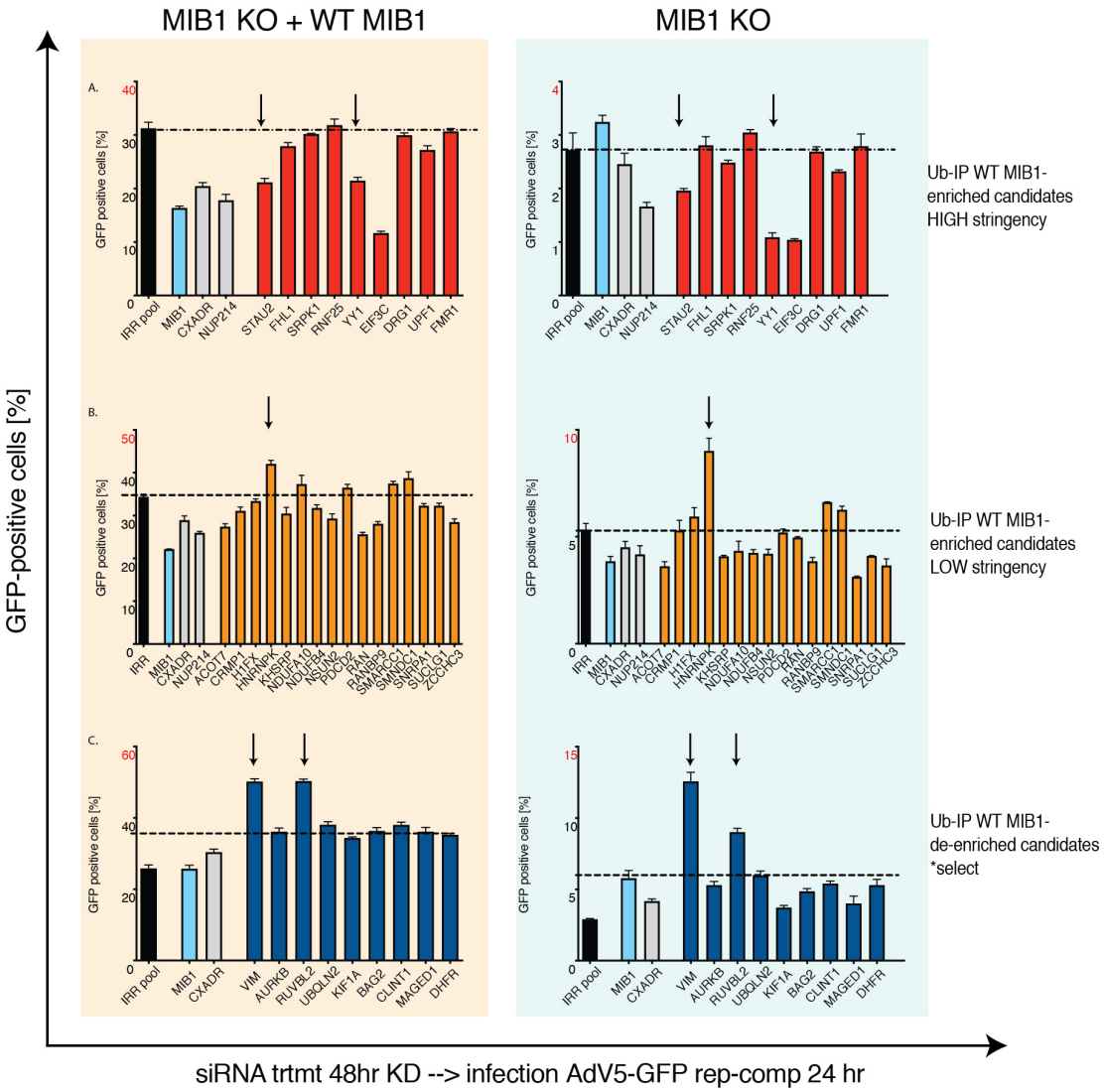

Figure 5.1 Effect of siRNA KD of select MIB1 ubiquitination target candidates on AdV5 infection in MIB1 KO and WT MIB1-reconstituted cells. WT MIB1-reconstituted cells or MIB1 KO cells were transfected with siRNAs targeting three class of genes based on their identification by Ub-IP: (A) high-stringency "enriched" (significantly enriched >=2-fold in the comparison of both WT MIB1/KO and WT MIB1/C985S) (B) low-stringency "enriched" (enriched >2-fold in the comparison of both WT MIB1/KO and WT MIB1/C985S but only significant in one or the other and (C) "de-enriched" (a curated subset of genes significantly deenriched >=2-fold in the comparison of both WT MIB1/KO and WT MIB1/C985S. After 48 hours of siRNA transfection (25 nM) to allow for protein reduction and turnover, cells were infected with replication-competent AdV5-GFP (75 p/cell) and assayed for %GFP-positive cells by flow-cytometry at 24 hpi. Dotted black line denotes level of infection in the irrelevant non-targeting siRNA control pool (or the average level of infection across all tested genes in the case of the de-enriched gene set in which the irrelevant siRNA pool control was oddly low for both KO and WT MIB1-reconstituted cells). Candidate genes whose KD showed moderate impact on AdV infection in either MIB1 KO or WT MIB1-reconstituted cells are noted with black arrows.

Alternative screening approaches for MIB1 target identification

In addition to mechanistic follow-up on several individual genes, we are concurrently preparing another unbiased genome-wide screen to identify the relevant MIB1 target utilizing AdV5 infection as the direct functional read-out. A gain-of-function genome-wide CRISPR KO screen but now in the background of MIB1 KO Hap1 cells will be used to select for those cells capable of supporting AdV infection upon KO of the MIB1 target. This is in contrast to the original Hap1 screen that had identified cells now resistant to infection that could then be expanded within the population. Instead, this strategy will require sorting of GFP-positive AdV5 infected MIB1 KO cells followed by sequencing to identify the disrupted gene. Again this is predicated on the hypothesis that overstabilization of a single MIB1 target inhibits AdV DNA release. It would also still fail to capture the contribution of genes that simultaneously impact cell viability. Nevertheless, given that our proteomic approaches (with the criteria we set for functional follow-up) may not have captured the MIB1 ubiquitination target relevant to AdV infection, this CRISPR screen will be a powerful alternative. It will hone in on not just general MIB1 targets or interactors but the specific ubiquitination target of direct functional relevance to the AdV infection phenotype in an unbiased and genome-wide manner.

Vimentin in AdV5 infection

Background

Vimentin (VIM) was depleted by Ub-IP in WT MIB1-expressing cells over both MIB1 KOs or cells expressing C985S MIB1 making it an unlikely direct target of ubiquitination by MIB1. Nevertheless, KD of VIM by siRNA resulted in a partial rescue of AdV infection in MIB1 KO cells. We therefore hypothesized that dissociation from VIM may be one consequence of MIB1's ubiquitination of the actual target protein and set about characterizing the relationship between vimentin, MIB1 and AdV further.

VIM is a type of intermediate filament, so called because these filaments occupy the structural niche in between the rigid, polarized structures of microtubules and the spindly networks of actin. VIM self-assembles into distinct non-polar rope-like structures which confer unique mechanical properties to cells and nuclei (Danielsson et al., 2018). While intermediate filaments themselves are not believed to act directly as scaffolds for molecular motors, association with microtubules via proteins called plectins allow these dynamic structural components to couple to mechanical forces. They have also been shown to traffic along microtubules via direct interaction with the kinesin-1 heavy chain, (incidentally the same kinesin implicated in adenovirus capsid trafficking) and under certain circumstances undergo rapid relocalization to the cell periphery along MT tracks (Prahlad et al., 1998; Robert et al., 2019).

VIM is most widely-studied in the context of cancer as a structural facilitator of the epithelial-to-mesenchymal transition (EMT) (Danielsson et al., 2018). However, VIM also has a number of reported roles in virus infections. Indeed, many viruses with DNA lifecycles appear to rely upon reorganization of VIM for successful infection (Sripada & Dayaraj, 2010). African Swine Fever virus, for example, replicates in induced VIM cages in the vicinity of the nucleus (Stefanovic et al., 2005). Parvoviruses and human cytomegalovirus (CMV) require VIM reorganization for efficient nuclear targeting (Fay & Panté, 2013; Miller & Hertel, 2009). During entry, the viral protease of HIV actively cleaves VIM into fragments resulting in dramatic alteration of the appearance of the nucleus from smooth and spherical to invaginated (corresponding with changes to chromatin architecture within the nucleus). This alteration is necessary for its infectivity (Sarria et al., 1994; Shoeman et al., 2001).

VIM has even been previously explored in the context of adenoviral entry. Entry by certain AdV serotypes (notably not AdV7) has been shown to trigger the fragmentation of VIM into discrete polypeptides. Furthermore, this fragmentation is a step-wise process exhibiting cleavage from 58 kDa to 56 kDa within the first 5 mins post-entry, with an 18 kDa cleavage product only emerging around 1 hpi (Belin & Boulanger, 1987). The mechanism of this fragmentation (attributed to a host cytoskeletal-associated proteolytic enzyme) and more importantly, the specific relevance of this fragmentation to the virus (beyond decreased virus production upon proteolytic inhibition) was not pursued further. We were intrigued whether this fragmentation could be the result of proteolytic processing by the proteasome. While the structure and activity of vimentin is well-known to be dynamically regulated by the PTM of phosphorylation, the contribution of ubiquitination to VIM regulation is only beginning to emerge. In a recent study of gastric cancer, the DUB USP14 has been shown to regulate VIM levels by deubiquitinating

VIM, while in ovarian cancer cells, vimentin levels are regulated by the ubiquitin ligase TRIM56 (Zhao et al., 2018; Zhu et al., 2017). In skeletal muscle, MTM1 and UBQLN2 guide vimentin to the proteasome to prevent aggregate formation (Gavriilidis et al. 2018). These studies provide precedent for the regulation of this protein by our PTM-of-interest.

VIM is also a defining feature of proteotoxic stress-induced structures called "aggresomes". These aggresomes serve as sites of protein aggregate sequestration and turnover through the clustering of proteasome degradation machinery around the MTOC or centrosome (Garcia-Mata et al., 2002). Vimentin forms a "cage" around this area to limit toxicity and promote rapid degradation of misfolded proteins. Interestingly, RUVBL2, which like VIM, was both depleted upon Ub-IP in WT MIB1 cells over MIB1 KO and C985S and subsequently boosted AdV infection upon siRNA KD, has been shown to localize to the centrosome and also play a key role in aggresome regulation. In a screen to identify factors governing aggresome formation upon treatment with MG132, siRNA KD of RUVBL2 suppressed aggresome formation, resulting instead in the appearance of multiple small cytoplasmic aggregates (Zaarur et al., 2015). While Zaarur et al. focused their mechanistic studies on RUVBL2, they identified in total 164 genes that inhibited aggresome formation upon siRNA KD. Of these, genes involved in RNA-processing constituted the largest functional category (24%) when analyzed by gene ontology classification (followed by cell cycle [13%], ubiquitin-proteasome system [6%], translation [5%] and MT-based processes [4%]). Their list of hits also included HNRNPK, an RNA-binding protein that was enriched by Ub-IP in our WT MIB1-expressing cells relative to the KO and C985S mutant (and thereby a potential direct ubiquitination target of MIB1) and that also increased AdV infection upon siRNA KD. The three hits that enhanced infection even in MIB1 KO cells, VIM, RUVBL2 and HNRNPK, therefore share classification as aggresome modulators. Taken together, these observations motivated our interest in pursuing VIM further—placing it spatially in precisely the region where MIB1 intervenes in virus infection and suggesting an intersection with other candidates and functional categories (RNA-binding proteins) identified through our proteomic approaches.

Influence of MIB1 and AdV5 infection on VIM organization

Given that KD of both VIM and RUVBL2 increased AdV5 infection in MIB1 KO cells we were curious whether they might have a cumulative effective when combined[41]. KD of either VIM or RUVBL2 or both in combination, however, increased virus infection in both MIB1 WT and KO cells to the same degree. This suggests that they might act within the same pathway **(Figure 5.2A)**.

[41] regrettably, we had not yet identified HNRNPK as a candidate and it was not tested for combinatorial effect with VIM and RUVBL2

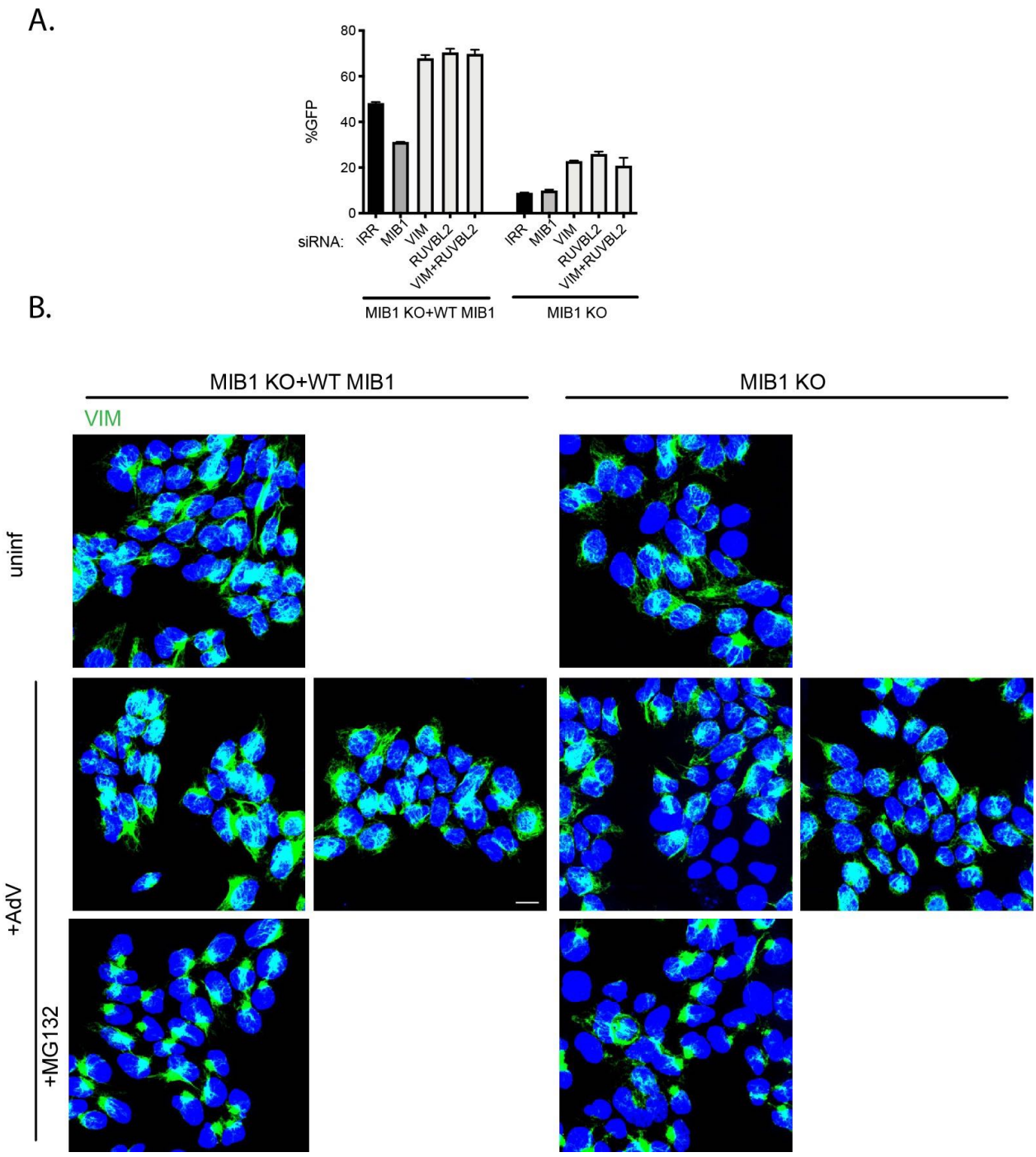

Figure 5.2 MIB1 KO and WT MIB1-reconstituted cells do not form aggresomes in an infection or MIB1- dependent manner. (A) 48 hr siRNA KD of MIB1, VIM, RUVBL2 or VIM and RUVBL2 in combination in either MIB1 KO or WT MIB1-reconstituted cells followed by infection with AdV5-GFP (75 p/cell). At 24 hpi cells were harvested, analyzed by flow cytometry and plotted as the percentage of GFP-positive cells. (B) Representative images (maximum-projected Z-stack) of MIB1 KO and WT MIB1-reconstituted cells infected with AdV5-JR34 (MOI= 2000 p/cell; 1.25 hpi) and stained for VIM (green; anti-VIM (N-term)). Two representative images shown for the AdV5-infected condition only. (Scale bar=10 μm).

Aggresomes had already been implicated in AdV infection but at a later stage when adenoviral protein E4 11K induces gross relocalization of P-body components (Lsm1, Ddx6, Ago2, Xrn1, Ge-1) to these structures and is proposed to facilitate viral late mRNA accumulation by inhibiting P-body-mediated mRNA decay pathways (Greer et al., 2011). However, we were curious whether we might observe formation of this stress-induced structure in cells even at the early stage of AdV infection. Indeed, there is precedent for viral hijacking of aggresome regulatory pathways even early in infection. Specifically, IAV packages Ub chains within its capsids to mimic protein aggregates and couple to HDAC6 (an aggresome regulator) (Banerjee et al., 2014). This coupling relays a shear force that breaks up the capsid and releases the viral genome[42]. In our AdV5-JR34 pVII-DNA release assays, we had observed that treatment with the proteasome inhibitor MG132 drastically inhibited DNA release similar to the absence of MIB1. MG132 is also a known inducer of aggresome formation due to proteotoxic stress resulting from the global inability to degrade ubiquitinated proteins. We hypothesized that aggresome formation (and/or inability to dissolve aggresomes in MIB1 KO cells) might be a shared consequence of both MG132 treatment and a lack of MIB1 that acts to inhibit AdV DNA release. However, staining for VIM in both uninfected and AdV5-infected MIB1 KO and WT MIB1-reconstituted cells did not show the dramatic aggresome formation observed upon MG132 treatment in both cell types **(Figure 5.2B)**. We therefore concluded that neither infection nor the presence or absence of MIB1 yields the stereotyped centrosomal aggregation of VIM into classical "aggresomes". However, infection in both WT MIB1 and KO cells did induce a change in VIM from longer more linear cytoplasmic projections to more compact perinuclear organization **(Figure 5.2B)**.

We were also interested in characterizing the relationship between VIM and the incoming AdV capsids in the vicinity of the MTOC and nucleus. Examining the distribution of individual virus particles relative to VIM fibrils revealed an interesting phenomenon. Capsids at the nuclear envelope appeared to adhere very closely to VIM fibrils, at times localizing to the very tip the VIM stain **(Figure 5.3)**. Interestingly, VIM has been shown to bind lamin B (LMNB) directly via its N-terminal 60 amino acids (presumably *through* the nuclear pore as lamin B lies on the inner face of the nuclear membrane) (Georgatos & Blobel, 1987). We considered then that VIM might act as a guiding path directly to these sites on the nuclear envelope. This would be in line with work from Wang et al. who noted a distinct "microtubule-independent transport machinery" in the immediate vicinity of the membrane. Particle tracking of individual virions between MTOC and NPC displayed slower MT-independent drifting motions that are nevertheless distinct from "random walks" (I.-H. Wang et al., 2017). While instances of AdV capsids along VIM tracks could be observed in both WT MIB1-reconstituted and KO cells, VIM tracks were more defined in MIB1 KO cells (clearly visualized in unmerged VIM channel images) **(Figure 5.3)**. We knew from work by Bauer et al. that in MIB1 KO cells AdV capsids become paralyzed on the NPC, unable to undergo capsid disassembly and genome release (Bauer et al., 2019). The spidery VIM tracks maintained across the surface of the MIB1 KO cells led us to suspect that in MIB1 KOs, VIM might also remain fixed at the NPC. The question remains whether the retention of VIM is cause or consequence of capsid paralysis at the pore. If VIM associates directly with AdV capsids which then attach to Nup214 at the NPC and are unable to be released in MIB1 KO cells, then perhaps this explains the maintenance of these tracks.

[42] the same step abrogated in MIB1 KO cells, although, in the case of IAV, taking place in the cytoplasm commensurate with endosomal release, not directly at the nuclear pore.

Alternatively, independent VIM processing and release from the NPC could perhaps actively contribute to AdV capsid disassembly by exerting mechanical force on the capsids. As mentioned above, AdV5 had been reported to induce stepwise fragmentation of VIM with one fragmentation event enacted at around 1 hpi (Belin & Boulanger, 1987). Of note, we did observe what appeared to be short VIM fragments in the vicinity of the nucleus when probing with a C-terminal but not an N-terminal recognizing antibody to VIM. In rare cases these appeared as very short punctate fragments on the surface of the nucleus but were observed in both WT MIB1 and MIB1 KO cells (visible in overblown images in **Figure 5.4C)**. In the future, we propose examining VIM fragmentation in MIB WT versus KO cells by western blot.

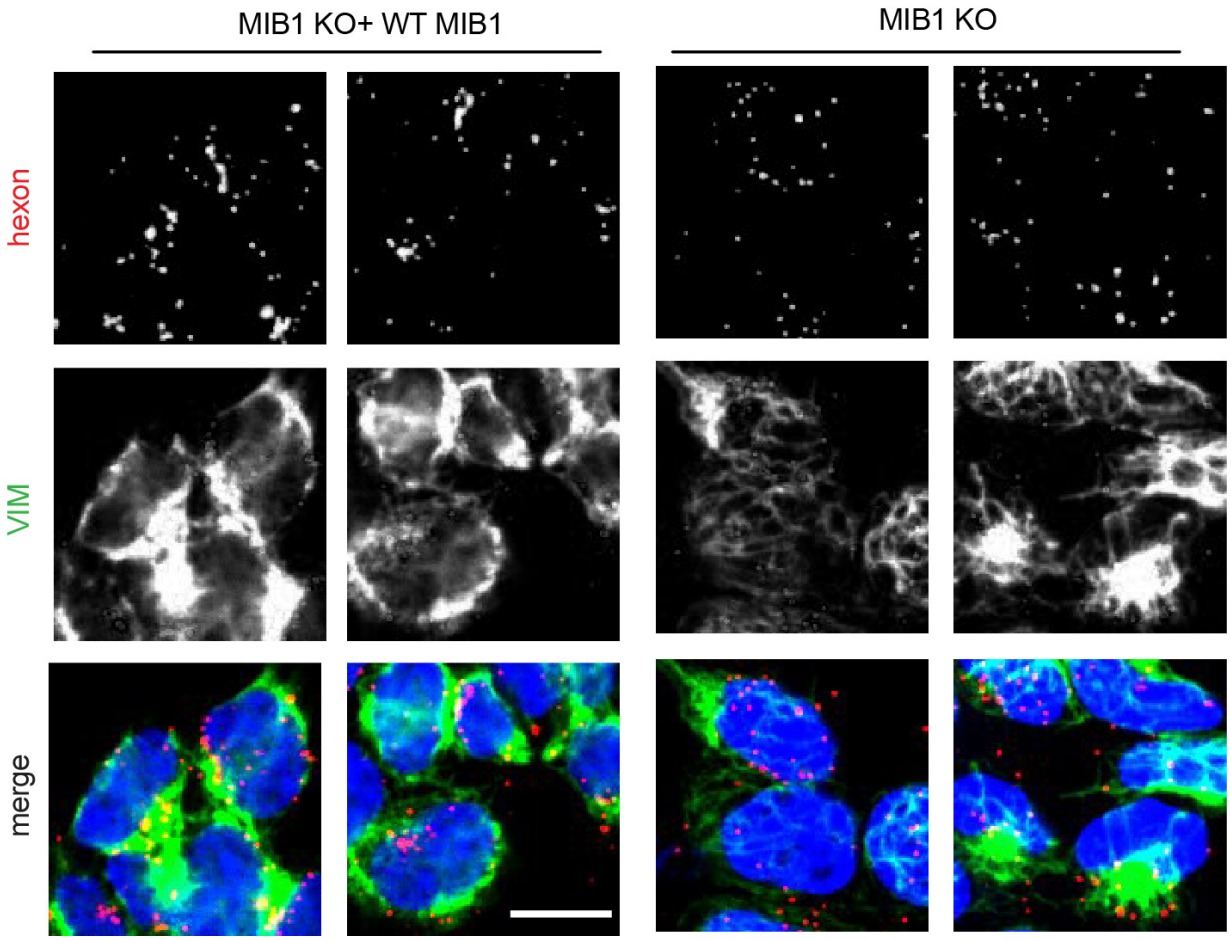

Figure 5.3 AdV5 capsids associate with vimentin "tracks" along nuclear envelope. Representative IF images (single selected Z-plane; 2 per condition) of MIB1 KO and WT MIB1-reconstituted cells infected with AdV5-JR34 (MOI= 2000 p/cell; 1.25 hpi) and stained for VIM (green; anti-VIM [N-terminal]) and AdV capsid (red; anti-hexon) shown as individual channels and merged images. (Scale bar=10 μm)

Generation and characterization of VIM CRISPR KOs

An interest in looking at the contribution of VIM to AdV infectivity was instigated by the observation that VIM was depleted upon Ub-IP in MIB1 WT relative to KO or C985S cells. Subsequent KD of VIM by siRNA increased infection in MIB1 KO cells (albeit in MIB1 WT cells as well). We chose to follow-up by generating CRISPR KOs of VIM in both MIB1 KO and WT MIB1-reconstituted cells using two different sgRNAs targeting two separate sequences within exon 2 (referred to as 77 or 494) (**Figure 5.4A)**. By western blot, clone 494-1 and 494-2 in MIB1 KO cells appeared to be full VIM KOs, while 77-1 and 77-2 showed very low residual levels of the protein. In WT MIB1-reconstituted cells all clones were verified VIM KOs by western blot. We then assessed infection by replication-competent AdV5-GFP in this preliminary set of WT MIB1/VIM KO and MIB1 KO/VIM KO clones (**Figure 5.4B)**. Surprisingly, despite the boost in infection in MIB1 KO cells upon siRNA KD of VIM, the dramatic reduction in VIM level in MIB1 KO clones 77-1 and 77-2 had no impact on infection. Complete VIM KO in clone 494-1 reduced infection further. By contrast VIM KO clone 494-2 restored infection of MIB1 KOs almost to the level of the parental WT MIB1-reconstituted cells. VIM KO in WT MIB1-reconstituted cells boosted AdV5 infection in all cases.

The extreme variability among the MIB1 KO VIM clones was puzzling. However, subsequent IF for VIM in the set of sg494-derived clones revealed that in fact, 494-2 was not a true KO but was dramatically reduced in expression level to a perinuclear population (observable by IF despite being undetectable by Western blot) (**Figure 5.4C)**. This low-level of remaining perinuclear VIM was most parallel to the effect of siRNA KD of VIM in which a population in the immediate vicinity of the nucleus was still observed at 48 hrs after transfection (data not shown)[43]. Sequence analysis of this clone indicated that whereas CRISPR editing resulted in frameshift and stop mutation for 494-1, 494-A and 494-B, clone 494-2 had a 3 nt deletion resulting instead in the in-frame deletion of single amino acid 167D localized to the coil 1B domain of the protein. This single AA deletion may destabilize VIM and/or alter its ability to self-polymerize (as coil 1B is the critical domain for the formation of tetramers) (Chernyatina et al., 2012).

Manipulation of VIM could alter AdV infection at any stage in the lifecycle. We were therefore interested in assessing the impact of VIM KO (or reduction in the case of 494-2) at the level of DNA release to the nucleus as assayed by AdV5-JR34 infection. MIB1 KO VIM "low" clone 494-2 showed a slight increase in pVII particles and yet these particles were found not within the nucleus but in the immediate vicinity in the cytoplasm (**Figure 5.4D)**. A similar strange phenomenon was observed in one of the WT MIB1 clones, 494-A upon VIM KO in which abundant DNA release was observed throughout the cytoplasm in addition to the nucleus. Why or how reduction of VIM would lead to mislocalized cytoplasmic capsid diassembly is unclear. Selection of additional clones will be necessary to confirm if this phenotype is merely a reflection of clonal variability or is a result of this dramatically reduced expression and altered arrangement of VIM in these cells.

[43] Indeed "knot" and "ring" structures of vimentin around the nucleus which form during cell spreading have been shown to have slower turnover than peripheral vimentin—precedent for the existence of distinctly arranged populations of vimentin (Terriac 2019).

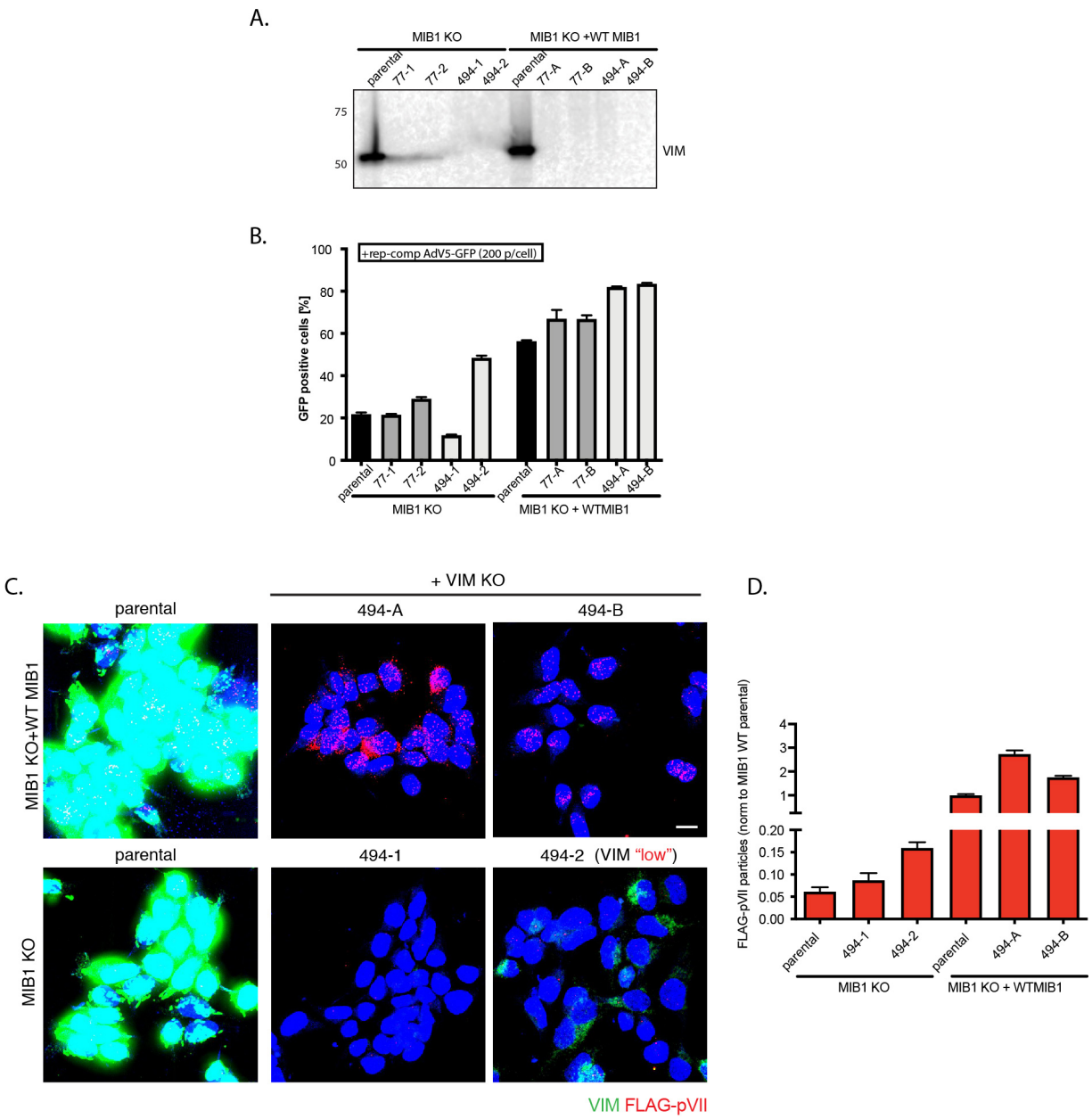

Figure 5.4 Generation and characterization of VIM KOs in MIB1 KO and WT-MIB1 reconstituted cells. (A) Western blot assessing expression of VIM in MIB1 KO or WT-MIB1 reconstituted cells and their respective potential VIM KO clones generated via CRISPR-Cas9 mediated gene disruption with sgRNAs targeting exon 2 at position 77 or 494 respectively. (B) Panel of MIB1 KO, WT MIB1-reconstituted parental and VIM KO clones in (A) infected with rep-competent AdV5-GFP (200 p/cell), harvested at 24 hpi, analyzed by flow cytometry and plotted as the percentage of GFP-positive cells. (C) Representative IF images (merged maximum-projections of Z-stack) of MIB1 KO and WT MIB1-reconstituted cells and their respective 494 VIM KO clones upon infection with AdV5-JR34 (2000 p/cell; 1.25 hpi) stained for vimentin (green; anti-vimentin [C-terminal] and FLAG-pVII (red; anti-FLAG). (D) Quantification of FLAG-pVII particles for MIB1 KO cells, WT MIB1-reconstituted cells and their respective VIM KO clones in (C) averaged across 3 FOV. (Scale bar= 10 µm).

Discussion of VIM results

The role of VIM in AdV entry remains an interesting open question as we certainly observe an intimate link between AdV capsids along VIM "tracks" on the surface of the nucleus. This finding on its own will be an exciting avenue for future research as the source of guided distribution of viral capsids along the nuclear envelope has not been previously described. Live-cell particle tracking in conjunction with fluorescently-labeled VIM and perhaps in larger cells in which distinct subpopulations or VIM reorganization would be more visible will be exciting paths to pursue in the future. If VIM does act as a guide in this vicinity, why its KO would serve to boost infection (suggesting VIM is overall antiviral) is also puzzling. Returning to other factors whose KD by siRNA also enhanced AdV infection, should HNRNPK, RUVBL2 and VIM functionally converge on the same pathway, we propose RUVBL2 or HNRNPK may be more tractable proteins to pursue for their role in AdV infection. Their study may yield indirect insight into VIM perhaps through interaction with only a relevant subset of VIM in the vicinity of the centrosome or nucleus. Differential dynamics of RUVBL2 and HNRNPK may be easier to monitor by IF relative to the dense masses of VIM. It will certainly be interesting to test whether the organization of VIM is changes upon RUVBL2 or HNRNPK depletion or KO.

Whether a role for VIM in AdV infection ultimately intersects substantively with the function of MIB1 at the NPC remains unclear. We therefore suspended experiments along the VIM vein to pursue other potential MIB1 ubiquitination targets and their role in AdV infection.

STAU2 in AdV5 infection

Background and rationale for follow-up

Another candidate from our Ub-IP selected for more extensive mechanistic follow-up was Staufen 2 (STAU2). STAU2 was a fascinating candidate for a number of reasons. First, not only did it emerge from the Ub-IP as significantly enriched by more than 4-fold in WT MIB1-expressing cells over KO and C985S but it was also enriched upon AdV infection in a comparison of WT MIB1 infected and uninfected cells. This made it the sole candidate to be both MIB1-dependent and infection-dependent. Second, while siRNA KD of STAU2 did not rescue infection in MIB1 KO cells, its KD did impact AdV infectivity, reducing infection to nearly the level observed upon MIB1 KD in WT cells (and reducing infection further in MIB1 KO cells) (**Figure 5.5A)**. It thereby fit the profile of a potential target protein that is both necessary for infection but must also undergo subsequent MIB1-mediated degradation or relocalization perhaps upon additional spatial cues. Since the inhibition seen upon siRNA KD of MIB1 could be due to a negative impact at any step in the AdV lifecycle, we were curious what the impact of STAU2 siRNA KD would be specifically at the step of viral DNA release. By our AdV5-JR34 assay, both MIB1 and STAU2 KD showed decreased DNA release relative to IRR siRNA control although not statistically significant and requiring imaging of additional FOV (**Figure 5.5B)**.

Like MIB1, STAU2 is perhaps best-known for its role in neurons where it mediates the trafficking of translationally-repressed RNPs along axonal MTs through its MT-binding domains, a function it shares with its more widely-studied family member STAU1. Nevertheless, STAU1 and STAU2 appear to localize to discrete RNP granules suggesting that

there may be important differences in their regulation and function (Duchaîne et al., 2002). Given the emerging picture from our proteomic datasets of a MIB1-dependent inverse association between ribonucleoproteins (RNPs) and cytoskeleton, STAU2 as an RNA-binding protein with direct MT-binding capability was intriguing, as it could be an ideal adaptor for mediating some sort of switch between these functional groups. We suspect that our Ub-IP using TUBEs captured not only the direct MIB1-ubiquitinated target but also their binding partners. Many of the proteins also enriched by Ub-IP in WT MIB1 vs KO or C985S cells are in fact, reported interactors of STAU2 (identified in rat brain lysate [in purple], in HeLa cells [UPF1 in orange] or in mouse neurons [NXF1 in green]) (**Figure 5.5C)** (Fritzsche et al., 2013; Park et al., 2013; Wang et al., 2015). Furthermore, STAU2 exists in multiple isoforms that show distinct localizations and shuttling dependence on CRM1-mediated export, a pathway also required for proper trafficking of AdV capsids between MTOC and NPC[44] (Miki & Yoneda, 2004).

While our follow-up studies based on the proximity labeling dataset gravitated first towards the exploration of more well-known and ubiquitous RNP species such as stress granules and P-bodies, the recognition of STAU2 as a candidate of particular interest implicates yet another class of RNP, transport granules. STAU1 and STAU2 are even thought to be the formative/nucleating members of these RNP granules due to an abundance of low complexity (LC) regions that favor aggregation. As a result the local concentration of these proteins can have a dramatic impact on granule formation and higher order structures such as fibers or aggregates (Kato et al., 2012). This makes localized post-translational regulation of the level of these proteins by a ubiquitin ligase, such as MIB1, very appealing. In *Drosophila,* STAU2- and FMR1[45]- containing RNPs in neurons have recently been likened to the P-bodies found in in somatic cells. However, other groups suggest that in mammalian neurons STAU2 RNPs and P-bodies coexist as distinct granules that often intimately interact by "docking" to one another (Barbee et al., 2006; Zeitelhofer et al., 2008). In general, STAU2 has been primarily studied in the context of neuronal RNA transport and therefore its role in RNP trafficking along MTs in less-specialized/polarized cell types is unexplored. However, a study in mouse oocytes that localized STAU2 to the MT structure of the meiotic spindle also noted its appearance as a single large puncta on one side of the nucleus in interphase BHK-21 and MEFs, a hallmark of centrosomal/MTOC localization[46], and which would place it in the general vicinity of MIB1's mechanism of action (Cao et al., 2016).

[44] This shuttling activity appears to be a feature somewhat unique to STAU2 relative to STAU1.
[45] Recall FMR1 was one of our "high-stringency" candidates enriched in WT MIB1-expressing cells by Ub-IP.
[46] although they provide co-staining suggesting actual colocalization with the Golgi. While underappreciated by us at the time this will become relevant in our discussion in Chapter 6.

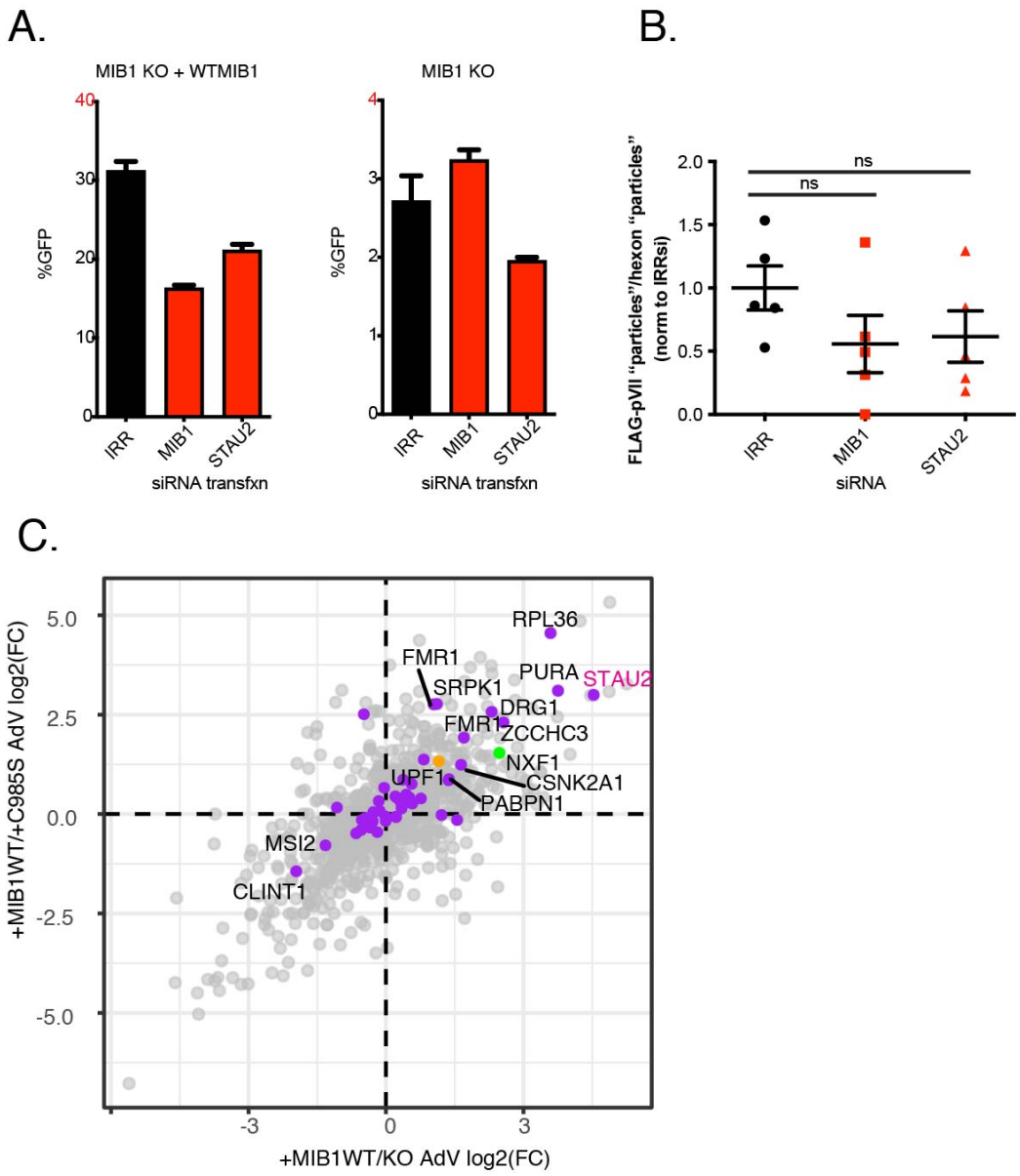

Figure 5.5 Characterizing the role of MIB1-ubiquitination candidate STAU2 in AdV5 infection. (A) 48 hr siRNA KD of MIB1 and STAU2 in either MIB1 KO or WT MIB1-reconstituted cells followed by infection with AdV5-GFP (75 p/cell). At 24 hpi cells were harvested, analyzed by flow cytometry and plotted as the percentage of GFP-positive cells (extracted from **Figure 5.1A)** (B) Quantification of FLAG-pVII "particles" normalized to number of hexon "particles" in WT MIB1-reconstituted cells infected with AdV5-JR34 (2000 p/cell; 1.25 hpi) following 48 h siRNA KD of MIB1 or STAU2 (averaged across 5 FOV). (C) Ub-IP data from **Figure 4.12A** replotted as the log2 fold-change of protein abundance between WT-MIB1 reconstituted cells and MIB1 KO cells (x-axis) and the log2 fold-change of protein abundance between WT MIB1-reconstituted cells and C985S-reconstituted cells (y-axis) with colored dots (and selected gene names) marking direct interactors of STAU2 compiled from Fritzsche et al. (purple), Park et al. (orange) and Wang et al. (green).

Influence of MIB1 and AdV5 infection on STAU2 organization

We were therefore eager to determine the localization pattern of STAU2 in our Hap1 cells particularly upon AdV infection. We were further curious whether the appearance of STAU2 would differ between infected MIB1 KO and WT MIB1-reconstituted cells. Staining these cells for STAU2[47], the protein did appear to localize to the vicinity of the centrosome as marked by proximity to dense foci of centriollar satellites (anti-PCM-1, the close proximal partner of MIB-1) in each cell (**Figure 5.6A)**. However, STAU2 also displayed strong nuclear staining in line with its reported function in assembling nuclear export-competent RNPs, but which obscured our analyses of the centrosome-associated population (Kiebler et al., 2005; Monshausen et al., 2004). To remove these confounding foci given our interest in the cytoplasmic STAU2 around the centrosome, we processed the 3D images to deplete all STAU2 signal from regions falling within our segmented nuclear stain. This exclusive look at cytoplasmic STAU2 allowed us to more clearly decipher differences in STAU2 organization around the centrosome in MIB1 KO and WT MIB1-reconstituted cells (**Figure 5.6B)**. We concluded that while in WT MIB1-expressing cells, STAU2 appears in thinner filaments adjacent/projecting off of the centrosome, in MIB1 KO cells the distribution of STAU2 was much more globular, encompassing the centrosome while still appearing to adhere to some sort of filamentous structure. While this difference was observed for both uninfected and AdV-infected cells this filamentous appearance in MIB1 KOs seemed to be exacerbated by AdV infection.

Our proteomic datasets had revealed an inverse MIB1-mediated relationship between RNPs and MTs. Given that STAU2 possesses MT-binding domains we were interested in visualizing this RNA-binding protein in conjunction with MTs. We chose to begin by looking at acetylated tubulin as this is the more stable population localized to the vicinity of the centrosome and constitutes the dynamic curved MTs along the surface of the nucleus[48]. STAU2 closely associated with acetylated tubulin in both WT MIB1-reconstituted and KO cells **(Fig 5.6C)**. However, again its appearance differed between these conditions. In WT-MIB1 reconstituted cells, STAU2 was distributed in discrete puncta or finer filaments along the acetylated tubulin whereas in MIB1 KO cells it was more globular and thicker in appearance even when still adhering to thin acetylated tubulin tracks. In WT MIB1-reconstituted cells STAU2 staining could be widely observed along the edge of the nucleus. While there were certainly instances of this organization in MIB1 KO cells, projections of acetylated tubulin and STAU2 away from the nuclear envelope were also widely observed. A more dense and globular STAU2 distribution in MIB1 KOs and a more fine (and at times even punctate) distribution of STAU2 along MTs in WT MIB1-reconstituted cells corroborated our observations in **Fig 5.6B** and suggest that MIB1 plays a role in the subcellular organization of STAU2. Here again, treatment with 1-6 hexanediol will be useful to determine whether this difference in appearance is reflective of a shift in the organization of STAU2 from granules to fibers as has been observed for FUS which exist as granules dissolvable by hexanediol but which can also aggregate into filaments then refractory to this treatment (Kroschwald et al. 2017).

[47] using an antibody targeting the central region that should capture all isoforms. Perhaps future experiments could test different antibodies capable of delineating between different isoforms.
[48] and more recently in Ad35 infection (Lee 2019)

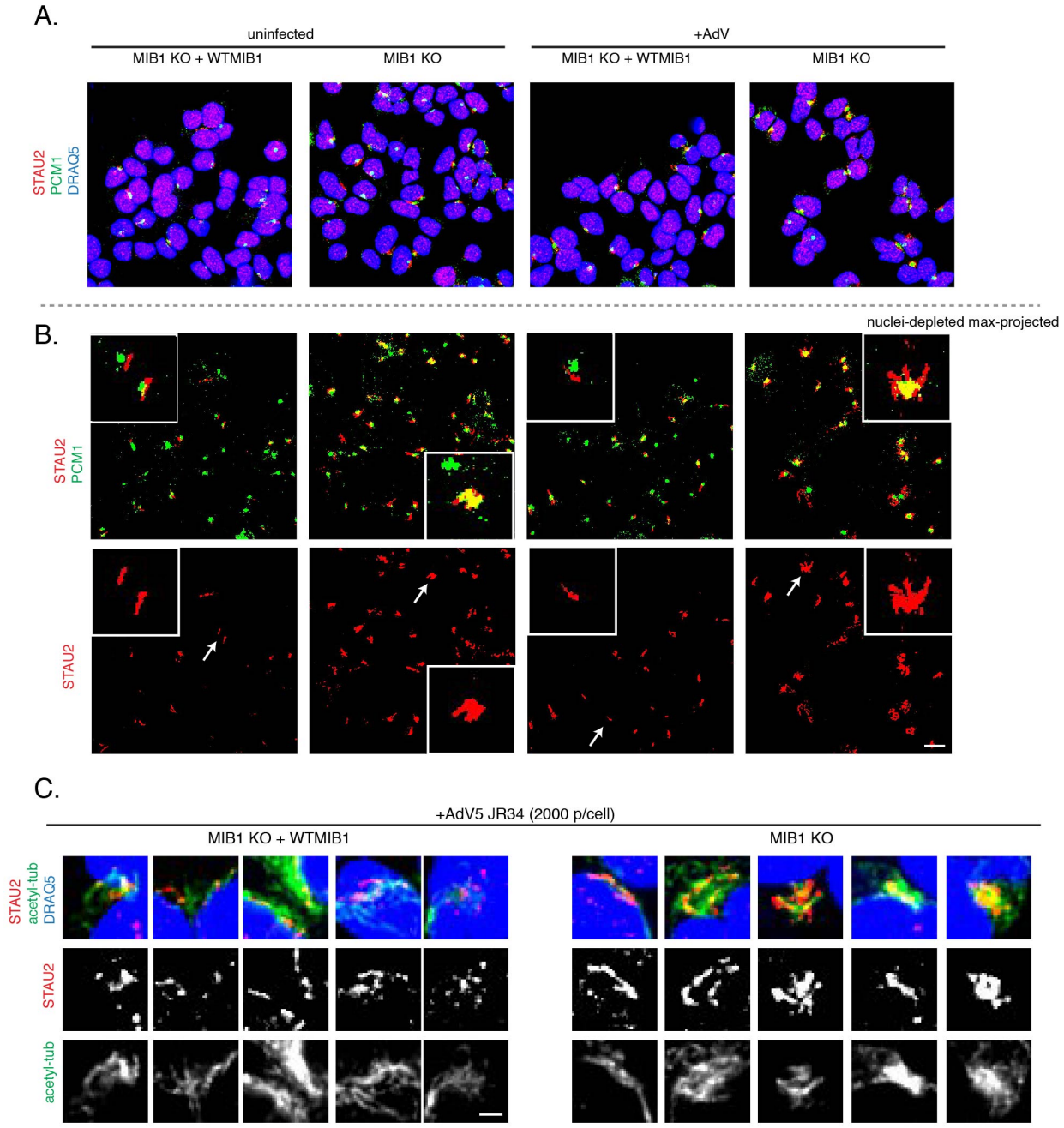

Figure 5.6 Differential STAU2 organization in MIB1 KO and WT MIB1-reconstituted cells and association with acetylated MTs. (A) Representative merged IF images of ±AdV5-JR34 (2000 p/cell) MIB1 KO and WT MIB1-reconstituted cells stained for STAU2 (red; anti-STAU2), centriollar satellites (green; anti-PCM1). (B) Images from (A) showing exclusively cytoplasmic STAU2 and PCM1 staining (thresholded and binarized) after processing to exclude signal from region encompassed by nuclear stain followed by maximum-projection of Z-stacks. (Scale bar= 10 µm). (C) IF images (5/condition) ±AdV5-JR34 (2000 p/cell) MIB1 KO and WT MIB1-reconstituted cells stained for STAU2 (red; anti-STAU2), acetylated MTs (green; anti-acetylated alpha-tubulin) displayed as merged and individual channels (single Z-plane). (Scale bar = 2 µm).

While we endeavored to generate STAU2 KOs in the background of either our MIB1 KO and WT MIB1-reconstituted cells, the inability to recover KO clones following even short term passaging suggested a growth defect for STAU2 KOs that then become overtaken by WT cells. Indeed, no reported STAU2 KOs can be found in existing literature. While making it a challenge to assess the contribution of STAU2 to MIB1's effect on AdV infection, this did help explain to us why STAU2 might not have emerged from our original Hap1 gene-trap screen despite its inhibitory effect on AdV infection upon KD. Instead, complete KO of STAU2 results in a growth defect that would cause these clones to be depleted from the population prior to infection and/or sequencing. In lieu of a STAU2 KO, we propose generating stable cell lines of MIB1 KO and WT MIB1-reconstituted cells expressing different isoforms of fluorescently-tagged STAU2 to both monitor their distribution relative to incoming AdV5 capsids and to probe the effect of their overexpression on AdV infectivity. Our immediate next steps will focus on validating the enrichment of STAU2 by Ub-IP in order to assess whether STAU2 is itself a direct ubiquitination target of MIB1 (accounting for its altered appearance in MIB1 KO cells) and if so to characterize the site of ubiquitination and type of linkage.

Chapter VI: Discussion

We have presented here our current body of work examining the role of MIB1 in AdV infection. We identified MIB1, an E3 ubiquitin ligase, as a host factor for AdV infection using a genome-wide gene-trap screen. Using microscopy, we narrowed MIB1's impact on virus infection to the poorly understood window between capsid arrival at the MTOC and disassembly and DNA release at the nuclear pore. In the absence of MIB1, capsids successfully arrive at the MTOC but fail to ultimately release their DNA into the nucleus. As an E3 ubiquitin ligase, MIB1 acts by ubiquitinating specific substrates resulting in either their degradation or altered signaling/localization. Using a series of point mutants we determined that virus infection indeed depends upon MIB1's ubiquitination activity. The observation that proteasome inhibition similarly blocked vDNA release to the nucleus downstream of MTOC arrival, led us to suspect that ubiquitination by MIB1 acts through degradation of a specific target by the proteasome rather than through other downstream and linkage-dependent consequences of this PTM. However, other consequences for the MIB1-mediated ubiquitinated protein such as relocalization or alteration of binding partners remain a possibility. The majority of our subsequent efforts have been towards the identification of that target which would provide a satisfying "ending" to our investigations and lay the next mechanistic stepping stone in understanding how MIB1 mediates AdV DNA delivery.

Our work had placed the block on AdV infection in MIB1 KO cells after arrival at the MTOC but before DNA release into the nucleus. However, beautiful work by Bauer et al (in a manuscript alluded to throughout this thesis that similarly identified and characterized MIB1 as a host factor for AdV infection) narrowed the action of MIB1 further, showing that in MIB1 KO cells capsids go so far as to dock at the NPC and yet the DNA is never released. Using live-cell particle tracking, they observed instances of transient overlap of GFP-tagged MIB1 with fluorescently-labeled AdV5 capsids at the nuclear rim suggesting that MIB1 carries out the relevant ubiquitination directly at that site (Bauer et al, 2019). Their proposed "hit-and-run" mechanism illuminated for us the nature of MIB1's interaction with the capsid but also made even clearer the unique challenge of identifying the ubiquitin target of MIB1 required for vDNA release. Capturing such a potentially fleeting and spatiotemporally controlled ubiquitination event may be a formidable challenge and difficult to recapitulate experimentally using more globally disruptive methods of KD or KO of the relevant target gene. The critical ubiquitination event may occur on only a small subset of the target and only a subset of the incoming viral capsid population within a very tight and dynamic window of virus trafficking. By choosing a timepoint (either for proteomics or IF) at which we already see appreciable DNA delivery we may have missed the relevant event. At last aware of each others efforts and in collaboration as an international team dedicated to uncovering the mystery of MIB1 and AdV, any mechanistic leads from our own lab will now be greatly benefited by turning to the Greber lab's expertise in live-cell imaging and AdV entry more generally.

While the specific target of MIB1 ubiquitination relevant to AdV infection has so far eluded both of our groups, we feel confident that our unbiased proteomic approaches have at the very least guided us towards a deeper exploration of certain functional pathways of potential relevance. Specifically, they revealed an intriguing balance between RNPs and cytoskeleton that may be altered upon KO of MIB1. A nuanced comparison of the proximal proteomes of WT

MIB1 relative to the mutant C985S generated during infection, revealed that while a broad association with centriollar satellites is conserved between both constructs, WT MIB1 shows greater enrichment in proximity to a number of well-characterized RNA-binding proteins while the C985S mutant displayed enhanced association with structural/cytoskeletal components. This observation was then independently corroborated upon isolation of ubiquitinated proteins in WT MIB1-expressing and KO or C985S-expressing cells during AdV5 infection in which dramatic enrichment of RNA-binding proteins and depletion of cytoskeletal factors was again dependent on the ubiquitination capacity of MIB1.

A MIB1-mediated balance between RNPs and filamentous structures has now been independently corroborated in the literature as well. Specifically, MIB1 has been recently connected to the organization of peri-"nuclear" RNPs in the somewhat obscure context of spermatogenesis in *Caenorhabditis elegans (C. elegans)*. While almost all eukaryotic cells (by definition) compartmentalize nucleus and cytoplasm via a membraneous nuclear envelope, *C. elegans* spermatids lack this nuclear envelope. Instead they possess a dense "perinuclear halo" composed of RNA and RNA-binding proteins that creates a parallel physical delineation between cytosol and chromatin that encompasses the centrosome as well **(Figure 6.1A)**. While it has been reported since 1981 that certain fertilization-defective (*fer*) mutants displayed loss/disruption of this halo, only in the past few years has sequencing narrowed this phenotype to nonsense mutations in *mib-1* (*fer-2*/*fer-4*) and *eri-3* (*fer-3*) (Herrera & Starr, 2018; Ward, Argon, & Nelson, 1981). In *mib-1* mutants not only does this perinuclear RNA halo disappear, but large tubules are observed in its place **(Figure 6.1B)**. Furthermore, the *mib-1* mutant spermatids are reported to contain an overabundance of tubulin at times forming a wreath around the nucleus (Gent et al., 2009; Ratliff et al., 2018). This too aligned with our own impression that MIB1 KO cells displayed denser tubulin networks. Taken together, these observations allude to some conserved role for MIB1[49] in regulating the balance of RNPs and cytoskeletal structures specifically at the boundary between cytoplasm and nucleus. This independent role for MIB1 localized to precisely the interface implicated in our observed block on virus infection in MIB1 KO cells at the NPC.

[49] C. *elegans mib1* is 765 AA and is homologous to the C-terminal region of human MIB1 possessing the ankyrin repeat and two C-terminal RING finger domains but lacking the N-terminal MZM substrate recognition domain (Mib/Herc2 and ZZ zinc finger) (Ratliff et al. 2018).

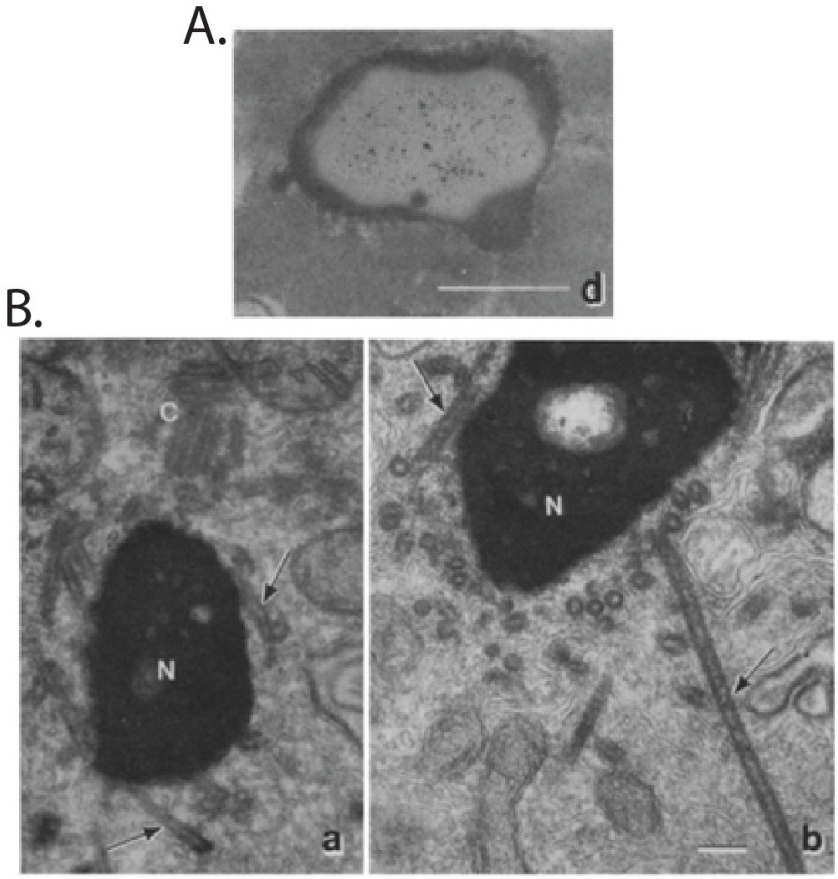

Figure 6.1. MIB1 mutants in C. *elegans* are characterized by loss of perinuclear RNA halo and appearance of aberrant tubules. Transmission electron microscopy (TEM) images of (A) nucleus of WT spermatid stained for RNA show characteristic perinuclear halo surrounding nucleus and centriole. Scale bar=0.5 μm. (B) nucleus and surrounding cytoplasm of fer-2 and fer-4 mutant spermatozoa with nonsense mutations in mib-1 display large tubules (arrows) in perinuclear region, C=centriole, N=nucleus. Scale bar = 0.1 μm. Images obtained from Ward et al. 1981.

We hypothesized that a better understanding of the composition of both the RNA halo and the perinuclear tubules in the *C. elegans* spermatids could yield insight into MIB1's action in our mammalian cells upon AdV infection. What might their counterparts be in our mammalian Hap1 cells? And ultimately, how might this intersect with AdV entry? As mentioned above, the RNA halo disruption and tubule formation upon *mib-1* mutation was also observed in *eri-3* mutants but also for a number of other endogenous RNAi mutants including Argonauts ALG-3 and -4 (Conine et al., 2010). The phenotypic similarities between these mutants suggest that MIB1 and eri-3 may lie within the same functional pathway and imply that one of these endo-RNAi proteins could be a target of MIB1. The intersection of nematode RNAi components and MIB1 reaffirmed to us that P-bodies, as parallel mammalian sites of RNA sequestration and decay made up of miRNA-processing and RISC components, are likely linked to the consequences of MIB1 ubiquitination. Proximity labeling by our group and others suggested an association of WT MIB1 and P-bodies. Subsequent IF examination of P-bodies during AdV infection revealed a phenomenon parallel to a MIB1-dependent RNA halo in which WT MIB1-expressing cells

retained a more perinuclear distribution of P-bodies at 1 hpi while P-bodies were mislocalized to the cytoplasm in MIB1 KO or C985S MIB1-expressing cells. However, the precise composition of the relevant RNP requires further investigation. While we began by focusing on P-bodies, we are also increasingly interested in closely-related STAU2/FMR1 transport RNPs, since STAU2 also shows interesting differences in organization between MIB1 WT and KO cells. While we have yet to perform co-staining of STAU2 and P-bodies, their organization does appear distinct, with STAU2 localizing in close association with acetylated tubulin near the centrosome and nucleus while P-bodies remain more widely dispersed both at the nucleus and in the cytoplasm.

Alongside these musings into the particular identity of a MIB1-interacting or MIB1-regulated RNP, we wondered what an RNP generally might have to do with AdV DNA delivery. RNPs had in fact already been implicated in the interaction between capsids and the NPC. Using *in vitro* assays examining factors necessary for AdV genome delivery, rabbit reticulocyte lysates (RRL) were found to inhibit capsid binding to nuclear envelopes via competition with hexon for the NPC binding site. This could be rescued by treatment with RNase (Trotman et al., 2001). Trotman et al. subsequently isolated this inhibitory RNP and noted that it contained a discrete set of proteins whose identities were not determined. We are curious as to whether any of the RNP granule-associated proteins we identified in our proteomic studies might overlap with components of this mystery inhibitory RNP. In this scenario, MIB1 might mediate a regulated reorganization or local enrichment of this RNP at the nuclear envelope that assists in releasing AdV capsids from the nuclear pore by outcompeting the Nup214-hexon interaction. Such a mechanism would still be compatible with the observations by Trotman et al in which direct addition of this RNP from a spatially-disrupted *in vitro* lysate would preclude the binding in the first place.

We were particularly interested in defining a role for RNPs in AdV infection that could speak to the corresponding depletion of cytoskeletal components by Ub-IP in WT MIB1-expressing cells observed in our proteomics data. Interestingly, beyond spermatogenesis, in *C. elegans*, germline RNPs called P granules (200-400 nm structures comprised of many of the endo-RNAi proteins whose mutagenesis phenocopies *mib-1* mutation) have been shown to dock directly on clusters of nuclear pores[50] while at times observed encasing microtubules **(Fig 6.2 A,B)** (Pitt, Schisa, & Priess, 2000). Upon oocyte formation[51], however, the P granules are detached from the nuclear envelope, transported to the periphery and dispersed into smaller cytoplasmic particles still in complex with nuclear pore components **(Fig 6.2 C)**. This process draws a striking parallel to the observations of Strunze et al. in which capsid disassembly and genome release is proposed to depend on a shear force generated by kinesin-mediated relocalization of AdV hexons to the periphery where they are found still in complex with Nup358, Nup214 and Nup62 (Strunze et al., 2011). Although the granules described here are unique to the germline in *C. elegans*[52], we speculate Trotman's RNP or another cytoplasmic RNP exists within

[50] these P granules, by physically blocking the entrance to NPCs, have even been proposed to serve an antiviral function in *C Elegans* by protecting the germline against nuclear import of virus-like particles (VLPs) derived from endogenous retroelements (Dennis et al., 2012).
[51] A mib1 mutant oogenesis phenotype has not been described.
[52] Although parallel to "polar granules" of Drosophila germline that include Staufen protein (unclear if 1 or 2) to coordinate trafficking of specific mRNAs to the polarized periphery and which become associated with nuclei after formation of the pole cells (Mahowald, 1971).

mammalian somatic cells and recapitulates some of the dynamics of these P granules (and associated nuclear pore components) either constitutively or upon specific stimuli such as virus infection. Again, mammalian P-bodies are an attractive candidate RNP. P-bodies are known to migrate along MTs and can be found in association with the centrosome. Furthermore, studies monitoring the dynamics of P-bodies through live-cell particle tracking have observed a phenomenon in which P-bodies arriving at the surface of the nuclear membrane are rapidly redirected away again (Aizer et al., 2008). Such dynamics imply a MT track switch triggered upon arrival at the surface of the nucleus again reminiscent of the one proposed by Strunze et al. for AdV capsids.

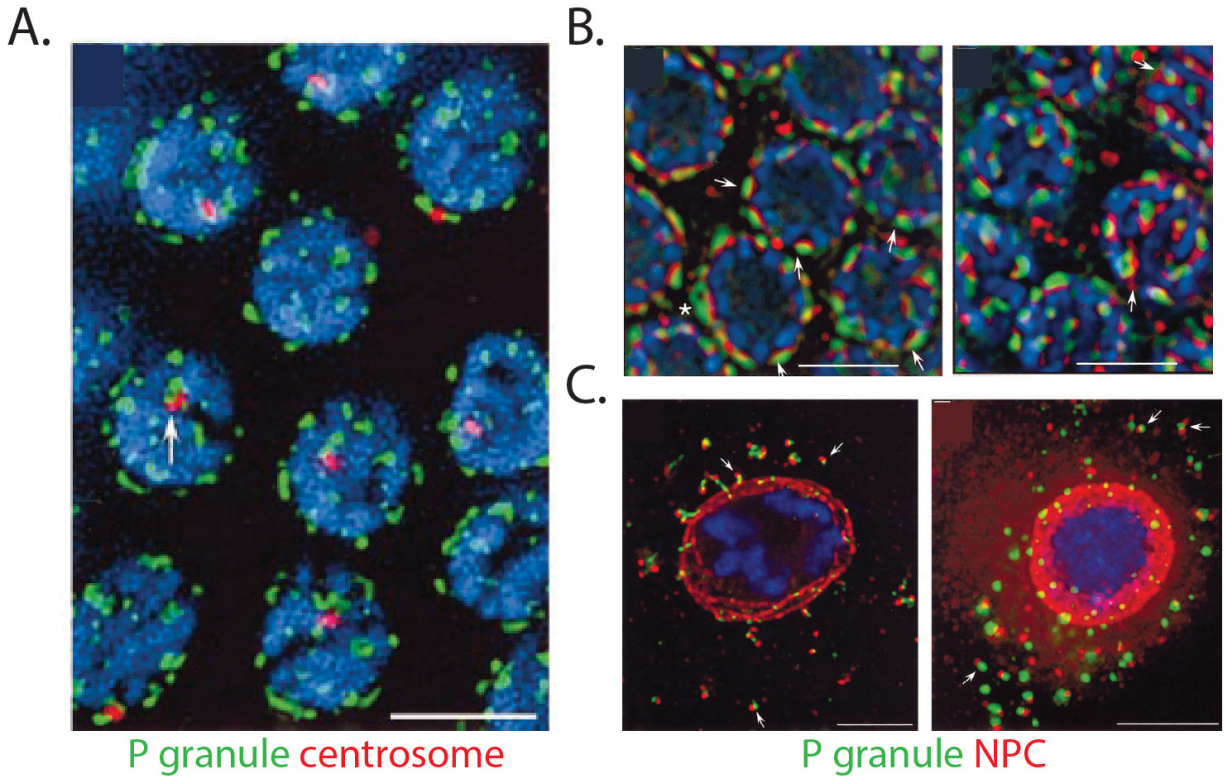

Figure 6.2. *C. elegans* germline RNPs — P granules— dock directly at nuclear pores prior to cytoplasmic displacement in association with NPC components. Confocal imaging *of germ nuclei*: (A) P granules (green) appear to dock at the nucleus and also associate closely with centrosome (red) adjacent to nucleus. Scale bar=5 µm. (B) *Germ nuclei*: P granules (green) associate with nuclear envelope specifically at NPCs (red) (*left*: cross-section through middle of nucleus, *right*: cross-section at surface of nucleus). Scale bar=2.5 µm. *of single oocyte*: (C) P granules (green) disperse within the cytoplasm still in association with NPC components (red). Left: *single oocyte*, right: *germ line blastomere P2* from four-cell stage embryo. Scale bar=5 µm. All images obtained from (Pitt et al., 2000).

The mediator of this MT track transition for P-bodies (which might serve to regulate trafficking of other RNPs as well) is unknown. However, my observations led me to wonder whether MIB1 might regulate this spatially-regulated track switch for P-bodies and also AdV capsids. The potential source of nuclear rim MTs is not directly addressed in Strunze's study despite the implied existence of a discrete population of MTs extending from the NPC to the

periphery and likely independent of either the radial population of MTs initiating from the centrosome or curved acetylated tubulin perinuclear tracks[53]. A better understanding of this track switch including the specifics of which molecular motors are involved may also yield insight into the role MIB1 is playing at this interface. A recent study by Zhou et al. used siRNA KD to analyze the contribution of individual kinesins to AdV infection but their readout was altered centrosomal targeting which lies upstream of capsid arrival at the NPC (J. Zhou et al., 2018). It will be interesting to reapply their screening and imaging approaches to instead assay which kinesins *decreased* capsid aggregation as a result of their distribution and then arrest at individual nuclear pores as we observe in MIB1 KO cells. This could uncover a more compex picture with additional motor proteins required for the final trafficking away from the nucleus (although proposed by Strunze et al to be facilitated by kinesin-1, specifically Kif5C). We remain intrigued by what the possible contribution of perinuclear MTs might be despite the relatively mild impact of pharmacological MT-manipulation on AdV genome release in our Hap1 cells.

While the composition of the 48 nm tubules observed upon *mib1* mutation in *C. elegans* spermatids have not been defined further, we used this early observation as a way to guide our own thinking about MIB1's role in the vicinity of the nucleus. We had observed striking enrichment of MT proteins in the *absence* of MIB1 upon Ub-IP. The term "perinuclear tubules" immediately brought to mind rigid and filamentous structures of the MT cytoskeleton. And yet *C. elegans* MTs are normally about 20 nm in diameter and mammalian MTs are 25 nm. In contrast, 50 nm tubules have been observed upon polymerization of clathrin by monomeric clathrin adaptor proteins (F. Zhang et al., 2007). These clathrin tubules have been observed *in vivo* as projections off of the trans-golgi network (TGN) made up of GGA1, clathrin and AP1 (Puertollano & Bonifacino, 2004). Interestingly, Gheiratmand et al had explicitly noted that even among centriollar satellite components, MIB1 showed a unique association with the AP-2 adaptor complex, the parallel clathrin-associated complex at the plasma membrane (Gheiratmand et al., 2019). While we did not detect the same AP-2 complex components in our proximity labeling data, the Golgi subcompartment did emerge as significantly enriched in proximity to both WT and C985S MIB1. In fact, now alerted to the Golgi in trying to understand the puzzling tubule phenotype in *C. elegans*, we are more deeply aware of the many intersections between this membraneous compartment and our own observations. This even extended to the initial haploid genetic screen in which we observed a number of Golgi vesicle trafficking factors STX18 and NSF as well as more general vesicular transport factors VPS33A, CHMPB, EXOC4 and RAB8B among weaker hits necessary for AdV5 infection.

Textbooks tend to depict the Golgi in cartoon form as a series of stacks lying beyond the endoplasmic reticulum (ER) mediating the orderly trafficking of secreted proteins from ER to plasma membrane. However, in vertebrates, the Golgi is in fact quite close to the nucleus in intimate association with the centrosome in a more lateral structure called the "Golgi ribbon" whose arrangement is governed by MTs (Corthésy-Theulaz et al., 1992). The association between Golgi and centrosome is maintained by centrosomal MTs while lateral associations between Golgi tubules and fragments are maintained by MTs nucleated off the Golgi itself (Rios,

[53] Although these could curve away from the nucleus to create – to + end tracks beginning at the pore, they are not tracks that then extend to the periphery that would be able to carry out long range transport away from the nucleus that has been observed by Strunze et al.

2014). Indeed in many cell types the Golgi is a dominant site of MT nucleation in addition to the centrosome. In RPE-1 cells, for example, nearly 50% of the MTs emanate from the TGN with the vast majority extending away from the nucleus (Efimov et al., 2007). This led us to speculate whether the Golgi, both as an alternate site of MT nucleation and as an organelle whose dynamics are governed by MTs, is important for particle trafficking from nucleus to the periphery.[54] Nucleation of MTs from the cis-Golgi requires AKAP9 as well as CDK5RAP2 (Rios, 2014; Shen et al., 2017). AKAP9 (alternately known as Centrosome and Golgi-localized PKN-associated protein) was notably enriched in proximity to both WT and C985S MIB1 and upon functional mapping of this shared proximal gene-set, acted as a link between clusters of genes reflecting either centrosome/cytoskeleton- and Golgi-associated factors. CDK5RAP2 was identified as enriched in proximity to WT MIB1 relative to mKate, which was noted previously in discussing its contribution to non-centrosomal MT nucleation (but at the NPC) in yeast. Another factor that localizes to the Golgi and regulates non-centrosomal MT nucleation, HSPB1, was a protein we had identified as extremely depleted (>30-fold [**Table 4.4**]) in WT MIB1-expressing cells relative to both MIB1 KO cells and C985S-expressing cells upon Ub-IP (Almeida-Souza et al., 2013). Regulation of acentrosomal MT nucleation also intersects with CRM1-mediated nuclear export since CRM1 regulates export of a component of DNA polymerase that acts to inhibit MT nucleation at the Golgi (Shen et al. 2017, Shen et al. 2019).

The protein CLINT1 also localizes to the Golgi and is involved in TGN regulation, binding to both the clathrin and AP1 that make up the 50 nm projections off of the TGN (Kalthoff et al., 2002; Mills et al., 2003). CLINT1 had emerged from our data in several different contexts yet always enriched in the *absence* of functional MIB1. Like HSPB1, CLINT1 was significantly depleted upon Ub-IP in WT MIB1-expressing cells relative to C985S and KO cells. It was also dramatically enriched (albeit with p-value >0.05) in proximity to the C985S MIB1 mutant relative to WT MIB1 while enriched in proximity to both WT and C985S MIB1 overall relative to the cytoplasmic mKATE control.

CLINT1 is also known as Epsin R and is a distant relative of EPS15, a validated MIB1 ubiquitination target at the plasma membrane (Dho et al., 2019). Interestingly, CLINT1 lacks the Ub-interacting motif that results in monoubiquitination of other epsins such as epsin 1-3 (Mills et al., 2003). While KD of CLINT1 by siRNA had no impact on AdV infection in our follow-up validations, CLINT1 *is* a reported interaction partner of one of our strongest MIB1 ubiquitination candidates, STAU2, which upon KD reduced AdV infection in WT and MIB1 KO cells. Comparing the organization of STAU2 between WT MIB1 and MIB1 KO cells by IF revealed distinct differences with WT MIB1 displaying finer or more punctate STAU2 stain while MIB1 KO staining displayed thicker filaments. In retrospect, the thicker filamentous STAU2 morphology observed in conjunction with acetylated MTs in AdV-infected MIB1 KO cells aligns closely with the pericentrosomal description and morphology of the Golgi which is also known to preferentially associate with this acetylated MT population (Thyberg & Moskalewski, 1993). Previous studies examining STAU2 organization in interphase cells had noted the colocalization with Golgi markers that had at the time been interpreted by us merely as "centrosomal" (Cao et al., 2016).

[54] Interestingly, there are also reports of Golgi linked in long tubules to vimentin intermediate filaments. Perhaps this would be one means by which Golgi could be guided to extend to NPCs directly (Y. Gao & Sztul, 2001).

Ward et al. had hypothesized that the since the tubules observed in the *mib1* mutant *C. elegans* replace the perinuclear RNA halo they might therefore be "aberrant polymerized forms of ribonucleoprotein particles". We similarly propose that in MIB1 WT cells, STAU2, either through careful maintenance of local abundance by ubiquitination and turnover, or through altered interaction partners via MIB1-mediated ubiquitination of STAU2 (or another protein), is maintained within discrete RNPs for trafficking along MTs in the vicinity of the nucleus. In contrast, in MIB1 KO cells, STAU2 RNPs are aberrantly oligomerized along the templated surface of Golgi tubules surrounding the centrosome and even along tubules extending to NPCs (via direct/indirect interaction with CLINT1 and/or MTs directly). This sequestration/immobilization of STAU2 RNPs might then prevent them from accessing and/or performing some function at the NPC that helps liberate AdV capsids either by competitively displacing them from the pore, or assisting their coupling to MTs for trafficking to the periphery. We favor the latter. Specifically, we hypothesize that Golgi-unloaded STAU2 RNPs bind to P-bodies[55], and sequester them at the nuclear rim to make periphery-directed trafficking pathways available to viral capsids **(Fig 6.3)**. Restricting P-bodies from binding kinesin motors could facilitate accumulation of these motors at the pore at a concentration necessary to compensate for the weaker binding interactions to viral capsids. Indeed, both particle-tracking and biochemical work on AdV capsids suggests that virus particles would need relatively high concentrations of motors for association with MTs as the direct binding to AdV particles is rather weak ((Bremner et al., 2009; Gazzola et al., 2009; I.-H. Wang et al., 2017). And yet strong association is imperative given that at the nuclear pore these motors are hypothesized to provide a shear stress or force capable of dismantling the capsid for genome release ((Strunze et al., 2011). Alternatively, accumulation of P-bodies at the nuclear rim may facilitate capsid relocalization to the periphery by assisting in detachment of their bound nuclear pore components (Nup214, CRM1) which are then carried away from the nucleus along with the capsid. This might reduce the force required for kinesin alone to disrupt the capsid and/or detach these components.

Determining whether this altered appearance of STAU2 in MIB1 KO cells reflects differential association of STAU2 with the Golgi or broader reorganizations to the structure of the Golgi itself will be the subject of our immediate next investigations. A thorough characterization of RNP distribution, MT and TGN morphology in WT and MIB1 KO cell lines by IF and even electron microscopy are clear future directions. It is our hope that these studies will point to the mechanism by which MIB1 mediates AdV genome release in parallel with continued efforts to identify the direct ubiquitination target.

[55] High frequency "docking" between STAU2 and P-bodies has been previously described in hippocampal neurons (Zeitelhofer et al., 2008).

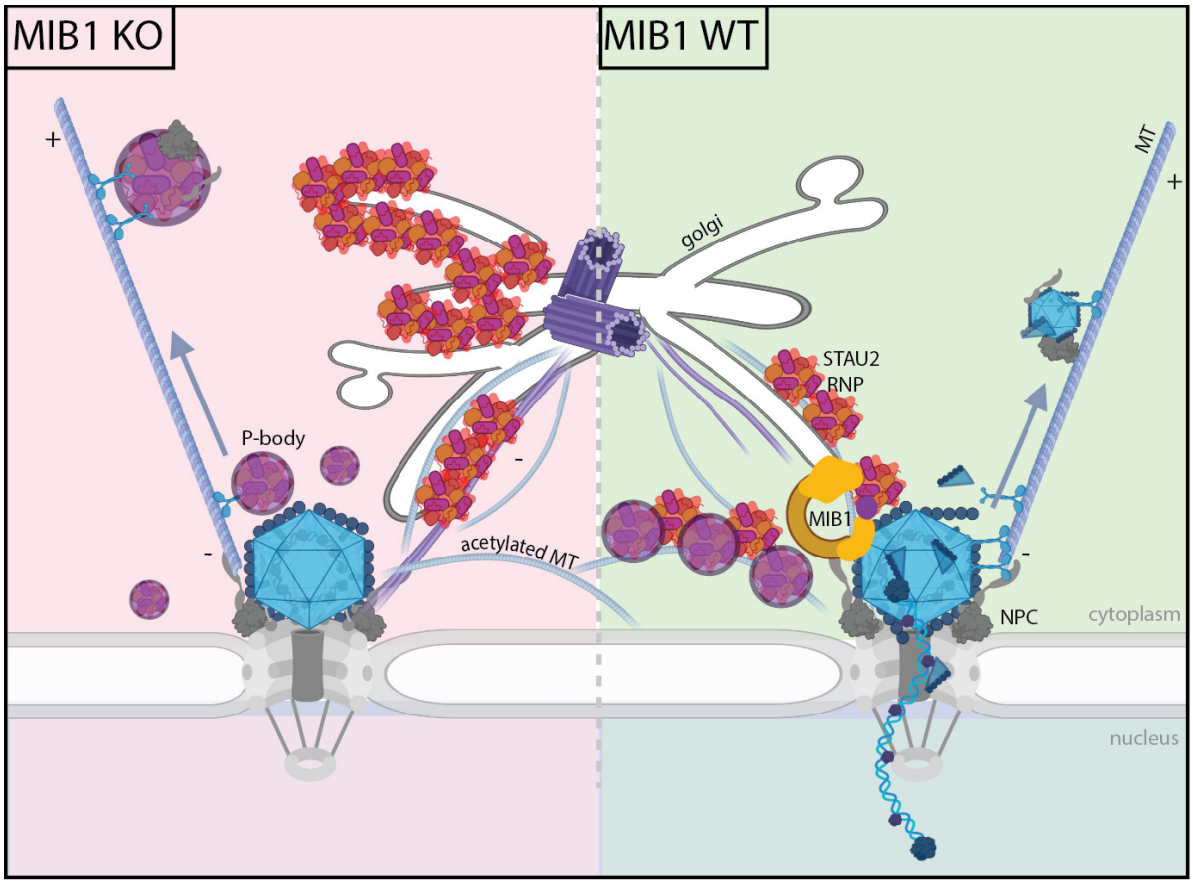

Fig 6.3 Proposed model for MIB1-mediated AdV genome delivery at NPC. In WT cells upon AdV infection, STAU2-containing RNPs traffic along Golgi/acetylated MT tracks towards the nucleus where MIB1 ubiquitination results in their regulated turnover and/or release and association with P-bodies at the nuclear rim. The interaction with STAU2 sequesters P-bodies from association with MT motor kinesin. Instead, the accumulating kinesin motors are readily available to bind the AdV capsid for trafficking to the periphery, generating a shear force that disrupts the capsid and allows for successful genome release into the nucleus. Vimentin tracks (purple) are released simultaneously. By contrast in MIB1 KO cells, lack of MIB1 results in overaccumulation/aggregation of STAU2-RNPs on Golgi/acetylated tubulin MTs which prevents their association with and sequestration of P-bodies. Untethered P-bodies then outcompete AdV capsids for kinesin motors for trafficking to the periphery where they accumulate in large granules, further depleting the motors available for AdV capsid trafficking and stranding the capsid at the NPC (image generated using biorender.com).

Conclusion

My efforts to understand the role of an E3 ubiquitin ligase, MIB1, in this very specific context of AdV infection have led me on a far-ranging expedition into basic and complex cell biology—from MTs to P-bodies, from intermediate filaments to Golgi ribbons and from centriollar satellites to RNPs. The window between the centrosome and the NPC emerges as a fascinating region in which many of these diverse cellular players meet. Our work exposes MIB1 as a dynamic actor within this region and serves as a model for how virus infections can illuminate fundamental processes within our own cells. Like an adenovirus particle docking at the nuclear pore our work has really only just begun. However, having navigated the early unknowns, we are poised at the brink, ready to enter the next realm in which our store of knowledge may be released and applied.

Chapter VII: Materials and Methods

Cell Culture

Hap1 (human; sex:male, chronic myeloid leukemia-derived) cells obtained from Thijn Brummelkamp (Netherlands Cancer Institute) and cultured in Iscove's Modified Dulbecco's Medium (IMDM, Gibco) supplemented to contain 10% fetal bovine serum (FBS) and 1% non-essential amino acids (NEAA). A549 (human; sex: male, lung epithelial), HeLa (human; sex: female, cervical epithelial), Vero (African green monkey; sex: female), Huh7.5-NTCP (human; sex:male), HepG2-NTCP (human; sex:male, liver hepatocellular carcinoma), HEK293 (human; sex:female), derivative Lenti-X 293T (human; sex: female) cells and derivative GP2-293 (which stably express MLV Gag-Pol) (Clontech) and STAT1-/- fibroblasts (human, immortalized by SV40 large T antigen) were all maintained in Dulbecco's Modified Eagle Medium (DMEM, Gibco) supplemented to contain 10% FBS and 1% NEAA. Huh7.5 and HepG2 NTCP-expressing derivatives were generated in the lab as previously described in Michailidis et al. 2017. HepG2-NTCP cells were cultured on collagen-coated plates. STAT1-/- hFibs were kindly provided by Jean-Laurent Casanova (Rockefeller University).

Hap1 cells were utilized for the haploid gene-trap screen as well as for follow-up validation and mechanistic studies into MIB1. A549, HeLa, STAT1-/- hFIBs, Huh7.5-NTCP and HepG2-NTCP were similarly used for follow-up MIB1 phenotype validation and alternate virus testing (specifically HBV for the latter two cell lines). 293 cells were used to produce replication-incompetent adenovirus, Vero cells were used to produce HSV US11-GFP, Lenti-X 293T cells were used to produce lentiviruses and GP2-293 cells were used to generate MLV particles.

All cells were grown at 37°C in a humidified incubator with a 5% CO2 atmosphere.

Haploid Genetic Screen

Gene trap virus was produced as previously described in 293T cells by transfection of gene trap plasmid combined with pAdvantage, CMV-VSVG and Gag-pol (Jae et al., 2013). The virus was harvested twice daily for 3 days and concentrated using ultracentrifugation for 2 h at 64000 x g in a Beckman SW28 rotor. To generate the mutagenized library, $1x10^8$ Hap1 cells were infected for 3 consecutive days in the presence of protamine sulfate (8 mg/ml) and passaged for 5 days prior to freezing. For the screen itself, a library of $1x10^8$ mutagenized cells was infected with replication-competent AdV5-GFP at a MOI $1x10^3$ virus particles/cell. The resistant colonies were expanded for 15 days and ~$1x10^7$ cells were used for genomic DNA isolation.

Sequence Analysis of Gene Trap Insertion Sites

Gene-trap insertion sites in AdV5-positive cells were identified by sequencing the genomic DNA flanking the gene trap insertion site as previously described (Blomen et al., 2015). Genomic DNA was subjected to a linear amplification PCR using a biotinylated primer followed by single-stranded DNA linker ligation, PCR and subsequent sequencing using the HiSeq 2000 platform (Illumina). The acquired reads were mapped to the human genome (hg19) using the Bowtie alignment tool allowing for a single mismatch, and insertion sites located in Refseq

genes were identified. For each Refseq gene, the longest transcript was chosen and overlapping gene regions in opposite orientations were disregarded, since orientation bias cannot be unambiguously assigned in these areas. The number of disruptive mutations (i.e. in sense with transcriptional orientation) and non-disruptive (i.e. in antisense with transcriptional orientation) mutations per individual gene was counted and genes significantly enriched for disruptive mutations following AdV5 infection were determined using a binomial test and corrected for multiple testing using a Benjamini-Hochberg false discovery rate (FDR). Significantly enriched genes with over 40 integrations in the AdV dataset were compared to a reference dataset of WT Hap1 cells (NCBI SRA accession no: SRP058962 dataset SRX1045464) that was analyzed similarly. Genes that were already significantly enriched in the WT dataset were subtracted from the identified AdV host factor genes.

Plasmid generation: MIB1 expression vector and point/domain mutant cloning

The MIB1 sequence was PCR-amplified off of p3HA-hMIB1 plasmid (gift from Vanessa Redecke (Addgene plasmid #33317; http;//n2t.net/addgene: 3331; RRID:Addgene_33317)) (Stempin et al., 2011) and sub cloned into the pDONR Gateway vector (ThermoFisher). The MIB1 ORF was then transferred via Gateway cloning into the lentiviral PLX304 backbone subsequently used for lentivirus production. MIB1 point mutants were generated using site-directed mutagenesis of the WTMIB1 construct with Phusion High-Fidelity PCR Master Mix (ThermoFisher). The plasmid was then digested with DpnI to remove template plasmid input and PCR-purified using the Qiaquick PCR Purification Kit (Qiagen). Domain mutants were generated via amplification of WT MIB1 sequence with primer-mediated incorporation off a 3xFLAG (MDYKDHDGDYKDHDIDYKDDDDK) tag sequence at the 5' end to permit detection by western blot.

All cloning was performed in DH5alpha competent cells. MIB1-sequence containing constructs specifically were grown at 30°C due to toxicity of this sequence when grown at 37°C. In addition, ligation rather than Gibson based cloning was used when possible due to the high GC content of MIB1 that made Gibson ligation highly inefficient.

Lentivirus Production and Transduction

Lentiviral stocks were generated in Lenti-X 293T (Clontech) cells by co-transfection of plasmids expressing (1) the ORF or sgRNA of interest (2), HIV gag-pol, and (3) the vesicular stomatitis virus glycoprotein (VSV-G) in a ratio of 0.55:0.35:0.1. For blasticidin-selectable lentiviral vectors, we used the pLX304 lentiviral backbone in which the V5 tag was removed, and for puromycin-selectable lentiviral vectors, we used the lentiCRISPRv2 lentiviral backbone (gift from Feng Zheng). Cells were transfected using Lipofectamine 2000 (Invitrogen) and media was replaced with DMEM supplemented to contain 3% FBS at 6 h post-transfection. Supernatants were collected at 24 and 48 h, clarified by centrifugation at 2,850 *x g*, filtered using 0.45-micron syringe filters and stored at -80°C. For lentiviral transduction, cells were seeded into 6-well plates at a density of $4x10^5$ cells/well and transduced with lentiviral pseudoparticles by spinoculation at 930 *x g* for 60 min at 37°C in medium containing 3% FBS, 20mM HEPES, and 4 mg/ml polybrene. Transduced cells were selected at 24 h post-transduction with either 2.5 mg/ml blasticidin or 1 mg/ml puromycin.

Generation and validation of CRISPR KOs

Small guide RNAs (sgRNA) for CRISPR editing targeting *MIB1* (sgRNA #1: 5'-CCGGAATAACCGGGTGATGG-3' and sgRNA #2: 5'-CACTTCCCGGTGTAGTAATT-3' targeting exon 1 and exon 2 respectively), *VIM* (sgRNA #1: 5'-CGTAGTCACGTAGCTCCGGC-3', sgRNA #2: 5'-CTCGACGCGGGCTTTGTCGT-3' both targeting exon 2), and *STAU2* (sgRNA#1: 5'-CCCTTGGCCATATTCTGGTC-3', sgRNA #2: 5'-ATCACAAATTCTCGACGTCG-3' both targeting exon 7) were designed using crispor.tefor.net (Haeussler et al., 2016) and cloned into pX330 or lentiCRISPRv2 plasmid for subsequent transfection. MIB1 CRISPR KOs in Hap1 cells were generated by transfection with the relevant guides in pX330 and cultured for four days prior to single-cell seeding into 96-well plates. MIB1 KOs in all other cell lines (in HeLa, A549, STAT1-/-hFibs, HepG2-NTCP and Huh7.5-NTCP cells) were generated by transducing with lentiviruses generated from lentiCRISPRv2 containing the relevant guides and selected for 3 days with puromycin (1ug/ml). Transduced cells were then seeded into a 96-well plate at a dilution of 0.7 cells/well to obtain single-cell clonal populations. In the case of VIM and STAU2 KOs, lentiCRISPRv2 containing the relevant guide was not transduced but transfected using XtremeGene9 at a ratio of 3 µl of XtremeGene9 to 1 ug DNA. At 24 hours post-transfection, puromycin was added to transfected cells at 2ug/ml for two days for rapid selection. Cells from this population were then seeded into a 96 well plate at a dilution of 0.7 cells/well to obtain single-cell clonal populations.

Clones were expanded and screened by western blot analysis. Genomic DNA extraction was extracted using the Qiagen DNeasy Blood and Tissue Kit (Qiagen) and used as a template for amplification of an approximately 800-1000 bp region flanking the PAM site and size-separated on a 1% agarose gel. Discrete bands were gel-extracted, cloned into pCR4-TOPO vector using the TOPO TA Cloning Kit (Invitrogen 45-0030) and Sanger sequenced. Relative proliferation of WT and verified KO clones were measured after 4 days by using CellTiter-Glo Assay Kit (Promega) according to manufacturer's instructions.

Virus stock production and infections

Virus stock preparation

Adenoviruses

Replication-incompetent adenovirus 5 also known as Ad5CiG (for CMV-driven **C**AT-**I**RES-**G**FP reporter) was kindly provided by Erik Falck-Pedersen at Weill Cornell. Stocks were prepared as previously described (Schoggins & Falck-Pedersen, 2006). Briefly, virus was produced via large scale infection of 293 cells (which complement the lack of E1A and B in the replication-incompetent virus) at low MOI (~500 p/cell). At 48-72 hours post infection (upon observation of CPE), cells and supernatant were collected, lysed in 5% DOC with DNase and centrifuged at 1500 xg to remove cell-debris followed by two rounds of CsCl banding and dialysis against 4% sucrose–50 mM Tris (pH 8.0)–2 mM MgCl2, and stored at −80°C. Viral particle numbers were quantified by spectrophotometric detection of intact virions according to the optical density at 260 nm (OD260) (1012 particles [p]/OD260 unit). WT AdV2, AdV7, AdV35, Ad5CiG-F7 (AdV7 fiber) and Ad5CiG-F35 (AdV35 fiber) viruses were also kind gifts from Erik Falck-Pedersen at Weill Cornell (Schoggins et al., 2003). Replication-competent wild-type human AdV5 (in which the E4-ORF3 ORF has been replaced by EGFP) was generously

provided by Patrick Hearing at Stony Brook University. The protein pVII FLAG-tagged JR34 adenovirus (E1/E3 deleted) provided by Erik Falck-Pedersen at Weill Cornell was a generous gift from Dr. Robin J. Parks (A. C. Smith et al., 2009).

Other viruses

The generation of viral stocks for additional viruses tested has been previously described: hPIV3-GFP (L. Zhang et al., 2005) (based on strain JS), BUNV-GFP (X. Shi, van Mierlo, French, & Elliott, 2010) (based on rBUN-del7GFP), YFV-Venus(C. T. Jones et al., 2010) (derived from YF17D-5′C25Venus2AUbi), VEEV-GFP (Petrakova et al., 2005) (derived from pTC83-GFP infectious clone), HSV1 US11-GFP (Benboudjema, Mulvey, Gao, Pimplikar, & Mohr, 2003) (generously provided by Ian Mohr, New York University), VSV-GFP (Dalton & Rose, 2001) (generously provided by John Rose, Yale), LCMV-GFP (generously provided by J.C. De la Torre, Scripps Research) and influenza A/WSN/33 (generously provided by Peter Palese, Mount Sinai). ZIKV (PRVABC59 obtained from the CDC, Ft. Collins) was amplified in Hap1 cells and titered by plaque assay on Huh-7.5 cells. Briefly, the HBV stock was prepared from the supernatant of HepDE19 cells (Cai et al., 2016) by culturing in tetracycline-free medium for 7 days to induce HBV replication. Supernatant containing the virus was collected every other day for two weeks and the virus was concentrated via centrifugation using Centricon Plus-70 centrifugal filter devices (Millipore-Sigma) and the titer (HBV genomes/ml) was determined via Taqman-based qPCR as described (Michailidis et al., 2017).
Lenti-GFP and Lenti-FLuc were generated in lentiX-293 cells as described. MLV-FLuc was prepared in GP2-293 cells as described. Coxsackievirus CVB3-GFP (Feuer, Mena, Pagarigan, Slifka, & Whitton, 2002) (derived from infectious clone pMKS1-GFP) was amplified in HeLa cells and titrated by TCID50.

Virus infections

Adenoviruses

Replication-competent and replication-incompetent AdV5-GFP infections as well as all other GFP-reporter virus infections and quantification were performed using the doses and timepoints reported in the figure legends for quantification by flow cytometry. For the infections, cells were seeded at a density of $2.5x10^4$-$5x10^4$ cells/well in 24-well plates. The next day, cells were washed 1x with Opti-MEM (Gibco) and adsorbed with 200 µl of virus inoculum prepared in Opti-MEM at 37°C. After 1.5 h, inoculum was removed, cells were washed with Opti-MEM, fresh media was added and cells were incubated at 37°C. At the final timepoint dependent on speed of each viral lifecycle, cells were lifted with Accumax cell dissociation medium (eBioscience) and fixed with 4% para-formaldehyde (PFA). Cells were pelleted at 930 *x g* for 5 min at 4°C, resuspended in cold phosphate-buffered saline (PBS) containing 3% FBS and stored at 4°C until analysis using a LSRII flow cytometer (BD Biosciences). FlowJo software (Treestar) was used to obtain the percentage of GFP-expressing cells and their mean fluorescent intensity (MFI). For non-GFP reporter viruses, cells were washed 1x in 2%FBS/PBS, permeabilized in 1xBD perm (BD Biosciences 554723) for 1 h at room temperature (RT) followed by overnight incubation with anti-NP antibody. Cells were then washed an additional 3x with BD perm, incubated with secondary antibody goat anti-mouse AF488 for 1 h at RT in aluminum foil, washed 3x with BD perm, once with 2%FBS/PBS and transferred to FACS tubes for flow-cytometry as for reporter viruses. Alternatively for luciferase-based infection read-out in the case of lenti-FLuc and MLV-FLuc, cells were washed with PBS and lysed in passive lysis buffer (Promega E1941) and processed according to manufacturer's instructions fr Dual-Glo

Luciferase Assay System (Promega).

For infection with AdV5 JR34 virus for imaging of FLAG-pVII DNA release, cells were seeded at 200,000 cells per well onto a glass coverslip pretreated with poly-lysine in 24-well plates. The next day, cells were washed one time with cold Opti-MEM, wash was replaced with 200 µl Opti-MEM and placed on ice for 10 mins to cool before spiking in 50 µl of JR34 virus at the indicated MOI (typically 2000 p/cell). Infection was synchronized on ice for 45 mins and cells were washed 1x with cold Opti-MEM and incubated with warmed IMDM at 37°C to initiate infection. For drug treatment experiments unless otherwise stated, cells were pretreated at 37°C for 30 mins prior to virus addition, and drug was included during the 45 min synchronization on ice and over the course of infection.

Infection with alternate WT adenoviruses serotypes of AdV2, AdV7 and AdV35 were performed using $1x10^5$ p/cell and quantified by qPCR for viral DNA at 72 hpi using the following primers: Ad2 (HAd2prF181- GCAAACGCTCTGCAACAAGA, HAd2prR181- CGATCAGCTCGCTCATGACT), Ad7 (HAd7AprF167- GACTCTGAGCGACGATCTGG, HAd7AprR167- AGTCCGCTCCCATGTCAAAG) and Ad35 (HAd35prF131- TTTCATTTTTCGCGCACGGT, HAd35prR131- ACCCCAAAGACGGCCTAATG).

Generation of [S^{35}]-labeled AdV was performed as previously described (Schoggins et al., 2003). Briefly, two p150 dishes were seeded with 7x10^6 293 cells and infected with 1000 p/cell of replication-incompetent AdV5-GFP (AdVCiG) in Opto-MEM for 1 hr at 37°C before replacement with 10% FBS 1% NEAA DMEM. At 16 hpi (approx onset of late-stage of viral infection) media was replaced with -Met/-Cys DMEM supplemented with 10% dialyzed FBS and 1 mCi of [S^{35}]-methionine at 100 uCi/ml. At 72 hpi cells were collected in 50 ml conicals, spun down at *1500 x g* for 10 mins and supernatant was discarded and pellet was washed twice with PBS before resuspension in 5 mls of 3% DMEM. Cells then underwent three rapid freeze-thaw cycles on a dry ice/ethanol slurry and 37°C incubator to release cell-associated virus, cell debris was pelleted and virus-containing supernatant was stored at -80°C. For subsequent infections of WT or MIB1 KO A549s, cells were seeded in 12-well plate and infected the following day with 1:5 dilution of viral and uninfected supernatants and at timepoint indicated (30 min, 1hr, 2hr, 4 hr) were washed 3x with PBS to remove inoculum virus and lysed in RIPA for western blot. Uninfected cells incubated with [S^{35}]-[Met/Cys] supplemented media were processed in parallel.

HBV

For HBV infections, HepG2-NTCP and Huh7.5-NTCP cells were seeded in 96-well collagen-coated plates at 25,000 cells/well in 10% FBS 1% NEAA DMEM. At 24 hrs after seeding, the media was changed to 3% FBS, 1% NEAA DMEM with the addition of 2% DMSO (ATCC). The next day cells were infected in 50 µl of HBV inoculum in freshly prepared 3% FBS, 1% NEAA, 2% DMSO with 4% PEG8000 with genome equivalents (GEQ) calculated for 33,000 cells/well by spinoculating at 1000 *x g* for 1 hr at 37°C and then placed in 37°C incubator. The following day, inoculum was removed, cells were washed 5x with PBS and replaced with 100 µl of 3% FBS, 1% NEAA, 2% DMSO in DMEM. After 7 days cells were processed for either HBSAg quantification by chemiluminescence immunoassay (CLIA) kit (Autobio Diagnostics Co.) according to manufacturer's instructions or core staining by

immunofluorescence as described in Michailidis et al.

Antibodies and drug treatments

Antibodies

Primary antibodies used for **western blot (WB)** include rabbit-anti-MIB1 (abcam 124929 1:2000), rabbit-anti-CAR (sc-15405 1:1000), rabbit anti-NTCP (Sigma 1:1000), mouse-anti-FLAG M2 (Sigma F3165 1:2000) and mouse-anti-vimentin (Santa Cruz sc-37371 1:1000). Secondary antibodies include Alexa Fluor 680- conjugated to streptavidin, (ThermoFisher), goat anti- rabbit or -mouse HRP and β-actin-HRP (1:10000). Primary antibodies for **immunofluorescence (IF)** experiments include mouse-anti-hexon (AdV5) (Development Studies Hybridoma TC21-9C12.C9 1:200), rabbit-anti-FLAG (Cell Signaling Technologies 14793S 1:1000), rabbit-anti-pericentrin (abcam ab4448 1:1000), mouse-anti-acetylated-alpha tubulin (lys40) (ThermoFisher 6-11B-1 1:500), rabbit-anti-alpha tubulin (Abcam ab18251 1:500), mouse-anti-PCM1 (Santa Cruz sc-398365 1:500), rabbit-anti-MSI2 (Abcam ab76148 EP1305Y 1:250), rabbit-anti-EDC4 (abcam 72408 1:500), rabbit-anti-vimentin (N-term) (Cell Signaling Technologies D21H3 5741S 1:500), mouse-anti-vimentin (C-term) (Santa Cruz sc-37371 1:500), and rabbit-anti-STAU2 (GeneTex GTX116458 1:250). Secondary antibodies include Alexa Fluor 488-, Alexa Fluor594- conjugated anti-mouse and anti-rabbit IgG (Thermo Fisher Molecular Probes). DRAQ5 (ThermoFisher 1:1000) was used for nuclear stain. HBV infection was quantified by IF using rabbit-anti-HBV core (Austral Biologicals 1:500) and influenza infection was quantified by flow-cytometry using mouse-anti-NP (Millipore MAB8251).

Drugs

Drugs were used at concentrations indicated in figure legends and include proteasome-inhibitor MG132 (Sigma Aldrich M7449), CRM1-mediated export inhibitor Leptomycin B (LMB) (Millipore Sigma L2913), and DUB-inhibitor PR-619 (LifeSensors). Microtubule manipulation experiments were performed using nocodazole (Sigma SML1665), vinblastine B (Sigma V1377) and paclitaxel (Sigma T7191). Centriollar satellite manipulation experiments were performed using anisomycin (Sigma A5862) and D-sorbitol (Sigma, 240850).

Immunofluorescence

Unless otherwise described, cells were fixed in 4% para-formaldehyde in PBS at RT for 10 mins followed by blocking with PBTG (PBS containing 10% normal goat serum, 1% bovine serum albumin (BSA), 0.1% Triton-X100) at RT for 1 to 2 hrs. Cells were then incubated with primary antibodies (diluted in PBTG at concentrations detailed above) at 4°C overnight. Following four washes with PBS-Tween (0.1%), cells were stained with Alexa-Fluor conjugated secondary antibodies (diluted in PBTG at concentrations detailed above) at RT for 1 hr in the dark. Following one wash with PBST, cells were incubated in nuclear stain TO-PRO-3 or DRAQ5 (diluted in PBS) at RT for 15 mins, followed by three additional washes with PBST, and a final wash in PBS. Coverslips were mounted on SuperFrost Plus Microscope Slides (Fisher 12-550-15) using ProLong Gold antifade reagent (Invitrogen P36934) and allowed to cure for at least 24 hours prior to imaging. Images were acquired using a 63x Oil immersion objective on an inverted Zeiss Axiovert 200 spinning disk confocal microscope using solid-state 491, 561 and

644 lasers (Spectral Applied) for excitation for collection with Andor iXon 512x512 EMCCD camera through MetaMorph software. Acquired images were analyzed as described using Fiji software (Schindelin et al., 2012) with representative examples below.

Representative script for analysis of AdV hexon stain around centrosome

```
selectWindow("2-1KO_untrt_w2561-620-60-TR_s6.TIF");
//run("Threshold...");
setThreshold(1500, 65535);
run("Make Binary", "method=Default background=Default black");
run("3D OC Options", "volume integrated_density mean_gray_value median_gray_value centroid centre_of_mass dots_size=5 font_size=10 show_numbers white_numbers store_results_within_a_table_named_after_the_image_(macro_friendly) redirect_to=2-1KO_untrt_w1491-525-50-FITC_s6.TIF");
run("3D Objects Counter", "threshold=128 slice=20 min.=100 max.=10747904 exclude_objects_on_edges objects statistics summary");
```

Representative script for analysis of centriollar satellite distribution around centrosome

```
selectWindow("2-1KO_JR34_aniso_w2561-620-60-TR_s1.TIF");
run("Z Project...", "projection=[Max Intensity]");
selectWindow("2-1KO_JR34_aniso_w1491-525-50-FITC_s1.TIF");
run("Z Project...", "projection=[Max Intensity]");
selectWindow("MAX_2-1KO_JR34_aniso_w2561-620-60-TR_s1.TIF");
setAutoThreshold("Default dark");
//run("Threshold...");
setThreshold(11900, 65535);
setOption("BlackBackground", true);
run("Make Binary");
run("Dilate");
run("Dilate");
run("Convert to Mask");
run("Set Measurements...", "area mean centroid integrated area_fraction redirect=MAX_2-1KO_JR34_aniso_w1491-525-50-FITC_s1.TIF decimal=3");
run("Analyze Particles...", "size=3-Infinity display summarize add");
```

Representative script for analysis of perinuclear P-body (EDC4) stain around nucleus

```
selectWindow("2-1plus_uninf_w3644-700-75-Cy5_s3.TIF");
run("Z Project...", "projection=[Max Intensity]");
run("Make Binary");
run("Convert to Mask");
run("Duplicate...", " ");
selectWindow("2-1plus_uninf_w3644-700-75-Cy5_s3.TIF");
selectWindow("2-1plus_uninf_w2561-620-60-TR_s3.TIF");
```

```
setThreshold(4400, 65535);
run("Make Binary", "method=Default background=Default black");
selectWindow("MAX_2-1plus_uninf_w3644-700-75-Cy5_s3.TIF");
run("Dilate");
run("Dilate");
run("Dilate");
run("Dilate");
selectWindow("2-1plus_uninf_w2561-620-60-TR_s3.TIF");
run("Make Substack...", "  slices=17");
selectWindow("MAX_2-1plus_uninf_w3644-700-75-Cy5_s3.TIF");
imageCalculator("Subtract create", "MAX_2-1plus_uninf_w3644-700-75-
Cy5_s3.TIF","MAX_2-1plus_uninf_w3644-700-75-Cy5_s3-1.TIF");
selectWindow("Result of MAX_2-1plus_uninf_w3644-700-75-Cy5_s3.TIF");
run("Merge Channels...", "c1=[Substack (17)] c3=[Result of MAX_2-1plus_uninf_w3644-
700-75-Cy5_s3.TIF] create keep");
selectWindow("Composite");
selectWindow("Result of MAX_2-1plus_uninf_w3644-700-75-Cy5_s3.TIF");
run("Set Measurements...", "area area_fraction redirect=[Substack (17)] decimal=3");
run("Measure");
selectWindow("Substack (17)");
imageCalculator("Multiply create", "Result of MAX_2-1plus_uninf_w3644-700-75-
Cy5_s3.TIF","Substack (17)");
selectWindow("Result of Result of MAX_2-1plus_uninf_w3644-700-75-Cy5_s3.TIF");
run("Set Measurements...", "area area_fraction redirect=None decimal=3");
run("Measure");
```

Representative script for visualization of exclusively cytoplasmic staining of PCM1 and STAU2

```
selectWindow("KO_uninf_w3644-700-75-Cy5_s4.TIF");
setAutoThreshold("Default dark");
//run("Threshold...");
setThreshold(3284, 65535);
setOption("BlackBackground", true);
run("Make Binary", "method=Default background=Default black");
selectWindow("KO_uninf_w2561-620-60-TR_s4.TIF");
setThreshold(2000, 65535);
setOption("BlackBackground", true);
run("Make Binary", "method=Default background=Default black");
selectWindow("KO_uninf_w3644-700-75-Cy5_s4.TIF");
run("Invert", "stack");
selectWindow("KO_uninf_w3644-700-75-Cy5_s4.TIF");
imageCalculator("Multiply create stack", "KO_uninf_w3644-700-75-
Cy5_s4.TIF","KO_uninf_w2561-620-60-TR_s4.TIF");
selectWindow("Result of KO_uninf_w3644-700-75-Cy5_s4.TIF");
selectWindow("KO_uninf_w1491-525-50-FITC_s4.TIF");
```

```
    setThreshold(2500, 65535);
    setOption("BlackBackground", true);
    run("Make Binary", "method=Default background=Default black")
    run("Merge Channels...", "c1=[Result of KO_uninf_w3644-700-75-Cy5_s4.TIF]
c2=KO_uninf_w1491-525-50-FITC_s4.TIF create keep");
```

Western blot

Cell lysates were prepared in RIPA buffer (50mM Tris-HCl pH 8.0, 150 mM NaCl, 0.1% SDS, 0.5% NaDoc, 1% NP-40 with addition of cOmplete Mini EDTA-free protease inhibitor tablet (Roche)) and incubated on ice for 30 mins with frequent vortexing and then clarified at 14,000 *x g* for 20 mins at 4°C. Protein concentration was determined by BCA protein assay and samples were resolved on 4-12% Bis-Tris gels (Invitrogen) followed by transfer onto either nitrocellulose 0.45 µm (Amersham Protran) or polyvinylidene fluoride (PVDF) membrane (EMD Millipore). Membranes were blocked with 5% milk in PBST and subsequent primary antibody incubations were performed at 4°C overnight in 5% milk PBST. Membranes were washed 3 times with PBST and incubated with secondary antibody. For fluorescence-based readout using the Azure biosystems c600, Li-Cor secondary antibodies IRDye 800CW and 680 CW were used. For chemiluminescent readout, the membrane was incubated with HRP-conjugated secondary antibody and exposed using SuperSignal West Pico or Femto PLUS Chemiluminescent Substrate (ThermoFisher) by film in a dark room.

Ub-IP using Tandem Ubiquitin Binding Entities (TUBEs)

Hap1 cells were seeded into 10 cm dishes at $6x10^6$ cells per dish. Each condition was seeded in quadruplicate to encompass three MS-submission samples and a diagnostic sample. The next day, cells were washed 1x Opti-MEM and wash was replaced with 3 mls Opti-MEM and placed on ice for 10 mins before spiking in replication-competent AdV5-GFP (200 p/cell) prepared in 500 µl of Opti-MEM. Following synchronization for 45 mins at 4°C, inoculum was removed and cells were washed with cold Opti-MEM. Pre-warmed Opti-MEM was added and cells were incubated at 37°C. At 1 hpi, cells were placed on ice, washed with cold PBS and lysed by adding 500 µl of TUBE lysis buffer (50mM Tris-HCl pH 7.5, 0.15M NaCl, 1mM EDTA, 1% NP-40, 10% glycerol) freshly supplemented with protease inhibitor tablet (Roche) and 50 µM DUB inhibitor PR-619 (LifeSensors SI9619–10mM stock in DMSO) and stored at -80°C. For TUBE-IP ("Ub-IP"), lysates were thawed and clarified lysates by centrifugation at maximum speed in a table-top centrifuge at 4°C[56]. Supernatants were transferred to fresh tubes, protein concentrations were quantified by BCA and IP input was normalized to 2 mg of protein lysate in a 500 µl of input volume for each condition for addition to the TUBE beads.

[56] This was a point of contention in preparation and clarification of the lysates given the knowledge that MIB1 is a centriollar satellite/centrosome associated protein and spinning down the lysates to remove insoluble material may deplete certain structures like microtubules or intermediate filaments that may be associated with proteins of interest to MIB1 biology.

100 µl of control magnetic beads (LifeSensors UM400M) and TUBE2 magnetic beads (LifeSensors UM402M) per sample were prepared in separate low-fluid-retention tubes by washing three times with TBST (20mM Tris-HCl pH 8.0, 0.15M NaCl, 0.1% Tween-20). To remove proteins that non-specifically bind to the TUBE beads, the 500 µl of normalized input lysate was added to the control beads and nutated for 1 hour at 4°C. To isolate ubiquitinated proteins, the supernatants were then transferred directly to the prepared TUBE2 magnetic beads and nutated at 4°C for 3 hrs. After incubation, beads with bound ubiquitinated proteins were washed 3x TBST, 2x with TBS to remove detergent and transferred to fresh tubes for an additional two final washes with TBS. Supernatants were removed and the beads were stored dry at -20°C prior to analysis by mass-spectrometry.

APEX2 proximity labeling

MIB1 WT and C985S constructs were tagged N- or C-terminally with FLAG-tagged APEX2 protein via Gibson assembly of overlapping PCR-amplified MIB1 fragment and FLAG-APEX2 fragment into the recipient pLX304 lentivirus expression vector followed by site-directed mutagenesis to introduce the V943F mutation. APEX2 was PCR-amplified off of plasmid pcDNA3 APEX2-NES (a gift from Alice Ting (Addgene plasmid # 49386; http://n2t.net/addgene:49386; RRID:Addgene_49386) (Lam et al., 2015). Lentiviruses from these three constructs were used to reconstitute MIB1 Hap1 KO clone 2-1 as described.

For proteomics, cells were seeded at $1.5x10^7$ cells per 15 cm dish in quadruplicate per condition. On the day of infection, cells were pre-incubated with 500 µM biotin-phenol (BP: sold as biotin tyramide—Iris Biotech Cat: LS-3500.1000) at 37°C for 30 mins. Media was then replaced with cold Opti-MEM containing BP (500 µM) and 500 µl of rep-competent AdV5-GFP adenovirus (MOI = 200p/cell) or plain Opti-MEM (for uninfected controls) was spiked into the medium. Cells were incubated at 4°C for synchronization of infection. At 40 mins post adsorption, inoculum was replaced with 25 mls of prewarmed IMDM (+BP) and plates were incubated at 37°C for 1 h 15 mins. At 1 h 10 min post infection, MIB1-proximal proteins were labeled by a 1 min incubation by spiking in H_2O_2 (Fisher Scientific H325) to 100 mM, immediately followed by media removal and addition of 10 ml of a freshly prepared "quencher" solution (10mM sodium ascorbate [Spectrum Chemical S1349], 5mM Trolox [Sigma 238813] in PBS) for 2 min at RT. Solution was aspirated and cells were incubated with another 10 mls of quencher and collected into 15-ml conical tubes on ice by scraping. Cells were then pelleted at 1200 *x g*, washed with 1 ml of quencher and transferred to 1.2 ml eppendorf tubes. Cells were pelleted at 5000 *x g*, supernatants were removed and pellets were stored at -80°C until further processing.

For subsequent enrichment of proximity-labeled proteins, pellets were lysed in 1 ml of RIPA-Quench (Quench prepared in RIPA buffer rather than PBS and supplemented with protease-inhibitor tablet), and disrupted by pipetting up and down. After a 15 min incubation on ice, samples were sonicated for 15 s and clarified by centrifugation at 15000 *x g* at 4°C. Meanwhile, 400 µl of High Capacity Neutravidin Agarose Resin bead slurry (ThermoFisher 29284) were transferred low-fluid retention 1.5 ml tubes (National Scientific CN1700L-BP) and washed 2x in 1 ml RIPA buffer prior to addition of proximity-labeled samples. Supernatants from clarified samples were added to the neutravidin beads and nutated overnight at 4°C. Supernatants were removed and beads were washed 2x with RIPA buffer, 1x with 1M KCl, 1x with 0.1M Na_2CO_3, 1x with freshly prepared 2M Urea in 10 mM Tris-HCl pH 8.0 and 3x in 10mM Tris-HCL pH 8.0

with transfer to a fresh tube before the final wash. Samples were eluted either directly in lysis buffer with reducing agent for western blot or beads were stored in 500 µl of Tris-HCL at -20°C prior to analysis by mass-spectrometry. As a control, 10% input and 10% post-IP fractions for each condition were analyzed by western blot to ensure H_2O_2 -dependent labeling and streptavidin-mediated depletion.

For IF readout, cells were seeded onto glass coverslips treated with poly-lysine in 24-well plates. The following day, cells were preincubated with BP and infection and H_2O_2 labeling steps were carried out as described above except cells were fixed by addition of 4% para-formaldehyde immediately following the first quencher incubation and processed for IF as described.

siRNA transfections

For screening of potential MIB1 ubiquitination target candidates for their influence on AdV5 infection by flow cytometry, a select set of siRNAs targeting MIB1-ubiquitinated candidates was obtained from Dharmacon as a custom ON-TARGETplus SMARTpool Cherry-pick Library (0.5 nmol) and resuspended to 5 µM in 1x siRNA resuspension buffer. Individual siRNAs of genes chosen for follow-up were purchased as 5 nmol ON-TARGETplus SMARTpools (Dharmacon) of four combined siRNAs and resuspended to 20 µM in 1x siRNA resuspension buffer (Dharmacon). Reverse transfection of siRNAs was performed in 24-well format at a final concentration of 25 nM siRNA per well at a total volume of 500 µl. In brief, siRNAs were prepared in Opti-MEM and combined with DharmaFect 3 diluted in Opti-MEM (1:50) to a total volume of 100 µl for 5 mins and added to 400 µl of IMDM containing 40,000 Hap1 cells/well. At 24 h post-transfection, media was replaced with fresh IMDM to minimize toxicity. At 48 h post-transfection cells were infected by spiking in 50 µl of replication-competent AdV5-GFP (75 p/cell) in Opti-MEM calculated for twice the originally seeded number of cells, and harvested at 24 hpi as described for flow-cytometry.

Proteomics and Proteomic Analysis

Digestion

Ub-MS:
Beads were incubated with 8M urea in 50 mM ammonium bicarbonate (AMBIC, Fluka Chemicals) for 1 hour at room temperature. The supernatant was withdrawn and the process was repeated. The two supernatants were pooled and disulfide bonds were reduced by additon of dithreitol (DTT, EMD Chemicals) to 10mM final concentration and incubation for 1 hour at room temperature with vigorous shaking. Iodoaceamide (IAA, Sigma) was added to 20mM and alkylation proceeded for 1 hour at room temperature in the dark. Samples were diluted to reduce urea concentration to 3.5M and digested using Lysyl Endopeptidase (Lys-C, Wako Chemicals) overnight at room temperature. The following day samples were further diluted to 1.5M urea and digested with1 µg sequencing grade trypsin (Promega). Digestion was stopped by acidification using trifluoroacetic acid (TFA, Thermo), and peptides were purified by in-house constructed reversed-phase micropurification tips.

APEX-MS:
Decanted agarose beads were subjected to on-bead digestion by the addition of 1µg sequencing grade trypsin (Promega). The supernatant was withdrawn, evaporated to dryness and dissolved in 50 mM ammonium bicarbonate (AMBIC, Fluka Chemicals), 10mM dithiothreitol (EMD Chemicals) in water, and disulfide bonds were reduced for 1 hour at room temperature with vigorous shaking. Iodoaceamide (Sigma) was added to 20mM and alkylation proceeded for 1 hour at room temperature in the dark. Samples were further digested for six hours at room temperature using trypsin. Digestion was stopped by acidification using trifluoroacetic acid (TFA, Thermo), and peptides were purified by in-house constructed reversed-phase micropurification tips.

LC-MS/MS

Solvent A was 0.1% formic acid in water and solvent B was 0.1% formic acid, 80 % acetonitrile (ACN) in water. All LC-MS solvents are of LC-MS grade and purchased from Fisher. Liquid chromatography was performed by a Dionex 3000 Ultimate HPLC equipped with a NCS3500RS nano- and microflow pump (Dionex). Peptides were loaded onto a 100 µm*20mm Acclaim PepMap C18 trap column (Thermo Scientific) at 3µL/min. Separation was achieved using a 75µm*120mm pulled-emitter nanocolumn (Nikkyo Technos). Solvent B went from 1% to 38 % over 90 minutes, followed by a sharp 1-minute increase to 90% where it was kept for 8 minutes. Peptides were analyzed using a Q-Exactive HF mass spectrometer (Thermo Scientific). Data was recorded in positive mode with Top 20 DDA acquisition. MS1 resolution was set to 60 000 and an MS2 resolution of 30 000. AGC targets of 3e6 (MS1) and 2e5 (MS2) were applied.

Data analysis

Data was analyzed MaxQuant v. 1.6.6.0 (Cox & Mann, 2008). Spectra were queried against the human proteome (downloaded from uniprot.org on Feb 12th 2019) concatenated with a custom adenovirus database and common contaminants. A false discovery rate of 1% at both peptide and protein level was applied. Further statistical analysis was perfomed within the Perseus framework (Tyanova et al., 2016). Significant changes were determined using a student's t-test (p=0.05). As all proteomics datasets were collected in triplicates for each sample condition, proteins were first filtered for representation by iBAQ values in at last 2/3 replicates in at least one sample condition followed by replacement of undetected values with a low-abundant imputed value to allow for fold-change calculation. Unless otherwise indicated in figure legend all datasets were first filtered for genes identified by more than a single unique peptides.

References

Aizer, A., Brody, Y., Ler, L. W., Sonenberg, N., Singer, R. H., & Shav-Tal, Y. (2008). The dynamics of mammalian P body transport, assembly, and disassembly in vivo. *Molecular Biology of the Cell*, *19*(10), 4154–4166. http://doi.org/10.1091/mbc.e08-05-0513

Akimov, V., Rigbolt, K. T. G., Nielsen, M. M., & Blagoev, B. (2011). Characterization of ubiquitination dependent dynamics in growth factor receptor signaling by quantitative proteomics. *Molecular BioSystems*, *7*(12), 3223–3233. http://doi.org/10.1039/c1mb05185g

Almeida-Souza, L., Asselbergh, B., De Winter, V., Goethals, S., Timmerman, V., & Janssens, S. (2013). HSPB1 facilitates the formation of non-centrosomal microtubules. *PLoS ONE*, *8*(6), e66541. http://doi.org/10.1371/journal.pone.0066541

Au, S., Wu, W., Zhou, L., Theilmann, D. A., & Panté, N. (2016). A new mechanism for nuclear import by actin-based propulsion used by a baculovirus nucleocapsid. *Journal of Cell Science*, *129*(15), 2905–2911. http://doi.org/10.1242/jcs.191668

Ayache, J., Bénard, M., Ernoult-Lange, M., Minshall, N., Standart, N., Kress, M., & Weil, D. (2015). P-body assembly requires DDX6 repression complexes rather than decay or Ataxin2/2L complexes. *Molecular Biology of the Cell*, *26*(14), 2579–2595. http://doi.org/10.1091/mbc.E15-03-0136

Aydin, I., Weber, S., Snijder, B., Samperio Ventayol, P., Kühbacher, A., Becker, M., et al. (2014). Large scale RNAi reveals the requirement of nuclear envelope breakdown for nuclear import of human papillomaviruses. *PLoS Pathogens*, *10*(5), e1004162. http://doi.org/10.1371/journal.ppat.1004162

Banerjee, I., Miyake, Y., Nobs, S. P., Schneider, C., Horvath, P., Kopf, M., et al. (2014). Influenza A virus uses the aggresome processing machinery for host cell entry. *Science*, *346*(6208), 473–477. http://doi.org/10.1126/science.1257037

Bao, X. X., Spanos, C., Kojidani, T., Lynch, E. M., Rappsilber, J., Hiraoka, Y., et al. (2018). Exportin Crm1 is repurposed as a docking protein to generate microtubule organizing centers at the nuclear pore. *eLife*, *7*, 1195. http://doi.org/10.7554/eLife.33465

Barbee, S. A., Estes, P. S., Cziko, A.-M., Hillebrand, J., Luedeman, R. A., Coller, J. M., et al. (2006). Staufen- and FMRP-containing neuronal RNPs are structurally and functionally related to somatic P bodies. *Neuron*, *52*(6), 997–1009. http://doi.org/10.1016/j.neuron.2006.10.028

Bauer, M., Flatt, J. W., Seiler, D., Cardel, B., Emmenlauer, M., Boucke, K., et al. (2019). The E3 Ubiquitin Ligase Mind Bomb 1 Controls Adenovirus Genome Release at the Nuclear Pore Complex. *Cell Reports*, *29*(12), 3785–3795.e8. http://doi.org/10.1016/j.celrep.2019.11.064

Belin, M. T., & Boulanger, P. (1987). Processing of vimentin occurs during the early stages of adenovirus infection. *Journal of Virology*, *61*(8), 2559–2566.

Benboudjema, L., Mulvey, M., Gao, Y., Pimplikar, S. W., & Mohr, I. (2003). Association of the herpes simplex virus type 1 Us11 gene product with the cellular kinesin light-chain-related protein PAT1 results in the redistribution of both polypeptides. *Journal of Virology*, *77*(17), 9192–9203. http://doi.org/10.1128/jvi.77.17.9192-9203.2003

Bergelson, J. M. (1999). Receptors mediating adenovirus attachment and internalization.

Biochemical Pharmacology, *57*(9), 975–979.
Bergelson, J. M., Cunningham, J. A., Droguett, G., Kurt-Jones, E. A., Krithivas, A., Hong, J. S., et al. (1997). Isolation of a common receptor for Coxsackie B viruses and adenoviruses 2 and 5. *Science*, *275*(5304), 1320–1323. http://doi.org/10.1126/science.275.5304.1320
Berk, A. J. (2016). Discovery of RNA splicing and genes in pieces. *Proceedings of the National Academy of Sciences of the United States of America* (Vol. 113, pp. 801–805). http://doi.org/10.1073/pnas.1525084113
Berndt, J. D., Aoyagi, A., Yang, P., Anastas, J. N., Tang, L., & Moon, R. T. (2011). Mindbomb 1, an E3 ubiquitin ligase, forms a complex with RYK to activate Wnt/β-catenin signaling. *The Journal of Cell Biology*, *194*(5), 737–750. http://doi.org/10.1083/jcb.201107021
Blair, G. E., & Blair-Zajdel, M. E. (2004). Evasion of the immune system by adenoviruses. *Current Topics in Microbiology and Immunology*, *273*(425), 3–28. http://doi.org/10.1007/978-3-662-05599-1_1
Blomen, V. A., Májek, P., Jae, L. T., Bigenzahn, J. W., Nieuwenhuis, J., Staring, J., et al. (2015). Gene essentiality and synthetic lethality in haploid human cells. *Science*, *350*(6264), 1092–1096. http://doi.org/10.1126/science.aac7557
Branon, T. C., Bosch, J. A., Sanchez, A. D., Udeshi, N. D., Svinkina, T., Carr, S. A., et al. (2018). Efficient proximity labeling in living cells and organisms with TurboID. *Nature Biotechnology*, *36*(9), 880–887. http://doi.org/10.1038/nbt.4201
Bremner, K. H., Scherer, J., Yi, J., Vershinin, M., Gross, S. P., & Vallee, R. B. (2009). Adenovirus transport via direct interaction of cytoplasmic dynein with the viral capsid hexon subunit. *Cell Host & Microbe*, *6*(6), 523–535. http://doi.org/10.1016/j.chom.2009.11.006
Brulois, K., Toth, Z., Wong, L.-Y., Feng, P., Gao, S.-J., Ensser, A., & Jung, J. U. (2014). Kaposi's sarcoma-associated herpesvirus K3 and K5 ubiquitin E3 ligases have stage-specific immune evasion roles during lytic replication. *Journal of Virology*, *88*(16), 9335–9349. http://doi.org/10.1128/JVI.00873-14
Byk, L.A., Iglesias, N.G., De Maio, F.A., Gebhard, L.G., Rossi, M. & Gamarnik, A.V. (2016) Dengue Virus Genome Uncoating Requires Ubiquitination. *mBio, 7*(3), 2nd p.504.
Cai, D., Wang, X., Yan, R., Mao, R., Liu, Y., Ji, C., et al. (2016). Establishment of an inducible HBV stable cell line that expresses cccDNA-dependent epitope-tagged HBeAg for screening of cccDNA modulators. *Antiviral Research*, *132*, 26–37. http://doi.org/10.1016/j.antiviral.2016.05.005
Cao, Y., Du, J., Chen, D., Wang, Q., Zhang, N., Liu, X., et al. (2016). RNA- binding protein Stau2 is important for spindle integrity and meiosis progression in mouse oocytes. *Cell Cycle (Georgetown, Tex.)*, *15*(19), 2608–2618. http://doi.org/10.1080/15384101.2016.1208869
Carette, J. E., Guimaraes, C. P., Varadarajan, M., Park, A. S., Wuethrich, I., Godarova, A., et al. (2009). Haploid genetic screens in human cells identify host factors used by pathogens. *Science*, *326*(5957), 1231–1235. http://doi.org/10.1126/science.1178955
Cassany, A., Ragues, J., Guan, T., Bégu, D., Wodrich, H., Kann, M., et al. (2015). Nuclear import of adenovirus DNA involves direct interaction of hexon with an N-terminal domain of the nucleoporin Nup214. *Journal of Virology*, *89*(3), 1719–1730. http://doi.org/10.1128/JVI.02639-14
Chen, J., Morral, N., & Engel, D. A. (2007). Transcription releases protein VII from adenovirus chromatin. *Virology*, *369*(2), 411–422. http://doi.org/10.1016/j.virol.2007.08.012
Chernyatina, A. A., Nicolet, S., Aebi, U., Herrmann, H., & Strelkov, S. V. (2012). Atomic structure of the vimentin central α-helical domain and its implications for intermediate

filament assembly. *Pnas*, *109*(34), 13620–13625. http://doi.org/10.1073/pnas.1206836109
Choe, E.-A., Liao, L., Zhou, J.-Y., Cheng, D., Duong, D. M., Jin, P., et al. (2007). Neuronal morphogenesis is regulated by the interplay between cyclin-dependent kinase 5 and the ubiquitin ligase mind bomb 1. *The Journal of Neuroscience : the Official Journal of the Society for Neuroscience*, *27*(35), 9503–9512. http://doi.org/10.1523/JNEUROSCI.1408-07.2007
Ciechanover, A., Elias, S., Heller, H., & Hershko, A. (1982). "Covalent affinity" purification of ubiquitin-activating enzyme. *The Journal of Biological Chemistry*, *257*(5), 2537–2542.
Cleat, P. H., & Hay, R. T. (1989). Co-operative interactions between NFI and the adenovirus DNA binding protein at the adenovirus origin of replication. *EMBO Journal*, *8*(6), 1841–1848.
Cohen, P., & Tcherpakov, M. (2010). Will the ubiquitin system furnish as many drug targets as protein kinases? *Cell*, *143*(5), 686–693. http://doi.org/10.1016/j.cell.2010.11.016
Cohen, S., Marr, A. K., Garcin, P., & Panté, N. (2011). Nuclear envelope disruption involving host caspases plays a role in the parvovirus replication cycle. *Journal of Virology*, *85*(10), 4863–4874. http://doi.org/10.1128/JVI.01999-10
Conine, C. C., Batista, P. J., Gu, W., Claycomb, J. M., Chaves, D. A., Shirayama, M., & Mello, C. C. (2010). Argonautes ALG-3 and ALG-4 are required for spermatogenesis-specific 26G-RNAs and thermotolerant sperm in Caenorhabditis elegans. *Pnas*, *107*(8), 3588–3593. http://doi.org/10.1073/pnas.0911685107
Conkar, D., Culfa, E., Odabasi, E., Rauniyar, N., Yates, J. R., & Firat-Karalar, E. N. (2017). The centriolar satellite protein CCDC66 interacts with CEP290 and functions in cilium formation and trafficking. *Journal of Cell Science*, *130*(8), 1450–1462. http://doi.org/10.1242/jcs.196832
Copeland, A. M., Newcomb, W. W., & Brown, J. C. (2009). Herpes simplex virus replication: roles of viral proteins and nucleoporins in capsid-nucleus attachment. *Journal of Virology*, *83*(4), 1660–1668. http://doi.org/10.1128/JVI.01139-08
Corthésy-Theulaz, I., Pauloin, A., & Pfeffer, S. R. (1992). Cytoplasmic dynein participates in the centrosomal localization of the Golgi complex. *The Journal of Cell Biology*, *118*(6), 1333–1345. http://doi.org/10.1083/jcb.118.6.1333
Cox, J., & Mann, M. (2008). MaxQuant enables high peptide identification rates, individualized p.p.b.-range mass accuracies and proteome-wide protein quantification. *Nature Biotechnology*, *26*(12), 1367–1372. http://doi.org/10.1038/nbt.1511
Crenshaw, B. J., Jones, L. B., Bell, C. R., Kumar, S., & Matthews, Q. L. (2019). Perspective on Adenoviruses: Epidemiology, Pathogenicity, and Gene Therapy. *Biomedicines*, *7*(3), 61. http://doi.org/10.3390/biomedicines7030061
Čajánek, L., Glatter, T., & Nigg, E. A. (2015). The E3 ubiquitin ligase Mib1 regulates Plk4 and centriole biogenesis. *Journal of Cell Science*, *128*(9), 1674–1682. http://doi.org/10.1242/jcs.166496
Dalton, K. P., & Rose, J. K. (2001). Vesicular stomatitis virus glycoprotein containing the entire green fluorescent protein on its cytoplasmic domain is incorporated efficiently into virus particles. *Virology*, *279*(2), 414–421. http://doi.org/10.1006/viro.2000.0736
Danielsson, F., Peterson, M. K., Caldeira Araújo, H., Lautenschläger, F., & Gad, A. K. B. (2018). Vimentin Diversity in Health and Disease. *Cells*, *7*(10), 147. http://doi.org/10.3390/cells7100147
Dao, T. P., Kolaitis, R.-M., Kim, H. J., O'Donovan, K., Martyniak, B., Colicino, E., et al. (2018).

Ubiquitin Modulates Liquid-Liquid Phase Separation of UBQLN2 via Disruption of Multivalent Interactions. *Molecular Cell*, *69*(6), 965–978.e6. http://doi.org/10.1016/j.molcel.2018.02.004

Delboy, M. G., & Nicola, A. V. (2011). A pre-immediate-early role for tegument ICP0 in the proteasome-dependent entry of herpes simplex virus. *Journal of Virology*, *85*(12), 5910–5918. http://doi.org/10.1128/JVI.00267-11

Dennis, S., Sheth, U., Feldman, J. L., English, K. A., & Priess, J. R. (2012). C. elegans germ cells show temperature and age-dependent expression of Cer1, a Gypsy/Ty3-related retrotransposon. *PLoS Pathogens*, *8*(3), e1002591. http://doi.org/10.1371/journal.ppat.1002591

Dho, S. E., Silva-Gagliardi, N., Morgese, F., Coyaud, É., Lamoureux, E., Berry, D. M., et al. (2019). Proximity interactions of the ubiquitin ligase Mind bomb 1 reveal a role in regulation of epithelial polarity complex proteins. *Scientific Reports*, *9*(1), 12471–18. http://doi.org/10.1038/s41598-019-48902-x

Di Nunzio, F., Danckaert, A., Fricke, T., Perez, P., Fernandez, J., Perret, E., et al. (2012). Human nucleoporins promote HIV-1 docking at the nuclear pore, nuclear import and integration. *PLoS ONE*, *7*(9), e46037. http://doi.org/10.1371/journal.pone.0046037

Didier, C., Merdes, A., Gairin, J.-E., & Jabrane-Ferrat, N. (2008). Inhibition of proteasome activity impairs centrosome-dependent microtubule nucleation and organization. *Molecular Biology of the Cell*, *19*(3), 1220–1229. http://doi.org/10.1091/mbc.e06-12-1140

Douanne, T., André-Grégoire, G., Thys, A., Trillet, K., Gavard, J., & Bidère, N. (2019). CYLD Regulates Centriolar Satellites Proteostasis by Counteracting the E3 Ligase MIB1. *Cell Reports*, *27*(6), 1657–1665.e4. http://doi.org/10.1016/j.celrep.2019.04.036

Dougherty, S. E., Maduka, A. O., Inada, T., & Silva, G. M. (2020). Expanding Role of Ubiquitin in Translational Control. *International Journal of Molecular Sciences*, *21*(3), 1151. http://doi.org/10.3390/ijms21031151

Duchaîne, T. F., Hemraj, I., Furic, L., Deitinghoff, A., Kiebler, M. A., & DesGroseillers, L. (2002). Staufen2 isoforms localize to the somatodendritic domain of neurons and interact with different organelles. *Journal of Cell Science*, *115*(Pt 16), 3285–3295.

Efimov, A., Kharitonov, A., Efimova, N., Loncarek, J., Miller, P. M., Andreyeva, N., et al. (2007). Asymmetric CLASP-dependent nucleation of noncentrosomal microtubules at the trans-Golgi network. *Developmental Cell*, *12*(6), 917–930. http://doi.org/10.1016/j.devcel.2007.04.002

Emmerich, C. H., & Cohen, P. (2015). Optimising methods for the preservation, capture and identification of ubiquitin chains and ubiquitylated proteins by immunoblotting. *Biochemical and Biophysical Research Communications*, *466*(1), 1–14. http://doi.org/10.1016/j.bbrc.2015.08.109

Enchev, R. I., Schulman, B. A., & Peter, M. (2015). Protein neddylation: beyond cullin-RING ligases. *Nature Reviews. Molecular Cell Biology*, *16*(1), 30–44. http://doi.org/10.1038/nrm3919

Endter, C., & Dobner, T. (2004). Cell transformation by human adenoviruses. *Current Topics in Microbiology and Immunology*, *273*(Chapter 6), 163–214. http://doi.org/10.1007/978-3-662-05599-1_6

Fay, N., & Panté, N. (2013). The intermediate filament network protein, vimentin, is required for parvoviral infection. *Virology*, *444*(1-2), 181–190. http://doi.org/10.1016/j.virol.2013.06.009

Fay, N., & Panté, N. (2015). Nuclear entry of DNA viruses. *Frontiers in Microbiology*,

6(e1004162), 467. http://doi.org/10.3389/fmicb.2015.00467
Feuer, R., Mena, I., Pagarigan, R., Slifka, M. K., & Whitton, J. L. (2002). Cell cycle status affects coxsackievirus replication, persistence, and reactivation in vitro. *Journal of Virology*, *76*(9), 4430–4440. http://doi.org/10.1128/JVI.76.9.4430-4440.2002
Firat-Karalar, E. N., & Stearns, T. (2015). Probing mammalian centrosome structure using BioID proximity-dependent biotinylation. *Methods in Cell Biology*, *129*, 153–170. http://doi.org/10.1016/bs.mcb.2015.03.016
Firat-Karalar, E. N., Rauniyar, N., Yates, J. R., & Stearns, T. (2014). Proximity interactions among centrosome components identify regulators of centriole duplication. *Current Biology : CB*, *24*(6), 664–670. http://doi.org/10.1016/j.cub.2014.01.067
Flint, S. J. (2004). *Principles of virology: Molecular biology, pathogenesis, and control of animal viruses*. Washington, D.C: ASM Press.
Friemuth, P., Philipson L., Carson S.D. (2008). The coxsackievirus and adenovirus receptor. *Current Top Microbiol Immunol*., 323:67-87.
Fritzsche, R., Karra, D., Bennett, K. L., Ang, F. Y., Heraud-Farlow, J. E., Tolino, M., et al. (2013). Interactome of two diverse RNA granules links mRNA localization to translational repression in neurons. *Cell Reports*, *5*(6), 1749–1762. http://doi.org/10.1016/j.celrep.2013.11.023
Gall, J., Kass-Eisler, A., Leinwand, L., & Falck-Pedersen, E. (1996). Adenovirus type 5 and 7 capsid chimera: fiber replacement alters receptor tropism without affecting primary immune neutralization epitopes. *Journal of Virology*, *70*(4), 2116–2123.
Gao, Y., & Sztul, E. (2001). A novel interaction of the Golgi complex with the vimentin intermediate filament cytoskeleton. *The Journal of Cell Biology*, *152*(5), 877–894. http://doi.org/10.1083/jcb.152.5.877
Garcia-Mata, R., Gao, Y.-S., & Sztul, E. (2002). Hassles with taking out the garbage: aggravating aggresomes. *Traffic (Copenhagen, Denmark)*, *3*(6), 388–396. http://doi.org/10.1034/j.1600-0854.2002.30602.x
Gavriilidis, C., Lardj, L., Solinhac, R., Messaddeq, N., Viaud, J., Laporte, J., Sumara I., & Hnia, K., (2018). The MTM1-UBQLN2-HSP complex mediates degradation of misfolded intermediate filaments in skeletal muscle. *Nature Cell Biology, 20*, 198-210, https://doi.org/10.1038/s41556-017-0024-9.
Gazzola, M., Burckhardt, C. J., Bayati, B., Engelke, M., Greber, U. F., & Koumoutsakos, P. (2009). A stochastic model for microtubule motors describes the in vivo cytoplasmic transport of human adenovirus. *PLoS Computational Biology*, *5*(12), e1000623. http://doi.org/10.1371/journal.pcbi.1000623
Gent, J. I., Schvarzstein, M., Villeneuve, A. M., Gu, S. G., Jantsch, V., Fire, A. Z., & Baudrimont, A. (2009). A Caenorhabditis elegans RNA-directed RNA polymerase in sperm development and endogenous RNA interference. *Genetics*, *183*(4), 1297–1314. http://doi.org/10.1534/genetics.109.109686
Georgatos, S. D., & Blobel, G. (1987). Lamin B constitutes an intermediate filament attachment site at the nuclear envelope. *The Journal of Cell Biology*, *105*(1), 117–125. http://doi.org/10.1083/jcb.105.1.117
Gheiratmand, L., Coyaud, É., Gupta, G. D., Laurent, E. M., Hasegan, M., Prosser, S. L., et al. (2019). Spatial and proteomic profiling reveals centrosome-independent features of centriolar satellites. *EMBO Journal*, *38*(14), e101109. http://doi.org/10.15252/embj.2018101109

GINSBERG, H. S., BADGER, G. F., DINGLE, J. H., JORDAN, W. S., & KATZ, S. (1955). Etiologic relationship of the RI-67 agent to acute respiratory disease (ARD). *Journal of Clinical Investigation*, *34*(6), 820–831. http://doi.org/10.1172/JCI103137

Goldknopf, I. L., & Busch, H. (1977). Isopeptide linkage between nonhistone and histone 2A polypeptides of chromosomal conjugate-protein A24. *Pnas*, *74*(3), 864–868. http://doi.org/10.1073/pnas.74.3.864

Goldstein, G., Scheid, M., Hammerling, U., Schlesinger, D. H., Niall, H. D., & Boyse, E. A. (1975). Isolation of a polypeptide that has lymphocyte-differentiating properties and is probably represented universally in living cells. *Pnas*, *72*(1), 11–15. http://doi.org/10.1073/pnas.72.1.11

Gordon, D.E., Jang, G.M., Bouhaddou, M., Xu, J., Obernier, K. et al. (2020). A SARS-CoV-2-Human Protein-Protein Interaction Map Reveals Drugs Targets and Potential Drug-Repurposing. *BioRxiv preprint*. doi: https://doi.org/10.1101/2020.03.22.002386

Gout, E., Gutkowska, M., Takayama, S., Reed, J. C., & Chroboczek, J. (2010). Co-chaperone BAG3 and adenovirus penton base protein partnership. *Journal of Cellular Biochemistry*, *111*(3), 699–708. http://doi.org/10.1002/jcb.22756

Graham, F. L., Smiley, J., Russell, W. C., & Nairn, R. (1977). Characteristics of a human cell line transformed by DNA from human adenovirus type 5. *Journal of General Virology*, *36*(1), 59–74. http://doi.org/10.1099/0022-1317-36-1-59

Greber, U. F., Willetts, M., Webster, P., & Helenius, A. (1993). Stepwise dismantling of adenovirus 2 during entry into cells. *Cell*, *75*(3), 477–486. http://doi.org/10.5167/uzh-510

Greber, U. F., Suomalainen M., Stidwell R. P., Boucke K., Ebersold M. W., & Helenius, A. (1997). The role of the nuclear pore complex in adenovirus DNA entry. *The EMBO Journal, 16*(19), 5998-6007.

Greer, A. E., Hearing, P., & Ketner, G. (2011). The adenovirus E4 11 k protein binds and relocalizes the cytoplasmic P-body component Ddx6 to aggresomes. *Virology*, *417*(1), 161–168. http://doi.org/10.1016/j.virol.2011.05.017

Guo, B., McMillan, B. J., & Blacklow, S. C. (2016). ScienceDirect Structure and function of the Mind bomb E3 ligase in the context of Notch signal transduction. *Current Opinion in Structural Biology*, *41*, 38–45. http://doi.org/10.1016/j.sbi.2016.05.012

Gupta, G. D., Coyaud, É., Gonçalves, J., Mojarad, B. A., Liu, Y., Wu, Q., et al. (2015). A Dynamic Protein Interaction Landscape of the Human Centrosome-Cilium Interface. *Cell*, *163*(6), 1484–1499. http://doi.org/10.1016/j.cell.2015.10.065

Haeussler, M., Schönig, K., Eckert, H., Eschstruth, A., Mianné, J., Renaud, J.-B., et al. (2016). Evaluation of off-target and on-target scoring algorithms and integration into the guide RNA selection tool CRISPOR. *Genome Biology*, *17*(1), 148–12. http://doi.org/10.1186/s13059-016-1012-2

Han, K.-J., Wu, Z., Pearson, C. G., Peng, J., Song, K., & Liu, C.-W. (2018). Deubiquitinase USP9X Maintains Centriolar Satellite Integrity by Stabilizing Pericentriolar Material 1 Protein. *Journal of Cell Science*, jcs.221663. http://doi.org/10.1242/jcs.221663

Han, Y., Branon, T. C., Martell, J. D., Boassa, D., Shechner, D., Ellisman, M. H., & Ting, A. (2019). Directed Evolution of Split APEX2 Peroxidase. *ACS Chemical Biology*, *14*(4), 619–635. http://doi.org/10.1021/acschembio.8b00919

Herrera, L. A., & Starr, D. A. (2018). The E3 Ubiquitin Ligase MIB-1 Is Necessary To Form the Nuclear Halo in Caenorhabditis elegans Sperm. *G3 (Bethesda, Md.)*, *8*(7), 2465–2470. http://doi.org/10.1534/g3.118.200426

Hershko, A., & Heller, H. (1985). Occurrence of a polyubiquitin structure in ubiquitin-protein conjugates. *Biochemical and Biophysical Research Communications*, *128*(3), 1079–1086. http://doi.org/10.1016/0006-291x(85)91050-2

Herrmann, Christin. (2019). Adenovirus Strategies For Altering The Cellular Environment In Favor Of Infection. *Publicly Accessible Penn Dissertations*. 3568. https://repository.upenn.edu/edissertations/3568

Hershko, A., Ciechanover, A., Heller, H., Haas, A. L., & Rose, I. A. (1980). Proposed role of ATP in protein breakdown: conjugation of protein with multiple chains of the polypeptide of ATP-dependent proteolysis. *Pnas*, *77*(4), 1783–1786. http://doi.org/10.1073/pnas.77.4.1783

Hershko, A., Heller, H., Elias, S., & Ciechanover, A. (1983). Components of ubiquitin-protein ligase system. Resolution, affinity purification, and role in protein breakdown. *The Journal of Biological Chemistry*, *258*(13), 8206–8214.

Higashino, F., Aoyagi, M., Takahashi, A., Ishino, M., Taoka, M., Isobe, T., et al. (2005). Adenovirus E4orf6 targets pp32/LANP to control the fate of ARE-containing mRNAs by perturbing the CRM1-dependent mechanism. *The Journal of Cell Biology*, *170*(1), 15–20. http://doi.org/10.1083/jcb.200405112

Hirokawa, N., Noda, Y., & Okada, Y. (1998). Kinesin and dynein superfamily proteins in organelle transport and cell division. *Current Opinion in Cell Biology*, *10*(1), 60–73. http://doi.org/10.1016/s0955-0674(98)80087-2

Hjerpe, R., Aillet, F., Lopitz-Otsoa, F., Lang, V., England, P., & Rodriguez, M. S. (2009). Efficient protection and isolation of ubiquitylated proteins using tandem ubiquitin-binding entities. *EMBO Reports*, *10*(11), 1250–1258. http://doi.org/10.1038/embor.2009.192

Hoffmann, H.-H., Schneider, W. M., Blomen, V. A., Scull, M. A., Hovnanian, A., Brummelkamp, T. R., & Rice, C. M. (2017). Diverse Viruses Require the Calcium Transporter SPCA1 for Maturation and Spread., *22*(4), 460–470.e5. http://doi.org/10.1016/j.chom.2017.09.002

Hoyt, M. A., Hyman, A. A., & Bähler, M. (1997). Motor proteins of the eukaryotic cytoskeleton. *Pnas*, *94*(24), 12747–12748. http://doi.org/10.1073/pnas.94.24.12747

Huang, X., & Dixit, V. M. (2016). Drugging the undruggables: exploring the ubiquitin system for drug development. *Cell Research*, *26*(4), 484–498. http://doi.org/10.1038/cr.2016.31

Hubbert, C., Guardiola, A., Shao, R., Kawaguchi, Y., Ito, A., Nixon, A., et al. (2002). HDAC6 is a microtubule-associated deacetylase. *Nature*, *417*(6887), 455–458. http://doi.org/10.1038/417455a

Huffman, J. B., Daniel, G. R., Falck-Pedersen, E., Huet, A., Smith, G. A., Conway, J. F., & Homa, F. L. (2017). The C Terminus of the Herpes Simplex Virus UL25 Protein Is Required for Release of Viral Genomes from Capsids Bound to Nuclear Pores. *Journal of Virology*, *91*(15), 171. http://doi.org/10.1128/JVI.00641-17

Hung, V., Udeshi, N. D., Lam, S. S., Loh, K. H., Cox, K. J., Pedram, K., et al. (2016). Spatially resolved proteomic mapping in living cells with the engineered peroxidase APEX2. *Nature Protocols*, *11*(3), 456–475. http://doi.org/10.1038/nprot.2016.018

Hunt, L. T., & Dayhoff, M. O. (1977). Amino-terminal sequence identity of ubiquitin and the nonhistone component of nuclear protein A24. *Biochemical and Biophysical Research Communications*, *74*(2), 650–655. http://doi.org/10.1016/0006-291x(77)90352-7

Iconomou, M., & Saunders, D. N. (2016). Systematic approaches to identify E3 ligase substrates. *The Biochemical Journal*, *473*(22), 4083–4101. http://doi.org/10.1042/BCJ20160719

Isaacson, M. K., & Ploegh, H. L. (2009). Ubiquitination, ubiquitin-like modifiers, and

deubiquitination in viral infection. *Cell Host & Microbe*, *5*(6), 559–570. http://doi.org/10.1016/j.chom.2009.05.012
Itoh, M., Kim, C.-H., Palardy, G., Oda, T., Jiang, Y.-J., Maust, D., et al. (2003). Mind bomb is a ubiquitin ligase that is essential for efficient activation of Notch signaling by Delta. *Developmental Cell*, *4*(1), 67–82.
Jae, L. T., Raaben, M., Riemersma, M., van Beusekom, E., Blomen, V. A., Velds, A., et al. (2013). Deciphering the glycosylome of dystroglycanopathies using haploid screens for lassa virus entry. *Science*, *340*(6131), 479–483. http://doi.org/10.1126/science.1233675
Jiang, H., White, E. J., Ríos-Vicil, C. I., Xu, J., Gomez-Manzano, C., & Fueyo, J. (2011). Human adenovirus type 5 induces cell lysis through autophagy and autophagy-triggered caspase activity. *Journal of Virology*, *85*(10), 4720–4729. http://doi.org/10.1128/JVI.02032-10
Joachim, J., Razi, M., Judith, D., Wirth, M., Calamita, E., Encheva, V., et al. (2017). Centriolar Satellites Control GABARAP Ubiquitination and GABARAP-Mediated Autophagy. *Current Biology : CB*, *27*(14), 2123–2136.e7. http://doi.org/10.1016/j.cub.2017.06.021
Jones, C. T., Catanese, M. T., Law, L. M. J., Khetani, S. R., Syder, A. J., Ploss, A., et al. (2010). Real-time imaging of hepatitis C virus infection using a fluorescent cell-based reporter system. *Nature Biotechnology*, *28*(2), 167–171. http://doi.org/10.1038/nbt.1604
Jovasevic, V., Liang, L., & Roizman, B. (2008). Proteolytic cleavage of VP1-2 is required for release of herpes simplex virus 1 DNA into the nucleus. *Journal of Virology*, *82*(7), 3311–3319. http://doi.org/10.1128/JVI.01919-07
Kalderon, D., Richardson, W. D., Markham, A. F., & Smith, A. E. (1984). Sequence requirements for nuclear location of simian virus 40 large-T antigen. *Nature*, *311*(5981), 33–38. http://doi.org/10.1038/311033a0
Kalthoff, C., Groos, S., Kohl, R., Mahrhold, S., & Ungewickell, E. J. (2002). Clint: a novel clathrin-binding ENTH-domain protein at the Golgi. *Molecular Biology of the Cell*, *13*(11), 4060–4073. http://doi.org/10.1091/mbc.e02-03-0171
Kane, M., Rebensburg, S. V., Takata, M. A., Zang, T. M., Yamashita, M., Kvaratskhelia, M., & Bieniasz, P. D. (2018). Nuclear pore heterogeneity influences HIV-1 infection and the antiviral activity of MX2. *eLife*, *7*, 4708. http://doi.org/10.7554/eLife.35738
Kato, M., Han, T. W., Xie, S., Shi, K., Du, X., Wu, L. C., et al. (2012). Cell-free formation of RNA granules: low complexity sequence domains form dynamic fibers within hydrogels. *Cell*, *149*(4), 753–767. http://doi.org/10.1016/j.cell.2012.04.017
Kelich, J. M., Ma, J., Dong, B., Wang, Q., Chin, M., Magura, C. M., et al. (2015). Super-resolution imaging of nuclear import of adeno-associated virus in live cells. *Molecular Therapy. Methods & Clinical Development*, *2*, 15047. http://doi.org/10.1038/mtm.2015.47
Kelkar, S. A., Pfister, K. K., Crystal, R. G., & Leopold, P. L. (2004). Cytoplasmic dynein mediates adenovirus binding to microtubules. *Journal of Virology*, *78*(18), 10122–10132. http://doi.org/10.1128/JVI.78.18.10122-10132.2004
Khanal, S., Ghimire, P., & Dhamoon, A. S. (2018). The Repertoire of Adenovirus in Human Disease: The Innocuous to the Deadly. *Biomedicines*, *6*(1), 30. http://doi.org/10.3390/biomedicines6010030
Khor, R., McElroy, L. J., & Whittaker, G. R. (2003). The ubiquitin-vacuolar protein sorting system is selectively required during entry of influenza virus into host cells. *Traffic (Copenhagen, Denmark)*, *4*(12), 857–868. http://doi.org/10.1046/j.1398-9219.2003.0140.x
Kiebler, M. A., Jansen, R.-P., Dahm, R., & Macchi, P. (2005). A putative nuclear function for mammalian Staufen. *Trends in Biochemical Sciences*, *30*(5), 228–231.

http://doi.org/10.1016/j.tibs.2005.03.005
Ko, C., Chakraborty, A., Chou, W.-M., Hasreiter, J., Wettengel, J. M., Stadler, D., et al. (2018). Hepatitis B virus genome recycling and de novo secondary infection events maintain stable cccDNA levels. *Journal of Hepatology*, *69*(6), 1231–1241. http://doi.org/10.1016/j.jhep.2018.08.012
Komatsu, T., Dacheux, D., Kreppel, F., Nagata, K., & Wodrich, H. (2015). A Method for Visualization of Incoming Adenovirus Chromatin Complexes in Fixed and Living Cells. *PLoS ONE*, *10*(9), e0137102. http://doi.org/10.1371/journal.pone.0137102
Kroschwald, S., Maharana, S., & Simon, A. (2017) Hexanediol: a chemical probe to investigate the material properties of membrane-less compartments. *Matters*. 10.19185/matters.201702000010.
Kulathu, Y., & Komander, D. (2012). Atypical ubiquitylation - the unexplored world of polyubiquitin beyond Lys48 and Lys63 linkages. *Nature Reviews. Molecular Cell Biology*, *13*(8), 508–523. http://doi.org/10.1038/nrm3394
Kwon, D. Y., Dimitriadi, M., Terzic, B., Cable, C., Hart, A. C., Chitnis, A., et al. (2013). The E3 ubiquitin ligase mind bomb 1 ubiquitinates and promotes the degradation of survival of motor neuron protein. *Molecular Biology of the Cell*, *24*(12), 1863–1871. http://doi.org/10.1091/mbc.E13-01-0042
Lam, S. S., Martell, J. D., Kamer, K. J., Deerinck, T. J., Ellisman, M. H., Mootha, V. K., & Ting, A. Y. (2015). Directed evolution of APEX2 for electron microscopy and proximity labeling. *Nature Methods*, *12*(1), 51–54. http://doi.org/10.1038/nmeth.3179
Lecland, N., & Merdes, A. (2018). Centriolar satellites prevent uncontrolled degradation of centrosome proteins: a speculative review. *Cell Stress*, *2*(2), 20–24. http://doi.org/10.15698/cst2018.02.122
Lee, J. S., Ismail, A. M., Lee, J. Y., Zhou, X., Materne, E. C., Chodosh, J., & Rajaiya, J. (2019). Impact of dynamin 2 on adenovirus nuclear entry. *Virology*, *529*, 43–56. http://doi.org/10.1016/j.virol.2019.01.008
Leopold, P. L., Kreitzer, G., Miyazawa, N., Rempel, S., Pfister, K. K., Rodriguez-Boulan, E., & Crystal, R. G. (2000). Dynein- and microtubule-mediated translocation of adenovirus serotype 5 occurs after endosomal lysis. *Human Gene Therapy*, *11*(1), 151–165. http://doi.org/10.1089/10430340050016238
Li, B., Yu, L., Liu, D., Yang, X., Zheng, Y., Gui, Y., & Wang, H. (2018). MIB1 mutations reduce Notch signaling activation and contribute to congenital heart disease. *Clinical Science (London, England : 1979)*, *132*(23), 2483–2491. http://doi.org/10.1042/CS20180732
Li, S., Wang, L., Berman, M., Kong, Y.-Y., & Dorf, M. E. (2011). Mapping a dynamic innate immunity protein interaction network regulating type I interferon production. *Immunity*, *35*(3), 426–440. http://doi.org/10.1016/j.immuni.2011.06.014
Lindberg, U., Persson, T., & Philipson, L. (1972). Isolation and characterization of adenovirus messenger ribonucleic acid in productive infection. *Journal of Virology*, *10*(5), 909–919.
Liu, Y., Gupta, G. D., Barnabas, D. D., Agircan, F. G., Mehmood, S., Wu, D., et al. (2018a). Direct binding of CEP85 to STIL ensures robust PLK4 activation and efficient centriole assembly. *Nature Communications*, *9*(1), 1731–15. http://doi.org/10.1038/s41467-018-04122-x
Liu, Z.-Q., Lee, J. N., Son, M., Lim, J.-Y., Dutta, R. K., Maharjan, Y., et al. (2018b). Ciliogenesis is reciprocally regulated by PPARA and NR1H4/FXR through controlling autophagy in vitro and in vivo. *Autophagy*, *14*(6), 1011–1027.

http://doi.org/10.1080/15548627.2018.1448326
Lopitz-Otsoa, F., Rodriguez-Suarez, E., Aillet, F., Casado-Vela, J., Lang, V., Matthiesen, R., et al. (2012). Integrative analysis of the ubiquitin proteome isolated using Tandem Ubiquitin Binding Entities (TUBEs). *Journal of Proteomics*, *75*(10), 2998–3014. http://doi.org/10.1016/j.jprot.2011.12.001
Luxán, G., Casanova, J. C., Martínez-Poveda, B., Prados, B., D'Amato, G., MacGrogan, D., et al. (2013). Mutations in the NOTCH pathway regulator MIB1 cause left ventricular noncompaction cardiomyopathy. *Nature Medicine*, *19*(2), 193–201. http://doi.org/10.1038/nm.3046
Mabit, H., Nakano, M. Y., Prank, U., Saam, B., Döhner, K., Sodeik, B., & Greber, U. F. (2002). Intact microtubules support adenovirus and herpes simplex virus infections. *Journal of Virology*, *76*(19), 9962–9971. http://doi.org/10.1128/jvi.76.19.9962-9971.2002
Mahowald, A. P. (1971). Polar granules of Drosophila. 3. The continuity of polar granules during the life cycle of Drosophila. *The Journal of Experimental Zoology*, *176*(3), 329–343. http://doi.org/10.1002/jez.1401760308
Mamon, L. A., Ginanova, V. R., Kliver, S. F., Yakimova, A. O., Atsapkina, A. A., & Golubkova, E. V. (2017). RNA-binding proteins of the NXF (nuclear export factor) family and their connection with the cytoskeleton. *Cytoskeleton (Hoboken, N.J.)*, *74*(4), 161–169. http://doi.org/10.1002/cm.21362
Matilla, A., Koshy, B. T., Cummings, C. J., Isobe, T., Orr, H. T., & Zoghbi, H. Y. (1997). The cerebellar leucine-rich acidic nuclear protein interacts with ataxin-1. *Nature*, *389*(6654), 974–978. http://doi.org/10.1038/40159
Matsuda, M., Rand, K., Palardy, G., Shimizu, N., Ikeda, H., Dalle Nogare, D., et al. (2016). Epb41l5 competes with Delta as a substrate for Mib1 to coordinate specification and differentiation of neurons. *Development (Cambridge, England)*, *143*(17), 3085–3096. http://doi.org/10.1242/dev.138743
Matsumoto, K., Minami, M., Shinozaki, F., Suzuki, Y., Abe, K., Zenno, S., et al. (2011). Hsp90 is involved in the formation of P-bodies and stress granules. *Biochemical and Biophysical Research Communications*, *407*(4), 720–724. http://doi.org/10.1016/j.bbrc.2011.03.088
McMillan, B. J., & Blacklow, S. C. (2015). Crystal structure of the MZM-REP domains of Mind bomb 1
. http://doi.org/10.2210/pdb4xi6/pdb
Melchior, F. (2000). SUMO--nonclassical ubiquitin. *Annual Review of Cell and Developmental Biology*, *16*(1), 591–626. http://doi.org/10.1146/annurev.cellbio.16.1.591
Melchior, F., Schergaut, M., & Pichler, A. (2003). SUMO: ligases, isopeptidases and nuclear pores. *Trends in Biochemical Sciences*, *28*(11), 612–618. http://doi.org/10.1016/j.tibs.2003.09.002
Mertz, J., Tan, H., Pagala, V., Bai, B., Chen, P.-C., Li, Y., et al. (2015). Sequential Elution Interactome Analysis of the Mind Bomb 1 Ubiquitin Ligase Reveals a Novel Role in Dendritic Spine Outgrowth. *Molecular & Cellular Proteomics : MCP*, *14*(7), 1898–1910. http://doi.org/10.1074/mcp.M114.045898
Michailidis, E., Pabon, J., Xiang, K., Park, P., Ramanan, V., Hoffmann, H.-H., et al. (2017). A robust cell culture system supporting the complete life cycle of hepatitis B virus. *Scientific Reports*, *7*(1), 16616–11. http://doi.org/10.1038/s41598-017-16882-5
Miki, T., & Yoneda, Y. (2004). Alternative splicing of Staufen2 creates the nuclear export signal for CRM1 (Exportin 1). *The Journal of Biological Chemistry*, *279*(46), 47473–47479.

http://doi.org/10.1074/jbc.M407883200
Miller, M. S., & Hertel, L. (2009). Onset of human cytomegalovirus replication in fibroblasts requires the presence of an intact vimentin cytoskeleton. *Journal of Virology*, *83*(14), 7015–7028. http://doi.org/10.1128/JVI.00398-09
Mills, I. G., Praefcke, G. J. K., Vallis, Y., Peter, B. J., Olesen, L. E., Gallop, J. L., et al. (2003). EpsinR: an AP1/clathrin interacting protein involved in vesicle trafficking. *The Journal of Cell Biology*, *160*(2), 213–222. http://doi.org/10.1083/jcb.200208023
Mitchison, T., & Kirschner, M. (1984). Dynamic instability of microtubule growth. *Nature*, *312*(5991), 237–242. http://doi.org/10.1038/312237a0
Miyazawa, N., Crystal, R. G., & Leopold, P. L. (2001). Adenovirus serotype 7 retention in a late endosomal compartment prior to cytosol escape is modulated by fiber protein. *Journal of Virology*, *75*(3), 1387–1400. http://doi.org/10.1128/JVI.75.3.1387-1400.2001
Monshausen, M., Gehring, N. H., & Kosik, K. S. (2004). The mammalian RNA-binding protein Staufen2 links nuclear and cytoplasmic RNA processing pathways in neurons. *Neuromolecular Medicine*, *6*(2-3), 127–144. http://doi.org/10.1385/NMM:6:2-3:127
Morreale, F. E., & Walden, H. (2016). Types of Ubiquitin Ligases. *Cell*, *165*(1), 248–248.e1. http://doi.org/10.1016/j.cell.2016.03.003
Mukherjee, J., Hermesh, O., Eliscovich, C., Nalpas, N., Franz-Wachtel, M., Maček, B., & Jansen, R.-P. (2019). β-Actin mRNA interactome mapping by proximity biotinylation. *Pnas*, *116*(26), 12863–12872. http://doi.org/10.1073/pnas.1820737116
Nicholson, B., Marblestone, J. G., Butt, T. R., & Mattern, M. R. (2007). Deubiquitinating enzymes as novel anticancer targets. *Future Oncology (London, England)*, *3*(2), 191–199. http://doi.org/10.2217/14796694.3.2.191
Nielsen, J. C., Nordgaard, C., Tollenaere, M. A. X., & Bekker-Jensen, S. (2018). Osmotic Stress Blocks Mobility and Dynamic Regulation of Centriolar Satellites. *Cells*, *7*(7), 65. http://doi.org/10.3390/cells7070065
Niemann, J., & Kühnel, F. (2017). Oncolytic viruses: adenoviruses. *Virus Genes*, *53*(5), 700–706. http://doi.org/10.1007/s11262-017-1488-1
Ojala, P. M., Sodeik, B., Ebersold, M. W., Kutay, U., & Helenius, A. (2000). Herpes simplex virus type 1 entry into host cells: reconstitution of capsid binding and uncoating at the nuclear pore complex in vitro. *Molecular and Cellular Biology*, *20*(13), 4922–4931. http://doi.org/10.1128/mcb.20.13.4922-4931.2000
Okano, M., Matsuo, H., Nishimura, Y., Hozumi, K., Yoshioka, S., Tonoki, A., & Itoh, M. (2016). Mib1 modulates dynamin 2 recruitment via Snx18 to promote Dll1 endocytosis for efficient Notch signaling. *Genes to Cells : Devoted to Molecular & Cellular Mechanisms*, *21*(5), 425–441. http://doi.org/10.1111/gtc.12350
Park, E., Gleghorn, M. L., & Maquat, L. E. (2013). Staufen2 functions in Staufen1-mediated mRNA decay by binding to itself and its paralog and promoting UPF1 helicase but not ATPase activity. *Pnas*, *110*(2), 405–412. http://doi.org/10.1073/pnas.1213508110
Perdiz, D., Mackeh, R., Poüs, C., & Baillet, A. (2011). The ins and outs of tubulin acetylation: more than just a post-translational modification? *Cellular Signalling*, *23*(5), 763–771. http://doi.org/10.1016/j.cellsig.2010.10.014
Petrakova, O., Volkova, E., Gorchakov, R., Paessler, S., Kinney, R. M., & Frolov, I. (2005). Noncytopathic replication of Venezuelan equine encephalitis virus and eastern equine encephalitis virus replicons in Mammalian cells. *Journal of Virology*, *79*(12), 7597–7608. http://doi.org/10.1128/JVI.79.12.7597-7608.2005

Philipson, L., Pettersson, U., Lindberg, U., Tibbetts, C., Vennström, B., & Persson, T. (1975). RNA synthesis and processing in adenovirus-infected cells. *Cold Spring Harbor Symposia on Quantitative Biology*, *39 Pt 1*(0), 447–456. http://doi.org/10.1101/sqb.1974.039.01.057

Pillay, S., & Carette, J. E. (2015). Hunting Viral Receptors Using Haploid Cells. *Annual Review of Virology*, *2*(1), 219–239. http://doi.org/10.1146/annurev-virology-100114-055119

Pitt, J. N., Schisa, J. A., & Priess, J. R. (2000). P granules in the germ cells of Caenorhabditis elegans adults are associated with clusters of nuclear pores and contain RNA. *Developmental Biology*, *219*(2), 315–333. http://doi.org/10.1006/dbio.2000.9607

Prahlad, V., Yoon, M., Moir, R. D., Vale, R. D., & Goldman, R. D. (1998). Rapid movements of vimentin on microtubule tracks: kinesin-dependent assembly of intermediate filament networks. *The Journal of Cell Biology*, *143*(1), 159–170. http://doi.org/10.1083/jcb.143.1.159

Puertollano, R., & Bonifacino, J. S. (2004). Interactions of GGA3 with the ubiquitin sorting machinery. *Nature Cell Biology*, *6*(3), 244–251. http://doi.org/10.1038/ncb1106

Puschnik, A. S., Majzoub, K., Ooi, Y. S., & Carette, J. E. (2017). A CRISPR toolbox to study virus-host interactions. *Nature Reviews. Microbiology*, *15*(6), 351–364. http://doi.org/10.1038/nrmicro.2017.29

Querido, E., Blanchette, P., Yan, Q., Kamura, T., Morrison, M., Boivin, D., et al. (2001). Degradation of p53 by adenovirus E4orf6 and E1B55K proteins occurs via a novel mechanism involving a Cullin-containing complex. *Genes & Development*, *15*(23), 3104–3117. http://doi.org/10.1101/gad.926401

Rabe, B., Vlachou, A., Panté, N., Helenius, A., & Kann, M. (2003). Nuclear import of hepatitis B virus capsids and release of the viral genome. *Pnas*, *100*(17), 9849–9854. http://doi.org/10.1073/pnas.1730940100

Ramanathan, H.N., Zhang, S., Douam, F., Mar, K.B., Chang, J., Yang, P.L., Schoggins, J.W., Ploss, A. & Lindenbach, B.D., A Sensitive Yellow Fever Virus Entry Reporter Identifies Valosin-Containing Protein (VCP/p97) as an Essential Host Factor for Flavivurs Uncoating. *mBio, 11*: e004670-20. https://doi.org/10.1128/mBio.00467-20.

Ratliff, M., Hill-Harfe, K. L., Gleason, E. J., Ling, H., Kroft, T. L., & L'Hernault, S. W. (2018). MIB-1 Is Required for Spermatogenesis and Facilitates LIN-12 and GLP-1 Activity in Caenorhabditis elegans. *Genetics*, *209*(1), 173–193. http://doi.org/10.1534/genetics.118.300807

Rios, R. M. (2014). The centrosome-Golgi apparatus nexus. *Philosophical Transactions of the Royal Society of London. Series B, Biological Sciences*, *369*(1650), 20130462. http://doi.org/10.1098/rstb.2013.0462

Ritchie, K. J., & Zhang, D.-E. (2004). ISG15: the immunological kin of ubiquitin. *Seminars in Cell & Developmental Biology*, *15*(2), 237–246. http://doi.org/10.1016/j.semcdb.2003.12.005

Robert, A., Tian, P., Adam, S. A., Kittisopikul, M., Jaqaman, K., Goldman, R. D., & Gelfand, V. I. (2019). Kinesin-dependent transport of keratin filaments: a unified mechanism for intermediate filament transport. *FASEB Journal : Official Publication of the Federation of American Societies for Experimental Biology*, *33*(1), 388–399. http://doi.org/10.1096/fj.201800604R

Roux, K. J., Kim, D. I., Raida, M., & Burke, B. (2012). A promiscuous biotin ligase fusion protein identifies proximal and interacting proteins in mammalian cells. *The Journal of Cell Biology*, *196*(6), 801–810. http://doi.org/10.1083/jcb.201112098

ROWE, W. P., HUEBNER, R. J., GILMORE, L. K., PARROTT, R. H., & WARD, T. G. (1953). Isolation of a cytopathogenic agent from human adenoids undergoing spontaneous degeneration in tissue culture. *Proceedings of the Society for Experimental Biology and Medicine. Society for Experimental Biology and Medicine (New York, N.Y.)*, *84*(3), 570–573. http://doi.org/10.3181/00379727-84-20714

Russell, W. C. (2009). Adenoviruses: update on structure and function. *Journal of General Virology*, *90*(Pt 1), 1–20. http://doi.org/10.1099/vir.0.003087-0

Sakin, V., Richter, S. M., Hsiao, H.-H., Urlaub, H., & Melchior, F. (2015). Sumoylation of the GTPase Ran by the RanBP2 SUMO E3 Ligase Complex. *The Journal of Biological Chemistry*, *290*(39), 23589–23602. http://doi.org/10.1074/jbc.M115.660118

Sanchez, A. D., & Feldman, J. L. (2017). Microtubule-organizing centers: from the centrosome to non-centrosomal sites. *Current Opinion in Cell Biology*, *44*, 93–101. http://doi.org/10.1016/j.ceb.2016.09.003

Saphire, A. C., Guan, T., Schirmer, E. C., Nemerow, G. R., & Gerace, L. (2000). Nuclear import of adenovirus DNA in vitro involves the nuclear protein import pathway and hsc70. *The Journal of Biological Chemistry*, *275*(6), 4298–4304. http://doi.org/10.1074/jbc.275.6.4298

Sarria, A. J., Lieber, J. G., Nordeen, S. K., & Evans, R. M. (1994). The presence or absence of a vimentin-type intermediate filament network affects the shape of the nucleus in human SW-13 cells. *Journal of Cell Science*, *107 (Pt 6)*, 1593–1607.

Sánchez, I., Piñol, P., Corral-Juan, M., Pandolfo, M., & Matilla-Dueñas, A. (2013). A novel function of Ataxin-1 in the modulation of PP2A activity is dysregulated in the spinocerebellar ataxia type 1. *Human Molecular Genetics*, *22*(17), 3425–3437. http://doi.org/10.1093/hmg/ddt197

Scheffner, M., Huibregtse, J. M., Vierstra, R. D., & Howley, P. M. (1993). The HPV-16 E6 and E6-AP complex functions as a ubiquitin-protein ligase in the ubiquitination of p53. *Cell*, *75*(3), 495–505. http://doi.org/10.1016/0092-8674(93)90384-3

Scherer, J., Yi, J., & Vallee, R. B. (2014). PKA-dependent dynein switching from lysosomes to adenovirus: a novel form of host-virus competition. *The Journal of Cell Biology*, *205*(2), 163–177. http://doi.org/10.1083/jcb.201307116

Schier, A. F., Neuhauss, S. C., Harvey, M., Malicki, J., Solnica-Krezel, L., Stainier, D. Y., et al. (1996). Mutations affecting the development of the embryonic zebrafish brain. *Development (Cambridge, England)*, *123*, 165–178.

Schindelin, J., Arganda-Carreras, I., Frise, E., Kaynig, V., Longair, M., Pietzsch, T., et al. (2012). Fiji: an open-source platform for biological-image analysis. *Nature Methods*, *9*(7), 676–682. http://doi.org/10.1038/nmeth.2019

Schmitz, A., Schwarz, A., Foss, M., Zhou, L., Rabe, B., Hoellenriegel, J., et al. (2010). Nucleoporin 153 arrests the nuclear import of hepatitis B virus capsids in the nuclear basket. *PLoS Pathogens*, *6*(1), e1000741. http://doi.org/10.1371/journal.ppat.1000741

Schoggins, J. W., & Falck-Pedersen, E. (2006). Fiber and penton base capsid modifications yield diminished adenovirus type 5 transduction and proinflammatory gene expression with retention of antigen-specific humoral immunity. *Journal of Virology*, *80*(21), 10634–10644. http://doi.org/10.1128/JVI.01359-06

Schoggins, J. W., Gall, J. G. D., & Falck-Pedersen, E. (2003). Subgroup B and F fiber chimeras eliminate normal adenovirus type 5 vector transduction in vitro and in vivo. *Journal of Virology*, *77*(2), 1039–1048. http://doi.org/10.1128/jvi.77.2.1039-1048.2003

Shen, Y., Liu, P., Jiang, T., Hu, Y., Au, F. K. C., & Qi, R. Z. (2017). The catalytic subunit of

DNA polymerase δ inhibits γTuRC activity and regulates Golgi-derived microtubules.(2017) *Nature Communications*, *8*(1), 554–13. http://doi.org/10.1038/s41467-017-00694-2
Shen, Y., Wang, K., & Qi, R.Z. (2019). The catalytic subunit of DNA polymerase δ is a nucleocytoplasmic shuttling protein. *Experimental Cell Research. 375*(2), 36-40. https://doi.org/10/1016/j.yexcr.2019.01.003.
Shi, X., van Mierlo, J. T., French, A., & Elliott, R. M. (2010). Visualizing the replication cycle of bunyamwera orthobunyavirus expressing fluorescent protein-tagged Gc glycoprotein. *Journal of Virology*, *84*(17), 8460–8469. http://doi.org/10.1128/JVI.00902-10
Shi, Y., Chan, D. W., Jung, S. Y., Malovannaya, A., Wang, Y., & Qin, J. (2011). A data set of human endogenous protein ubiquitination sites. *Molecular & Cellular Proteomics : MCP*, *10*(5), M110.002089. http://doi.org/10.1074/mcp.M110.002089
Shoeman, R. L., Hüttermann, C., Hartig, R., & Traub, P. (2001). Amino-terminal polypeptides of vimentin are responsible for the changes in nuclear architecture associated with human immunodeficiency virus type 1 protease activity in tissue culture cells. *Molecular Biology of the Cell*, *12*(1), 143–154. http://doi.org/10.1091/mbc.12.1.143
Shpetner, H. S., & Vallee, R. B. (1989). Identification of dynamin, a novel mechanochemical enzyme that mediates interactions between microtubules. *Cell*, *59*(3), 421–432. http://doi.org/10.1016/0092-8674(89)90027-5
Shpetner, H. S., & Vallee, R. B. (1992). Dynamin is a GTPase stimulated to high levels of activity by microtubules. *Nature*, *355*(6362), 733–735. http://doi.org/10.1038/355733a0
Smith, A. C., Poulin, K. L., & Parks, R. J. (2009). DNA genome size affects the stability of the adenovirus virion. *Journal of Virology*, *83*(4), 2025–2028. http://doi.org/10.1128/JVI.01644-08
Smith, J. G., Cassany, A., Gerace, L., Ralston, R., & Nemerow, G. R. (2008). Neutralizing antibody blocks adenovirus infection by arresting microtubule-dependent cytoplasmic transport. *Journal of Virology*, *82*(13), 6492–6500. http://doi.org/10.1128/JVI.00557-08
Sripada, S. & Dayaraj, C. (2010). Viral interactions with intermediate filaments: Paths less explored. Cell Health and Cytoskeleton. 2, 1-7. https://doi.org/10.2147/CHC.S8782
Stefanovic, S., Windsor, M., Nagata, K.-I., Inagaki, M., & Wileman, T. (2005). Vimentin rearrangement during African swine fever virus infection involves retrograde transport along microtubules and phosphorylation of vimentin by calcium calmodulin kinase II. *Journal of Virology*, *79*(18), 11766–11775. http://doi.org/10.1128/JVI.79.18.11766-11775.2005
Stempin, C. C., Chi, L., Giraldo-Vela, J. P., High, A. A., Häcker, H., & Redecke, V. (2011). The E3 ubiquitin ligase mind bomb-2 (MIB2) protein controls B-cell CLL/lymphoma 10 (BCL10)-dependent NF-κB activation. *The Journal of Biological Chemistry*, *286*(43), 37147–37157. http://doi.org/10.1074/jbc.M111.263384
Stopak, K., de Noronha, C., Yonemoto, W., & Greene, W. C. (2003). HIV-1 Vif blocks the antiviral activity of APOBEC3G by impairing both its translation and intracellular stability. *Molecular Cell*, *12*(3), 591–601. http://doi.org/10.1016/s1097-2765(03)00353-8
Stracker, T. H., Carson, C. T., & Weitzman, M. D. (2002). Adenovirus oncoproteins inactivate the Mre11-Rad50-NBS1 DNA repair complex. *Nature*, *418*(6895), 348–352. http://doi.org/10.1038/nature00863
Strunze, S., Engelke, M. F., Wang, I.-H., Puntener, D., Boucke, K., Schleich, S., et al. (2011). Kinesin-1-mediated capsid disassembly and disruption of the nuclear pore complex promote virus infection., *10*(3), 210–223. http://doi.org/10.1016/j.chom.2011.08.010
Sun, C., Luecke, S., Bodda, C., Jonsson, K.L., Cai, Y., Zhang, B-C., Jensen, S.B., Nordentoft, I.,

Jensen, J.M., Jakobsen, M.R., & Paludan, S.R. (2019). Cellular Requirements for Sensing and Elimination of Incoming HSV-1 DNA and Capsids. J*ournal of Interferon and Cytokine Research*, *39*(4), 191-204. http://doi.org/10.1089/jir.2018.0141.

Suomalainen, M., Nakano, M. Y., Boucke, K., Keller, S., & Greber, U. F. (2001). Adenovirus-activated PKA and p38/MAPK pathways boost microtubule-mediated nuclear targeting of virus. *EMBO Journal*, *20*(6), 1310–1319. http://doi.org/10.1093/emboj/20.6.1310

Suomalainen, M., Nakano, M. Y., Keller, S., Boucke, K., Stidwill, R. P., & Greber, U. F. (1999). Microtubule-dependent plus- and minus end-directed motilities are competing processes for nuclear targeting of adenovirus. *The Journal of Cell Biology*, *144*(4), 657–672. http://doi.org/10.1083/jcb.144.4.657

Swatek, K. N., & Komander, D. (2016). Ubiquitin modifications. *Cell Research*, *26*(4), 399–422. http://doi.org/10.1038/cr.2016.39

Teigler, J. E., Kagan, J. C., & Barouch, D. H. (2014). Late endosomal trafficking of alternative serotype adenovirus vaccine vectors augments antiviral innate immunity. *Journal of Virology*, *88*(18), 10354–10363. http://doi.org/10.1128/JVI.00936-14

Thakar, K., Karaca, S., Port, S. A., Urlaub, H., & Kehlenbach, R. H. (2013). Identification of CRM1-dependent Nuclear Export Cargos Using Quantitative Mass Spectrometry. *Molecular & Cellular Proteomics : MCP*, *12*(3), 664–678. http://doi.org/10.1074/mcp.M112.024877

Thyberg, J., & Moskalewski, S. (1993). Relationship between the Golgi complex and microtubules enriched in detyrosinated or acetylated alpha-tubulin: studies on cells recovering from nocodazole and cells in the terminal phase of cytokinesis. *Cell and Tissue Research*, *273*(3), 457–466. http://doi.org/10.1007/bf00333700

Tollefson, A. E., Scaria, A., Hermiston, T. W., Ryerse, J. S., Wold, L. J., & Wold, W. S. (1996). The adenovirus death protein (E3-11.6K) is required at very late stages of infection for efficient cell lysis and release of adenovirus from infected cells. *Journal of Virology*, *70*(4), 2296–2306.

Trotman, L. C., Mosberger, N., Fornerod, M., Stidwill, R. P., & Greber, U. F. (2001). Import of adenovirus DNA involves the nuclear pore complex receptor CAN/Nup214 and histone H1. *Nature Cell Biology*, *3*(12), 1092–1100. http://doi.org/10.1038/ncb1201-1092

Tseng, L.-C., Zhang, C., Cheng, C.-M., Xu, H., Hsu, C.-H., & Jiang, Y.-J. (2014). New classes of mind bomb-interacting proteins identified from yeast two-hybrid screens. *PLoS ONE*, *9*(4), e93394. http://doi.org/10.1371/journal.pone.0093394

Tyanova, S., Temu, T., Sinitcyn, P., Carlson, A., Hein, M. Y., Geiger, T., et al. (2016). The Perseus computational platform for comprehensive analysis of (prote)omics data. *Nature Methods*, *13*(9), 731–740. http://doi.org/10.1038/nmeth.3901

Ungerechts, G., Bossow, S., Leuchs, B., Holm, P. S., Rommelaere, J., Coffey, M., et al. (2016). Moving oncolytic viruses into the clinic: clinical-grade production, purification, and characterization of diverse oncolytic viruses. *Molecular Therapy. Methods & Clinical Development*, *3*, 16018. http://doi.org/10.1038/mtm.2016.18

Vallee, R. B., & Sheetz, M. P. (1996). Targeting of motor proteins. *Science*, *271*(5255), 1539–1544. http://doi.org/10.1126/science.271.5255.1539

Varshavsky, A. (2006). The early history of the ubiquitin field. *Protein science : a publication of the Protein Society* (Vol. 15, pp. 647–654). John Wiley & Sons, Ltd. http://doi.org/10.1110/ps.052012306

Villumsen, B. H., Danielsen, J. R., Povlsen, L., Sylvestersen, K. B., Merdes, A., Beli, P., et al. (2013). A new cellular stress response that triggers centriolar satellite reorganization and

ciliogenesis. *EMBO Journal*, *32*(23), 3029–3040. http://doi.org/10.1038/emboj.2013.223
Wang, B., Rekosh, D., & Hammarskjold, M.-L. (2015). Evolutionary conservation of a molecular machinery for export and expression of mRNAs with retained introns. *RNA (New York, N.Y.)*, *21*(3), 426–437. http://doi.org/10.1261/rna.048520.114
Wang, H., Li, Z.-Y., Liu, Y., Persson, J., Beyer, I., Möller, T., et al. (2011). Desmoglein 2 is a receptor for adenovirus serotypes 3, 7, 11 and 14. *Nature Medicine*, *17*(1), 96–104. http://doi.org/10.1038/nm.2270
Wang, I.-H., Burckhardt, C. J., Yakimovich, A., Morf, M. K., & Greber, U. F. (2017). The nuclear export factor CRM1 controls juxta-nuclear microtubule-dependent virus transport. *Journal of Cell Science*, *130*(13), 2185–2195. http://doi.org/10.1242/jcs.203794
Ward, S., Argon, Y., & Nelson, G. A. (1981). Sperm morphogenesis in wild-type and fertilization-defective mutants of Caenorhabditis elegans. *The Journal of Cell Biology*, *91*(1), 26–44. http://doi.org/10.1083/jcb.91.1.26
Wen, F., Armstrong, N., Hou, W., Cruz-Cosme, R., Obwolo, L. A., Ishizuka, K., et al. (2019). Zika virus increases mind bomb 1 levels, causing degradation of pericentriolar material 1 (PCM1) and dispersion of PCM1 granules from the centrosome. *The Journal of Biological Chemistry*, jbc.RA119.010973. http://doi.org/10.1074/jbc.RA119.010973
Whittaker, G. R., & Helenius, A. (1998). Nuclear import and export of viruses and virus genomes. *Virology*, *246*(1), 1–23. http://doi.org/10.1006/viro.1998.9165
Wickham, T. J., Filardo, E. J., Cheresh, D. A., & Nemerow, G. R. (1994). Integrin alpha v beta 5 selectively promotes adenovirus mediated cell membrane permeabilization. *The Journal of Cell Biology*, *127*(1), 257–264.
Widjaja, I., de Vries, E., Tscherne, D. M., García-Sastre, A., Rottier, P. J. M., & de Haan, C. A. M. (2010). Inhibition of the ubiquitin-proteasome system affects influenza A virus infection at a postfusion step. *Journal of Virology*, *84*(18), 9625–9631. http://doi.org/10.1128/JVI.01048-10
Wiethoff, C. M., Wodrich, H., Gerace, L., & Nemerow, G. R. (2005). Adenovirus protein VI mediates membrane disruption following capsid disassembly. *Journal of Virology*, *79*(4), 1992–2000. http://doi.org/10.1128/JVI.79.4.1992-2000.2005
Wilkinson, K. D., Urban, M. K., & Haas, A. L. (1980). Ubiquitin is the ATP-dependent proteolysis factor I of rabbit reticulocytes. *The Journal of Biological Chemistry*, *255*(16), 7529–7532.
Wodrich, H., Henaff, D., Jammart, B., Segura-Morales, C., Seelmeir, S., Coux, O., et al. (2010). A capsid-encoded PPxY-motif facilitates adenovirus entry. *PLoS Pathogens*, *6*(3), e1000808. http://doi.org/10.1371/journal.ppat.1000808
Wold, W. S. M., & Toth, K. (2013). Adenovirus vectors for gene therapy, vaccination and cancer gene therapy. *Current Gene Therapy*, *13*(6), 421–433. http://doi.org/10.2174/1566523213666131125095046
Xu, G., Deglincerti, A., Paige, J. S., & Jaffrey, S. R. (2014). Profiling lysine ubiquitination by selective enrichment of ubiquitin remnant-containing peptides. *Methods in Molecular Biology (Clifton, N.J.)*, *1174*(Chapter 4), 57–71. http://doi.org/10.1007/978-1-4939-0944-5_4
Xue, Y., Johnson, J. S., Ornelles, D. A., Lieberman, J., & Engel, D. A. (2005). Adenovirus protein VII functions throughout early phase and interacts with cellular proteins SET and pp32. *Journal of Virology*, *79*(4), 2474–2483. http://doi.org/10.1128/JVI.79.4.2474-2483.2005

Yau, R., & Rape, M. (2016). The increasing complexity of the ubiquitin code. *Nature Cell Biology*, *18*(6), 579–586. http://doi.org/10.1038/ncb3358

Yea, C., Dembowy, J., Pacione, L., & Brown, M. (2007). Microtubule-mediated and microtubule-independent transport of adenovirus type 5 in HEK293 cells. *Journal of Virology*, *81*(13), 6899–6908. http://doi.org/10.1128/JVI.02330-05

Yu, G.-Y., & Lai, M. M. C. (2005). The ubiquitin-proteasome system facilitates the transfer of murine coronavirus from endosome to cytoplasm during virus entry. *Journal of Virology*, *79*(1), 644–648. http://doi.org/10.1128/JVI.79.1.644-648.2005

Zaarur, N., Xu, X., Lestienne, P., Meriin, A. B., McComb, M., Costello, C. E., et al. (2015). RuvbL1 and RuvbL2 enhance aggresome formation and disaggregate amyloid fibrils. *EMBO Journal*, *34*(18), 2363–2382. http://doi.org/10.15252/embj.201591245

Zeitelhofer, M., Karra, D., Macchi, P., Tolino, M., Thomas, S., Schwarz, M., et al. (2008). Dynamic interaction between P-bodies and transport ribonucleoprotein particles in dendrites of mature hippocampal neurons. *The Journal of Neuroscience : the Official Journal of the Society for Neuroscience*, *28*(30), 7555–7562. http://doi.org/10.1523/JNEUROSCI.0104-08.2008

Zhang, F., Yim, Y.-I., Scarselletta, S., Norton, M., Eisenberg, E., & Greene, L. E. (2007). Clathrin adaptor GGA1 polymerizes clathrin into tubules. *The Journal of Biological Chemistry*, *282*(18), 13282–13289. http://doi.org/10.1074/jbc.M700936200

Zhang, K., Daigle, J. G., Cunningham, K. M., Coyne, A. N., Ruan, K., Grima, J. C., et al. (2018). Stress Granule Assembly Disrupts Nucleocytoplasmic Transport. *Cell*, *173*(4), 958–971.e17. http://doi.org/10.1016/j.cell.2018.03.025

Zhang, L., & Gallagher, P. J. (2009). Mind bomb 1 regulation of cFLIP interactions. *American Journal of Physiology. Cell Physiology*, *297*(5), C1275–83. http://doi.org/10.1152/ajpcell.00214.2009

Zhang, L., Bukreyev, A., Thompson, C. I., Watson, B., Peeples, M. E., Collins, P. L., & Pickles, R. J. (2005). Infection of ciliated cells by human parainfluenza virus type 3 in an in vitro model of human airway epithelium. *Journal of Virology*, *79*(2), 1113–1124. http://doi.org/10.1128/JVI.79.2.1113-1124.2005

Zhang, N.-H., Song, L.-B., Wu, X.-J., Li, R.-P., Zeng, M.-S., Zhu, X.-F., et al. (2008). Proteasome inhibitor MG-132 modifies coxsackie and adenovirus receptor expression in colon cancer cell line lovo. *Cell Cycle (Georgetown, Tex.)*, *7*(7), 925–933. http://doi.org/10.4161/cc.7.7.5621

Zhang, Q., Sharma, N. R., Zheng, Z.-M., & Chen, M. (2019). Viral Regulation of RNA Granules in Infected Cells. *Virologica Sinica*, *34*(2), 175–191. http://doi.org/10.1007/s12250-019-00122-3

Zhao, L., Zhang, P., Su, X.-J., & Zhang, B. (2018). The ubiquitin ligase TRIM56 inhibits ovarian cancer progression by targeting vimentin. *Journal of Cellular Physiology*, *233*(3), 2420–2425. http://doi.org/10.1002/jcp.26114

Zhou, J., Scherer, J., Yi, J., & Vallee, R. B. (2018). Role of kinesins in directed adenovirus transport and cytoplasmic exploration. *PLoS Pathogens*, *14*(5), e1007055. http://doi.org/10.1371/journal.ppat.1007055

Zhu, Y., Zhang, Y., Sui, Z., Zhang, Y., Liu, M., & Tang, H. (2017). USP14 de-ubiquitinates vimentin and miR-320a modulates USP14 and vimentin to contribute to malignancy in gastric cancer cells. *Oncotarget*, *8*(30), 48725–48736. http://doi.org/10.18632/oncotarget.10706